Interactive bioinspired polymers to mediate specific and non-specific adhesion

Inaugural-Dissertation

to obtain the academic degree
Doctor rerum naturalium (Dr. rer. nat)
of the Faculty of Mathematics and Natural Sciences
at the Heinrich-Heine-University Düsseldorf

submitted by

Alexander Klaus Strzelczyk
from Aachen

Düsseldorf, August 2020

From the Institute of Organic Chemistry and Macromolecular Chemistry
at the Heinrich-Heine-University Düsseldorf

Published by permission of the
Faculty of Mathematics and Natural Sciences at
Heinrich-Heine-University Düsseldorf

Supervisor: Jun. Prof. Dr. Stephan Schmidt
Co-supervisor: Prof. Dr. Matthias Karg

Date of the oral examination: 06.10.2020

The work presented in this thesis was accomplished in a period between Oktober 2016 and July 2020 at the Chair of Macromolecular Chemistry at the Institute of Organic and Macromolecular Chemistry at the Heinrich Heine University of Düsseldorf under supervision of Jun. Prof. Dr. Stephan Schmidt.

Declaration of authorship

I hereby declare that the thesis submitted is my own work without making use of impermissible aids, considering the “Rules on the Principles for Safeguarding Good Scientific Practice at Heinrich Heine University Düsseldorf”. All direct or indirect sources are acknowledged in the bibliography as references. I further declare that I have not submitted this nor a similar thesis at any other examination board in order to obtain a degree.

Düsseldorf, 06.08.2020

_____

(Alexander Klaus Strzelczyk)

„Alle Wahrheiten sind einfach zu verstehen,
sobald sie entdeckt wurden;
die Schwierigkeit ist sie zu entdecken“

Galileo Galilei (1564-1642)

Table of Contents

Abstract

This work investigates and utilizes two types of biomolecular motifs that are widely known for their adhesive properties: carbohydrates and catechols. Carbohydrates are involved in almost all adhesive interactions between cells and catechols are the prime molecular groups for biological wet adhesion, e.g. employed by mussels. However, despite the vigorous research activities in the area of carbohydrate and catechol adhesion as well as the high demand for smart and accessible adhesives, synthetic polymers with the nature-equivalent functions and performance were not yet achieved. This is because our current understanding of how the involved specific adhesion processes are mechanistically executed, remain fragmented at best. Therefore, this work quantifies the adhesive interactions of functional catechol and carbohydrate bearing macromolecules.

First, the adhesive properties of catechol-based molecules inspired by adhesive mussel foot proteins were investigated. Therefore, different oligomers with varying combinations and positioning of catechol, tertiary amine, and primary amide on the oligomer backbone were analyzed. The tertiary amines were chosen to study if the cation is responsible for the displacement of salt and water layer by which the adhesion would be amplified. The primary amides were chosen because the mussel foot protein-3 (MFP-3), one of the major constituents of the mussel glue, is rich in primary amides, which might synergize with catechols and amines for strong underwater adhesion. The results of the soft colloidal probe adhesion assay (SCP-RICM) over a pH range from pH 3 to pH 8 provides a quantitative insight to the catechol, amine and/or amide functionalized oligomers on glass surfaces. The combination of amine and catechol synergize to increase adhesion and show dependence towards the positioning of the functional groups in the oligomer sequence. Additionally, the distance between both groups is important. Interestingly, combinations of primary amides with catechol and amine, respectively, show very high adhesion energies at low pH values. Since these combinations are present in the MFP-3 this hints at an intricate interplay of intra- and intermolecular hydrogen bonding of the catechol, amine, and amide groups in the natural sequence, which is controlled by the positioning of the residues along the sequence.

The second part is of this thesis is the investigation of carbohydrate mediated specific adhesion between ligand and receptor. Therefore, the well-known model system mannose concanavalin A (ConA) is used. First, carbohydrate bearing polymers with thermoresponsive properties are synthesized. Here, a poly(active ester) is synthesized and functionalized with amine bearing carbohydrates and isopropylamine, where the latter gives thermoresponsive poly(*N*-isopropyl acrylamide) (PNIPAM) repeating units. The effect of different carbohydrate and PNIPAM ratios and the effect of linkers with varying hydrophilicity, as well as the effects of the coil to globule transition upon temperature increase are analyzed. The polymers are used as temperature-dependent adhesion inhibitors of ConA and *Escherichia coli* (*E. coli*) binding to a mannan model surface. Depending on the amount of carbohydrates incorporated into the polymer, changes in the adhesion inhibition can be observed. For low amounts of carbohydrates around 1% or 2%, the inhibitory effect is strongly temperature-dependent but for higher functionalization degrees the cloud point cannot be reached and, therefore, a coil to globule transition takes not place. Interestingly, the inhibition of ConA decreases at elevated temperature whereas for *E. coli* it increases. This can be explained by the size of the receptors, where, when collapsed, the accessibility of ligands is reduced for the molecularly-sized ConA but increased for the micrometer-sized bacteria.

In addition to their inhibitory potential, those polymers are used for adhesion studies to investigate the ligand-receptor interaction at soft/solid interfaces. Here, the SCP-RICM adhesion assay is used to quantify adhesion energies. For this experiment, the polymers are grafted on a poly(ethylene glycol) diacrylamide based hydrogel, the soft colloidal probe (SCP), and the binding protein ConA on a glass surface. Using reflection interference contrast microscopy, the contact areas between polymer functionalized SCPs and protein-coated glass surfaces are measured at different temperatures and adhesion energies are calculated using the Johnson-Kendall-Roberts (JKR) theory. These studies showed that for temperatures above the LCST, the adhesion energies can be switched via temperature change. Additionally, the carbohydrate linker hydrophilicity shows an influence on the adhesion, where the more hydrophilic linker improved the temperature switch, whereas the hydrophobic linker shows no clear temperature dependence. The linker seems to play an important role in the ligand presentation on either the polymer coil or the collapsed globule. Moreover, the adhesion shows a strong hysteresis when cooling back to 20 °C indicating that irreversible non-specific binding may occur at elevated temperatures.

Using the JKR model for the SCP adhesion assay requires the determination of the elastic modulus of the SCPs. Therefore, atomic force microscopy (AFM) indentation measurements were done to quantify the elastic moduli of the SCPs. PEG-SCPs are microgels composed of crosslinked bifunctional PEG chains. Non-functionalized PEG microgels, show an increase in elastic modulus with increasing temperature, which is in accordance with De Gennes scaling between the temperature and the elastic modulus for polymer networks in good solvents. When the thermoresponsive polymers are grafted onto the PEG microgels, this behavior changes. Below the LCST an increase in elastic modulus can be seen, owing to the decreasing effective mesh size by the extended PNIPAM chains grafted into the PEG network. When increasing the temperature, the grafted PNIPAM polymers collapse, which results in decreasing elastic moduli, in contrast to the De Gennes scaling. Due to the thermoresponsiveness of the PNIPAM grafts and their collapse at elevated temperature the effective mesh width is increased, which has a strong influence on the elastic modulus. This unexpected change in the elastic modulus may be important for different applications, especially in medical applications, because the stiffness of tissue influences many different cell-cell interactions and communication processes.

List of publications

Publications included in this thesis

Sequence-defined positioning of amine and amide residues to control catechol driven wet adhesion

Lukas Fischer[#], **Alexander K. Strzelczyk**[#], Nils Wedler, Christian Kropf, Stephan Schmidt, Laura Hartmann

Manuscript submitted in *Chemical Science*

[#]equal contributions

Temperature switchable glycopolymers and their conformation-dependent binding to receptor targets

Tanja Paul[#], **Alexander K. Strzelczyk**[#], Melina I. Feldhof, Stephan Schmidt

Biomacromolecules **2020**, *21*, 7, 2913–2921.

[#]equal contributions

Quantifying thermo-switchable carbohydrate mediated interactions via soft colloidal probe adhesion studies

Alexander K. Strzelczyk, Tanja Paul, Stephan Schmidt

Manuscript accepted in *Macromolecular Bioscience*

Publications not included in this thesis

Interactive polymer gels as biomimetic sensors for carbohydrate interactions and capture-release devices for pathogens

Stephan Schmidt, Tanja Paul, **Alexander K. Strzelczyk**

Macromolecular Chemistry and Physics, **2019**, *22*, 1900323.

Thermosensitive display of carbohydrate ligands on microgels for switchable binding of proteins and bacteria

Tanja J. Paul, Sophie Rübel, Marco Hildebrandt, **Alexander K. Strzelczyk**, Carina Spormann, Thisbe K. Lindhorst, Stephan Schmidt

ACS Applied Materials & Interfaces, **2019**, 11, 26674.

Hydrogel Microparticles as Sensors for Specific Adhesion: Case Studies on Antibody Detection and Soil Release Polymers

Alexander K. Strzelczyk, Hanqing Wang, Andreas Lindhorst, Johannes Waschke, Tilo Pompe, Christian Kropf, Benoit Luneau, Stephan Schmidt.

Gels, **2017**, *3*(3), 31.

Presentations on Professional Conferences

Alexander Strzelczyk, Tanja Paul, Melina Feldhof, Florian Malotke, Stephan Schmidt, „Quantifying specific adhesion under water via Soft Colloidal Probes", *International Conference on Adhesion in Aqueous Media: From Biology to Synthetic Materials, AAM2019,* September 09-12, **2019**, Dresden.

Alexander Strzelczyk, Tanja Paul, Melina Feldhof, Florian Malotke, Stephan Schmidt, „Adhesion studies of thermoswitchable ligand receptor interactions via Soft Colloidal Probe adhesion assay", *15th Zsigmondy Colloquium,* Juli 10-12, **2019**, Dresden.

Alexander Strzelczyk, Melina Feldhof, Florian Malotke, Stephan Schmidt, „Study of temperature switchable adhesion between ligands and receptors by Soft Colloidal Probe", *14th Zsigmondy Colloquium,* April 09-11, **2018**, Mainz.

1. General Introduction

The term bioadhesion describes interaction processes between surfaces by interfacial forces, where at least one of those surfaces is of biological nature.[1] Bioadhesion phenomena occur in different settings, e.g. between natural living tissue (e.g. cell-cell adhesion) or between natural non-living materials (e.g. rocks and mussel byssus threads). The interaction forces between the adhering interfaces are discriminated between ”specific” and “non-specific”. Broadly speaking, specific bioadhesion are adhesion events mediated by ligand-receptor interactions, working after the lock-key principle. Hence, non-specific bioadhesion are adhesion events that do not fit this condition. This differentiation being more dependent on structural properties, the molecular interactions taking place in both kinds of bioadhesion are the same.[2,3] Non-covalent binding can occur through different types of interactions. One group of interactions are the van der Waals forces that can be distinguished in the following: dipole-dipole, induced dipole-dipole, and induced dipole-induced dipole. Those forces are defined by the IUPAC as following:

> “The attractive or repulsive forces between molecular entities (or between groups within the same molecular entity) other than those due to bond formation or to the electrostatic interaction of ions or of ionic groups with one another or with neutral molecules. The term includes: dipole–dipole, dipole-induced dipole and London (instantaneous induced dipole-induced dipole) forces. The term is sometimes used loosely for the totality of non-specific attractive or repulsive intermolecular forces.”[4]

Moreover, the London forces are always present due to polarization of the electron cloud leading to attraction between nonpolar molecules and explain condensation of noble gases. Another group of interactions are ionic interactions. These are coulombic interactions that attract opposing or repulse same charges. Many functional groups can receive or deliver protons depending on the pH to build ions.

Additionally, there are two “special cases” of non-covalent interactions: hydrogen bonds and π-stacking or π-π-interactions. Hydrogen bonds occur when a functional group X-H presenting a hydrogen bound to an electronegative atom, e.g. O, N, and an electronegative lone pair presenting atom Y, e.g. Cl, N, approach. Here, X and Y can be the same atom. π-stacking occurs when two π-systems or more approach facing with planar sites of the

molecule.[5] Those can occur either in a sandwich conformation or in a parallel displaced one.[6]

These are parts of interactions occurring between molecules in bulk or in solvent. Considering the combinations of those interactions influencing bioadhesion processes in many different ways, there are many adjustments that can be done when mimicking bioadhesives.

Natural bioadhesives show a range of features that are highly desirable in synthetic adhesives, for example, the strong underwater adhesion of mussel glues or the response to environmental parameters that lead to well defined specific interaction processes on the cellular level and downstream biological functions. Therefore, natural bioadhesives inspire scientists to create technical innovations in the area of hard- as well as soft-tissue applications.[7] But for bioadhesion in biological systems, it can be distinguished between the following types of bioadhesion:[8]

Type I: adhesion between two biological systems

Type II: adhesion of biological phase to artificial surface

Type III: artificial material adheres to biological substrate

1.1. Mussel inspired adhesion

For a long time, synthetic adhesives were developed to bind dry, water-free material interfaces, but most bioadhesion processes take place in the presence of water.[9] Some organisms for example use mucins with a high amount of water to generate adhesive secretes for defense[10,11] but one of the best-studied underwater adhesives is produced by marine organisms such as mussels and barnacles.[12] Those organisms have developed adhesion mechanisms that enable the adhesion to natural but also to artificial surfaces,[13] even to those that are considered to be anti-adhesive like Teflon®.[14] Therefore, for industry and research it is important to understand the adhesion mechanisms of these mussels to such surfaces. For example, the marine organism adhesion to ship hulls leads to high costs in a range of one billion dollars for the US Navy alone (estimation from 2002)[15] due to changes in hydrodynamics of the hull and related higher fuel consumption.[16] In the history of anti-fouling, the used agents were toxic additives to paints or coatings but those are

banned for environmental reasons.[17] By understanding underlying adhesion mechanisms that take place it is possible to modify the surfaces to become anti-adhesive.[18,19]

Additionally, marine organisms not only adhere to surfaces in wet conditions but also at high salt concentrations, which is quite challenging for existing adhesives. Therefore, mussel inspired adhesives can have applications in medical areas for example as a tissue adhesive.[20] Due to biocompatibility mussel inspired adhesives can be applied broadly when compared to common tissue adhesives such as cyanoacrylate or gelatin-resorcinol-formaldehyde based adhesives, that are not only toxic but also generate heat during the consolidation process.[21] Therefore, understanding the process of mussel adhesion is very important to be able to prevent undesirable marine adhesion or to create synthetic mimicries with superior underwater adhesive properties.

1.1.1. Mechanism of mussel adhesion

Mussels adhere to surfaces by deposition of a protein mixture onto the surface with the mussel foot, a distal region usually outside the shell. After deposition, the foot detaches from the surface forming a byssal filament and a plaque.[22] The byssal filament and the plaque contain at least 20 different proteins that can be localized in the filament and plaque.[23] In the footprints of detached mussels, the mussel foot proteins (MFP) MFP-3, MFP-5, and MFP-6 were found which are thought to prime the surface for adhesion.[24] The analysis of amino acid sequences in MFP-3[25] and MFP-5[24] showed high content of 3,4-dihydroxyphenylalanine (DOPA) of roughly 20% and 30%, respectively. Moreover, cationic amino acids especially arginine in MFP-3 and lysine in MFP-5 were found (see Figure 1). These two MFPs are considered to have a high influence on the adhesion process.[26]

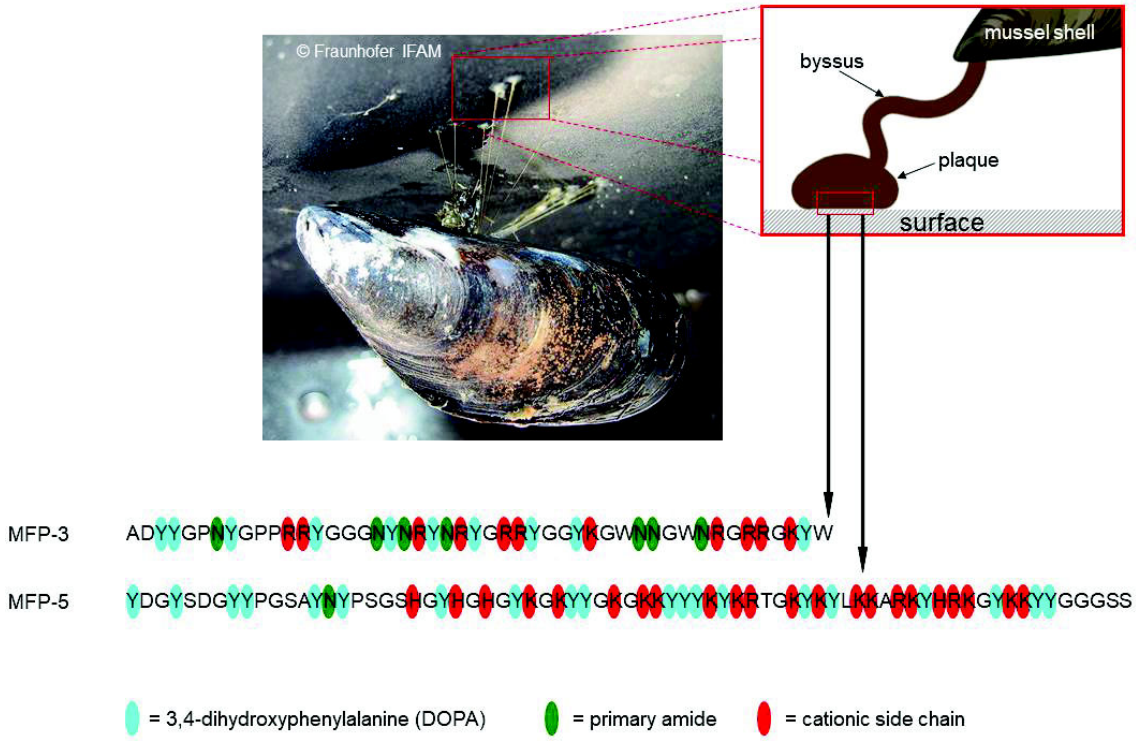

Figure 1 Image of a mussel adhering to a surface after deposition of proteins by mussel foot and formation of plaque and byssus filament (printed with permission from Fraunhofer IFAM) and the schematic representation (created with BioRender). The amino acid sequence of MFP-3[25] and -5,[24] that are active in the adhesion process of mussels, with marking of 3,4-dihydroxyphenylalanine (DOPA), primary amide and cationic side chains.

Every MFP appears to have different functions in the adhesion process. For example, MFP-6, even when it is found in residues of detached mussels, has, due to its high amount of thiol groups (nine cysteines[27]), a strong influence on the reducing activity[28] but overall weak adhesive properties.[29] Therefore, it is responsible for the reduction of O_2 and quinone formation.[30]

The mechanism of mussel adhesion is believed to depend on the interactions between cationic and DOPA residues in MFP-3 and MFP-5. Even though the amount of DOPA in those proteins is very high, the number of cationic groups is even higher for both of them. The cationic groups are supposed to initiate the contact between protein and the negatively charged surface by displacing of the hydration shell and ion barrier due to their cationic charge.[31,32] Afterwards, the catechol residues can attach to the surface and form hydrogen bonds and stronger covalent bonds leading to high adhesion energies (see Figure 2).

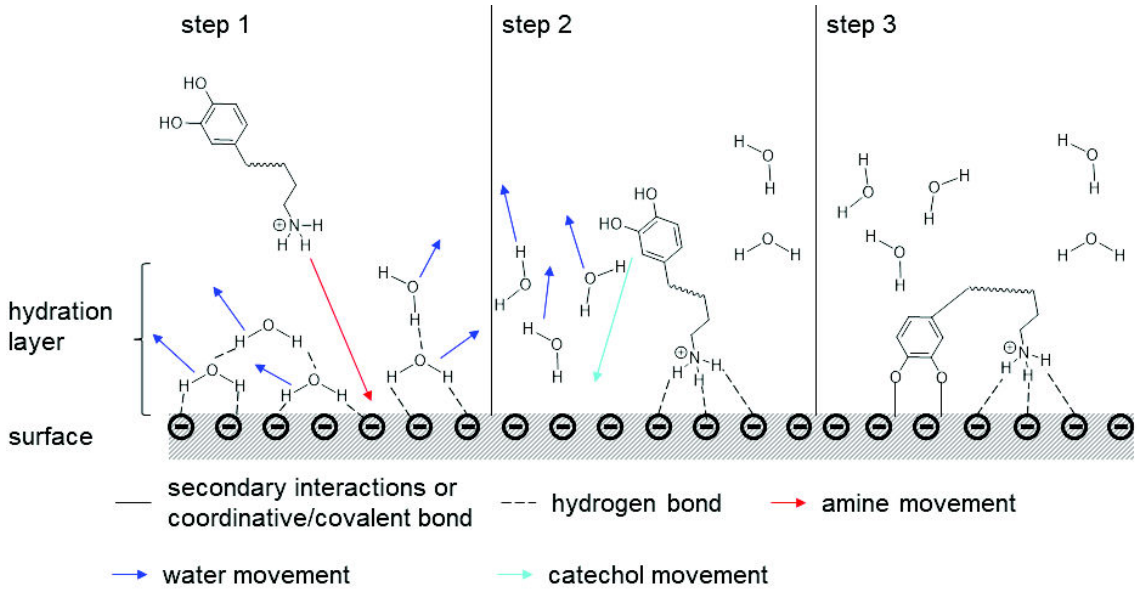

Figure 2 Proposed mechanism of mussel adhesion. The cationic amino acid of MFP-3 or MFP-5 interacts with the surface removing the hydration layer and building hydrogen bonds (step 1). Next, the catechol can attach to the surface due to the removal of water (step 2). In the end the catechol can build hydrogen bonds or other secondary interactions, coordinative bonds or covalent bonds depending on the surface properties (step 3).[32,31]

In this proposed mechanism the highly abundant primary amides in the MFP-3 sequence appear to play no role as described in more detail later in this work in chapter 5.1. The amount of primary amides in MFP-3 is with 15% in the range of both catechol and cationic groups but not noted in literature. It is believed that these "helix breaker" amino acids increase the flexibility of the proteins to enhance the DOPA availability. The first part of this work investigates the role of amides on DOPA mediated adhesion. We hypothesize that the amide resonance leads to a partially ionic state (see Figure 3), which can possibly work the same way as the amine and removing the hydration layer from the surface. The amount of the zwitterionic form is roughly 30%[33] and thus the potential to influence the adhesion due to strong electrostatic interactions. Therefore, the amides may play a more decisive role in natural mussel adhesives.

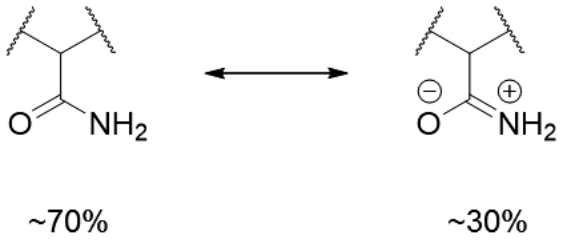

Figure 3 Amide resonance leading to a zwitterionic form of amides. The double bond between nitrogen and carbon (right) lead to double bond characteristics of this bond leading to a high rotation barrier for amides. The percentage numbers indicate the amount of each mesomeric form in solution.[33]

1.2. Carbohydrate mediated adhesion on the cellular level

Generally, all types of interactions that have a cell involved in the bioadhesive process can be summed up with the term "cytoadhesion".[34] Compared to other bioadhesion processes cytoadhesion is often based on specific interactions that take place between both cell surfaces. Specific ligands and receptors at cell surfaces interact with each other and lead to adhesion, i.e. cell contacts, and downstream processes such as signaling and cell-cell communication.[35,36,37] Pathological cells do not differ in the mechanism when adhering to a normal cell but in the presentation of certain proteins on the cell surface. Some cancer cells for example have different proteins that they overexpress such as EGF receptors in squamous tumors[38] or the CD44 receptor in breast cancer cells (see Table 1).[39] Thereby depending on the receptor it is possible to target certain cells by using the receptor-specific ligand. This is one way for targeted drug delivery or marker applications.[40] Moreover, this possibility can be used to target receptors on bacteria or viruses.[41,42] By targeting bacterial or viral receptors the adhesion to cells can be inhibited and, therefore, the infection can potentially be prevented, because the attachment of bacteria or virus onto the cell is considered to be the initial step of infection before the protective barrier of the cell is destroyed.[43] Due to the high amount of deaths caused by infections of three million in 2012 and increasing problems with bacterial resistances against conservative treatments such as antibiotics, this field of research has become more important over the past years.[44]

Table 1 Examples of ligand-receptor pairs that play an important role in different for cell-cell interactions such as adhesion or communication processes.[45,46,47,48,49,50,51]

ligand	receptor	physiological function
sialic acid	sialoadhesin	cell adhesion
mannose, glucose	concanavalin A	model system for sugar-protein interactions
hyaluronan	CD44	cell adhesion
galactose	LecA	biofilm formation of *P. aeruginosa*
fucose	LecB	biofilm formation of *P. aeruginosa*
sialic acid	hemagglutinin	virus (influenza) adhesion to cells
mannose	FimH	*E. Coli* adhesion

1.2.1. The Glycocalyx

Adhesion, communication, and signaling processes that take place between cells are mediated mainly by carbohydrate interactions, in particular in the first phases of contact. The carbohydrate layer on cell surfaces is called “glycocalyx” and can be found on every mammalian cell.[52] The carbohydrate chains are bound to lipids from the cell membrane but can also be bound to proteins (see Figure 4). Those lipids and proteins are therefore called glycolipids and -proteins.[53]

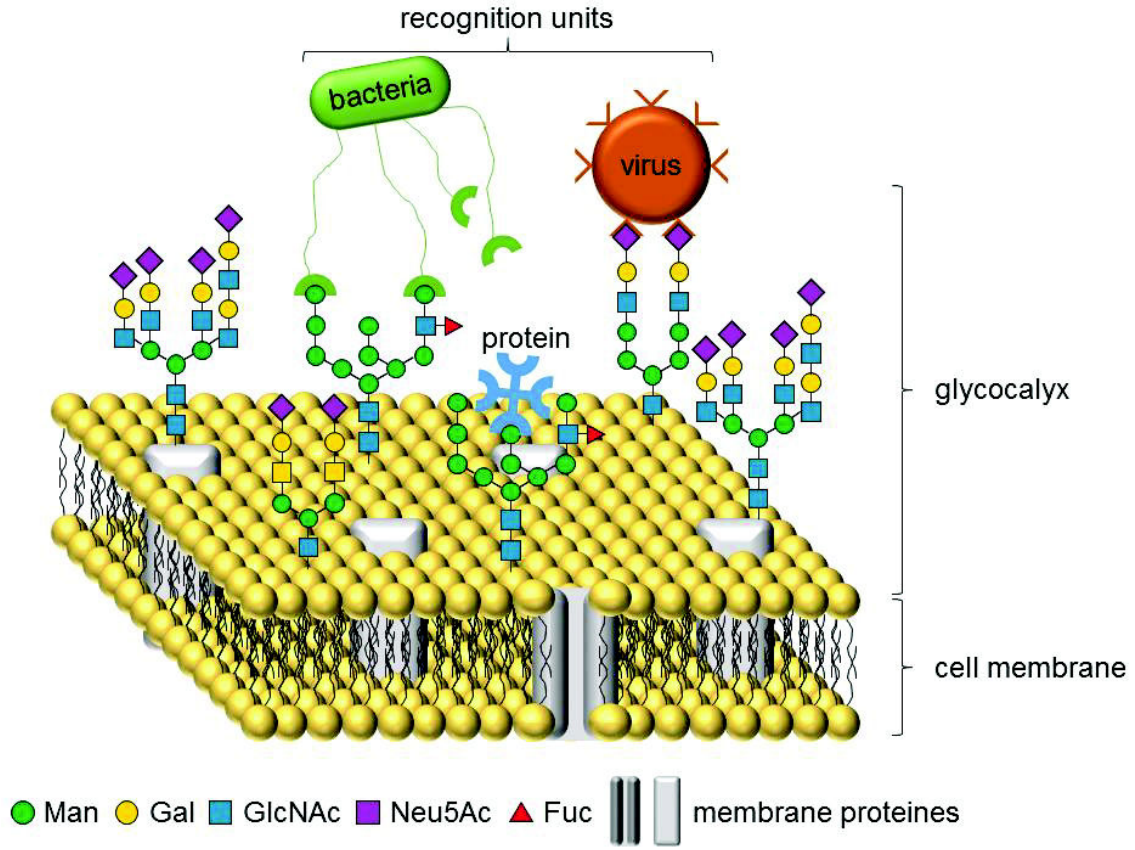

Figure 4 Schematic presentation of a cell surface. The cell membrane is decorated with covalently bound carbohydrate chains. Those carbohydrates can interact with different receptors like cell proteins or antibodies for signaling and adhesion processes, but also viruses or bacteria can adhere to those ligands to infect the cell. (Glycans adapted from 54).

Ligands and receptors are molecules that interact with each other on a non-covalent basis as for example carbohydrates and lectins. The specificity for those ligand and receptor pairs result from the hydrogen bonds formed between functional groups on the

carbohydrate and amino acid of the protein or coordination bonds to metal ions needed for the interactions in certain lectins.[55] This interaction can be described with the lock-key principle.

A particularly important factor for carbohydrate-lectin interactions is an effect called "multivalency". Single interactions between ligand and receptor are usually very weak due to its characteristics of being secondary interactions. To overcome this weakness in affinity nature presents multiple ligands and receptors to form many binding events and therefore increase the strength of the overall interactions.[56] Multivalency is not only important in specific but also non-specific interactions. With nature as a model, e.g. burr, artificial materials such as velcro have been invented and adapted for everyday life.[57] For weak non-covalent but highly multivalent carbohydrate interactions in addition to their equilibrium between bound and unbound, in comparison to burr, not only the strength of those interactions is an issue but also the association and dissociation. By multivalent binding ligands and receptors have more bound modes in comparison to single ligand-receptor interactions were only one bound and unbound mode is possible (see Figure 5). In comparison, a multivalent interaction of only two ligands and receptors increases the number of bound modes from one to three. Therefore, multivalent presentation does not only increase the number of interactions but also decreases the influence of dissociation due to the other bound ligands.

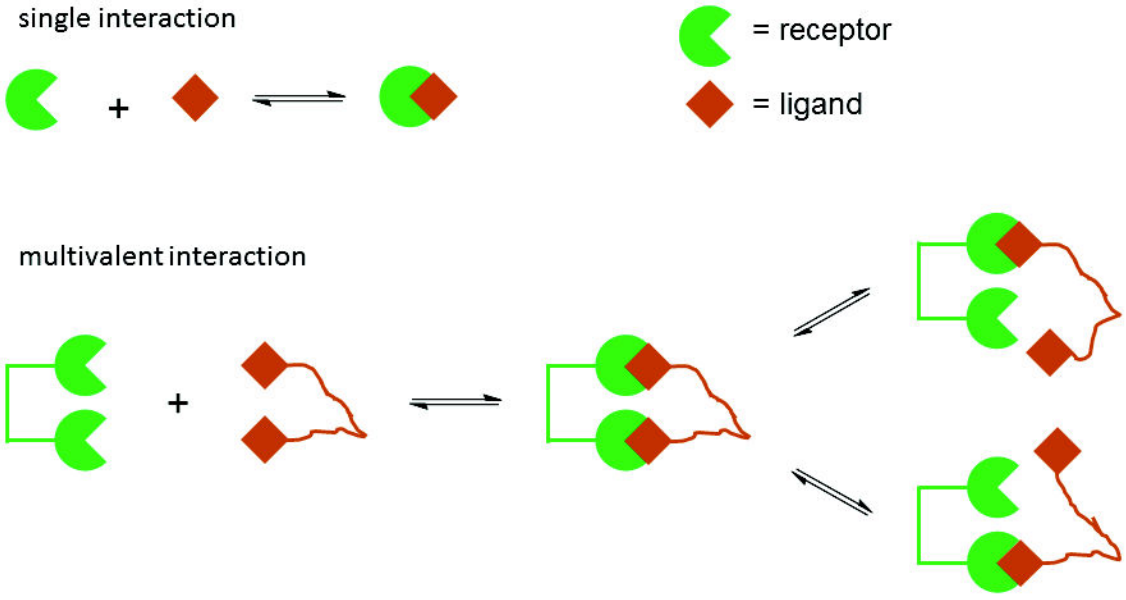

Figure 5 Schematic presentation of ligand receptor interactions as comparison between bound and unbound state. Single interaction (top) with one unbound and one bound state and multivalent interaction (bottom) with one unbound and three different bound states.

Additionally, different multivalent binding effects influence the interactions (see Figure 6). The fast binding and rebinding of the weak lectin-carbohydrate interaction with a multivalent ligand is called statistical rebinding. The binding increases due to the physical proximity of an unbound ligand to a bound ligand. The bound ligand is hereby replaced by the unbound one.[58] The chelate effect is well-known from complexation of metal ions with ligands that bear more than one functional metal-binding group.[59] The principle in carbohydrate-receptor interactions is the same. One molecule bears two or more carbohydrate subunits that can bind to the receptor. Presenting those ligands on a rigid scaffold that fits the distance of binding sites leads to lower entropy loss upon binding compared to binding of the free non-scaffold bound ligands. This is because the translational entropy is lower for the rigid scaffold compared to the free separated ligands.[60] This changes when the ligands are presented on a flexible scaffold, where every single binding entails a loss in translational entropy.[61] "Clustering" of multivalent ligand-receptor pairs is related to the chelate effect. In this case, the multivalent ligand does not bind to the same receptor as a chelate ligand but instead, it binds more than one receptor leading to a clustering of receptors. Additionally, receptor-bound ligands can be shielded by the backbone of the multivalent ligand, preventing other ligands from reaching the receptor binding site. This steric shielding effect is very important for the development and design of receptor binding molecules.[62]

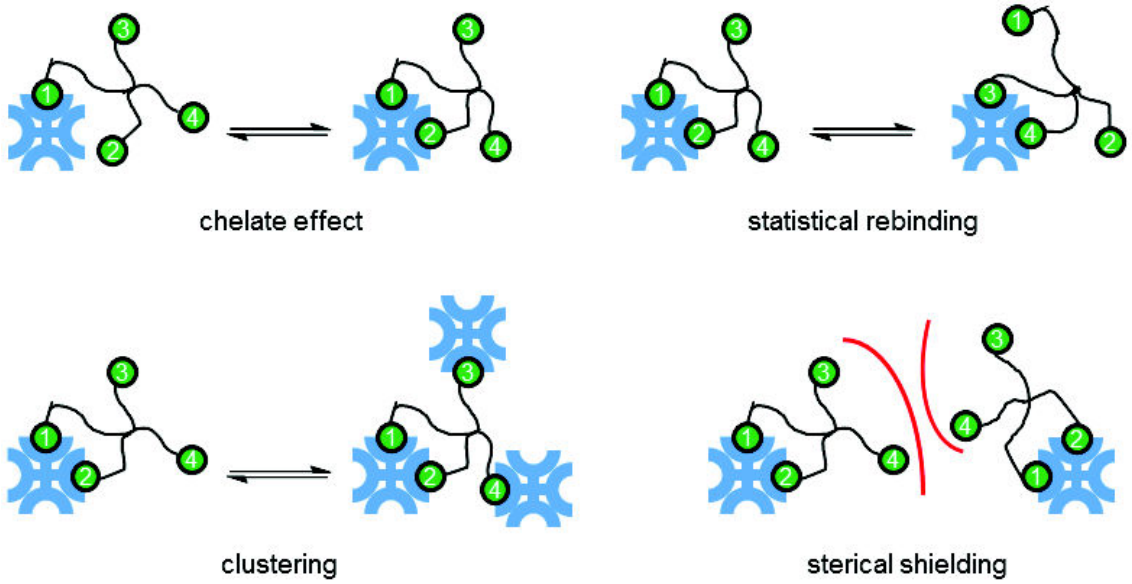

Figure 6 Schematic presentation of different multivalency effects. The chelate effect (left, top) shows the binding of more than one ligand to one receptor in comparison to clustering (left, bottom) where one ligand binds to more than one receptor building clusters.

Statistical rebinding shows, that the number of binding events stays the same but the ligands bound to the receptor change (right, top) and sterical shielding where the ligands (3 and 4) hinder the others from binding to the second receptor (right, bottom).

Due to the interactions of the glycocalyx and lectins in a multivalent fashion certain carbohydrate units are found more often at the terminal position of cellular glycans, e.g. α-$_D$-sialic acid, α-$_L$-fucose, and β-$_D$-galactose make roughly three quarters of the terminal sugar moieties on cell-bound carbohydrate chains according to Seeberger (see Figure 7).[63] Pathogens can use those sugars for adhesion processes to form biofilms and infect cells.[64] The influenza virus uses sialic acid as a ligand for its hemagglutinin receptor and the bacterial FimH receptor of *E. coli* binds to mannose units on the cell surface or p.aeruginosa using galactose and fucose as ligands for their LecA and LecB proteins (see Table 1). But this specificity can also be used as an advantage to fight bacterial and viral infection by preventing their adhesion to cell surfaces.

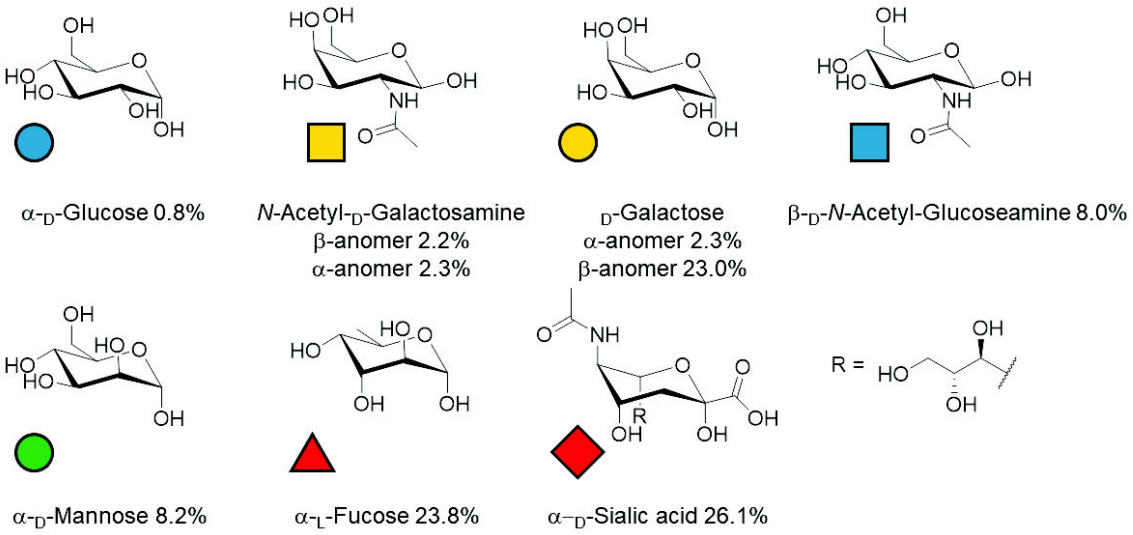

Figure 7 Structures of terminal monosaccharide moieties found on cell surfaces and their frequency of occurrence as determined by the group of Seeberger.[63] Colored symbols are the symbol nomenclature of those carbohydrates for a schematic presentation of oligo- and polysaccharides.

1.2.2. Ligand receptor interactions

Carbohydrates are structural very complex molecules. They bear a huge variability depending on the positioning of their hydroxyl groups, exchange with other functional groups or hydrogen atoms and by their binding to other carbohydrate units forming oligo- and polysaccharides, with the last named option giving the largest variability. A Combination of only three carbohydrates can lead to a variety of more than 1000 different oligosaccharides.[65,66] The smallest change in their structure can lead from recognition and binding to non-binding. For example, the receptor concanavalin A binds to α-$_D$-mannose (Man) and α-$_D$-glucose (Glu) because the important hydroxyl groups for binding are located at C3, C4, and C6 but changing one of those for example at C4 to α-$_D$-galactose and no binding occurs (see Figure 8). However, for recognition of receptors, their pyranose form is required.

Lectins are carbohydrate binding receptors and, therefore, the counterpart to the carbohydrate ligands. Lectins are non-enzymatic and non-antibody carbohydrate binding proteins for not only mono- but also oligo- and polysaccharides.[67,68] Additionally, lectins bear two or more binding sites, leading to cross-linking abilities when interacting with cells.[69] Moreover, lectins can be classified in different lectin families distinguished between plant and animal lectins. Each family of lectins can be found in different parts of cells, e.g. C-type- and I-type lectins are mainly membrane bound whereas M-type and L-type lectins are located in the endoplasmatic reticulum.[70] These families of lectins have, besides their different locations, also different binding mechanisms, as for example C-type lectins requires calcium ions for binding (see Figure 8).[71]

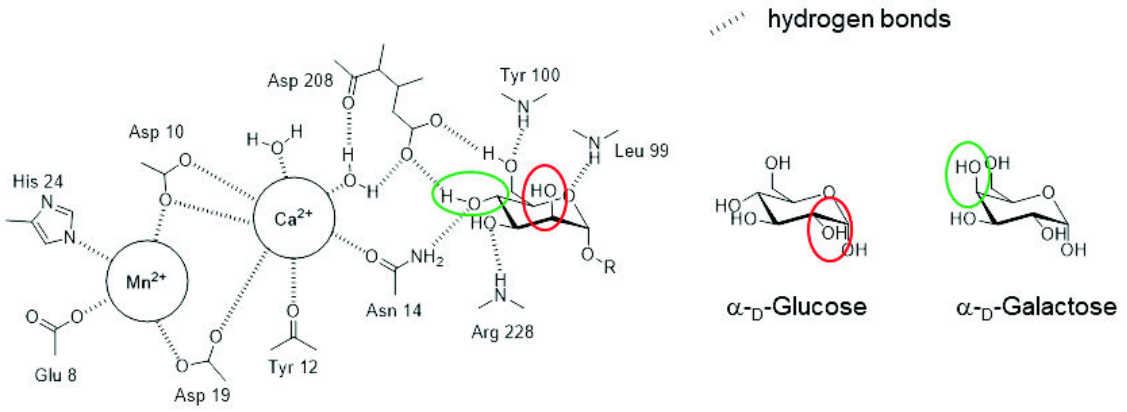

Figure 8 Binding site of Concanavalin A with manganese and calcium ions and mannose moiety in the binding site with hydrogen bonds between amino acids and binding partners

(left) (adapted from 71). Additionally, α-$_D$-Glucose and α-$_D$-Galactose for comparison (right). The hydroxyl group on C2 (red circle) does not have an influence on the binding between mannose and ConA, therefore glucose can also bind to ConA, whereas the difference in the binding hydroxyl group at C4 (green circle) leads to non-binding of galactose.

ConA is a well-known and intensely studied C-type lectin. This protein is, besides of Urease, one of the first proteins that were purified and crystallized and the first one that was commercially available.[72] It can, in dependence of the pH, be present as a homodimer below a pH of 6 or, above it, as a homotetramer.[73] Each subunit has one binding site capable of binding to mannose and glucose and, therefore, ConA can work as a crosslinker in both forms, dimeric or tetrameric.[74] Due to its early purification and commercial availability, ConA has been used in many studies as a model lectin.[62]

1.2.3. Glycocalyx mimetics

Oligo- and polysaccharides (also termed glycans) on cell surfaces are very complex structures. Due to the high amount of sugars and high number of possible structural permutations to form polysaccharides it is nearly impossible for scientists to synthesize them via a multi-step or one-pot synthesis.[75] To overcome this problem of complexity one approach is to synthesize cell glycan-like polysaccharides and assemblies thereof (see Figure 9). Mimetic glycans simplify the carbohydrate structure and only the terminal sugar, in particular cases like lactose binding the last two, is presented on an artificial scaffold. Those scaffolds can have multiple architectures such as a polymer,[76] dendrimer[77] or particle[51] and can be used for mechanism studies[78] or for the development of diagnostics and therapeutics.[79]

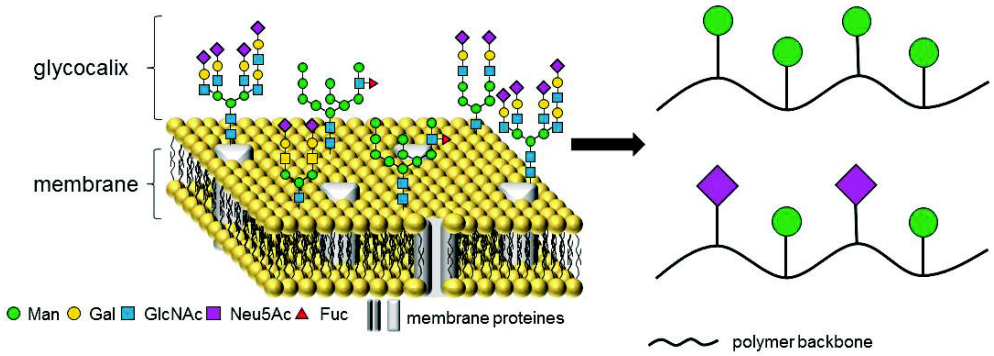

Figure 9 Schematic presentation of mimicking the membrane bound glycocalyx. The membrane of the cell (left) is exchanged by a polymer backbone and the terminal sugar of membrane bound oligo- and polysaccharides are presented on the polymer backbone (right) in a homovalent (right top) or heterovalent (right bottom) fashion. (Glycans adapted from 54).

1.2.3.1. Glycopolymers

A synthetic polymer that has incorporated carbohydrate ligands is called “glycopolymer”. The ligands in these polymers can either be terminal, in side chains, or both.[80,81,] This biomimetic approach is viable since glycopolymers not only mimic functionalities and binding of naturally occurring carbohydrate moieties[82,83] but even exceed them.[84] Additionally, research confirmed the use of glycopolymers in different fields of biomedical applications such as drugs,[85,86] bioassays,[87] inhibitors,[88] and drug delivery.[89,90,91] A common way to synthesize glycopolymers is by radical polymerization techniques. Due to their hydroxyl groups, carbohydrates can interfere with other polymerization techniques and make the ligand inactive for biological applications.[92] However, due to the lack of a radically polymerizable unit on carbohydrates, different methods for the synthesis of glycomonomers have been established, e.g. acrylate or acrylamide based glycomonomers have become a part of common educts for glycopolymer synthesis.[93] Homovalent glycopolymers have a high density of ligands and can cause negative multivalent effects.[94] To decrease ligand density on glycopolymers different techniques can be used (see Figure 10). Copolymerization is one possibility to decrease ligand density. An advantage of this technique is that by choosing a certain co-monomer the architecture of the copolymer can be adjusted from statistical to alternating or gradient- up to block copolymers. But to adjust the architecture by changing the co-monomer is difficult because the changed co-monomer can also have an influence on the binding towards the recognition unit and solubility of the glycopolymer.[95] Another possibility to decrease the ligand density is by using polymeric analog reactions. Here, a polymer, such as a poly active ester, can be functionalized with a nucleophilic modified carbohydrate in the first and any other nucleophile in a second step resulting in a copolymer. This approach can be used to synthesize many different copolymers in a short amount of time.[96] In contrast to a copolymerization, this method gives only statistical copolymers but if two monomers cannot be copolymerized with each other this method can be used to get the copolymer anyway.

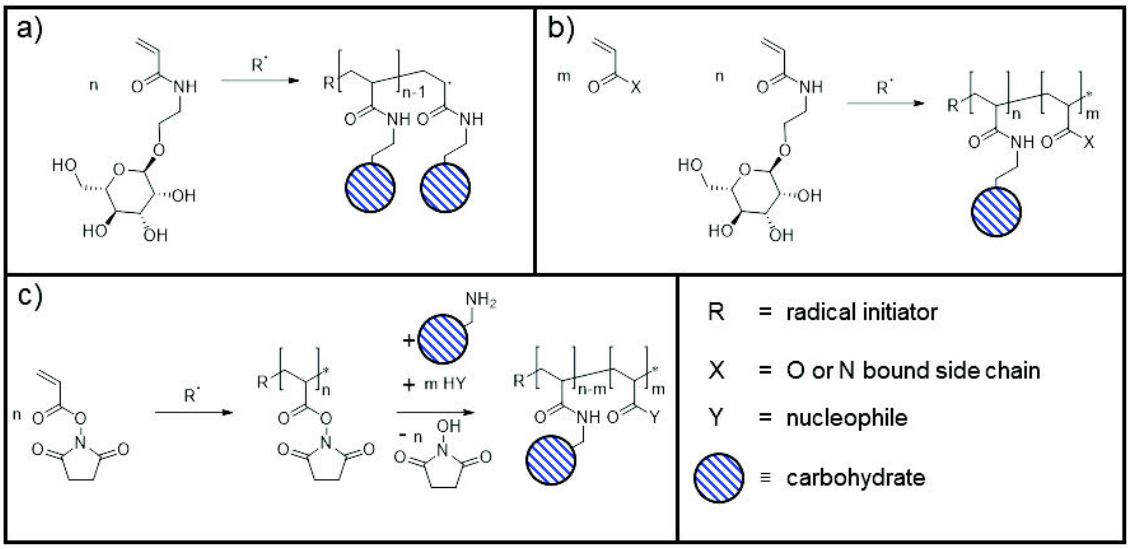

Figure 10 Typical routes providing glycopolymers via radical polymerization. Homopolymerization of glycomonomer giving a homopolymer with high ligand density (a), copolymerization of glycomonomer with acrylate or acrylamide based co-monomer giving a copolymer with adjustable ligand density depending on the ratio of m and n and potentially adjustable architecture (b) and polymeric analog reaction based on polymerization of an active ester and functionalization afterwards to adjust ligand density exemplary on active ester *N*-acryloxysuccinimide (NAS) (c).

1.2.3.2. Stimuli-responsive polymers

Special classes of polymers are so-called smart or stimuli-responsive polymers.[97] When exposed to a small change in physical-chemical parameters (temperature, solute conditions) they undergo a conformational change.[98,99] There classification can depend on different aspects. On the one hand, they can be classified by the stimulus they respond to as named before or by their physical appearances such as covalently bond and physical/reversible bond hydrogels grafted on surface or chains in solution (see Figure 11).[100]

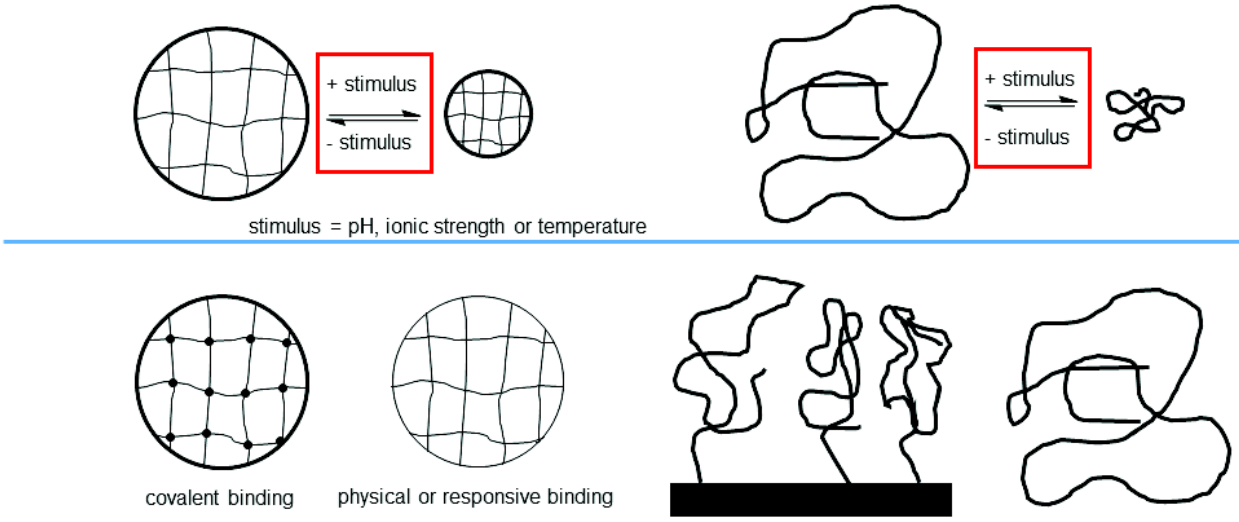

Figure 11 Illustration of different classification possibilities of stimuli-responsive polymers. One possibility is the classification by the stimulus (top) and the other one by physical appearance (bottom).

This classification is very rigorous and, therefore, mostly a combination of both is used in literature in form of stimulus-responsiveness and physical appearance, e.g. thermoresponsive polymer[101] or pH-responsive hydrogel.[102]

Biological macromolecules also respond to environmental changes, such as pH or temperature, they undergo a conformational change as for example proteins that unfold or denature when heated above a certain temperature or when exposed to a change of pH.[103] This response, even if not reversible, has found a major interest in research and has been the impulse to transfer this property onto synthetic polymers.[104] Many different stimuli have been found and studied besides pH[105] and temperature[106] such as ionic strength,[107]

light,[108] redox,[109] presence of molecules,[110] or electric fields[111] even though the temperature is the most studied and understood stimulus.[112] Polymers responsive to the mentioned stimuli are suitable for biomedical application such as gene[113] and drug delivery[114] and their controlled release,[115] bioanalytics,[116] and tissue engineering.[117]

1.2.3.2.1. Thermoresponsive glycopolymers

Polymer chains in a solvent react on temperature as an external stimulus and undergo a change in their physical appearance. Therefore, they are called thermoresponsive polymers. Two different types of thermoresponsive polymers can be distinguished. On one hand, some polymers exhibit a so-called upper critical solution temperature (UCST) where the polymer dissolves with increasing temperature.[118] This behavior is also known for many other substances that show increased miscibility with higher temperatures. On the other hand, some polymers exhibit a lower critical solution temperature (LCST).[119] Below this temperature the polymer is soluble in a polar solvent but after exceeding this LCST the polymer collapses and becomes insoluble.[120] Most of the stimuli-responsive polymers studied show a LCST in water.[121] Well-known synthetic thermoresponsive polymers are poly(*N*-isopropyl acrylamide) (PNIPAM),[122] poly(ethylene oxide),[123] poly(oligo(ethylene glycol) acrylates and methacrylates.[124] PNIPAM is the thermoresponsive polymer that is studied the most due to the very sharp transition from coil to globule at its LCST of 32 °C.[125] By synthesizing PNIPAM based copolymers the LCST can be varied and kinetically as well as thermodynamically controlled.[100] By using hydrophilic monomers as a comonomer the LCST is increased whereas the use of hydrophobic comonomers leads to a decrease in LCST.[126] Moreover, control of the polymer architecture, e.g. block copolymers, can change the polymer properties when exceeding the LCST from the transition solved to precipitated to a transition from sol to gel.[127]

The collapse of polymer chains is mediated by a change in polymer interactions. An LCST polymer is composed of a hydrophilic and a hydrophobic part[128] and the hydrophilic and hydrophobic interactions between polymer and solvent are the main driving force for the collapse.[129] Therefore, increasing hydrophilicity or hydrophobicity, especially for copolymers, can lead to a loss of LCST behavior.[97] A thermoresponsive polymer in its soluble state below the LCST forms an entropically costly solvation shell, e.g. by hydrogen bonding between hydrophilic polymer parts and water molecules. By increasing the

temperature, the entropy gain upon the release of water prevails and the hydrophobic polymer parts interact with each other, going from a mainly intermolecular (polymer-solvent) to a mainly intramolecular (polymer-polymer) interaction, leading to a coil-to-globule transition (see Figure 12).[130,131,132.]

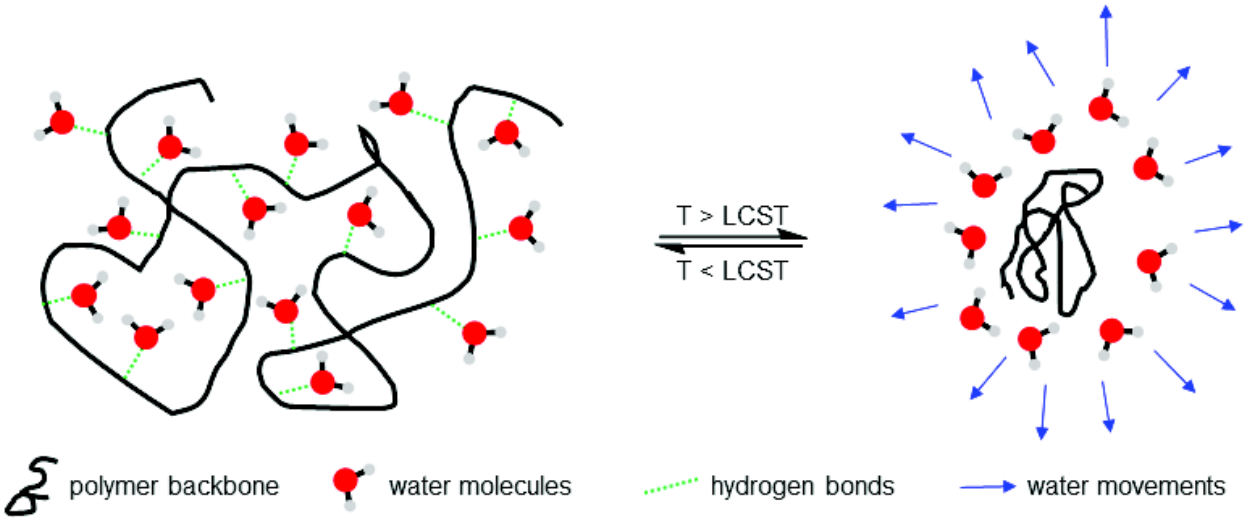

Figure 12 Schematic presentation of a stimulus-responsive polymer undergoing a temperature induced change in water. Below the lower critical solution temperature (LCST) the polymer backbone of the polymer coil builds hydrogen bonds to water molecules. After exceeding the LCST hydrogen bonds are broken and intramolecular polymer-polymer interactions take place increasing the order in the polymer globule in comparison to the swollen coil. The release of water increases the systems entropy.

Combining thermoresponsivness and glycopolymers can lead to a combination of advantages of both polymer classes: thermal control and specific binding. Moreover, different architectures of thermoresponsive glycopolymers are suitable. Linear polymer chains can be synthesized via controlled polymerization techniques for analysis of architectural influence or polymeric analogous reactions for statistical distribution and unpolymerizable monomers.[133,134] But also bigger structures such as hydrogels are suitable architectures for control of ligand-receptor interactions.[51] Additionally, hybrid materials are one possibility to control ligand-receptor interactions and protein or bacteria adhesion. Those are often gold or glass surfaces grafted with thermoresponsive polymers and are, therefore, called “smart surfaces”[135,136,137] and by grafting glycopolymers onto surface biocompatibility can be improved.[138]

To get a better insight into the mechanisms of temperature controlled ligand-receptor interactions, linear polymer chains are suitable. By using the most “simple” architectural linear polymer chains different analytical methods can be executed. Those polymers can be analyzed in solution but also at different surfaces when they are grafted onto them. Therefore, the following work is based on the analysis of linear thermoresponsive glycopolymers. Those are very promising to get a deeper insight in the mechanisms of controlled ligand-receptor interactions.

1.3. Quantification of ligand receptor interactions

To quantify interactions between ligands and receptors different methods can be used. One very common method that is used is surface plasmon resonance (SPR).[139] Even though this method can be used to determine different parameters for ligand-receptor interactions such as binding and dissociation constants,[140] this method is indirect. Moreover, it gives inside into a solid-liquid interfacial system, because the ligand or the receptor is bound to the surface and the binding partner is added in liquid phase with a certain flow the same as for example Quartz Crystal Microbalance (QCM).[141,142] A method for a direct measurement for the forces between two surfaces is atomic force microscopy (AFM). With AFM different aspects can be considered. This method can go from unfolding of proteins[143] to single ligand-receptor interactions using single-molecule-AFM (SM-AFM),[144] but also functionalized particles can be used to measure adhesion between two surfaces.[145] One major disadvantage of this method is, besides the price to operate the AFM during the measurements using one cantilever for each measured particle, the complex operation technique, and quantification of the results. Therefore, a fast and easy method has been developed to overcome these problems: The Soft Colloidal Probe adhesion assay (SCP-RICM) (see Figure 13).

1.3.1. Reflection interference contrast microscopy-based SCP adhesion assay

The reflection interference contrast microscopy (RICM) method is well known from cell adhesion studies to determine contact points between cells and surfaces.[146] By conical and annular illumination, it is possible to display ultrathin sections down to 5 nm, making it possible to measure distances between reflecting surfaces.[147,148,149] As the name indicates RICM is based on the reflection of light, coming from different refractive indices between two media, in case of cells for example external water and lipid bilayer membranes or membranes and cytoplasm.[150] Due to the weak reflection intensity at those interfaces, compared to incoming light intensity, stray reflection has to be reduced and contrast has to be increased. To reach that the so-called antiflex microscope method, developed by Piller in 1959, is used, where light has to pass crossed polarizers.[151] This method reduces the stray light giving a darker image background. Additionally, a quarter waveplate and polarizers reduce the unwanted reflection.[152,153]

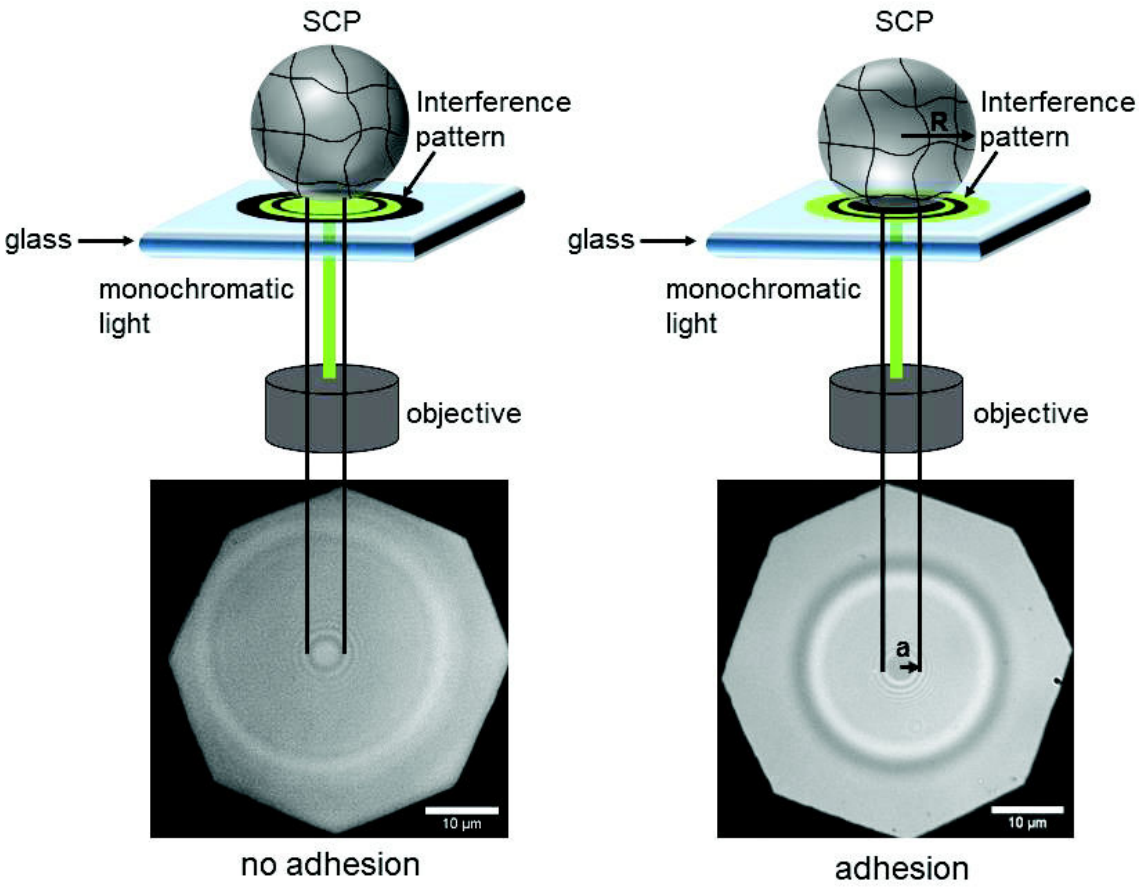

Figure 13 Schematic image of reflection interference contrast microscopy based soft colloidal probe (SCP) adhesion assay. When the SCP is not in contact with the glass surface the interference pattern formed by reflected light leads to a bright spot in the middle (left). When the SCP gets in contact with the surface the interference pattern has a dark spot in the middle (right). From this interference pattern radius of contact area (a) and radius of the particle (R) can be calculated. Two different exemplary images show the differences visible during the measurement (bottom).

The RICM method can be used to quantify the contact area and adhesion energies by the JKR method (see section 1.3.1.1) of well-controlled soft particles called soft colloidal probes (SCPs).

In this assay, SCPs are added to a glass surface in aqueous media. To quantify biomolecular interactions the SCPs are functionalized with a specific ligand-receptor pair as specific binding partners or with polymers for investigation of unspecific adhesion.[154] After sedimentation of the SCP a monochromatic light (wavelength around 530 nm) is used to create the RICM image and read out the contact area. Light is reflected at every

interface between two media with different refractive indices. The light that is reflected at the glass/SCP interface gives the contact area and the reflected light from the SCP/water interface gives an interference pattern for calculation of the particle radius (see Figure 14). The glass/SCP interface is only present when the SCP and the surface interact with each other and due to the change in refractive index from glass to SCP the contact area is turned black. When no contact between SCP and glass appears then there are two interfaces: glass/water and water/SCP and, therefore, a bright area appears. Depending on the probed system the measurement condition can be varied by adjusting the measurement solution according to pH, temperature or ionic strength.[155] Due to this huge variety of possible changes in the measurement conditions this method can be used to measure not only specific and unspecific interactions[156] but, moreover, distinguish between electrostatic[157] and hydrophobic interactions and even measure microscopic scale pressures when combined with AFM.[158]

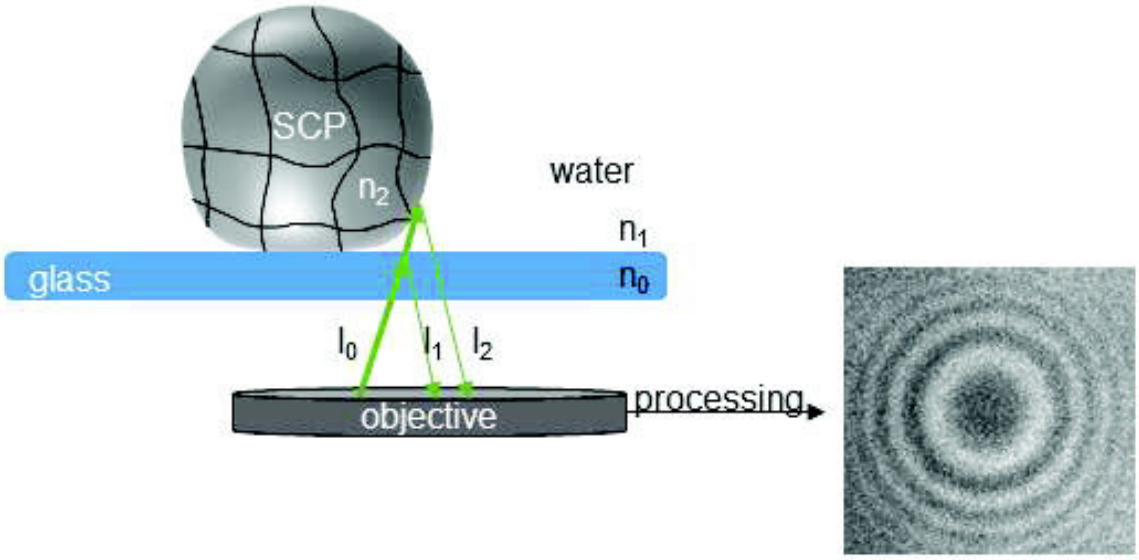

Figure 14 Schematic light beam path during the RICM measurement leading to the interference pattern by reflection at the interfaces with different refractive indices.

1.3.1.1. The Johnson-Kendall-Roberts (JKR) theory

The SCP assay takes advantage of the fact that soft bodies deform upon coming in adhesive contact with another surface. Evaluating mechanical energies that lead to the deformation of the soft particles gives the adhesion energy between the SCP and the planar surface.

The theory of contact between two smooth and elastic bodies was first investigated by Heinrich Hertz in 1881.[159] His investigated equation for the contact radius between two spheres pressed together is as followed:

$$a_0^3 = \frac{3}{4}\,\pi(k_1 + k_2)\frac{R_1 R_2}{R_1+R_2}\,P_0 \qquad (1)$$

With contact radius a_0, R_1 and R_2 as radii of the spheres, P_0 as the external load and k_1 and k_2 as elastic constants of the spheres. The elastic constants include the Youngs modulus E and the Poisson ratio υ for each sphere:

$$k_{1/2} = \frac{1-\upsilon_{1/2}^2}{\pi\, E_{1/2}} \qquad (2)$$

But Roberts could not prove the results in 1968 using rubber spheres and neither could Kendall in 1969 using glass.[160,161] Both found larger contact areas (a_1) than expected with the Hertz theory (see Figure 15). The results they found agreed with the Hertz model only at high loading forces, but when reducing the external load up to zero large residual contact area was observed. Therefore, they investigated, together with Johnson, the influence of attractive forces onto the contact area between those elastomeric bodies and differentiated the attractive forces in three parts: the stored elastic energy, the surface energy and the mechanical energy.[162] A detailed mathematical description of this model is shown in literature 162 and 163. By taking the attractive forces into account the Hertz equation can be modified according to the JKR theory as followed:

$$a^3 = \frac{R}{K}\,(P + 3\gamma\pi R + \sqrt{6\gamma\pi RP + (3\gamma\pi R)^2} \qquad (3)$$

With $R = (R_1R_2)/(R_1+R_2)$, $K = 4/3\ \pi(k_1+k_2)$ and γ as the energy per unit of contact area.

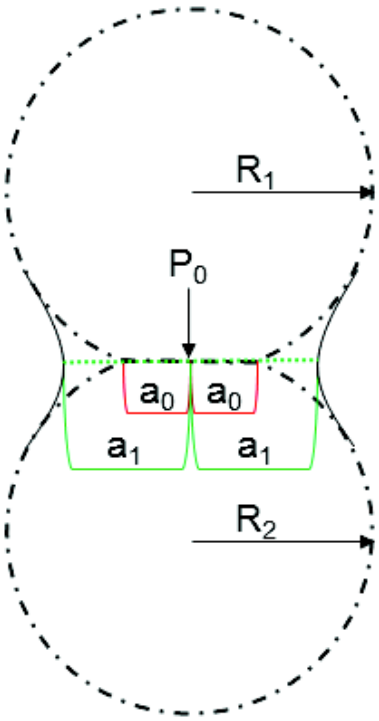

Figure 15 Schematic display of the difference between Hertz and JKR theory. Two spheres are pressed together with R_1 and R_2 as sphere radii, load P_0, and contact radii a_0 depending on Hertz theory and a_1 considering additional attractive forces depending on JKR theory (adapted from 162).

The JKR theory was investigated for two spherical bodies pressed together.[164] The SCP adhesion assay does not use two spheres for the measurement of adhesion energies. But the JKR theory can be adapted by assuming that the glass surface in the experiment is a sphere with an infinite radius. In addition to this, because the SCPs sediment onto the surface and are not pressed to it with an external load the load during the measurements equals zero. This leads to the following equation for the calculation of the adhesion energies using the Soft Colloidal Probe adhesion assay:[156]

$$a^3 = 6\pi \frac{W_{adh}}{E_{eff}} R^2 \qquad (4)$$

With a as contact radius between SCP and surface, W_{adh} as adhesion energy, E_{eff} as effective elastic modulus: $E_{eff} = [4E/3*(1-\upsilon^2)]$, with the Poisson ratio ν and the elastic modulus E of the SCP and R as SCP radius.

1.3.1.2. Determination of elastic modulus

The deformation of a soft material needs less energy compared to a hard material, e.g. rubber in comparison to glass or steel. Therefore, it is important to know the elastic properties of the SCP for the calculation of adhesion energy as it is shown in equation 4. AFM has been shown to be a suitable method to determine the elastic modulus of SCPs.[165] AFM is a nanoscale high-resolution method and was introduced in the middle of the 1980s.[166] Due to its use in measurements of forces in the nanoscale between two surfaces[167] it can also be used for force-indentation measurements.[168] A setup for AFM force indentation measurements is shown in Figure 16. In a first step, a glass bead is glued onto a tipless cantilever with epoxy glue. For the calculation of the E-modulus, the effective radius of contact has to be calculated. Using a glass bead instead of a pyramidal tip, that is commonly used for surface scanning, simplifies the calculation of the effective radius as followed:

$$\frac{1}{R_{eff}} = \frac{1}{R_1} + \frac{1}{R_2} \qquad (5)$$

with R_1 and R_2 as the spheres radii.

The glass bead is pressed onto the glass bead to deform the particle and upon contact, the cantilever bends moving the laser on the photodiode indicating the contact between both spheres. When retracting the glass bead from the SCP the cantilever bends in the other direction moving the laser on the photodiode. This peak indicates an adhesive force between glass and SCP. For calculation of the E-modulus, the extend curve is used. A very common model for calculation of the elastic modulus is the Hertz model. The equation for the Hertz model is shown below:

$$F = \frac{4E}{3(1-\upsilon^2)}\sqrt{R_{eff}}\delta^{3/2} \qquad (6)$$

with F as applied force, E as elastic modulus, υ as Poisson ratio, R_{eff} as effective radius between spheres and δ as indentation. The Poisson ratio can be set to 0.5 for this due to the assumption of volume conservation during the indentation.[169] This model assumes that the only upper side of the SCP deforms upon contact with the glass bead, but also on the contact between SCP and glass surface deforms. Therefore, in this work a novel model for calculation of E-modulus is used developed by Glaubitz et al.[170] taking the deformation at both sides into account.

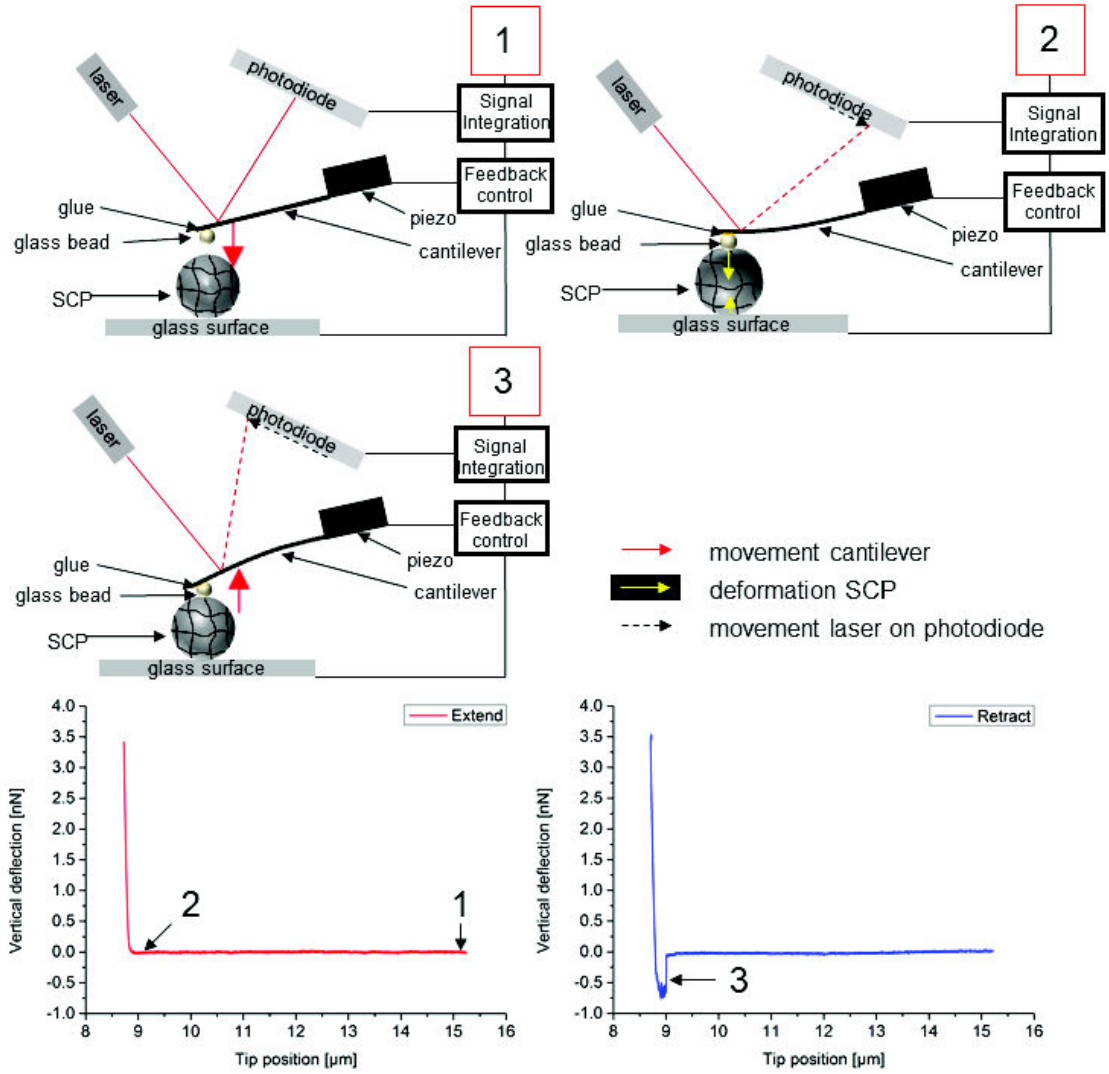

Figure 16 Schematic presentation of an AFM force indentation measurement to determine the SCP´s elastic modulus. Shown are the three steps that a measurement can be divided into (top). The first step (left) is the positioning of the cantilever in the center above the SCP. In the second step (middle) the glass bead glued to the cantilever is pressed onto the SCP (extend) before it is drawn into the starting position (retract, right). On the bottom exemplary extend and retract curves are shown. The numbers show the influence of each step onto the curve. 1) is the starting position, 2) is the contact between glass bead and SCP and 3) is the energy needed to overcome adhesive interactions between the glass bead the SCP.

2. Aims and Outline

The aim of this work is to analyze two archetypical examples of bioadhesion processes: 1) mussel inspired adhesion of catechol, amine and amide motifs and 2) the adhesion of stimulus-responsive glycopolymers.

In the first part of this work, the adhesion mussel foot protein (MFP) inspired oligomers, synthesized by a collaboration partner, are analyzed to get a deeper understanding of how the combination and the positioning of certain functional groups influence the underwater adhesion. The synthesis of the oligomers is conducted using solid phase synthesis of oligo(amidoamines) developed in the Hartmann lab.[171,172] The functional groups to be investigated are catechols, tertiary amines and primary amides. These groups are present MFPs and, especially amines and catechols, are considered to be responsible for the strong adhesion as assumed and investigated by Israelachvilli and coworkers.[31] The cationic charge of the amines is considered to be important for the displacement of salt and hydration layer as a prerequisite for underwater adhesion. Therefore, tertiary amines at the oligo(amidoamines) are used to confirm this hypothesis while also reducing side reactions with the catechol. Due to the high amount of primary amides present in MFP-3, these are additionally incorporated into the oligomers. The adhesion of the oligomers to glass surfaces will be analyzed using the soft colloidal probe (SCP) adhesion assay to determine the influence of the functional groups positioning and their pH dependence.

In the second part of this work, the specific adhesion between switchable glycopolymers and lectins is investigated. Smart polymers provide avenues toward drug delivery/carrier systems or as potential drugs themselves. Therefore, thermoresponsive glycopolymers are synthesized with varying functionalization degrees of carbohydrates and different linker hydrophobicity. In the literature, the influence of the temperature-induced coil-to-globule transition of thermoresponsive glycopolymers on their lectin affinity show inconsistent results. As thermoresponsive polymer the well-known poly(*N*-isopropyl acrylamide) is used. Additionally, the influence of the linker hydrophilicity on the adhesion process is investigated. After the successful synthesis of these mannose functionalized polymers their inhibition potential towards mannose-specific ConA and type 1 fimbriated *E. coli* is investigated. Additionally, using the SCP adhesion assay, the changes of temperature-induced polymer collapse towards ligand-receptor interactions is investigated. Moreover,

due to earlier results generated in the group of Schmidt, showing the influence of the hydrogel stiffness upon ligand receptor mediated adhesion,[165] the influence of temperature upon thermoresponsive polymer functionalized hydrogels is studied.

3. Conclusion

The first part of this work was focused on providing a deeper insight into the underwater adhesion mechanism of catechols. Therefore, the underwater adhesion of a series of MFP-inspired oligomers with varying composition and positioning of functional groups was analyzed towards their properties. In total nine different oligomers, provided by a collaboration partner, were analyzed. For the adhesion studies, the following three functional groups were combined on the oligomers: catechol, tertiary amine and primary amide. Catechols are considered to be responsible for the long-term adhesion and amines to be responsible for removing the hydration and salt layers from underwater surfaces. MFPs present primary amines in their amino acid sequence and it is believed that the cationic charge is needed to remove the hydration and ion layer from natural silica surfaces to induce catechol-based adhesion. To reflect this behavior we used tertiary amines to reduce side reactions with the catechols. Primary amides were previously not considered to play any role in the adhesion process of mussels although they are present in MFP-3 at a molar ratio of >15%. Therefore, to investigate the role of amides on adhesion they were also chosen as functional groups for the adhesion studies. The oligomers showed all combinations of functional groups and also the positioning and spacing of functional groups was varied (see Figure 17). For the adhesion assay oligomer functionalized PEG-based SCPs were used and allowed to adhere to glass surfaces. To reach high oligomer functionalization degrees in the SCPs network the functionalization was done twice giving functionalization degrees of >90% and 13.5-14.2 wt% oligomer per PEG SCP. The SCP contact areas on glass surfaces were measured via RICM in water with high salt concentration (0.1 M NaCl) and over a pH range from pH 3 to pH 8. It was noted that the adhesion energies for most oligomer structures decreased from pH 3 to pH 8 which is explained by the deprotonation of silanol groups on the glass surface at higher pH values and the entailed reduction of hydrogen bond donation. Additionally, the deprotonation of those groups leads to a higher surface charge and a stronger hydration barrier. In accordance with literature, it could be seen that the combination of catechol and amine lead to higher adhesion energies as the homovalent catechol-catechol structure. This shows that cationic charges as imposed by the tertiary amines synergize with catechols to increase adhesion similarly to the natural primary amines. Moreover, positioning plays an important role. Having the amine at the terminating end of the oligomer facing the glass surface

resulted in a smaller decrease in adhesion energies from pH 3 to pH 5 as when compared to the reversed positioning where the catechol is the terminating functional group. An even stronger effect was observed when varying the spacing between the functional groups. Having no building block between amine and catechol, the adhesion energy increased by a factor of two. Combining catechols with primary amides showed an even higher dependence on the positioning. In contrast to the amine oligomers, the amide at the terminating position showed significantly lower adhesion compared to the catechol terminated oligomer. This result suggests that the amides present in MFP-3 amplify the adhesion towards the surface. The synergism between amide and catechol might be conferred due to the ionic resonance structure of primary amides that may help to remove the hydration and ion layers.

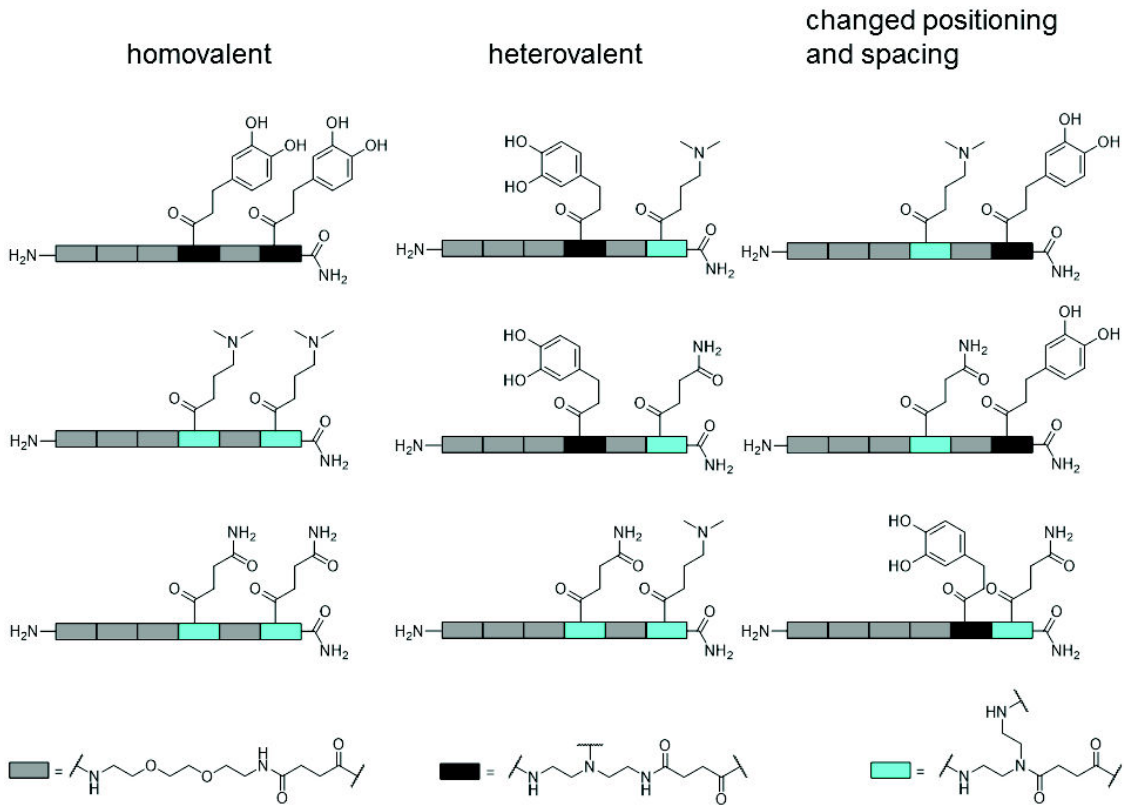

Figure 17 Schematic structures of oligomers used for adhesion studies. Three groups of oligomers can be differed: homovalent structures bearing the same functional groups (left), heterovalent structures bearing two different functional groups (middle) and heterovalent structures with changed positioning and spacing (right).

The second part of this work was focused on the specific interactions between switchable glycopolymers and lectins. The aim was to obtain a deeper understanding of glycopolymer interactions and the effect of coil-globule transitions which showed contradicting results in literature. Additionally, the adhesive interactions were investigated in solution and at soft solid interfaces. Here, two carbohydrate recognizing species of different size were used. The lectin ConA and the bacteria *E. coli* were used. ConA is a well-known lectin that binds specifically to α-$_D$-mannopyranoside. The FimH receptor on the tips of the fimbriae bound to the cell surface of *E. coli* also binds to α-$_D$-mannopyranoside.

First, a scaffold presenting α-$_D$-mannopyranoside with thermoresponsive properties was synthesized. As a well-known thermoresponsive polymer part poly (*N*-isopropyl acrylamide) (PNIPAM) was chosen with a lower critical solution temperature (LCST) in the range of the human body temperature. To create a series of glycopolymers with different mannose functionalization degrees and different linkers a polymer analog reaction approach was chosen. In the first step, the synthesis of the monomer *N*-Acryloxysuccinimide was adapted from literature and the reaction yield was improved by nearly 20%. After successful monomer synthesis, it was polymerized using free radical polymerization initiator 4,4'-Azobis(4-cyanovaleric acid) giving poly (*N*-Acryloxysuccinimide) (PNAS) with a carboxylic acid end group for further functionalization and grafting onto SCPs. For functionalizing the PNAS with mannose the carbohydrate was first functionalized with two different linkers of different hydrophilicity. The used linkers were an ethyl linker (EL) as hydrophobic and 2-hydroxypropyl (HPL) as a more hydrophilic one. The polymer analog reaction was then performed in two steps. In the first step, mannose was grafted onto the polymer backbone followed by quenching all remaining active esters with isopropyl amine to obtain the thermoresponsive PNIPAM part of the polymer. Using this synthesis route eight different mannose bearing polymers were synthesized with different mannose functionalization degrees with the two different linkers to the polymer backbone in a range from 1% to 97%. Additionally, one negative control polymer only bearing PNIPAM and one nonbinding control polymer with galactose grafted were synthesized. The analysis of coil-to-globule transition showed that the polymers LCST increased with a higher carbohydrate functionalization degree, in accordance with the literature. At more than 7% carbohydrate functionalization degree a LCST could not be observed below 45 °C. Additionally, the linker used for linking mannose to the polymer did not have an influence on the LCST. The first binding studies in solution using ConA as a receptor that showed that specific binding occurs and that the dissolution of the polymer-

lectin complex formed is faster for the more hydrophilic linker HPL. Inhibition studies using the synthesized polymers as an inhibitor for ConA and *E. coli* binding to mannan coated surfaces showed that the affinity shifts at low mannose functionalization degrees <2%. The results of those studies showed different shifts depending on the size of the mannose-binding species. Inhibition of the micrometer-sized *E. coli* was increased whereas the inhibition of the nanometer-sized ConA was decreased when exceeding the LCST of the glycopolymer. This is likely due to the size-dependent accessibility of mannose units. ConA binding benefits from extended glycopolymer coils below the LCST where it has access to more mannose units when compared to the collapsed glycopolymer globules above the LCST. On the other hand, owing to their large size *E. coli* has access to the surface of the glycopolymer coils only. Therefore, *E. coli* binding benefits from the collapsed polymer conformation resulting in a high surface density of mannose units.

For analyzing the glycopolymer-lectin interactions at interfaces, the glycopolymers above were grafted onto PEG-SCPs. To determine the adhesion of those polymers against ConA coated glass surfaces the SCP-RICM adhesion assay was used. The temperature-dependent adhesion studies confirmed that increase mannose functionalization degrees lead to increased adhesion energies and that the adhesion can be switched upon increasing temperature. Moreover, the linker seems to have an influence upon the switchability of adhesion. The hydrophilic linker HPL showed an increase in adhesion energies but the more hydrophobic EL linker did not show any clear temperature dependence. It is suggested that the linker affects the ligand presentation of grafted glycopolymer chains. Importantly, cooling back to temperatures below the LCST showed a large hysteresis and the initial value before starting the heating cycle could not be reached again. Additionally, *E. coli* binding to the polymer chains grafted onto the PEG-SCP could not be reduced by cooling back to 20 °C. These results showed that non-specific binding towards the receptor needs to be avoided to achieve reversible ligand-receptor binding.

The elastic modulus of the thermosensitive polymers grafted to the SCPs plays a very important role for ligand-receptor interactions. Therefore, AFM force indentation measurements were executed to investigate the influence of temperature on the elastic modulus. When heating from 20 °C to 45 °C SCPs with thermosensitive polymers showed decreasing elastic moduli, whereas SCPs with non-thermosensitive grafts showed increasing elastic moduli This can be explained by changes in mesh size. The mesh size decrease for SCPs without polymer or non-LCST polymers upon temperature increase due

to the “entropic spring” effect. LCST polymers on the other hand show an increase of the mesh size due to the collapse of grafted polymer coils. This collapse has a higher influence on the elastic modulus than the “entropic spring” effect upon heating. Importantly, the elasticity reaches a maximum value for the initial (ungrafted) SCPs. Due to the high importance of tissue elasticity on many different biological processes, these results have to be considered for different applications of polymer hydrogels used as drug delivery systems or others

.

4. References

1. Palacio, M. L. B.; Bhushan, B., Bioadhesion: a review of concepts and applications. *Philos. Trans. R. Soc. A-Math. Phys. Eng. Sci.* **2012,** *370* (1967), 2321-2347.
2. Baron, R.; McCammon, J. A., Molecular Recognition and Ligand Association. In *Annual Review of Physical Chemistry, Vol 64*, Johnson, M. A.; Martinez, T. J., Eds. Annual Reviews: Palo Alto, 2013; Vol. 64, pp 151-175.
3. Bhushan, B., Adhesion and stiction: Mechanisms, measurement techniques, and methods for reduction. *J. Vac. Sci. Technol. B* **2003,** *21* (6), 2262-2296.
4. Muller, P., GLOSSARY OF TERMS USED IN PHYSICAL ORGANIC-CHEMISTRY. *Pure Appl. Chem.* **1994,** *66* (5), 1077-1184.
5. Janiak, C., A critical account on pi-pi stacking in metal complexes with aromatic nitrogen-containing ligands. *J. Chem. Soc.-Dalton Trans.* **2000,** (21), 3885-3896.
6. Wheeler, S. E.; Bloom, J. W. G., Toward a More Complete Understanding of Noncovalent Interactions Involving Aromatic Rings. *J. Phys. Chem. A* **2014,** *118* (32), 6133-6147.
7. Lee, W. F.; Chen, Y. C., Effect of bentonite on the physical properties and drug-release behavior of poly(AA-co-PEGMEA)/bentonite nanocomposite hydrogels for mucoadhesive. *J. Appl. Polym. Sci.* **2004,** *91* (5), 2934-2941.
8. Ahuja, A.; Khar, R. K.; Ali, J., Mucoadhesive drug delivery systems. *Drug Dev. Ind. Pharm.* **1997,** *23* (5), 489-515.
9. Waite, J. H., NATURES UNDERWATER ADHESIVE SPECIALIST. *Int. J. Adhes. Adhes.* **1987,** *7* (1), 9-14.
10. Baer, A.; Oliveira, I. D.; Steinhagen, M.; Beck-Sickinger, A. G.; Mayer, G., Slime protein profiling: a non-invasive tool for species identification in Onychophora (velvet worms). *J. Zool. Syst. Evol. Res.* **2014,** *52* (4), 265-272.
11. DeMoor, S.; Waite, J. H.; Jangoux, M.; Flammang, P., Characterization of the adhesive from Cuvierian tubules of the sea cucumber Holothuria forskali (Echinodermata, Holothuroidea). *Mar. Biotechnol.* **2003,** *5* (1), 45-57.
12. Wiegemann, M., Adhesion in blue mussels (Mytilus edulis) and barnacles (genus Balanus): Mechanisms and technical applications. *Aquat. Sci.* **2005,** *67* (2), 166-176.
13. Almeida, E.; Diamantino, T. C.; de Sousa, O., Marine paints: The particular case of antifouling paints. *Prog. Org. Coat.* **2007,** *59* (1), 2-20.
14. Silverman, H. G.; Roberto, F. F., Understanding marine mussel adhesion. *Mar. Biotechnol.* **2007,** *9* (6), 661-681.
15. Khandeparker, L.; Anil, A. C., Underwater adhesion: The barnacle way. *Int. J. Adhes. Adhes.* **2007,** *27* (2), 165-172.
16. Chambers, L. D.; Stokes, K. R.; Walsh, F. C.; Wood, R. J. K., Modern approaches to marine antifouling coatings. *Surf. Coat. Technol.* **2006,** *201* (6), 3642-3652.
17. Strand, J.; Larsen, M. M.; Lockyer, C., Accumulation of organotin compounds and mercury in harbour porpoises (Phocoena Phocoena) from the Danish waters and West Greenland. *Sci. Total Environ.* **2005,** *350* (1-3), 59-71.
18. Gudipati, C. S.; Finlay, J. A.; Callow, J. A.; Callow, M. E.; Wooley, K. L., The antifouling and fouling-release perfomance of hyperbranched fluoropolymer (HBFP)-poly(ethylene glycol) (PEG) composite coatings evaluated by adsorption of biomacromolecules and the green fouling alga Ulva. *Langmuir* **2005,** *21* (7), 3044-3053.
19. Pettitt, M. E.; Henry, S. L.; Callow, M. E.; Callow, J. A.; Clare, A. S., Activity of commercial enzymes on settlement and adhesion of cypris larvae of the barnacle Balanus amphitrite, spores of the green alga Ulva linza, and the diatom Navicula perminuta. *Biofouling* **2004,** *20* (6), 299-311.

20. Kim, B. J.; Oh, D. X.; Kim, S.; Seo, J. H.; Hwang, D. S.; Masic, A.; Han, D. K.; Cha, H. J., Mussel-Mimetic Protein-Based Adhesive Hydrogel. *Biomacromolecules* **2014,** *15* (5), 1579-1585.
21. Ciapetti, G.; Stea, S.; Cenni, E.; Sudanese, A.; Marraro, D.; Toni, A.; Pizzoferrato, A., TOXICITY OF CYANOACRYLATES IN-VITRO USING EXTRACT DILUTION ASSAY ON CELL-CULTURES. *Biomaterials* **1994,** *15* (2), 92-96.
22. Nicklisch, S. C. T.; Waite, J. H., Mini-review: The role of redox in Dopa-mediated marine adhesion. *Biofouling* **2012,** *28* (8), 865-877.
23. Waite, J. H., Mussel adhesion - essential footwork. *J. Exp. Biol.* **2017,** *220* (4), 517-530.
24. Zhao, H.; Waite, J. H., Linking adhesive and structural proteins in the attachment plaque of Mytilus californianus. *J. Biol. Chem.* **2006,** *281* (36), 26150-26158.
25. Papov, V. V.; Diamond, T. V.; Biemann, K.; Waite, J. H., HYDROXYARGININE-CONTAINING POLYPHENOLIC PROTEINS IN THE ADHESIVE PLAQUES OF THE MARINE MUSSEL MYTILUS-EDULIS. *J. Biol. Chem.* **1995,** *270* (34), 20183-20192.
26. Lee, B. P.; Messersmith, P. B.; Israelachvili, J. N.; Waite, J. H., Mussel-Inspired Adhesives and Coatings. In *Annual Review of Materials Research, Vol 41*, Clarke, D. R.; Fratzl, P., Eds. Annual Reviews: Palo Alto, 2011; Vol. 41, pp 99-132.
27. Mirshafian, R.; Wei, W.; Israelachvili, J. N.; Waite, J. H., alpha,beta-Dehydro-Dopa: A Hidden Participant in Mussel Adhesion. *Biochemistry* **2016,** *55* (5), 743-750.
28. Nicklisch, S. C. T.; Spahn, J. E.; Zhou, H. J.; Gruian, C. M.; Waite, J. H., Redox Capacity of an Extracellular Matrix Protein Associated with Adhesion in Mytilus californianus. *Biochemistry* **2016,** *55* (13), 2022-2030.
29. Yu, J.; Wei, W.; Danner, E.; Israelachvili, J. N.; Waite, J. H., Effects of Interfacial Redox in Mussel Adhesive Protein Films on Mica. *Adv. Mater.* **2011,** *23* (20), 2362-+.
30. Barrett, D. G.; Fullenkamp, D. E.; He, L. H.; Holten-Andersen, N.; Lee, K. Y. C.; Messersmith, P. B., pH-Based Regulation of Hydrogel Mechanical Properties Through Mussel-Inspired Chemistry and Processing. *Adv. Funct. Mater.* **2013,** *23* (9), 1111-1119.
31. Maier, G. P.; Rapp, M. V.; Waite, J. H.; Israelachvili, J. N.; Butler, A., Adaptive synergy between catechol and lysine promotes wet adhesion by surface salt displacement. *Science* **2015,** *349* (6248), 628-632.
32. Rapp, M. V.; Maier, G. P.; Dobbs, H. A.; Higdon, N. J.; Waite, J. H.; Butler, A.; Israelachvili, J. N., Defining the Catechol-Cation Synergy for Enhanced Wet Adhesion to Mineral Surfaces. *J. Am. Chem. Soc.* **2016,** *138* (29), 9013-9016.
33. Kemnitz, C. R.; Loewen, M. J., "Amide resonance" correlates with a breadth of C-N rotation barriers. *J. Am. Chem. Soc.* **2007,** *129* (9), 2521-2528.
34. Vasir, J. K.; Tambwekar, K.; Garg, S., Bioadhesive microspheres as a controlled drug delivery system. *Int. J. Pharm.* **2003,** *255* (1-2), 13-32.
35. Bertozzi, C. R.; Kiessling, L. L., Chemical glycobiology. *Science* **2001,** *291* (5512), 2357-2364.
36. Kiessling, L. L.; Gestwicki, J. E.; Strong, L. E., Synthetic multivalent ligands as probes of signal transduction. *Angew. Chem.-Int. Edit.* **2006,** *45* (15), 2348-2368.
37. Springer, T. A., ADHESION RECEPTORS OF THE IMMUNE-SYSTEM. *Nature* **1990,** *346* (6283), 425-434.
38. Ozanne, B.; Richards, C. S.; Hendler, F.; Burns, D.; Gusterson, B., OVER-EXPRESSION OF THE EGF RECEPTOR IS A HALLMARK OF SQUAMOUS-CELL CARCINOMAS. *J. Pathol.* **1986,** *149* (1), 9-14.
39. Senbanjo, L. T.; Chellaiah, M. A., CD44: A Multifunctional Cell Surface Adhesion Receptor Is a Regulator of Progression and Metastasis of Cancer Cells. *Front. Cell. Dev. Biol.* **2017,** *5*, 6.

40. Peer, D.; Karp, J. M.; Hong, S.; FaroKhzad, O. C.; Margalit, R.; Langer, R., Nanocarriers as an emerging platform for cancer therapy. *Nat. Nanotechnol.* **2007,** *2* (12), 751-760.
41. Pasparakis, G.; Cockayne, A.; Alexander, C., Control of bacterial aggregation by thermoresponsive glycopolymers. *J. Am. Chem. Soc.* **2007,** *129* (36), 11014-+.
42. Lu, W. J.; Pieters, R. J., Carbohydrate-protein interactions and multivalency: implications for the inhibition of influenza A virus infections. *Expert. Opin. Drug Discov.* **2019,** *14* (4), 387-395.
43. Aquino, R. S.; Teng, Y. H. F.; Park, P. W., Glycobiology of syndecan-1 in bacterial infections. *Biochem. Soc. Trans.* **2018,** *46*, 371-377.
44. Garcia, B.; Merayo-Lloves, J.; Martin, C.; Alcalde, I.; Quiros, L. M.; Vazquez, F., Surface Proteoglycans as Mediators in Bacterial Pathogens Infections. *Front. Microbiol.* **2016,** *7*, 11.
45. Crocker, P. R.; Paulson, J. C.; Varki, A., Siglecs and their roles in the immune system. *Nat. Rev. Immunol.* **2007,** *7* (4), 255-266.
46. Derewenda, Z.; Yariv, J.; Helliwell, J. R.; Kalb, A. J.; Dodson, E. J.; Papiz, M. Z.; Wan, T.; Campbell, J., THE STRUCTURE OF THE SACCHARIDE-BINDING SITE OF CONCANAVALIN-A. *Embo J.* **1989,** *8* (8), 2189-2193.
47. Ponta, H.; Sherman, L.; Herrlich, P. A., CD44: From adhesion molecules to signalling regulators. *Nat. Rev. Mol. Cell Biol.* **2003,** *4* (1), 33-45.
48. Kadam, R. U.; Bergmann, M.; Hurley, M.; Garg, D.; Cacciarini, M.; Swiderska, M. A.; Nativi, C.; Sattler, M.; Smyth, A. R.; Williams, P.; Camara, M.; Stocker, A.; Darbre, T.; Reymond, J. L., A Glycopeptide Dendrimer Inhibitor of the Galactose-Specific Lectin LecA and of Pseudomonas aeruginosa Biofilms. *Angew. Chem.-Int. Edit.* **2011,** *50* (45), 10631-10635.
49. Tielker, D.; Hacker, S.; Loris, R.; Strathmann, M.; Wingender, J.; Wilhelm, S.; Rosenau, F.; Jaeger, K. E., Pseudomonas aeruginosa lectin LecB is located in the outer membrane and is involved in biofilm formation. *Microbiology-(UK)* **2005,** *151*, 1313-1323.
50. Skehel, J. J.; Wiley, D. C., Receptor binding and membrane fusion in virus entry: The influenza hemagglutinin. *Annu. Rev. Biochem.* **2000,** *69*, 531-569.
51. Paul, T. J.; Rubel, S.; Hildebrandt, M.; Strzelczyk, A. K.; Spormann, C.; Lindhorst, T. K.; Schmidt, S., Thermosensitive Display of Carbohydrate Ligands on Microgels for Switchable Binding of Proteins and Bacteria. *ACS Appl. Mater. Interfaces* **2019,** *11* (30), 26674-26683.
52. Abdouni, Y.; Yilmaz, G.; Becer, C. R., Sequence and Architectural Control in Glycopolymer Synthesis. *Macromol. Rapid Commun.* **2017,** *38* (24), 16.
53. Feizi, T., DEMONSTRATION BY MONOCLONAL-ANTIBODIES THAT CARBOHYDRATE STRUCTURES OF GLYCOPROTEINS AND GLYCOLIPIDS ARE ONCO-DEVELOPMENTAL ANTIGENS. *Nature* **1985,** *314* (6006), 53-57.
54. Varki, A.; Cummings, R. D.; Esko, J. D.; Stanley, P.; Hart, G. W.; Aebi, M.; Darvill, A. G.; Kinoshita, T.; Packer, N. H.; Prestegard, J. H.; Schnaar, R. L.; Seeberger, P. H., Essentials of Glycobiology. *Cold Spring Harbor Laboratory Press* **2009**.
55. Drickamer, K., Making a fitting choice: Common aspects of sugar-binding sites in plant and animal lectins. *Structure* **1997,** *5* (4), 465-468.
56. Dam, T. K.; Roy, R.; Das, S. K.; Oscarson, S.; Brewer, C. F., Binding of multivalent carbohydrates to concanavalin A and Dioclea grandiflora lectin - Thermodynamic analysis of the "multivalency effect". *J. Biol. Chem.* **2000,** *275* (19), 14223-14230.

57. Fasting, C.; Schalley, C. A.; Weber, M.; Seitz, O.; Hecht, S.; Koksch, B.; Dernedde, J.; Graf, C.; Knapp, E. W.; Haag, R., Multivalency as a Chemical Organization and Action Principle. *Angew. Chem.-Int. Edit.* **2012,** *51* (42), 10472-10498.
58. Pieters, R. J., Maximising multivalency effects in protein-carbohydrate interactions. *Org. Biomol. Chem.* **2009,** *7* (10), 2013-2025.
59. Adamson, A. W., A PROPOSED APPROACH TO THE CHELATE EFFECT. *J. Am. Chem. Soc.* **1954,** *76* (6), 1578-1579.
60. Kitov, P. I.; Bundle, D. R., On the nature of the multivalency effect: A thermodynamic model. *J. Am. Chem. Soc.* **2003,** *125* (52), 16271-16284.
61. Mack, E. T.; Snyder, P. W.; Perez-Castillejos, R.; Bilgicer, B.; Moustakas, D. T.; Butte, M. J.; Whitesides, G. M., Dependence of Avidity on Linker Length for a Bivalent Ligand-Bivalent Receptor Model System. *J. Am. Chem. Soc.* **2012,** *134* (1), 333-345.
62. Gestwicki, J. E.; Cairo, C. W.; Strong, L. E.; Oetjen, K. A.; Kiessling, L. L., Influencing receptor-ligand binding mechanisms with multivalent ligand architecture. *J. Am. Chem. Soc.* **2002,** *124* (50), 14922-14933.
63. Werz, D. B.; Ranzinger, R.; Herget, S.; Adibekian, A.; von der Lieth, C. W.; Seeberger, P. H., Exploring the structural diversity of mammalian carbohydrates ("Glycospace") by statistical databank analysis. *ACS Chem. Biol.* **2007,** *2* (10), 685-691.
64. Weis, W. I.; Drickamer, K., Structural basis of lectin-carbohydrate recognition. *Annu. Rev. Biochem.* **1996,** *65*, 441-473.
65. Davis, B. G., Recent developments in glycoconjugates. *J. Chem. Soc.-Perkin Trans. 1* **1999,** (22), 3215-3237.
66. Gabius, H. J.; Siebert, H. C.; Andre, S.; Jimenez-Barbero, J.; Rudiger, H., Chemical biology of the sugar code. *ChemBioChem* **2004,** *5* (6), 740-764.
67. Vornholt, W.; Hartmann, M.; Keusgen, M., SPR studies of carbohydrate-lectin interactions as useful tool for screening on lectin sources. *Biosens. Bioelectron.* **2007,** *22* (12), 2983-2988.
68. Perillo, N. L.; Marcus, M. E.; Baum, L. G., Galectins: versatile modulators of cell adhesion, cell proliferation, and cell death. *J. Mol. Med.* **1998,** *76* (6), 402-412.
69. Gallagher, J. T., CARBOHYDRATE-BINDING PROPERTIES OF LECTINS - A POSSIBLE APPROACH TO LECTIN NOMENCLATURE AND CLASSIFICATION - REVIEW. *Biosci. Rep.* **1984,** *4* (8), 621-632.
70. De Schutter, K.; Van Damme, E. J. M., Protein-Carbohydrate Interactions as Part of Plant Defense and Animal Immunity. *Molecules* **2015,** *20* (5), 9029-9053.
71. Lis, H.; Sharon, N., Lectins: Carbohydrate-specific proteins that mediate cellular recognition. *Chem. Rev.* **1998,** *98* (2), 637-674.
72. Saleemuddin, M.; Husain, Q., CONCANAVALIN-A - A USEFUL LIGAND FOR GLYCOENZYME IMMOBILIZATION - A REVIEW. *Enzyme Microb. Technol.* **1991,** *13* (4), 290-295.
73. Reeke, G. N.; Becker, J. W.; Edelman, G. M., COVALENT AND 3-DIMENSIONAL STRUCTURE OF CONCANAVALIN-A .4. ATOMIC COORDINATES, HYDROGEN-BONDING, AND QUATERNARY STRUCTURE. *J. Biol. Chem.* **1975,** *250* (4), 1525-1547.
74. Hardman, K. D.; Ainsworth, C. F., STRUCTURE OF CONCANAVALIN-A AT 2.4-A RESOLUTION. *Biochemistry* **1972,** *11* (26), 4910-4919.
75. Ernst, B.; Magnani, J. L., From carbohydrate leads to glycomimetic drugs. *Nat. Rev. Drug Discov.* **2009,** *8* (8), 661-677.
76. Chabre, Y. M.; Roy, R., Recent trends in glycodendrimer syntheses and applications. *Curr. Top. Med. Chem.* **2008,** *8* (14), 1237-1285.
77. Galan, M. C.; Dumy, P.; Renaudet, O., Multivalent glyco(cyclo)peptides. *Chem. Soc. Rev.* **2013,** *42* (11), 4599-4612.

78. Baier, M.; Rustmeier, N. H.; Harr, J.; Cyrus, N.; Reiss, G. J.; Grafmuller, A.; Blaum, B. S.; Stehle, T.; Hartmann, L., Divalent Sialylated Precision Glycooligomers Binding to Polyomaviruses and the Effect of Different Linkers. *Macromol. Biosci.* **2019,** *19* (5), 7.
79. Boden, S.; Wagner, K. G.; Karg, M.; Hartmann, L., Presenting Precision Glycomacromolecules on Gold Nanoparticles for Increased Lectin Binding. *Polymers* **2017,** *9* (12), 27.
80. Pramudya, I.; Chung, H. Y., Recent progress of glycopolymer synthesis for biomedical applications. *Biomater. Sci.* **2019,** *7* (12), 4848-4872.
81. Kiessling, L. L.; Grim, J. C., Glycopolymer probes of signal transduction. *Chem. Soc. Rev.* **2013,** *42* (10), 4476-4491.
82. Li, X.; Chen, G. J., Glycopolymer-based nanoparticles: synthesis and application. *Polym. Chem.* **2015,** *6* (9), 1417-1430.
83. Becer, C. R., The Glycopolymer Code: Synthesis of Glycopolymers and Multivalent Carbohydrate-Lectin Interactions. *Macromol. Rapid Commun.* **2012,** *33* (9), 742-752.
84. Ghadban, A.; Albertin, L., Synthesis of Glycopolymer Architectures by Reversible-Deactivation Radical Polymerization. *Polymers* **2013,** *5* (2), 431-526.
85. David, A.; Kopeckova, P.; Kopecek, J.; Rubinstein, A., The role of galactose, lactose, and galactose valency in the biorecognition of N-(2-hydroxypropyl)methacrylamide copolymers by human colon adenocarcinoma cells. *Pharm. Res.* **2002,** *19* (8), 1114-1122.
86. Basuki, J. S.; Esser, L.; Duong, H. T. T.; Zhang, Q.; Wilson, P.; Whittaker, M. R.; Haddleton, D. M.; Boyer, C.; Davis, T. P., Magnetic nanoparticles with diblock glycopolymer shells give lectin concentration-dependent MRI signals and selective cell uptake. *Chem. Sci.* **2014,** *5* (2), 715-726.
87. Baek, M. G.; Roy, R., Design and synthesis of water-soluble glycopolymers bearing breast tumor marker and enhanced lipophilicity for solid-phase assays. *Biomacromolecules* **2000,** *1* (4), 768-770.
88. Polizzotti, B. D.; Kiick, K. L., Effects of polymer structure on the inhibition of cholera toxin by linear polypeptide-based glycopolymers. *Biomacromolecules* **2006,** *7* (2), 483-490.
89. Wang, Y. X.; Zhang, X. G.; Han, Y. C.; Cheng, C.; Li, C. X., pH- and glucose-sensitive glycopolymer nanoparticles based on phenylboronic acid for triggered release of insulin. *Carbohydr. Polym.* **2012,** *89* (1), 124-131.
90. Pearson, S.; Scarano, W.; Stenzel, M. H., Micelles based on gold-glycopolymer complexes as new chemotherapy drug delivery agents. *Chem. Commun.* **2012,** *48* (39), 4695-4697.
91. Zheng, C.; Guo, Q. Q.; Wu, Z. M.; Sun, L.; Zhang, Z. P.; Li, C. X.; Zhang, X. G., Amphiphilic glycopolymer nanoparticles as vehicles for nasal delivery of peptides and proteins. *Eur. J. Pharm. Sci.* **2013,** *49* (4), 474-482.
92. Miura, Y.; Hoshino, Y.; Seto, H., Glycopolymer Nanobiotechnology. *Chem. Rev.* **2016,** *116* (4), 1673-1692.
93. Ting, S. R. S.; Chen, G. J.; Stenzel, M. H., Synthesis of glycopolymers and their multivalent recognitions with lectins. *Polym. Chem.* **2010,** *1* (9), 1392-1412.
94. Miura, Y., Design and synthesis of well-defined glycopolymers for the control of biological functionalities. *Polym. J.* **2012,** *44* (7), 679-689.
95. Boden, S.; Reise, F.; Kania, J.; Lindhorst, T. K.; Hartmann, L., Sequence-Defined Introduction of Hydrophobic Motifs and Effects in Lectin Binding of Precision Glycomacromolecules. *Macromol. Biosci.* **2019,** *19* (4), 11.

96. Ulrich, S.; Sadeghpour, A.; Rossi, R. M.; Bruns, N.; Boesel, L. F., Wide Range of Functionalized Poly(N-alkyl acrylamide)-Based Amphiphilic Polymer Conetworks via Active Ester Precursors. *Macromolecules* **2018,** *51* (14), 5267-5277.
97. Kumar, A.; Srivastava, A.; Galaev, I. Y.; Mattiasson, B., Smart polymers: Physical forms and bioengineering applications. *Prog. Polym. Sci.* **2007,** *32* (10), 1205-1237.
98. Galaev, I. Y.; Mattiasson, B., 'Smart' polymers and what they could do in biotechnology and medicine. *Trends Biotechnol.* **1999,** *17* (8), 335-340.
99. Stuart, M. A. C.; Huck, W. T. S.; Genzer, J.; Muller, M.; Ober, C.; Stamm, M.; Sukhorukov, G. B.; Szleifer, I.; Tsukruk, V. V.; Urban, M.; Winnik, F.; Zauscher, S.; Luzinov, I.; Minko, S., Emerging applications of stimuli-responsive polymer materials. *Nat. Mater.* **2010,** *9* (2), 101-113.
100. Jeong, B.; Gutowska, A., Lessons from nature: stimuli-responsive polymers and their biomedical applications. *Trends Biotechnol.* **2002,** *20* (7), 305-311.
101. Roy, D.; Brooks, W. L. A.; Sumerlin, B. S., New directions in thermoresponsive polymers. *Chem. Soc. Rev.* **2013,** *42* (17), 7214-7243.
102. Bhat, A.; Amanor-Boadu, J. M.; Guiseppi-Elie, A., Toward Impedimetric Measurement of Acidosis with a pH-Responsive Hydrogel Sensor. *ACS Sens.* **2020,** *5* (2), 500-509.
103. Chi, E. Y.; Krishnan, S.; Randolph, T. W.; Carpenter, J. F., Physical stability of proteins in aqueous solution: Mechanism and driving forces in nonnative protein aggregation. *Pharm. Res.* **2003,** *20* (9), 1325-1336.
104. Mano, J. F., Stimuli-responsive polymeric systems for biomedical applications. *Adv. Eng. Mater.* **2008,** *10* (6), 515-527.
105. Gil, E. S.; Hudson, S. M., Stimuli-reponsive polymers and their bioconjugates. *Prog. Polym. Sci.* **2004,** *29* (12), 1173-1222.
106. Schmaljohann, D., Thermo- and pH-responsive polymers in drug delivery. *Adv. Drug Deliv. Rev.* **2006,** *58* (15), 1655-1670.
107. Huang, J.; Hu, X. B.; Zhang, W. X.; Zhang, Y. H.; Li, G. T., pH and ionic strength responsive photonic polymers fabricated by using colloidal crystal templating. *Colloid Polym. Sci.* **2008,** *286* (1), 113-118.
108. Ercole, F.; Davis, T. P.; Evans, R. A., Photo-responsive systems and biomaterials: photochromic polymers, light-triggered self-assembly, surface modification, fluorescence modulation and beyond. *Polym. Chem.* **2010,** *1* (1), 37-54.
109. Nakahata, M.; Takashima, Y.; Yamaguchi, H.; Harada, A., Redox-responsive self-healing materials formed from host-guest polymers. *Nat. Commun.* **2011,** *2*, 6.
110. Lee, J.; Ko, J. H.; Mansfield, K. M.; Nauka, P. C.; Bat, E.; Maynard, H. D., Glucose-Responsive Trehalose Hydrogel for Insulin Stabilization and Delivery. *Macromol. Biosci.* **2018,** *18* (5), 7.
111. Zhang, W. L.; Choi, H. J., Stimuli-Responsive Polymers and Colloids under Electric and Magnetic Fields. *Polymers* **2014,** *6* (11), 2803-2818.
112. Wei, M. L.; Gao, Y. F.; Li, X.; Serpe, M. J., Stimuli-responsive polymers and their applications. *Polym. Chem.* **2017,** *8* (1), 127-143.
113. Cao, Z. Q.; Wang, G. J., Multi-Stimuli-Responsive Polymer Materials: Particles, Films, and Bulk Gels. *Chem. Rec.* **2016,** *16* (3), 1398-1435.
114. Wells, C. M.; Harris, M.; Choi, L.; Murali, V. P.; Guerra, F. D.; Jennings, J. A., Stimuli-Responsive Drug Release from Smart Polymers. *J. Func. Biomater.* **2019,** *10* (3), 20.
115. Yavuz, M. S.; Cheng, Y. Y.; Chen, J. Y.; Cobley, C. M.; Zhang, Q.; Rycenga, M.; Xie, J. W.; Kim, C.; Song, K. H.; Schwartz, A. G.; Wang, L. H. V.; Xia, Y. N., Gold nanocages covered by smart polymers for controlled release with near-infrared light. *Nat. Mater.* **2009,** *8* (12), 935-939.

116. Kulkarni, S.; Schilli, C.; Muller, A. H. E.; Hoffman, A. S.; Stayton, P. S., Reversible meso-scale smart polymer-protein particles of controlled sizes. *Bioconjugate Chem.* **2004,** *15* (4), 747-753.
117. Ward, M. A.; Georgiou, T. K., Thermoresponsive Polymers for Biomedical Applications. *Polymers* **2011,** *3* (3), 1215-1242.
118. Li, S. H.; Woo, E. M., Effects of Chain Configuration on UCST Behavior in Blends of Poly(L-lactic acid) with Tactic Poly(methyl methacrylate)s. *J. Polym. Sci. Pt. B-Polym. Phys.* **2008,** *46* (21), 2355-2369.
119. Cakir, N.; Hizal, G.; Becer, C. R., Supramolecular glycopolymers with thermo-responsive self-assembly and lectin binding. *Polym. Chem.* **2015,** *6* (37), 6623-6631.
120. Schild, H. G., POLY (N-ISOPROPYLACRYLAMIDE) - EXPERIMENT, THEORY AND APPLICATION. *Prog. Polym. Sci.* **1992,** *17* (2), 163-249.
121. Jochum, F. D.; Theato, P., Temperature- and light-responsive smart polymer materials. *Chem. Soc. Rev.* **2013,** *42* (17), 7468-7483.
122. Ganachaud, F.; Monteiro, M. J.; Gilbert, R. G.; Dourges, M. A.; Thang, S. H.; Rizzardo, E., Molecular weight characterization of poly(N-isopropylacrylamide) prepared by living free-radical polymerization. *Macromolecules* **2000,** *33* (18), 6738-6745.
123. Hoffman, A. S.; Stayton, P. S.; Bulmus, V.; Chen, G. H.; Chen, J. P.; Cheung, C.; Chilkoti, A.; Ding, Z. L.; Dong, L. C.; Fong, R.; Lackey, C. A.; Long, C. J.; Miura, M.; Morris, J. E.; Murthy, N.; Nabeshima, Y.; Park, T. G.; Press, O. W.; Shimoboji, T.; Shoemaker, S.; Yang, H. J.; Monji, N.; Nowinski, R. C.; Cole, C. A.; Priest, J. H.; Harris, J. M.; Nakamae, K.; Nishino, T.; Miyata, T., Really smart bioconjugates of smart polymers and receptor proteins. *J. Biomed. Mater. Res.* **2000,** *52* (4), 577-586.
124. Lutz, J. F., Polymerization of oligo(ethylene glycol) (meth)acrylates: Toward new generations of smart biocompatible materials. *J. Polym. Sci. Pol. Chem.* **2008,** *46* (11), 3459-3470.
125. Alarcon, C. D. H.; Pennadam, S.; Alexander, C., Stimuli responsive polymers for biomedical applications. *Chem. Soc. Rev.* **2005,** *34* (3), 276-285.
126. Kujawa, P.; Winnik, F. M., Volumetric studies of aqueous polymer solutions using pressure perturbation calorimetry: A new look at the temperature-induced phase transition of poly(N-isopropylacrylamide) in water and D2O. *Macromolecules* **2001,** *34* (12), 4130-4135.
127. Topp, M. D. C.; Dijkstra, P. J.; Talsma, H.; Feijen, J., Thermosensitive micelle-forming block copolymers of poly(ethylene glycol) and poly(N-isopropylacrylamide). *Macromolecules* **1997,** *30* (26), 8518-8520.
128. Bawa, P.; Pillay, V.; Choonara, Y. E.; du Toit, L. C., Stimuli-responsive polymers and their applications in drug delivery. *Biomed. Mater.* **2009,** *4* (2), 15.
129. Wu, C., A comparison between the 'coil-to-globule' transition of linear chains and the "volume phase transition" of spherical microgels. *Polymer* **1998,** *39* (19), 4609-4619.
130. Chee, C. K.; Rimmer, S.; Soutar, I.; Swanson, L., Time-resolved fluorescence anisotropy studies of the temperature-induced intramolecular conformational transition of poly(N-isopropylacrylamide) in dilute aqueous solution. *Polymer* **1997,** *38* (2), 483-486.
131. Fujishige, S.; Kubota, K.; Ando, I., PHASE-TRANSITION OF AQUEOUS-SOLUTIONS OF POLY(N-ISOPROPYLACRYLAMIDE) AND POLY(N-ISOPROPYLMETHACRYLAMIDE). *J. Phys. Chem.* **1989,** *93* (8), 3311-3313.
132. Liu, R. X.; Fraylich, M.; Saunders, B. R., Thermoresponsive copolymers: from fundamental studies to applications. *Colloid Polym. Sci.* **2009,** *287* (6), 627-643.
133. Ozyurek, Z.; Komber, H.; Gramm, S.; Schmaljohann, D.; Muller, A. H. E.; Voit, B., Thermoresponsive glycopolymers via controlled radical polymerization. *Macromol. Chem. Phys.* **2007,** *208* (10), 1035-1049.

134. Dalier, F.; Eghiaian, F.; Scheuring, S.; Marie, E.; Tribet, C., Temperature-Switchable Control of Ligand Display on Adlayers of Mixed Poly(lysine)-g-(PEO) and Poly(lysine)-g-(ligand-modified poly-N-isopropylacrylamide). *Biomacromolecules* **2016,** *17* (5), 1727-1736.
135. Nath, N.; Chilkoti, A., Creating "Smart" surfaces using stimuli responsive polymers. *Adv. Mater.* **2002,** *14* (17), 1243-+.
136. Mendes, P. M., Stimuli-responsive surfaces for bio-applications. *Chem. Soc. Rev.* **2008,** *37* (11), 2512-2529.
137. Wang, Y. N.; Kotsuchibashi, Y.; Liu, Y.; Narain, R., Study of Bacterial Adhesion on Biomimetic Temperature Responsive Glycopolymer Surfaces. *ACS Appl. Mater. Interfaces* **2015,** *7* (3), 1652-1661.
138. Min, E. H.; Ting, S. R. S.; Billon, L.; Stenzel, M. H., Thermo-Responsive Glycopolymer Chains Grafted onto Honeycomb Structured Porous Films via RAFT Polymerization as a Thermo-Dependent Switcher for Lectin Concanavalin A Conjugation. *J. Polym. Sci. Pol. Chem.* **2010,** *48* (15), 3440-3455.
139. Green, R. J.; Frazier, R. A.; Shakesheff, K. M.; Davies, M. C.; Roberts, C. J.; Tendler, S. J. B., Surface plasmon resonance analysis of dynamic biological interactions with biomaterials. *Biomaterials* **2000,** *21* (18), 1823-1835.
140. Homola, J., Present and future of surface plasmon resonance biosensors. *Anal. Bioanal. Chem.* **2003,** *377* (3), 528-539.
141. Daniels, J. S.; Pourmand, N., Label-free impedance biosensors: Opportunities and challenges. *Electroanalysis* **2007,** *19* (12), 1239-1257.
142. Abellan-Flos, M.; Timmer, B. J. J.; Altun, S.; Aastrup, T.; Vincent, S. P.; Ramstrom, O., QCM sensing of multivalent interactions between lectins and well-defined glycosylated nanoplatforms. *Biosens. Bioelectron.* **2019,** *139*, 8.
143. Rief, M.; Gautel, M.; Oesterhelt, F.; Fernandez, J. M.; Gaub, H. E., Reversible unfolding of individual titin immunoglobulin domains by AFM. *Science* **1997,** *276* (5315), 1109-1112.
144. de la Calle, A. C.; Gerke, C.; Chang, X. J.; Grafmuller, A.; Hartmann, L.; Schmidt, S., Multivalent Interactions of Polyamide Based Sequence-Controlled Glycomacromolecules with Concanavalin A. *Macromol. Biosci.* **2019,** *19* (6), 9.
145. Pussak, D.; Ponader, D.; Mosca, S.; Pompe, T.; Hartmann, L.; Schmidt, S., Specific Adhesion of Carbohydrate Hydrogel Particles in Competition with Multivalent Inhibitors Evaluated by AFM. *Langmuir* **2014,** *30* (21), 6142-6150.
146. Filler, T. J.; Peuker, E. T., Reflection contrast microscopy (RCM): a forgotten technique? *J. Pathol.* **2000,** *190* (5), 635-638.
147. Hoefsmit, E. C. M.; Korn, C.; Blijleven, N.; Ploem, J. S., LIGHT MICROSCOPIC DETECTION OF SINGLE 5 AND 20 NM GOLD PARTICLES USED FOR IMMUNOLABELING OF PLASMA-MEMBRANE ANTIGENS WITH SILVER ENHANCEMENT AND REFLECTION CONTRAST. *J. Microsc.-Oxf.* **1986,** *143*, 161-169.
148. Prins, F. A.; Vandiemensteenvoorde, R.; Bonnet, J.; Cornelesetenvelde, I., REFLECTION CONTRAST MICROSCOPY OF ULTRATHIN SECTIONS IN IMMUNOCYTOCHEMICAL LOCALIZATION STUDIES - A VERSATILE TECHNIQUE BRIDGING ELECTRON-MICROSCOPY WITH LIGHT-MICROSCOPY. *Histochemistry* **1993,** *99* (6), 417-425.
149. Zidovska, A.; Sackmann, E., Brownian motion of nucleated cell envelopes impedes adhesion. *Physical Review Letters* **2006,** *96* (4).
150. Weber, I., Reflection interference contrast microscopy. *Methods Enzymol.* **2003,** *361*, 34-47.

151. Piller, H., Enhancement of contrast in reflected-light microscopy. *Zeiss Werkschrift* **1959,** *34*, 89-90.
152. Ploem, J., Applications of reflection-contrast microscopy, including the sensitive detection of the results of in situ hybridisation a review. *J. Microsc.* **2019,** *274* (2), 79-86.
153. Cornelesetenvelde, I.; Bonnet, J.; Tanke, H. J.; Ploem, J. S., REFLECTION CONTRAST MICROSCOPY PERFORMED ON EPI-ILLUMINATION MICROSCOPE STANDS - COMPARISON OF REFLECTION CONTRAST-POLARIZATION AND EPI-POLARIZATION MICROSCOPY. *J. Microsc.-Oxf.* **1990,** *159*, 1-13.
154. Strzelczyk, A. K.; Wang, H. Q.; Lindhorst, A.; Waschke, J.; Pompe, T.; Kropf, C.; Luneau, B.; Schmidt, S., Hydrogel Microparticles as Sensors for Specific Adhesion: Case Studies on Antibody Detection and Soil Release Polymers. *Gels* **2017,** *3* (3), 13.
155. Schmidt, S.; Wang, H. Q.; Pussak, D.; Mosca, S.; Hartmann, L., Probing multivalency in ligand-receptor-mediated adhesion of soft, biomimetic interfaces. *Beilstein J. Org. Chem.* **2015,** *11*, 720-729.
156. Pussak, D.; Ponader, D.; Mosca, S.; Ruiz, S. V.; Hartmann, L.; Schmidt, S., Mechanical Carbohydrate Sensors Based on Soft Hydrogel Particles. *Angew. Chem.-Int. Edit.* **2013,** *52* (23), 6084-6087.
157. Pussak, D.; Behra, M.; Schmidt, S.; Hartmann, L., Synthesis and functionalization of poly(ethylene glycol) microparticles as soft colloidal probes for adhesion energy measurements. *Soft Matter* **2012,** *8* (5), 1664-1672.
158. Erath, J.; Schmidt, S.; Fery, A., Characterization of adhesion phenomena and contact of surfaces by soft colloidal probe AFM. *Soft Matter* **2010,** *6* (7), 1432-1437.
159. Hertz, H., Ueber die Berührung fester elastischer Körper. *Journal für die reine und angewandte Mathematik* **1881,** *92*, 156-171.
160. Roberts, A. D., Ph. D. dissertation. *Cambridge University, England* **1968**.
161. Kendall, K., Ph. D. dissertation. *Cambridge University, England* **1969**.
162. Johnson, K. L.; Kendall, K.; A.D., R., Surface energy and the contact of elastic solids. *Proceedings of the Royal Society A: Mathematical, Physical and Engineering Sciences* **1971,** *324* (1558), 301-313.
163. Hughes, B. D.; White, L. R., IMPLICATIONS OF ELASTIC-DEFORMATION ON THE DIRECT MEASUREMENT OF SURFACE FORCES. *Journal of the Chemical Society-Faraday Transactions I* **1980,** *76*, 963-978.
164. Maugis, D., ADHESION OF SPHERES - THE JKR-DMT TRANSITION USING A DUGDALE MODEL. *J. Colloid Interface Sci.* **1992,** *150* (1), 243-269.
165. Wang, H. Q.; Jacobi, F.; Waschke, J.; Hartmann, L.; Lowen, H.; Schmidt, S., Elastic Modulus Dependence on the Specific Adhesion of Hydrogels. *Adv. Funct. Mater.* **2017,** *27* (41), 9.
166. Binnig, G.; Quate, C. F.; Gerber, C., Atomic Force Microscope. *Physical Review Letters* **1986,** *56* (9), 930-933.
167. Meagher, L., DIRECT MEASUREMENT OF FORCES BETWEEN SILICA SURFACES IN AQUEOUS CACL2 SOLUTIONS USING AN ATOMIC FORCE MICROSCOPE. *J. Colloid Interface Sci.* **1992,** *152* (1), 293-295.
168. Gultekinoglu, M.; Oh, Y. J.; Hinterdorfer, P.; Duman, M.; Catcat, D.; Ulubayram, K., Nanoscale characteristics of antibacterial cationic polymeric brushes and single bacterium interactions probed by force microscopy. *RSC Adv.* **2016,** *6* (21), 17092-17099.
169. Lekka, M.; Sainz-Serp, D.; Kulik, A. J.; Wandrey, C., Hydrogel microspheres: Influence of chemical composition on surface morphology, local elastic properties, and bulk mechanical characteristics. *Langmuir* **2004,** *20* (23), 9968-9977.
170. Glaubitz, M.; Medvedev, N.; Pussak, D.; Hartmann, L.; Schmidt, S.; Helm, C. A.; Delcea, M., A novel contact model for AFM indentation experiments on soft spherical cell-like particles. *Soft Matter* **2014,** *10* (35), 6732-6741.

171. Ponader, D.; Wojcik, F.; Beceren-Braun, F.; Dernedde, J.; Hartmann, L., Sequence-Defined Glycopolymer Segments Presenting Mannose: Synthesis and Lectin Binding Affinity. *Biomacromolecules* **2012,** *13* (6), 1845-1852.
172. Baier, M.; Giesler, M.; Hartmann, L., Split-and-Combine Approach Towards Branched Precision Glycomacromolecules and Their Lectin Binding Behavior. *Chem.-Eur. J.* **2018,** *24* (7), 1619-1630.
173. Goldmann, W. H.; Schindl, M.; Cardozo, T. J.; Ezzell, R. M., MOTILITY OF VINCULIN-DEFICIENT F9 EMBRYONIC CARCINOMA-CELLS ANALYZED BY VIDEO, LASER CONFOCAL, AND REFLECTION INTERFERENCE CONTRAST MICROSCOPY. *Exp. Cell Res.* **1995,** *221* (2), 311-319.
174. Ingber, D. E., Cellular mechanotransduction: putting all the pieces together again. *Faseb J.* **2006,** *20* (7), 811-827.
175. Dupont, S.; Morsut, L.; Aragona, M.; Enzo, E.; Giulitti, S.; Cordenonsi, M.; Zanconato, F.; Le Digabel, J.; Forcato, M.; Bicciato, S.; Elvassore, N.; Piccolo, S., Role of YAP/TAZ in mechanotransduction. *Nature* **2011,** *474* (7350), 179-U212.

5. Publications

5.1. Sequence-defined positioning of amine and amide residues to control catechol driven wet adhesion

Authors:	Lukas Fischer[#], **Alexander K. Strzelczyk[#]**, Nils Wedler, Christian Kropf, Stephan Schmidt, Laura Hartmann
Journal:	*Chemical Science*.
Issue:	Manuscript submitted
Type of Paper:	Full Paper
Impact Factor:	9.556 (2019)

Own Contribution (first author, equal contribution)

Synthesis of poly(ethylene glycol) based crotonic acid functionalized SCPs as well as functionalization with oligomers and analysis of elastic modulus and functionalization degree. Measurement of adhesion energies of oligomer functionalized SCPs and glass surfaces. Collaborative writing of the paper.

ARTICLE

Sequence-defined positioning of amine and amide residues to control catechol driven wet adhesion.

Received 00th January 20xx,
Accepted 00th January 20xx

DOI: 10.1039/x0xx00000x

Lukas Fischer,†[a] Alexander K. Strzelczyk, †[a] Nils Wedler,[b] Christian Kropf,[b] Stephan Schmidt*[a] and Laura Hartmann*[a]

Catechol and amine residues, both abundantly present in mussel adhesion proteins, are known to act cooperatively by displacing hydration barriers before binding to mineral surfaces. In spite of synthetic efforts toward mussel-inspired adhesives, the effect of positioning of the involved functional groups along a polymer chain is not well understood. By using sequence-defined oligomers grafted to soft hydrogel particles as adhesion probes, we study the effect of catechol-amine spacing, as well as positioning relative to the oligomer terminus. We demonstrate that the catechol-amine spacing has a significant effect on adhesion, while shifting their position has a small effect. Notably, combinations of non-charged amides and catechols can achieve similar cooperative effects on adhesion when compared to amine and catechol residues. Thus, these findings provide a blueprint for the design of next generation mussel-inspired adhesives.

Introduction

Marine organisms such as mussels, barnacles, or sandcastle worms are prime examples of biological wet adhesion. They exhibit strong attachments to inorganic and organic surfaces in aqueous medium, even in the presence of high salt concentrations.[1, 2] In aqueous environment, the adhesion is inhibited by both water and hydrated salt ions through the formation of thin layers preventing the direct contact between adhesive groups at the material surfaces.[3, 4] Mussels in particular have evolved adhesive proteins (mussel foot proteins, Mfps) that circumvent this problem by displacing the hydration layers and then bridging to the surface via strong bonding primarily through L-3,4-dihydroxyphenylalanine (DOPA) groups.[5-7] Recent findings state that the high amount of DOPA in proximity to cationic amino acids is responsible for these unique properties.[8, 9] This synergistic effect between DOPA and primary amines is due to dispatching the hydration layer of the surface via charged amines allowing the catechol residues to bind to the surface. Such synergy between catechol (DOPA) and charged groups could be confirmed using synthetic polymers combining anionic and cationic residues.[10-12] Inspired by the adhesive properties of the Mfps, a wide range of polymers with high DOPA content were synthesized toward advanced adhesives and surface coatings.[1, 6, 13-22] However, sequence effects like the spacing of the charged groups and catechol residues were given little attention for the design of such mussel-inspired synthetic adhesives.

The adhesive proteins of mussels contain a large amount of DOPA and amine residues, e.g. Mfp-5 carries 30 mol% DOPA and 28% mol% amines, which are usually in close proximity.[23] However, another class of residue typically represented at higher than 10 mol% (in Mfp-2, Mfp-3, Mfp-4, and Mfp-6) is asparagine carrying a primary amide.[23-26] Asparagine as a "helix-breaker" residue is believed to increase the flexibility of the Mfps improving the accessibility of the adhesive DOPA groups. Intriguingly, for Mfp-3 the amide side chains are predominantly found in direct proximity to amine and DOPA residues.[26] The function of Mfp-3 as a primer for strong underwater adhesion has been shown by direct adhesion measurements via atomic force microscopy or the surface force apparatus,[7, 27] but the role of amide side chains on adhesion has not been studied so far. Therefore, in this study we present the synthesis of sequence-defined oligo(amidoamine)s carrying selected combinations of catechol, tertiary amine and primary amide residues, similar to the arrangement of arginine, DOPA and amine residues found in Mfp-3 and study their adhesion energies on glass surfaces.

Results and Discussion

Synthesis of sequence defined oligomers

As a cationic residue a tertiary amine was chosen to prevent crosslinking with the catechols particularly at higher pH. In addition, choosing this non-natural cationic residue instead of primary amines might provide additional indication that the catechol-amine synergy is due to the removal of the hydration layer by the charge effect and not due to additional hydrogen bonding by the amines. Along these lines, as a non-natural

[a] Institut für Organische und Makromolekulare Chemie, Heinrich-Heine-Universität Düsseldorf, Universitätsstr. 1, 40225 Düsseldorf, Germany.
[b] Laundry & Home Care, Henkel AG & Co. KGaA, Henkelstr. 67, 40589 Düsseldorf, Germany.
† LF and AKS contributed equally to this work.
Electronic Supplementary Information (ESI) available: materials and methods, chemical analysis, See DOI: 10.1039/x0xx00000x

spacer building block between the catechol, amine and amide residues we use a short ethylene glycol chain (EDS block) to show the feasibility of transferring the catechol driven adhesion mechanism to synthetic polymers. The oligomer synthesis was adapted from an already established method using tailor-made building blocks for solid phase assembly to generate the sequence-defined structures.[28, 29] Similar to solid phase peptide synthesis, the building blocks carry both, a carboxy and an Fmoc protected primary amine group, that allow step-wise chain growth on an amine functionalized resin. Here two new building blocks were synthesized, one carrying a protected catechol moiety and one carrying an orthogonal protected primary amine, to later introduce the tertiary amine and primary amide via amide coupling on solid support (Figure 1).

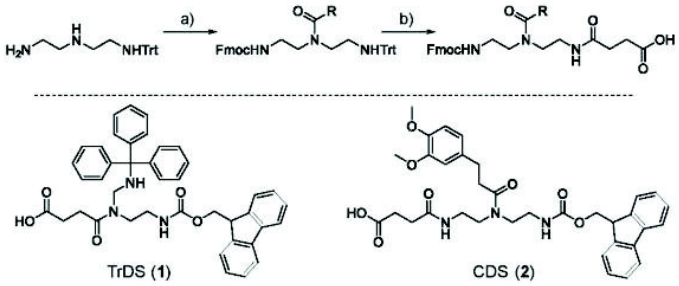

Figure 1 New synthesis route towards functional building blocks; a) Fmoc-OSu, 3 eq. triethylamine in THF at -78°C followed by 1 eq. activated acid; b) 10 eq. TFA in DCM followed by precipitation and 1 eq. succinic anhydride, 3 eq. triethylamine in DCM.

A major challenge in the solid phase synthesis of sequence-defined polymers is the access to tailor-made building blocks in sufficient quantity and purity, ideally in a time and cost-efficient manner. Here, an advanced method providing the required building blocks was developed streamlining the previous approach to a straightforward 3-step route with greatly improved atom economy and higher yields.[28, 30-33] In the first step, one of the two primary amines of diethylenetriamine was protected using trityl chloride. Afterward, the second primary amine was selectively converted using Fmoc-OSu in THF at -78°C, with subsequent addition of an activated acid which carries the desired side chain functionality. The last step includes the cleavage of the trityl group and reaction with succinic anhydride. With this new protocol two different building blocks were synthesized. The first building block TrDS (**1**) offers a trityl protected amine, orthogonal to the Fmoc protection group, for further functionalization during solid phase synthesis. The second novel building block CDS (**2**) was developed to introduce a methyl ether protected catechol moiety in the side chain using the acyl chloride of 3-(3,4-dimethoxyphenyl)propionic acid. This protecting strategy ensured stability during acidic conditions of the building block synthesis as well as basic conditions during solid phase synthesis. Together with the previously introduced building blocks EDS, TrDS, and CDS, solid phase supported synthesis following previously reported coupling conditions was applied (Figure 2). The oligomer scaffold was assembled by step-wise amide coupling and subsequent Fmoc deprotection of the terminal amine. For the introduction of side chains presenting a tertiary amine or primary amide groups, the TrDS building block was used: After full synthesis of the backbone, the trityl group of TrDS was cleaved using 0.15 M HCl in trifluorethanol, a condition resulting in full release of the trityl group while maintaining stability of the acid labile solid support.[34] Next, the desired side chain functionalities were introduced by coupling the corresponding carboxylic acid using PyBOP as a coupling reagent. After cleavage of the oligomer from the solid phase, the catechol moieties were deprotected using trifluormethanesulfonic acid and thioanisole in trifluoracetic acid following a procedure previously introduced by Kiso et al.[35] Full deprotection and successful isolation of the desired oligomer structures were confirmed by ^{1}H-NMR, ^{13}C-NMR and HR-ESI MS (see supporting information S4).

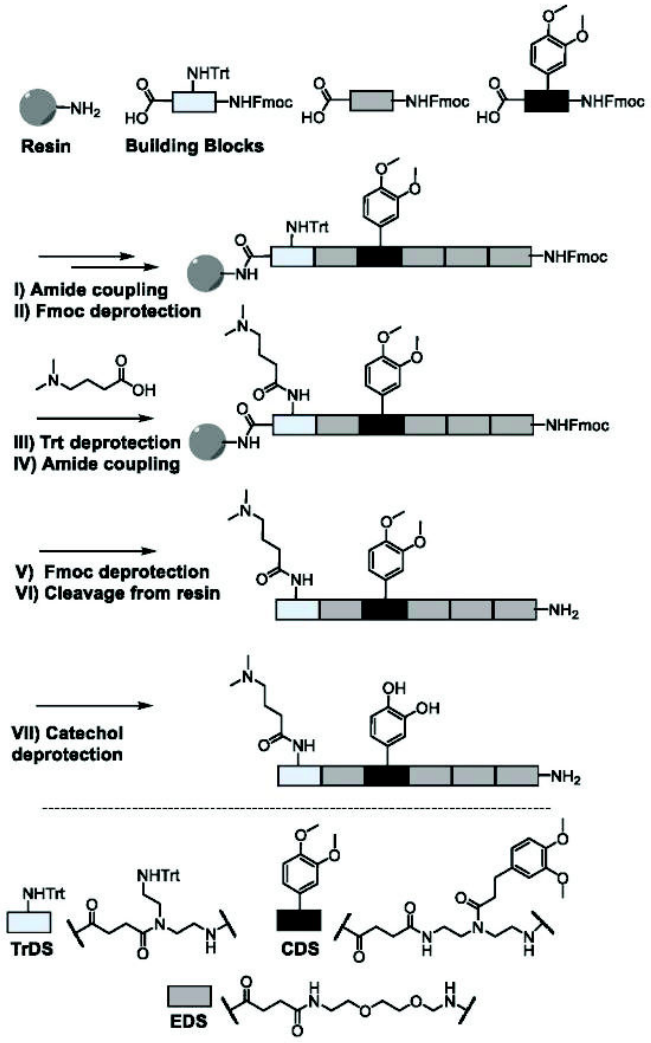

Figure 2 Exemplary scheme for solid phase synthesis of an oligomer using a rink amide resin; I) 5 eq. building block, 5 eq. PyBOP, 10 eq. DIPEA in DMF; II+V) 20% piperidine in DMF; III) 0.15 M HCl in trifluoroethanol; IV) 10 eq. acid, 10 eq. PyBOP, 20 eq. DIPEA; VI) 95% TFA, 2.5% DCM and 2.5% triisoproylsilane; VII) 16 eq. trifluoromethanesulfonic acid, 8eq. thioanisole in TFA.

In total 9 different oligomers were synthesized (Figure 3). All structures carry a terminal amine group for later coupling onto

microgels and use in adhesion studies. In order to study combination and positioning effects of the different functional

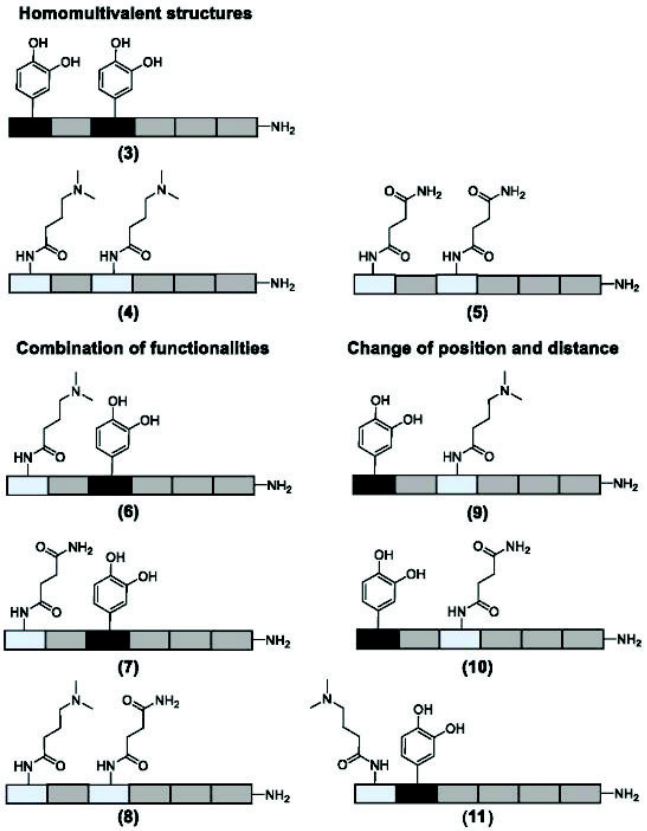

Figure 3 Overview of the oligomers.

groups on adhesion, various sets of oligomers were synthesized. As homofunctional structures, the oligomers **3-5** each carry two identical functional groups, either catechol, tertiary amine, or primary amide both in position 1 and 3. Oligomers **6**, **7** and **8** combine two of the functional groups to form the three possible combinations. Oligomers **9** and **10** change the position of catechol and amine or amide, to investigate the influence of the order of functional groups. In addition, oligomer **11** reduces the spacing between amine and catechol. All oligomers have a length of six building blocks with the EDS building blocks serving as spacers between the functional building blocks keeping the overall size of all oligomers the same. Importantly, for all catechol bearing structures, oxidation in water was not observed within several days (see supporting information S7). Therefore, we assume that in the course of the following adhesion studies, catechol-quinone transitions did not take place.

SCP preparation and adhesion measurements

For the adhesion measurements, soft microgels (soft colloidal probes, SCPs) based on poly(ethlylene glycol) (PEG) were functionalized with the sequence-defined oligomers (**3-11**) and allowed to settle and bind to glass surfaces.[37] The glass surfaces were used here as a model for inorganic silica-based materials. To prepare the SCPs, microdroplets of poly(ethylene glycol diacrylamide) were formed via liquid-liquid phase separation in a concentrated sodium sulphate solution followed by UV crosslinking (**Fehler! Verweisquelle konnte nicht gefunden werden.**).[36] The oligomers were introduced by grafting of crotonic acid under UV irradiation in presence of benzophenone followed by the repeated coupling of the oligomers via carbodiimide chemistry. The degree of oligomer functionalization in the PEG network was determined in two steps via titration with toluidine blue, a crotonic acid binding dye.[37] First, the amount of crotonic acid was determined before coupling the oligomers. Second, the residual, unreacted crotonic acid residues were titrated after the oligomer coupling step. The coupling efficiency was larger than 90%, and the oligomer functionalization degrees were determined as ~86 µmol per gram PEG (see supporting information S5). Hence, 13.5-14.2 wt% of the PEG-SCPs are oligomers. Using the SCP elastic moduli as an estimate for the specific volume in of PEG in water,[38] the PEG swelling degree can be calculated giving an oligomer concentration of 11 mmol l^{-1} in the SCP scaffold.[38]

Upon adhesion, the SCPs mechanically deform and form distinct contact areas with the glass surface. To quantify the SCP-adhesion energies (W_{adh}) on glass, the contact radii (a) were measured by micro-interferometry (Fehler! Verweisquelle konnte nicht gefunden werden.) and evaluated by the Jonson-Kendall-Roberts (JKR) model of adhesion:[39-41]

$$a^3 = \frac{9\pi R^2 W_{adh}(1-\nu^2)}{2E}$$

where W_{adh} is the adhesion energy, E is the elastic modulus of the SCPs, and ν the Poisson ratio. The adhesion energies were read from the plots of the contact area a and the SCP radius R (***Fehler! Verweisquelle konnte nicht gefunden werden.***). The SCP method allows detecting adhesion energies with high precision and has been broadly applied, e.g. to study biomolecular interactions,[39, 40] hydrophobic forces,[41] and analytes in the solute by very sensitive competitive binding assays.[42, 43]

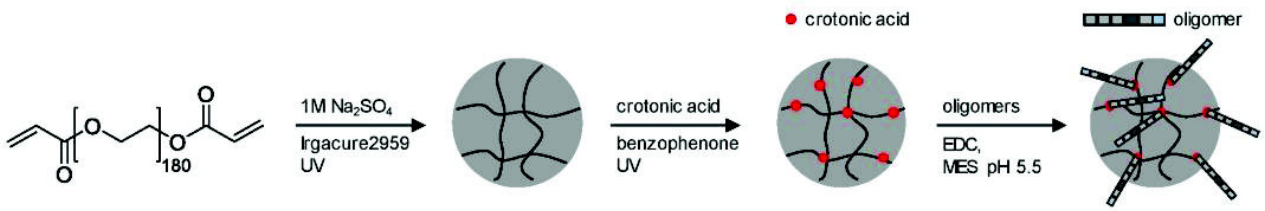

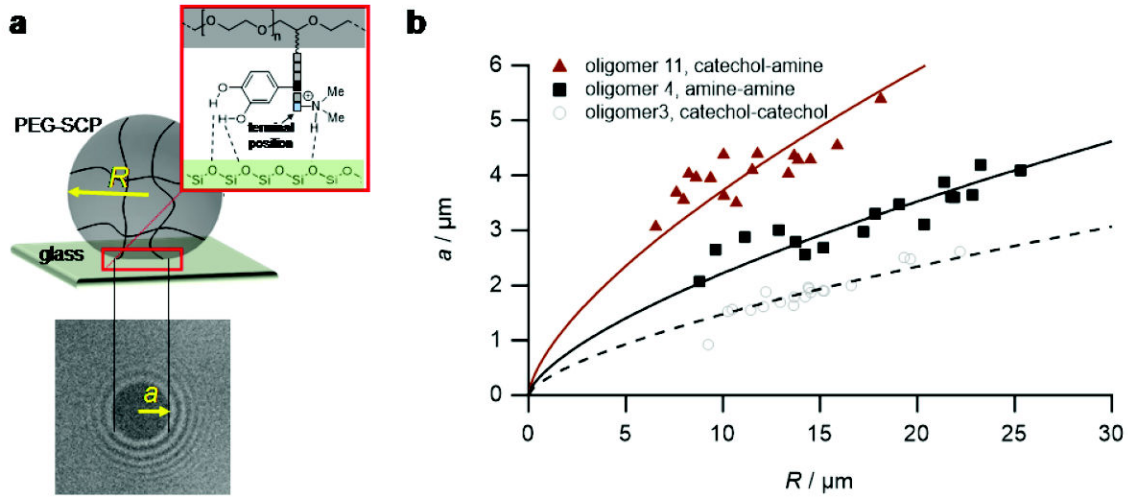

Figure 5 The SCP adhesion assay. a) Schematic representation of an oligomer-functionalized SCP adhering to a glass slide. The reflection interference contrast microscopy image (bottom) shows a typical contact area (dark area in the center) and newton rings providing the geometry of the SCP, i.e. the parameters a and R. b) Typical JKR plots and fits (lines) according to equation 1 depicting the oligomers 3 (empty circles), 4 (squares) and 11 (triangles).

To control the solute conditions, the SCP-adhesion assay was conducted in 0.1 M sodium chloride and between pH 3-8 (Figure 6). The pH controls the glass surface charge by protonation/deprotonation of the silanol groups, which broadly affects the adhesion. At low pH the surface is able to donate hydrogen bonds to the ethylene glycol groups at the PEG and EDS backbone, whereas almost complete deprotonation is expected at pH 7,[42] rendering the surface unable to donate hydrogen bonds. In addition, the hydration barrier is stronger for charged surfaces at high pH.[43] This explains the observed overall decreasing adhesion energies with increasing pH for all oligomers (Figure 6b). The measurements confirmed the synergistic effect between cationic amines and catechols since the catechol/amine (**6**,**9**,**11**) combinations always achieve higher adhesion when compared to catechol/catechol (**3**). This shows that the catechol/amine synergy also works with tertiary amines instead of the natural primary amines supporting the hypothesis that it is the charge-induced displacement of the hydration layer that increases catechol binding. With the sequence-controlled oligomers we could additionally show the effect of catechol/amine spacing. In case where the catechol and amine residues are in close vicinity (**11**), the adhesion energy is drastically amplified compared to the oligomers with an additional EDS spacer between catechol and amine (**6**,**9**). In addition, the adhesion was affected by changing the position of the catechol and amine residues (**6**,**9**). When the amine is located at the terminating position (the free chain end not attached to the SCP) (**6**), the decrease in adhesion between pH 3 and pH 5 is not as strong when compared to the oligomer with the catechol at the terminating position (**9**). This could be due to the increased ionic interactions between the terminal amine and the partially deprotonated surface at pH 5 compensating the loss of silanol hydrogen bonding at elevated pH. Comparison with structures that do not contain catechol but combinations of amines and primary amide side chains confirm this trend (**4**,**5**,**8**). The amides can interact with the silica groups at the surface via hydrogen bonding but when cationic amines are included (**8**) the adhesion appears to be stronger at elevated pH on the anionic glass surface due to additional ionic bonding. Overall, these results agree with earlier studies on the synergistic adhesion effects of amine and catechol residues,[8-10] but for the first time show that their positioning and spacing is of key importance to maximize such synergy.

Surprisingly, the combination of amide and catechol residues showed an even larger dependence on the residue positioning. In case the catechol is the terminating group (**10**), the adhesion energy is significantly stronger when compared to placing the amide at the chain end (**7**). The adhesion is even stronger when compared to amine/catechol combinations with similar spacing (**6**,**9**). This suggests that there are additional interactions amplifying the catechol-mediated adhesion with the glass surface, similar to the amine/catechol synergism. For amide/catechol combinations this could be in part due to the

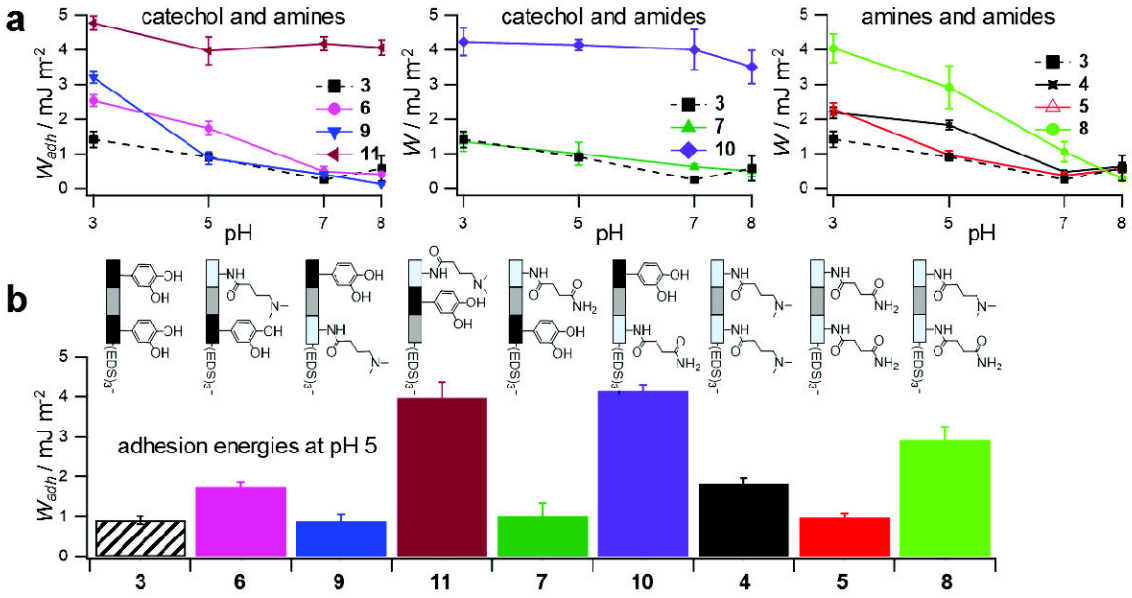

Figure 6 Adhesion energies measured for oligomer-functionalized SCPs a) Measurements against a glass surface in 0.1 M sodium chloride solution from pH 3 to pH 8. b) adhesion energies mimicking the pH during protein secretion in initial mussel adhesion.[2]

ionic resonance structure of the primary amide (25-30% ionic character)[44] helping to displace the surface hydration layer on the glass surface. In addition, we hypothesize that there is an intricate balance between intra- and intermolecular hydrogen bond interactions. Intramolecular hydrogen bonding of the functional side chains would reduce their interaction with the surface and thus the overall adhesion. It seems that the introduction of primary amide side chains shifts this balance toward promoting adhesion. We have observed previously for sequence-controlled oligomers mimicking biopolymers that indeed the positioning of residues and the resulting variations in the conformation of the molecule play a key role for their intermolecular interactions e.g. when targeting protein receptors.[45] We cannot conclude yet on the mechanisms of increasing catechol-mediated adhesion when introducing primary amide side chains but when looking back at the natural role model, Mfp-3, DOPA moieties are indeed very often accompanied by neighbouring asparagine building blocks. Thus the effect we observe here is likely to take place also in the natural mussel adhesives.

Conclusions

Taken together, combining catechols and amines on a scaffold promotes wet adhesion in accordance with the literature.[10] Intriguingly, the spacing of these residues on the polymer chain strongly affects adhesion to negatively charged silica surfaces. Charged moieties and catechols should be very close to maximize adhesion, which is also in accordance with their positioning in the mussel adhesion proteins. Notably also non-natural charged residues such as the tertiary amines used here are capable of increasing the catechol binding due to the displacement of hydration layers and condensed ions. In addition, introducing other functional groups present in the natural sequences such as primary amides may also have synergistic effects on adhesion as they showed increased adhesion in comparison to the amine/catechol combinations in this study. Although details of the potential mechanism remain unknown, this shows that there is still much to be learned and much to be gained by controlling the positioning of interacting residues in bio-inspired sequence-controlled polymers.

Conflicts of interest

The authors filed a patent application DE 102019208832.5 "Polymere für die Behandlung von Oberflächen"

Acknowledgements

The authors acknowledge funding by Henkel AG & Co. KGaA.

Notes and references

1. A. H. Hofman, I. A. van Hees, J. Yang and M. Kamperman, *Adv. Mater.*, 2018, **30**, e1704640.
2. J. H. Waite, *J. Exp. Biol.*, 2017, **220**, 517-530.
3. J. Israelachvili and H. Wennerström, *Nature*, 1996, **379**, 219-225.
4. Y. Li, C. Liang, L. Gao, S. Y. Li, Y. Z. Zhang, J. Zhang and Y. Cao, *Mat. Chem. Front.*, 2017, **1**, 2664-2668.
5. M. Yu, J. Hwang and T. J. Deming, *J. Am. Chem. Soc.*, 1999, **121**, 5825-5826.
6. B. P. Lee, P. B. Messersmith, J. N. Israelachvili and J. H. Waite, *Annu. Rev. Mater. Res.*, 2011, **41**, 99-132.
7. H. Lee, N. F. Scherer and P. B. Messersmith, *Proc. Natl. Acad. Sci. U. S. A.*, 2006, **103**, 12999-13003.
8. G. P. Maier, M. V. Rapp, J. H. Waite, J. N. Israelachvili and A. Butler, *Science*, 2015, **349**, 628-632.
9. M. V. Rapp, G. P. Maier, H. A. Dobbs, N. J. Higdon, J. H. Waite, A. Butler and J. N. Israelachvili, *J. Am. Chem. Soc.*, 2016, **138**, 9013-9016.
10. A. R. Narkar, J. D. Kelley, R. Pinnaratip and B. P. Lee, *Biomacromolecules*, 2018, **19**, 1416-1424.
11. Q. Zhao, D. W. Lee, B. K. Ahn, S. Seo, Y. Kaufman, Jacob N. Israelachvili and J. H. Waite, *Nat. Mater.*, 2016, **15**, 407-412.
12. B. K. Ahn, S. Das, R. Linstadt, Y. Kaufman, N. R. Martinez-Rodriguez, R. Mirshafian, E. Kesselman, Y. Talmon, B. H. Lipshutz, J. N. Israelachvili and J. H. Waite, *Nat. Commun.*, 2015, **6**, 8663.
13. J. H. Ryu, P. B. Messersmith and H. Lee, *ACS Appl. Mater. Interfaces*, 2018, **10**, 7523-7540.
14. Q. Zhang, G. Nurumbetov, A. Simula, C. Y. Zhu, M. X. Li, P. Wilson, K. Kempe, B. Yang, L. Tao and D. M. Haddleton, *Polym. Chem.*, 2016, **7**, 7002-7010.
15. H. Lee, S. M. Dellatore, W. M. Miller and P. B. Messersmith, *Science*, 2007, **318**, 426-430.
16. Q. Ye, F. Zhou and W. M. Liu, *Chem. Soc. Rev.*, 2011, **40**, 4244-4258.
17. S. Moulay, *Polym. Rev.*, 2014, **54**, 436-513.
18. E. Faure, C. Falentin-Daudre, C. Jerome, J. Lyskawa, D. Fournier, P. Woisel and C. Detrembleur, *Prog. Polym. Sci.*, 2013, **38**, 236-270.
19. J. Yang, J. Keijsers, M. van Heek, A. Stuiver, M. A. C. Stuart and M. Kamperman, *Polym. Chem.*, 2015, **6**, 3121-3130.
20. N. Patil, C. Jerome and C. Detrembleur, *Prog. Polym. Sci.*, 2018, **82**, 34-91.
21. N. L. Venkatareddy, P. Wilke, N. Ernst, J. Horsch, M. Weber, A. Dallmann and H. G. Boerner, *Adv. Mater. Interfaces*, 2019, **6**.
22. Q. Wei, K. Achazi, H. Liebe, A. Schulz, P. L. M. Noeske, I. Grunwald and R. Haag, *Angew. Chem. Int. Ed.*, 2014, **53**, 11650-11655.
23. H. Zhao and J. H. Waite, *Biochemistry*, 2006, **45**, 14223-14231.
24. H. Zhao and J. H. Waite, *J. Biol. Chem.*, 2006, **281**, 26150-26158.
25. L. M. Rzepecki, K. M. Hansen and J. H. Waite, *The Biological Bulletin*, 1992, **183**, 123-137.
26. V. V. Papov, T. V. Diamond, K. Biemann and J. H. Waite, *J. Biol. Chem.*, 1995, **270**, 20183-20192.
27. Q. Lin, D. Gourdon, C. Sun, N. Holten-Andersen, T. H. Anderson, J. H. Waite and J. N. Israelachvili, *Proc. Natl. Acad. Sci. U. S. A.*, 2007, **104**, 3782-3786.
28. D. Ponader, F. Wojcik, F. Beceren-Braun, J. Dernedde and L. Hartmann, *Biomacromolecules*, 2012, **13**, 1845-1852.
29. D. Ponader, P. Maffre, J. Aretz, D. Pussak, N. M. Ninnemann, S. Schmidt, P. H. Seeberger, C. Rademacher, G. U. Nienhaus and L. Hartmann, *J. Am. Chem. Soc.*, 2014, **136**, 2008-2016.
30. K. S. Bucher, P. B. Konietzny, N. L. Snyder and L. Hartmann, *Chemistry (Easton)*, 2018, DOI: 10.1002/chem.201804505.
31. M. Baier, M. Giesler and L. Hartmann, *Chem. Eur. J.*, 2018, **24**, 1619-1630.
32. F. Wojcik, A. G. O'Brien, S. Gotze, P. H. Seeberger and L. Hartmann, *Chem. Eur. J.*, 2013, **19**, 3090-3098.
33. T. Freichel, S. Eierhoff, N. L. Snyder and L. Hartmann, *J. Org. Chem.*, 2017, **82**, 9400-9409.
34. P. Palladino and D. A. Stetsenko, *Org. Lett.*, 2012, **14**, 6346-6349.
35. Y. Kiso, K. Ukawa, S. Nakamura K. Ito and T. Akita, *Chem. Pharm. Bull.*, 1980, **28**, 673-676.
36. D. Pussak, M. Behra, S. Schmidt and L. Hartmann, *Soft Matter*, 2012, **8**, 1664-1672.
37. H. Q. Wang, F. Jacobi, J. Waschke, L. Hartmann, H. Lowen and S. Schmidt, *Advanced Functional Materials*, 2017, **27**, 1702040-n/a.
38. G. Hild, R. Okasha, M. Macret and Y. Gnanou, *Die Makromolekulare Chemie*, 1986, **187**, 2271-2288.
39. V. T. Moy, Y. K. Jiao, T. Hillmann, H. Lehmann and T. Sano, *Biophys. J.*, 1999, **76**, 1632-1638.
40. F. Jacobi, A. Camaleño de la Calle, S. Boden, A. Grafmüller, L. Hartmann and S. Schmidt, *Biomacromolecules*, 2018, **19**, 3479-3488.
41. J. Erath, S. Schmidt and A. Fery, *Soft Matter*, 2010, **6**, 1432-1437.
42. D. Pussak, D. Ponader, S. Mosca, S. V. Ruiz, L. Hartmann and S. Schmidt, *Angew. Chem. Int. Ed.*, 2013, **52**, 6084-6087.
43. D. Rettke, J. Döring, S. Martin, T. Venus, I. Estrela-Lopis, S. Schmidt, K. Ostermann and T. Pompe, *Biosens. Bioelectron.*, 2020, 112262.

Supporting Information

Sequence-defined positioning of amine and amide residues to control catechol driven wet adhesion.

Lukas Fischer,†[a] Alexander K. Strzelczyk, †[a] Nils Wedler,[b] Christian Kropf,[b] Stephan Schmidt*[a] and Laura Hartmann*[a]

[a.] *Institut für Organische und Makromolekulare Chemie, Heinrich-Heine-Universität Düsseldorf, Universitätsstr. 1, 40225 Düsseldorf, Germany.*

[b.] *Laundry & Home Care, Henkel AG & Co. KGaA, Henkelstr. 67, 40589 Düsseldorf, Germany.*

Contents

Supporting Information

S1 Materials and methods

Materials

Triisopropylsilane (TIPS) (98%), triethylsilane (99%) and 4-(dimethylamino)butyric acid hydrochloride (98%) were purchased from Sigma-Aldrich. Diisopropylethylamine (DIPEA) (≥99%) was purchased from Carl Roth. Dimethylformamide (DMF) (99.8%, for peptide synthesis), piperidine (99%), triphenylmethyl chloride (Trt-Cl) (98%) and succinic anhydride (99%) were purchased from Acros Organics. Dichloromethane (DCM) (99.99%), sodium chloride (99.98%), tetrahydrofuran (THF) (analytical reagent grade), ethyl acetate (analytical reagent grade) and sodium hydrogen carbonate (analytical reagent grade) were purchased from Fisher Scientific. Triethylamine (pure) was purchased from AppliChem. Trifluoroacetic acid (TFA) (99%) and (benzotriazol-1-yloxy)tripyrrolidinophosphonium hexafluorophosphate (PyBOP) (98%) were purchased from Fluorochem. Succinamic acid (97%) and Thioanisol (99%) were purchased from Alfa Aesar. 3-(3,4-Dimethoxyphenyl)propionic acid (99%) was purchased from BLD Pharmatech Ltd. Fmoc-Osu (99%), trifluoromethanesulfonic acid (98%) and trifluoroethanol (99%) were purchased from Carbolution. Diethyl ether (contains BHT as inhibitor, >99%) was purchased from Honeywell. Tentagel® S RAM resin was purchased from Rapp Polymere. Sodium sulfate (99.5%) was purchased from fisher chemicals. Polyethylene glycol diacrylate (PEG(8000)-DiAc) was purchased from Alfa Aesar. Irgacure 2959 (98%) and crotonic acid (98%) were purchased from Sigma-Aldrich. Benzophenone (99%) was purchased from Acros Organics. 1-Ethyl-3-(3-dimethylaminopropyl)carbodiimid-hydrochlorid (EDC HCl) (≥99%) was purchased from Carl Roth. Water was purified with a Milli-Q system (Millipore) obtaining a final resistivity of 18 MΩcm.

Oligomer synthesis

All oligomers were synthesized using the building blocks EDS, TrDS and CDS as previously described.[1] The oligomers were assembled via iterative deprotection and amide coupling on a Tentagel® S RAM resin. For deprotection, the resin was treated with 20% piperidine in DMF (2x 15 min) and washed with DMF (10x). For the coupling step, the building block (5 eq.) and PyBOP (5 eq.) were dissolved in DMF and DIPEA (10 eq.) was added. The resin was treated with the coupling solution for 1 hr with subsequent DMF washing (10x). After assembly of the full sequence, the trityl groups were cleaved by treating the resin with 0.1 M HCl in trifluorethanol (2x1.5 h). Then the resin was washed with DMF (5x) and the free amines were deprotonated with 20% DIPEA in DMF for 10 minutes. For introducing the side chains, the resin was treated for 1 hr with a solution of solution of either succinamic acid or 4-(dimethylamino)butyric acid (5 eq.), PyBOP (5 eq.) and DIPEA (10 eq.) in DMF and washing in DMF (10x) afterward. The structures were cleaved from solid support with a solution of TFA/TIPS (95/5), precipitated in diethyl ether and the precipitate was lyophilized. All oligomers with a protected catechol moiety were

deprotected by treatment with 16 eq. trifluoromethanesulfonic acid and 8 eq. thioanisole per methyl ether in TFA for 16 h. Afterward the reaction solution was precipitated in diethyl ether and the deprotected oligomers were lyophilized. The chemical analysis of the building block and oligomers are shown in the supporting information S1-S4)

Soft colloidal probe (SCP) synthesis

A dispersion of poly(ethylene glycol diacrylamide) (PEGdAAm, 50 mg, 6.3 µmol, Mn = 8000 Da) microdroplets was prepared by phase separation in 10 mL 1M sodium sulfate solution under vigorous agitation.[2] Irgacure 2959 (2.1 mg, 5.4 µmol) was added and the dispersion was photopolymerized under UV light for 90 s (Heraeus HiLite Power curing unit (Heraeus Kulzer, Germany). The diameter of received microgels was between 10-40 µm. After centrifugation/washing, crotonic acid was grafted onto the SCPs by exchange of water with ethanol, addition of benzophenone (250 mg, 1.4 mmol) and crotonic acid (1.5 g, 17.7 mmol) flushing with nitrogen for 60 s followed by UV irradiation for 1080 s.[3] The particles were washed with ethanol and water to remove all reactants. In the final step, the oligomers with unprotected amine end groups were coupled to crotonic acid on the SCPs in 0.1 M MES buffer pH 5.5 containing 32.5 mM (1-ethyl-3-[3-dimethylaminopropyl]carbodiimide hydrochloride), and 0.225 mM oligomers followed by washing with water. The carbodiimide coupling was repeated to maximize the functionalization degree for all oligomers (supporting information S5).

SCP characterization

AFM force-indentation measurements with a NanoWizard 2 system (JPK instruments AG, Berlin, Germany) was performed to determine the elastic moduli of the SCPs. As AFM probe a silica particle with a diameter of 4.6 µm was adhered with epoxy glue onto a tipless, non-coated cantilever (spring constant 0.32 N/m; CSC12, NanoAndMore GmbH). Several force curves were recorded for different SCPs and analyzed with an appropriate contact model developed by Glaubitz et al. (supporting information S6). The degree of oligomer functionalization in the SCP network was determined by titrating crotonic acid residues with toluidine blue O (TBO). 1.0 mL of a dispersion containing crotonic acid functionalized SCPs were dried by first exchanging the water by ethanol in the continuous phase and then treating in a vacuum oven at 50°C until constant weight. After the dry mass was determined, 1.0 mL of 312.5 µM TBO solution at pH10 was added and shaken in the dark for 12 hrs. Next, 0.3 mL of the TBO solution supernatant of the was diluted with 1.7 mL water at pH 10 and the absorbance at 633 nm was detected and compared to the TBO reference (no infusion of SCPs) to calculate the degree of crotonic acid functionalization. Comparing the amount of SCP crotonic acid functionalization before and after the oligomer coupling gave the oligomer functionalization degree (supporting information S5).

Supporting Information

S2 Instrumentation

Nuclear Magnetic Resonance Spectroscopy (NMR)

^{1}H-NMR and ^{13}C NMR were recorded on a Bruker Avance III 300, a Bruker Avance DRX-500 or a Bruker Avance III 600. Chemical shifts were reported as delta (δ) in parts per million (ppm) and coupling constants as *J* in Hertz (Hz). Multiplicities are stated as following: s = singlet, d = doublet, t = triplet, q = quartet, m = multiplet.

High Resolution – Mass Spectrometry (HR-MS)

HR-MS measurements were conducted on a Bruker UHR-QTOF maxis 4G with a direct inlet via syringe pump, an ESI source and a quadrupole Time of Flight (QTOF) analyzer. Samples were dissolved in water with a concentration of 1 mg/mL.

Reversed Phase – High Pressure Liquid Chromatography (RP-HPLC)

RP-HPLC was performed with an Agilent 1260 Infinity instrument coupled to a variable wavelength detector (VWD) set to 214 nm. As a column a Poroshell 120 EC-C18 1.8 µM (3.0x50 mm, 2.5 µm) reversed phase column was used. The mobile phase A consisted of 95/5 H_2O/MeCN with 0.1% formic acid and mobile phase B consisted of 95/5 MeCN/H_2O with 0.1% formic acid. The flowrate for all measurements was 0.4 mL/min.

Preparative Reversed Phase – High Pressure Liquid Chromatography (Prep-RP-HPLC)

Prep-RP-HPLC was conducted on an Agilent 1260 Infinity instrument coupled to a variable wavelength detector (VWD) set to 214 nm. As a column a CAPCELL PAL C18 (20mml.D. x 250 mm, 5 µm) reversed phase column was used. The mobile phase A consisted of H_2O with 0.1% formic acid and mobile phase B consisted of MeCN with 0.1% formic acid. All samples were purified with a flowrate of 10 ml/min and a gradient of 100% A to 50% A over 15 min. Fractions were collected by an automated collector and were then lyophilized.

Freeze Dryer

Lyophilization of the final structures was conducted on an Alpha 1-4 LD plus instrument from Martin Christ Freeze Dryers GmbH. The lyophilization was done at a pressure of 0.1 mbar.

S3 Building Block Synthesis and Chemical Analysis

The building block EDS was synthesized according to literature.[4]

Synthesis Route for Functional Building Blocks

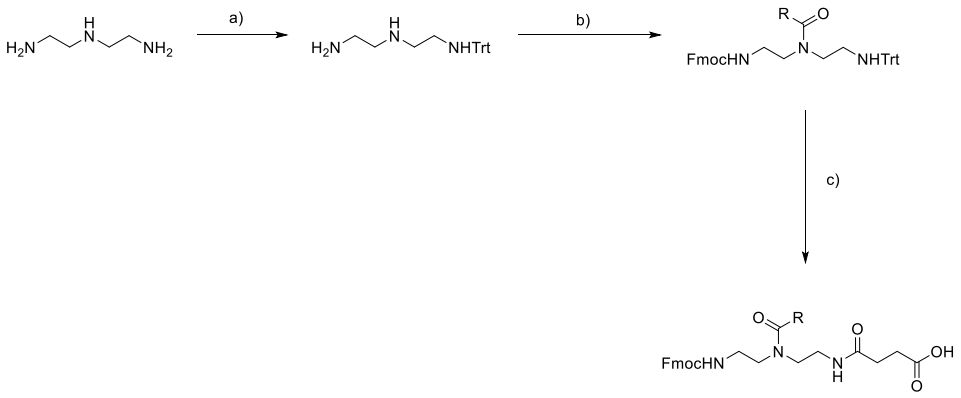

Figure S1. Overview of building block synthesis route: a) 0.25 eq. trityl chloride in DCM; b) 1 eq. Fmoc-OSu, 3 eq. triethylamine in THF at -78°C for 2 h followed by 1 eq. activated acid; c) 10 eq. TFA in DCM for 1 h followed by precipitation and 1 eq. succinic anhydride, 3 eq. triethylamine in DCM for 2 h.

Functional building blocks were synthesized with the new synthesis route shown in Figure S1.

a) To a solution of diethylenetriamine in DCM a solution of trityl chloride (0.25 eq.) in DCM was added over 1 h at 0°C. The reaction was stirred for 16 h at room temperature and afterwards extracted with a saturated $NaHCO_3$ solution (3x). The organic phase was dried with $MgSO_4$ and the solvent was evaporated under reduced pressure to give the crude product as a brown oil.

b) The crude product of a) was dissolved in THF and triethylamine (3 eq.) and a solution of Fmoc-OSu (1 eq.) in THF was added over 2 h at -78°C. Afterwards the activated acid (1 eq.) in THF was added and the reaction was stirred for 16 h at room temperature. The reaction mixture was extracted with a saturated NaCl solution (3x) and the organic phase was dried with $MgSO_4$ and the solvent was evaporated under reduced pressure to give the crude product as a brown foam.

c) The crude product of b) was dissolved in DCM and triethylsilane (10 eq.) and 10 vol-% TFA were added. The reaction was stirred at room temperature for 1 h. Afterwards the solvent was evaporated under reduced pressure and the product was precipitated in diethyl ether. The precipitate was dissolved in DCM and triethylamine (3 eq.) and succinic anhydride (1 eq.) were added. The reaction was stirred for 2 h at room temperature and afterwards extracted with a citric acid solution (3x). The organic phase was dried with $MgSO_4$ and the solvent was evaporated under reduced pressure to give the crude product as a brown foam.

Supporting Information

4-((2-((((9H-fluoren-9-yl)methoxy)carbonyl)amino)ethyl)(2-(tritylamino)ethyl)amino)-4-oxobutanoic acid (TrDS) **(1)**

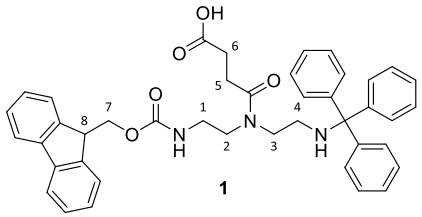

TrDS (**1**) was synthesized following the synthesis route in Figure S1 (step a and b). The crude product was recrystallized in DCM and diethyl ether (1:1) to give a white powder with a yield of 24 g (72%).

^{1}H-NMR (600 MHz, DMSO-d_6,, 80°C) δ [ppm]: 7.86 (d, J = 7.6 Hz, 2H, Fmoc-H), 7.67 (d, J = 7.4 Hz, 2H, Fmoc-H), 7.45-7.35 (m, 8H, Fmoc-H, Trt-H), 7.32 (t, J = 7.6 Hz, 2H, Fmoc-H), 7.29 (t, J = 7.7 Hz, 6H, Trt-H), 7.19 (t, J = 7.3 Hz, 3H, Trt-H), 4.44-4.29 (m, 2H, H-7), 4.25-4.20 (m, 1H, H-8), 3.30-2.55 (m, 8H, H-1,H-2,H-3,H-4), 2.50-2.20 (m, 4H, H-5,H-6).

^{13}C-NMR (126 MHz, $CDCl_3$+DMSO-d_6) δ [ppm]: 174.25, 172.26, 156.26, 156.13, 145.16, 143.47, 140.65, 128.05, 127.94, 127.43, 127.15, 126.56, 125.92, 124.70, 124.61, 119.40, 119.38, 70.43, 65.73, 65.21, 53.20, 48.47, 46.73, 45.95, 45.35, 42.00, 38.79, 31.00, 29.24, 29.10, 28.67, 27.67, 27.36, 24.93, 22.08, 14.81, 13.66.

HR-ESI-MS: calculated mass for $C_{42}H_{42}N_3O_5$ $[M+H]^+$ 668.3119, found 668.3119.

RP-HPLC (gradient from 0% to 100% eluent B over 30 min at 25°C): t_r=20.9 min, relative purity 98%.

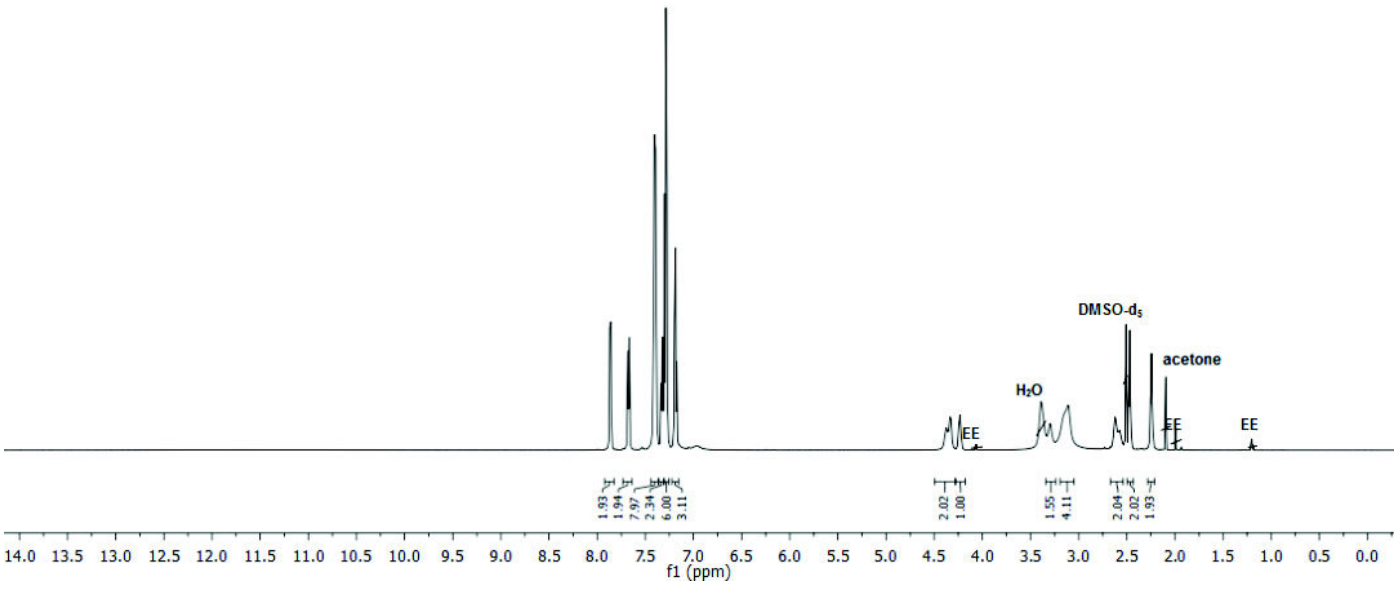

Supporting Information

^{1}H-NMR spectrum of compound **1** (600 MHz, DMSO-d_6, 80°C).

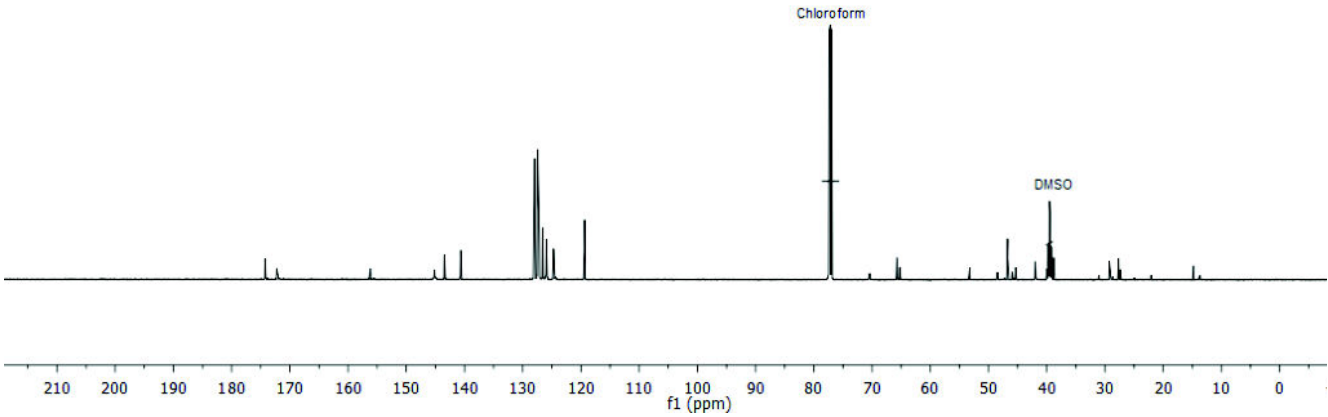

^{13}C-NMR spectrum of compound **1** (126 MHz, $CDCl_3$+DMSO-d_6).

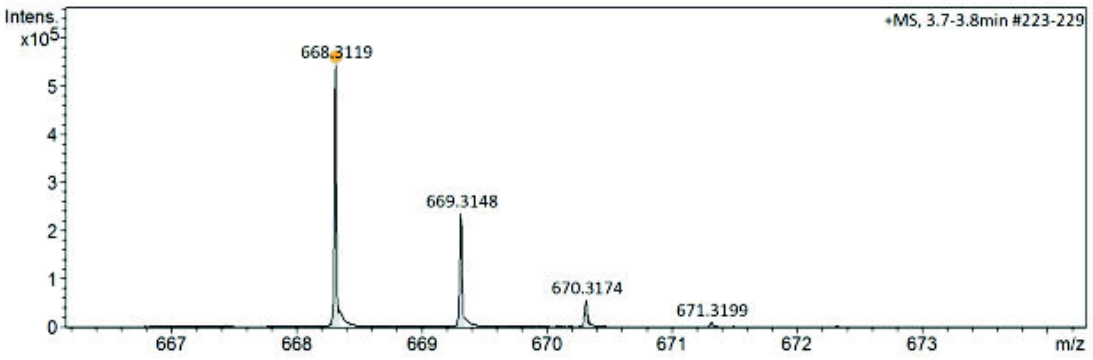

HR-ESI (ESI^{+} Q-TOF) of compound **1**.

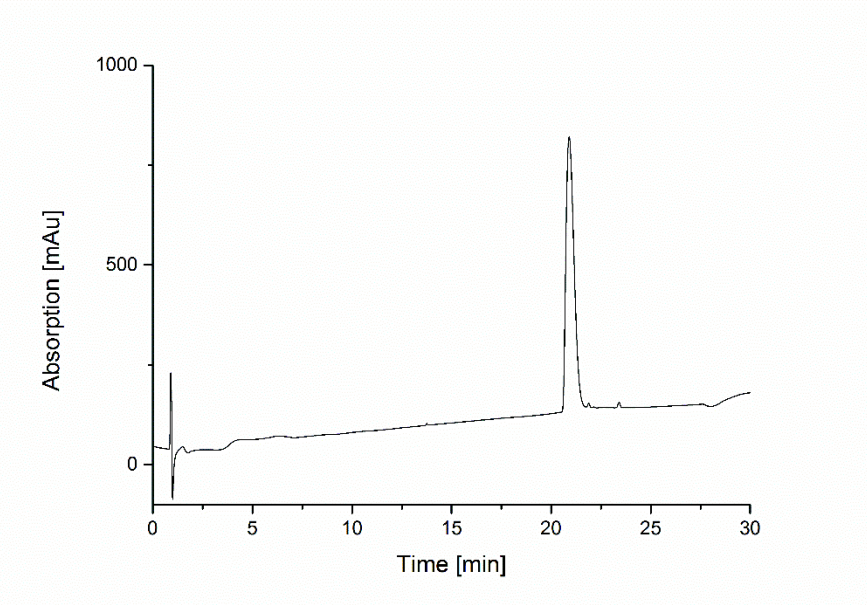

RP-HPLC chromatogram of compound **1** (gradient from 0% to 100% eluent B over 30 min at 25°C).

7-(3-(3,4-dimethoxyphenyl)propanoyl)-1-(9H-fluoren-9-yl)-3,11-dioxo-2-oxa-4,7,10-triazatetradecan-14-oic acid (CDS) (2)

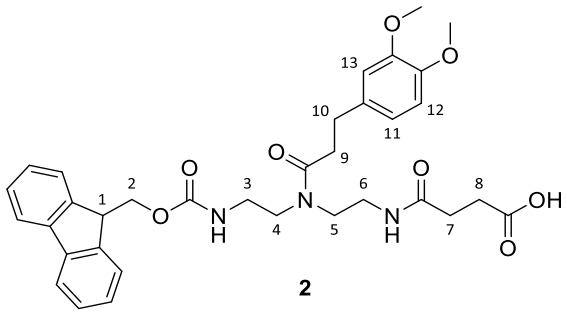

2

CDS (**2**) was synthesized following the synthesis route in Figure S1. The crude product was recrystallized in acetone and DCM (1:1) to give a white powder with a yield of 17 g (60%).

^{1}H-NMR (600 MHz, DMSO-d_6) δ [ppm]: 8.1 (m, NH), 7.9 (m, NH), 7.88 (d, J = 7.7 Hz, 2H, Fmoc-H), 7.68 (d, J = 7.4 Hz, 1H, Fmoc-H), 7.64 (d, J = 7.5 Hz, 1H. Fmoc-H), 7.47 (m, NH), 7.41 (t, J = 7.5 Hz, 2H, Fmoc-H), 7.36-7.29 (m, 2H, Fmoc-H,NH), 6.83-6.60 (m, 3H, H-11, H-12, H-13), 4.28 (dd, J = 17.4, 7.0 Hz, 2H, H-2), 4.21 (t, J = 7.0 Hz, 0.5H, H-1), 4.16 (t, J = 7.0 Hz, 0.5H, H-1), 3.75-3.63 (m, 6H, H-14), 3.29 (m, 4H, H-4, H-5), 3.19-3.07 (m, 4H, H-3, H-6), 2.75-2.69 (m, 2H, H-9), 2.60-2.55 (m, 2H, H-10), 2.45-2.38 (m, 2H, H-7), 2.35-2.27 (m, 2H, H-8).

^{13}C-NMR (126 MHz, DMSO-d_6) δ [ppm]: 174.25, 172.26, 156.26, 156.13, 145.16, 143.47, 140.65, 128.05, 127.94, 127.43, 127.15, 126.56, 125.92, 124.70, 124.61, 119.40, 119.38, 70.43, 65.73, 65.21, 53.20, 48.47, 46.73, 45.95, 45.35, 42.00, 38.79, 31.00, 29.24, 29.10, 28.67, 27.67, 27.36, 24.93, 22.08, 14.81, 13.66.

Supporting Information

HR-ESI-MS: calculated mass for $C_{34}H_{40}N_3O_8$ $[M+H]^+$ 618.2810, found 618.2807.

RP-HPLC (gradient from 0% to 100% eluent B over 30 min at 25°C):t_r=21.1 min, purity 99%.

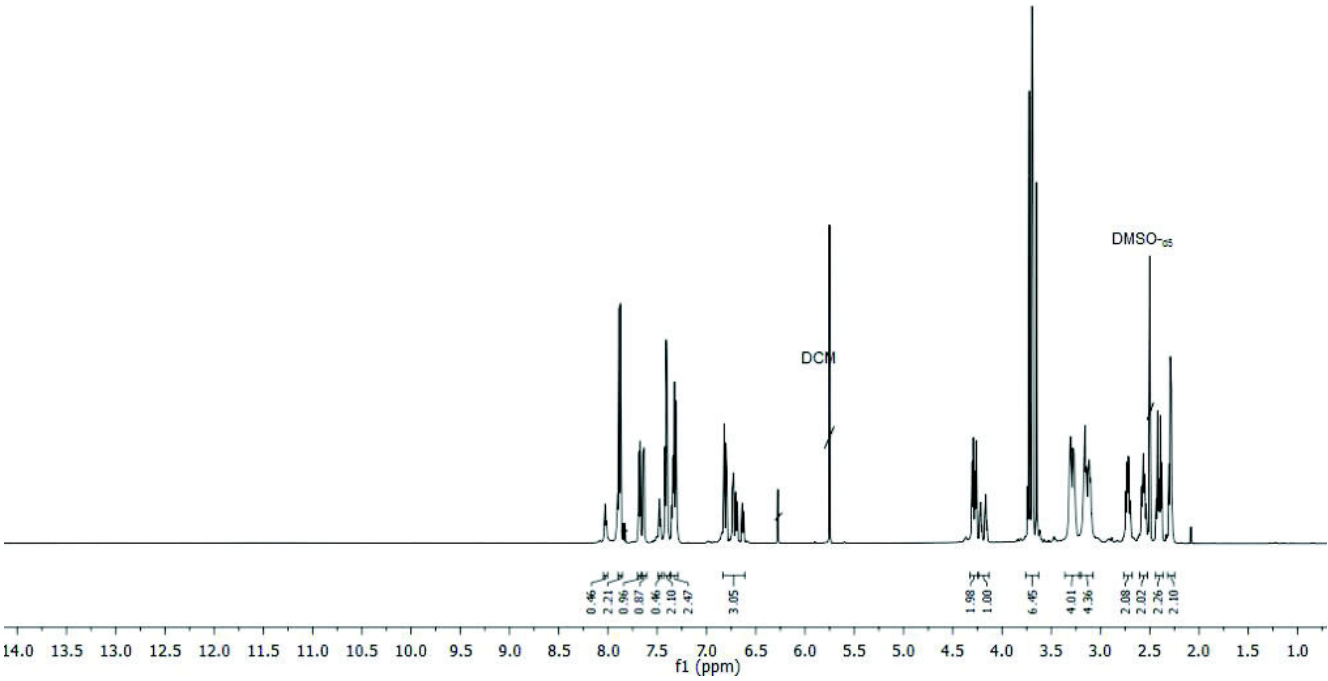

^{1}H-NMR spectrum of compound **2** (600 MHz, DMSO-d_6).

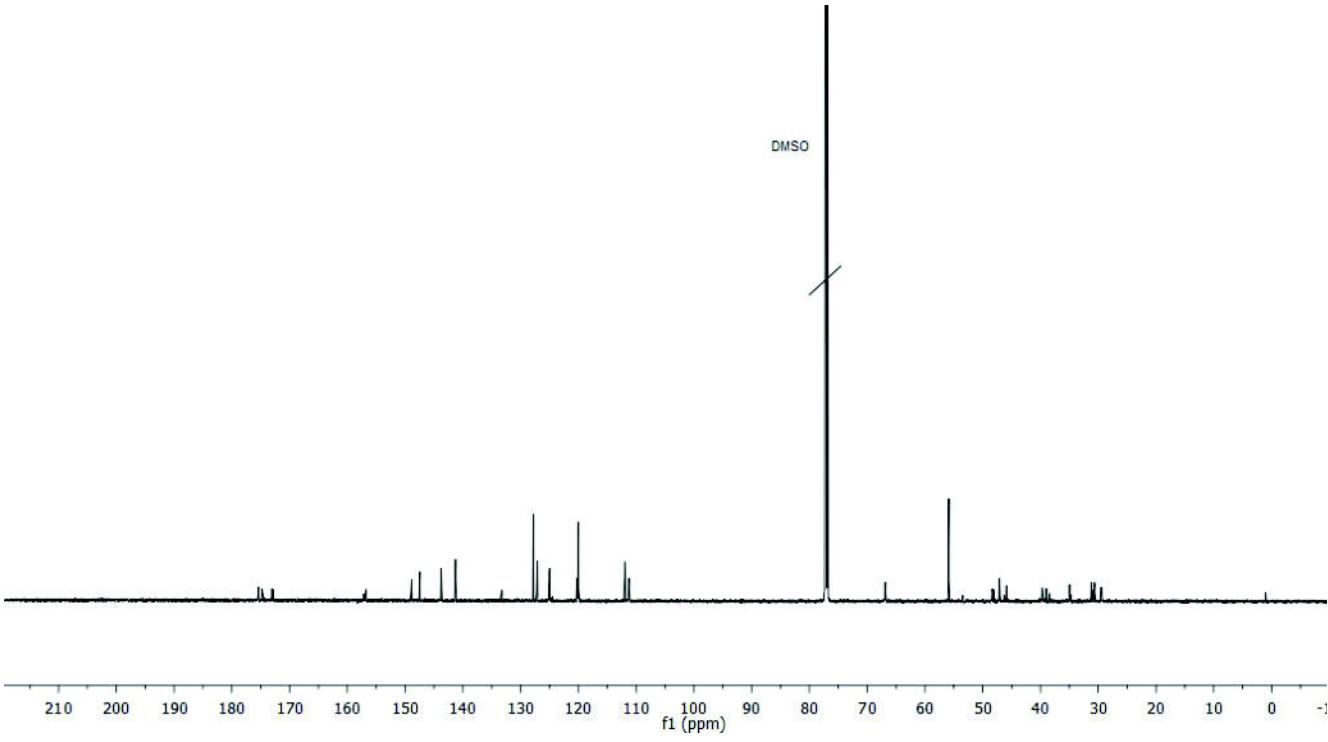

^{13}C-NMR spectrum of compound **2** (126 MHz, DMSO-d_6).

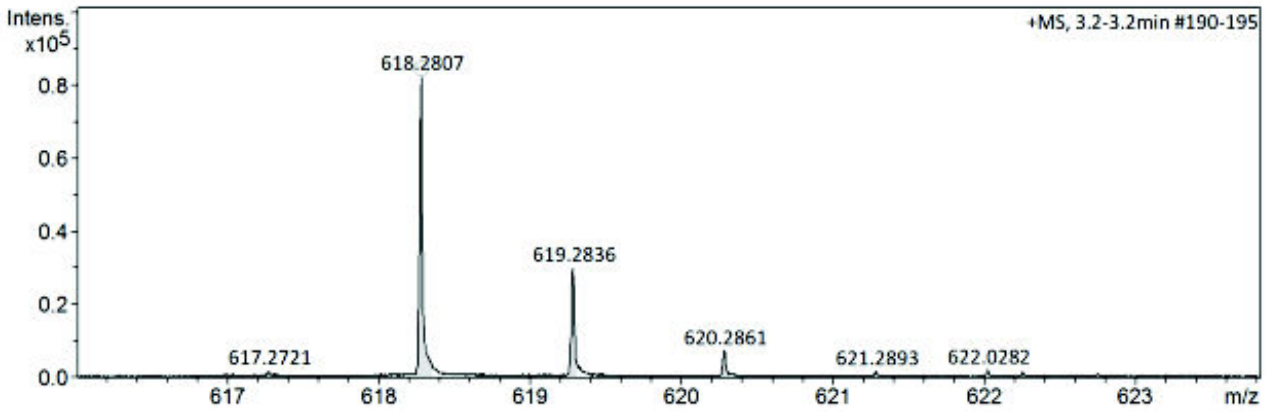

HR-ESI (ESI$^+$ Q-TOF) of compound **2**.

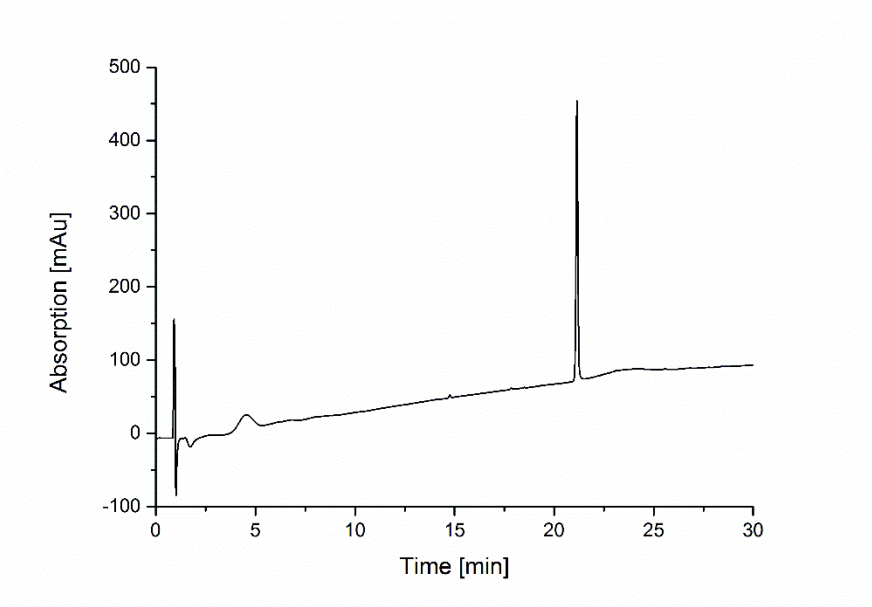

RP-HPLC chromatogram of compound **2** (gradient from 0% to 100% eluent B over 30 min at 25°C).

S4 Oligomer Synthesis and Chemical Analysis

All oligomers were synthesized on solid support according to literature[1] using the building blocks EDS, TrDS and CDS.

On Resin Deprotection Of Trityl

The resin was treated with 0.1 M HCl in trifluorethanol (2x1.5 h). Afterwards the resin was washed with DMF (5x) and the free amines were deprotonated with 20% DIPEA in DMF for 10 minutes.

Side Chain Coupling

After trityl deprotection the resin was treated for 1 h with a solution of 5 eq. acid, 5 eq. PyBOP and 10 eq. DIPEA in DMF. Afterwards the resin was washed with DMF (10x).

Deprotection Of Catechols

Supporting Information

All oligomers with a protected catechol moiety were deprotected in solution. For this they were treated with 16 eq. trifluoromethanesulfonic acid and 8 eq. thioanisole per methyl ether in TFA for 16 h. Afterwards the reaction solution was precipitated in diethyl ether and the deprotected oligomers were freeze dried.

Oligomer Chemical Analysis

(**3**) *protected*

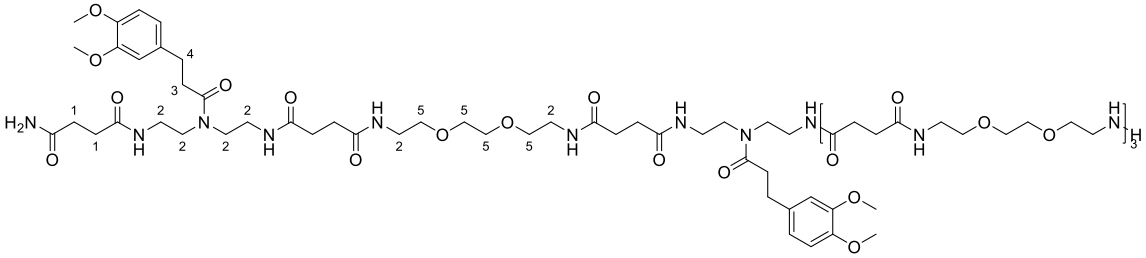

Compound **3 protected** was obtained with a yield of 64% after cleavage from solid support and lyophilization. .

^{1}H-NMR (600 MHz, D_2O) δ [ppm]: 6.90 (m, 4H, $H_{Aromatic}$), 6.79 (d, J = 8.3 Hz, 2H, $H_{Aromatic}$), 6.75 (d, J = 8.0 Hz, 2H, $H_{Aromatic}$), 3.80 (s, 6H, OCH_3), 3.78 (s, 6H, OCH_3) 3.74-3.54 (m, 32H, H-5), 3.40-3.17 (m, 32H, H-2), 2.82 (m, 4H, H-4), 2.64 (m, 4H, H-3), 2.51-2.36 (m, 24H, H-1).

^{13}C-NMR (126 MHz, D_2O) δ [ppm]: 178.36, 178.23, 176.63, 175.73, 175.68, 175.64, 175.59, 175.55, 175.53, 175.51, 175.49, 175.38, 175.36, 149.04, 147.63, 134.91, 121.82, 113.12, 112.81, 70.55, 70.42, 69.82, 67.36, 56.61, 56.56, 48.05, 45.86, 45.77, 40.09, 39.89, 39.82, 38.29, 37.99, 35.20, 35.14, 31.97, 31.93, 31.90, 31.84, 31.76, 31.70, 31.67, 31.58, 31.17, 31.03.

HR-ESI-MS: calculated mass for $C_{78}H_{132}N_{15}O_{26}$ $[M+3H]^{3+}$ 564.9817, found 564.9825.

RP-HPLC (gradient from 0% to 50% eluent B over 30 min at 25°C):t_r=14.0 min, purity 92%.

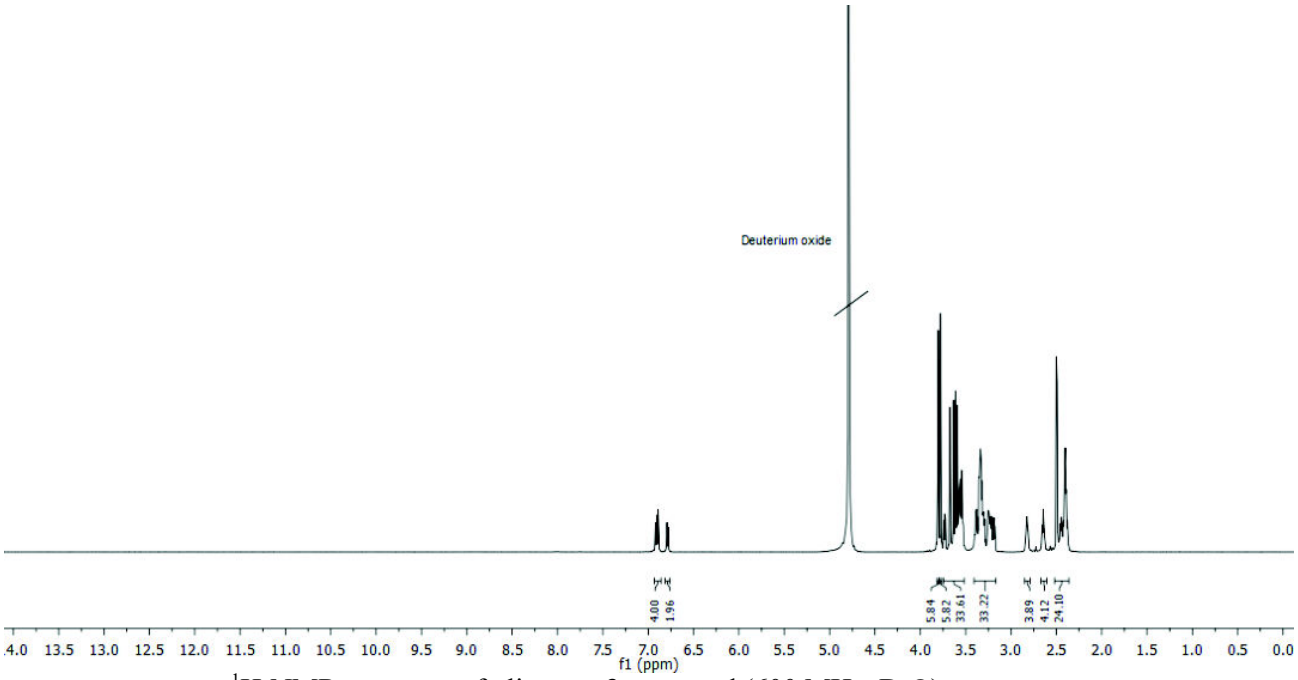

^{1}H-NMR spectrum of oligomer **3** protected (600 MHz, D_2O).

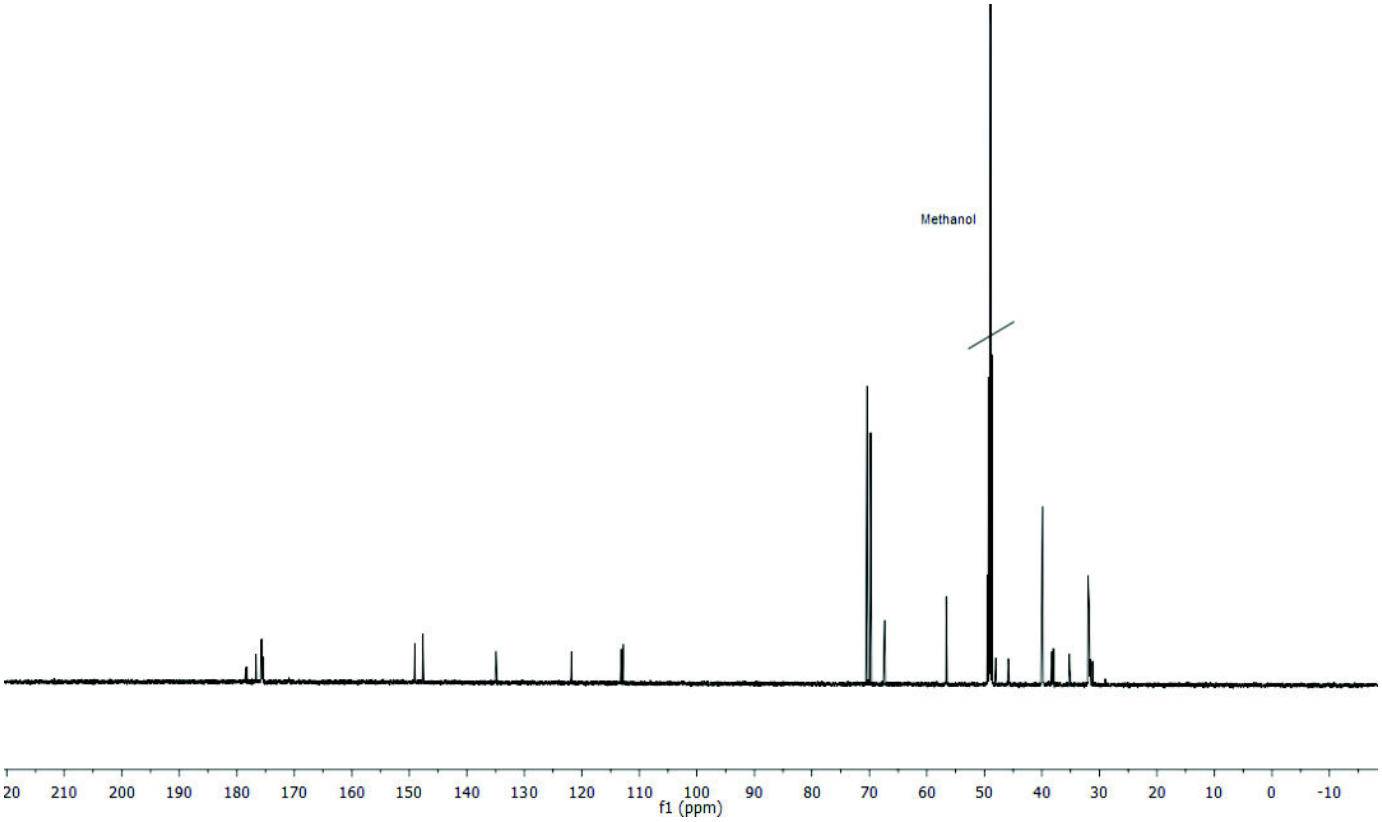

^{13}C-NMR spectrum of oligomer **3** protected (126 MHz, D_2O).

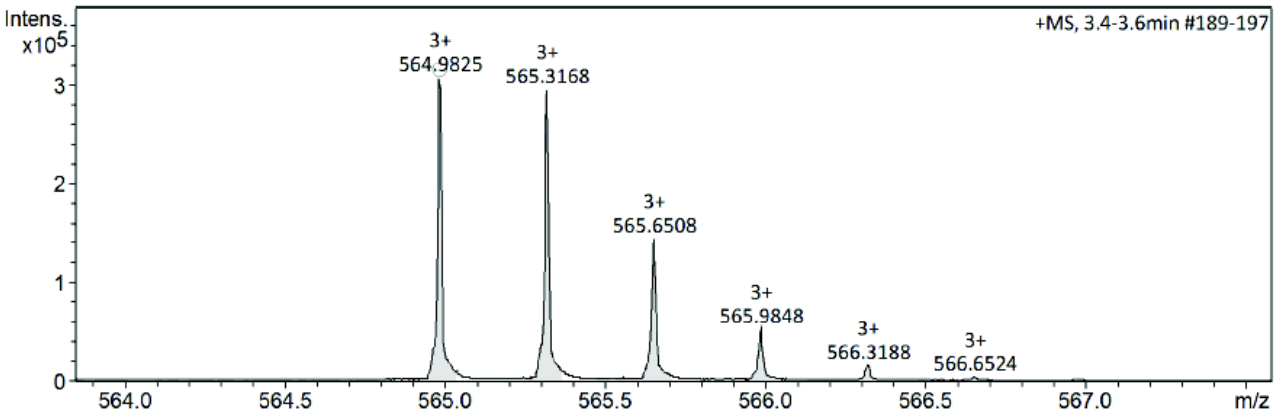

HR-ESI (ESI$^+$ Q-TOF) of oligomer **3** protected.

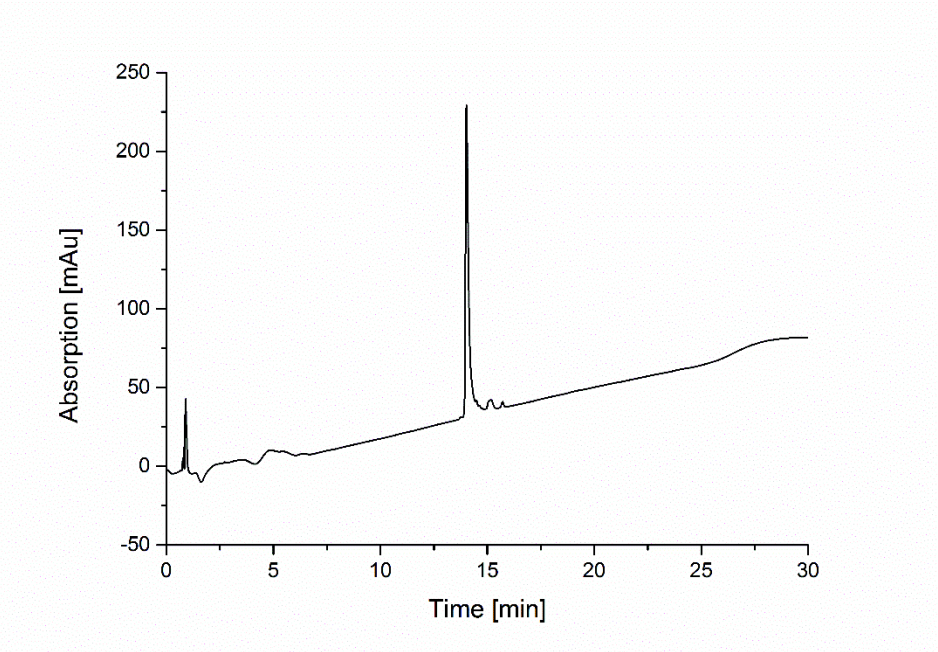

RP-HPLC chromatogram of compound **3** protected (gradient from 0% to 50% eluent B over 30 min at 25°C).

(**3**)

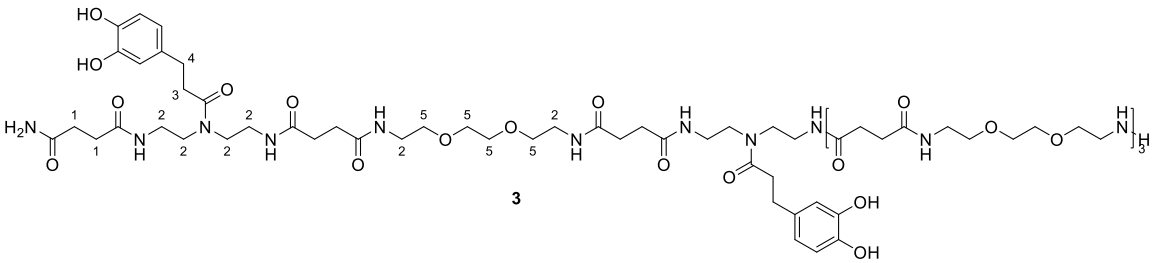

Compound **3** was obtained with a yield of 32% after deprotection, purification by preparative RP-HPLC and lyophilization.

Supporting Information

^{1}H-NMR (500 MHz, D_2O) δ [ppm]: 8.32 (s, NH), 6.91 (dd, J = 8.0 Hz, 1.8 Hz, 2H, $H_{Aromatic}$), 6.85 (s, 2H, $H_{Aromatic}$), 6.75 (d, J = 8.0 Hz, 2H, $H_{Aromatic}$), 3.86-3.64 (m, 32H, H-5), 3.52-3.27 (m, 32H, H-2), 2.85 (m, 4H, H-4), 2.71 (m, 4H, H-3), 2.62-2.48 (m, 24H, H-1).

^{13}C-NMR (126 MHz, D_2O) δ [ppm]: 176.46, 176.39, 176.37, 175.40, 175.37, 175.29, 175.20, 175.09, 144.54, 144.48, 142.86, 134.10, 134.07, 121.17, 121.13, 118.92, 116.82, 116.78, 116.70, 70.12, 69.97, 69.37, 66.90, 45.41, 45.33, 39.67, 39.47, 39.40, 37.88, 37.62, 34.79, 31.61, 31.57, 31.53, 31.48, 31.42, 31.38, 31.23, 30.96, 30.79, 30.69.

HR-ESI-MS: calculated mass for $C_{78}H_{132}N_{15}O_{26}$ $[M+3H]^{3+}$ 564.9817, found 564.9825.

RP-HPLC (gradient from 0% to 50% eluent B over 30 min at 25°C):t_r=12.3 min, purity 93%.

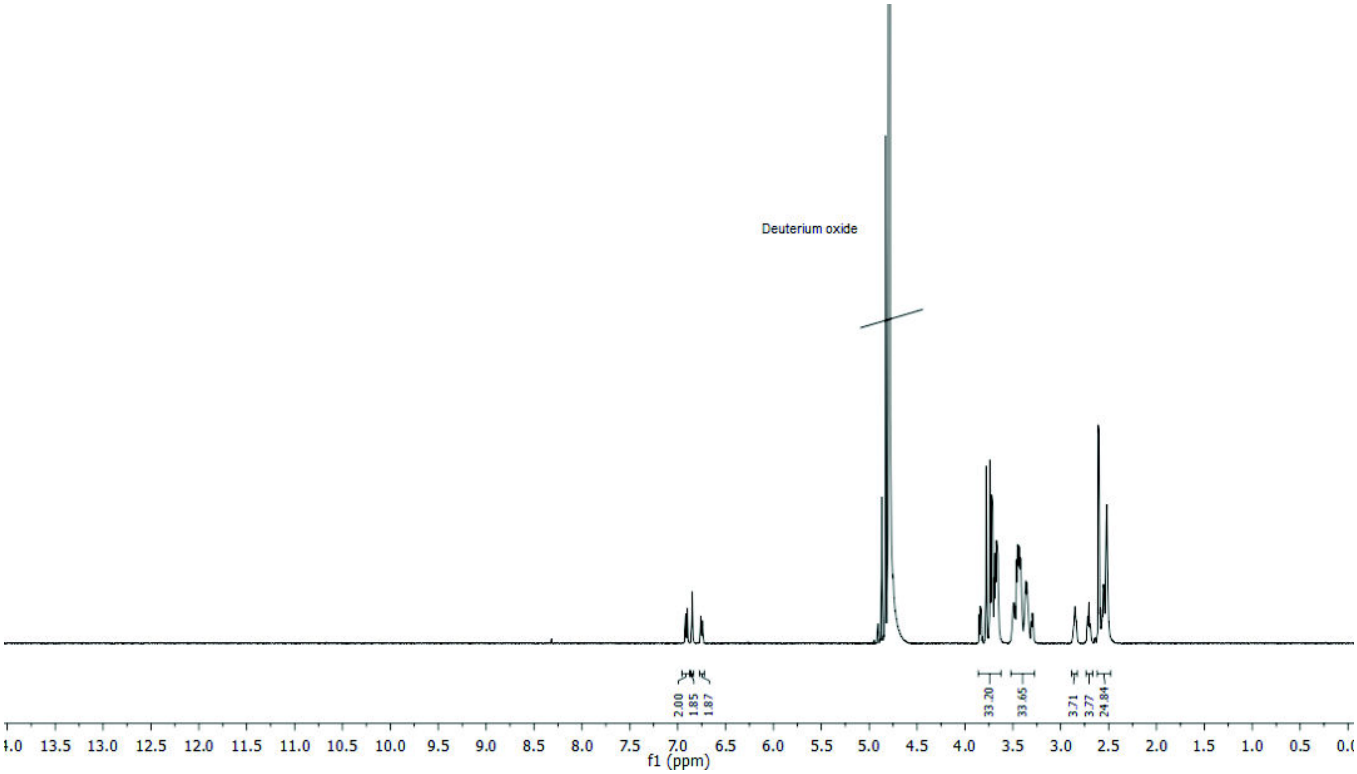

^{1}H-NMR spectrum of compound **3** (500 MHz, D_2O).

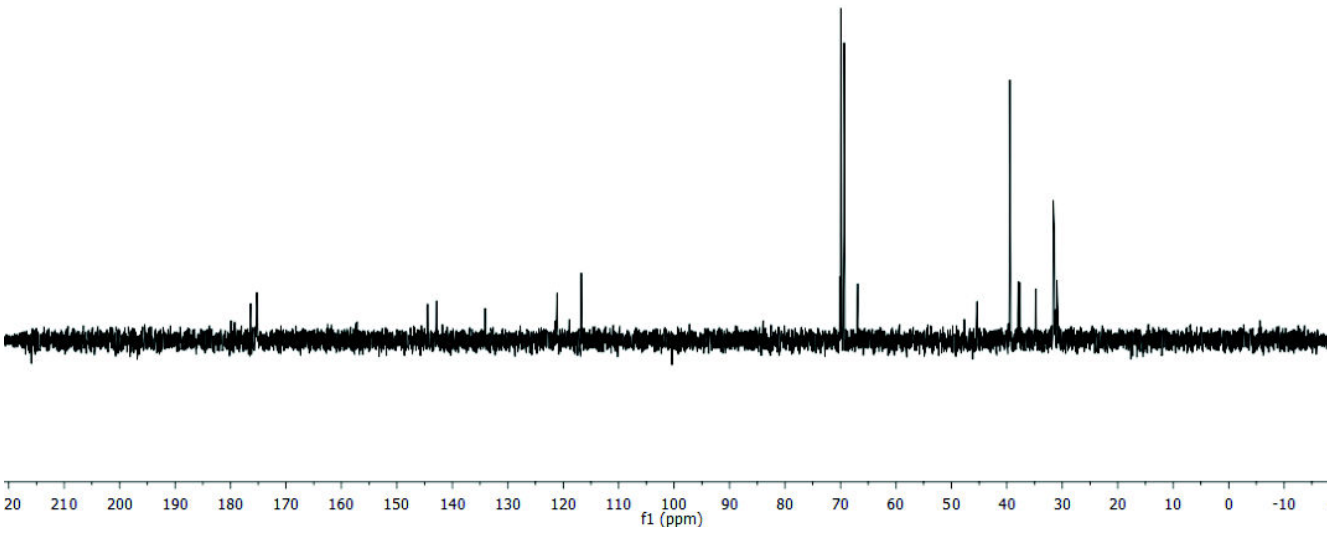

^{13}C-NMR spectrum of compound **3** (126 MHz, D_2O).

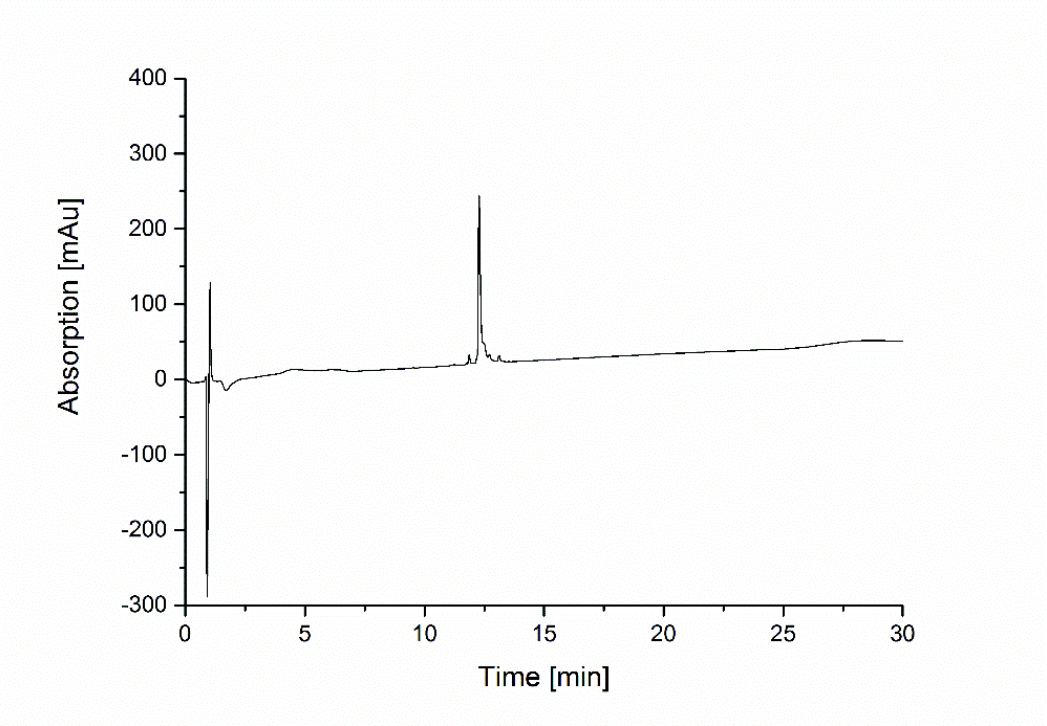

RP-HPLC chromatogram of compound **3** (gradient from 0% to 50% eluent B over 30 min at 25°C).

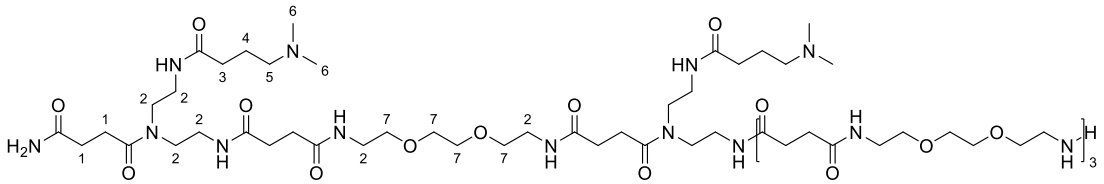

4

(**4**)

Compound **4** was obtained with a yield of 45% after purification by preparative RP-HPLC and lyophilization.^{1}H-NMR (500 MHz, D_2O) δ [ppm]: 8.47 (s, NH), 3.79-3.58 (m, 32H, H-7), 3.57-3.28 (m, 32H, H-2), 3.25-3.10 (m, 4H, H-5), 2.89 (s, 12H, H-6), 2.80 (m, 2H, H-8), 2.69 (m, 4H, H-3), 2.60-2.30 (m, 24H, H-1), 2.98 (m, 4H, 4-H).

^{13}C-NMR (126 MHz, D_2O) δ [ppm]: 175.85, 175.79, 175.65, 175.60, 175.56, 171.71, 70.42, 69.81, 57.96, 43.63, 39.87, 37.90, 31.98, 31.91, 31.84, 21.01, 20.98.

HR-ESI-MS: calculated mass for $C_{68}H_{130}N_{17}O_{22}$ $[M+3H]^{3+}$ 512.3187, found 512.3183.

RP-HPLC (gradient from 0% to 50% eluent B over 30 min at 25°C):t_r=7.1 min, purity 99%.

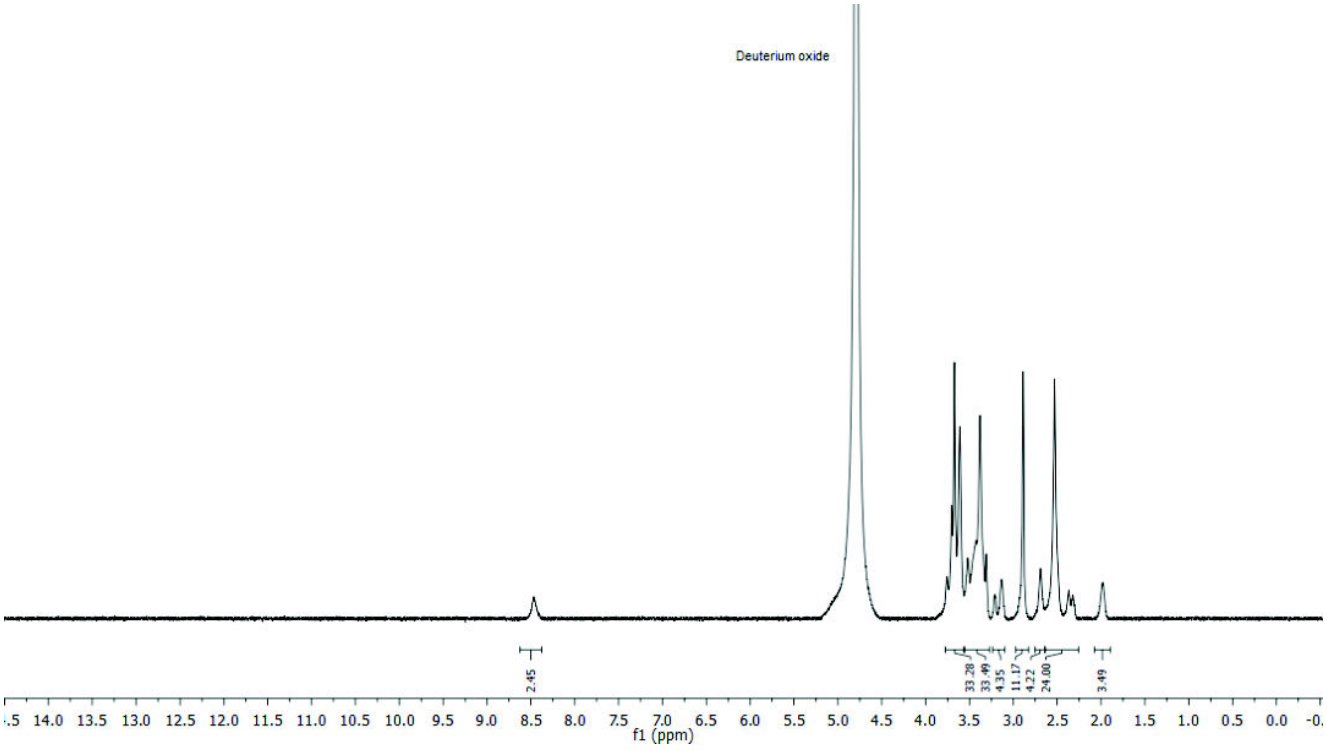

^{1}H-NMR spectrum of compound **4** (500 MHz, D_2O).

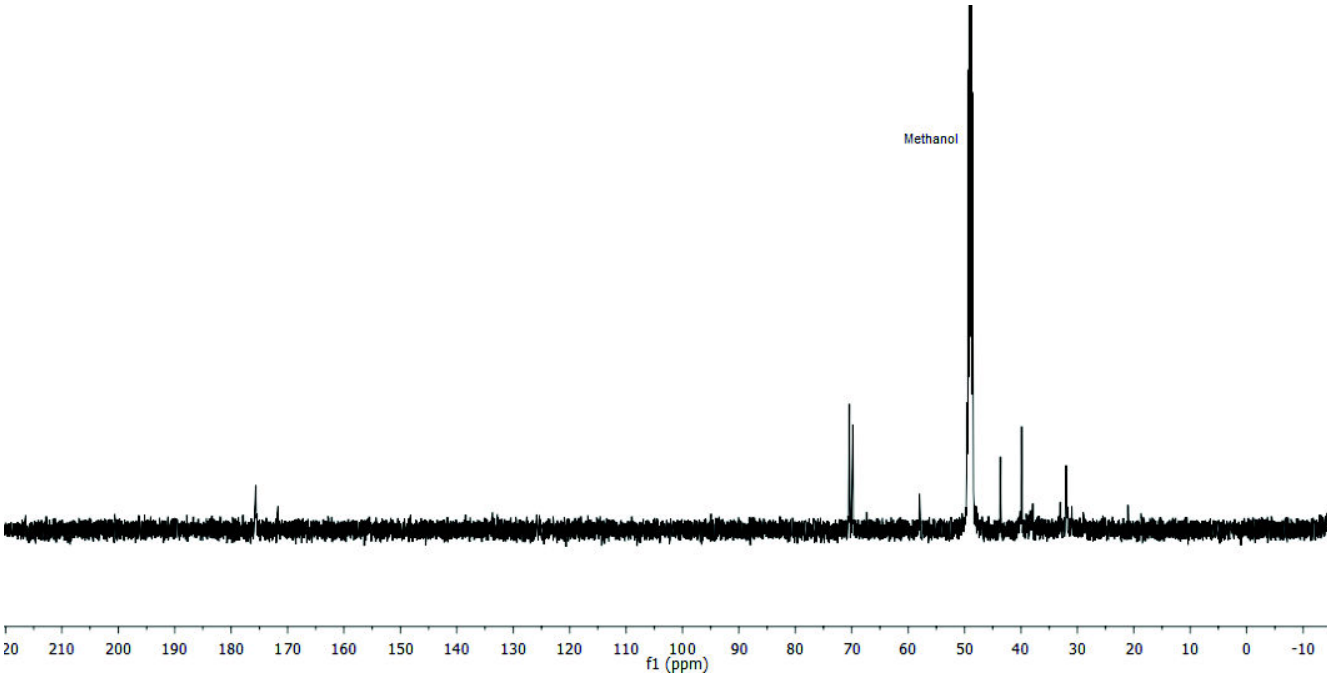

^{13}C-NMR spectrum of compound **4** (126 MHz, D_2O).

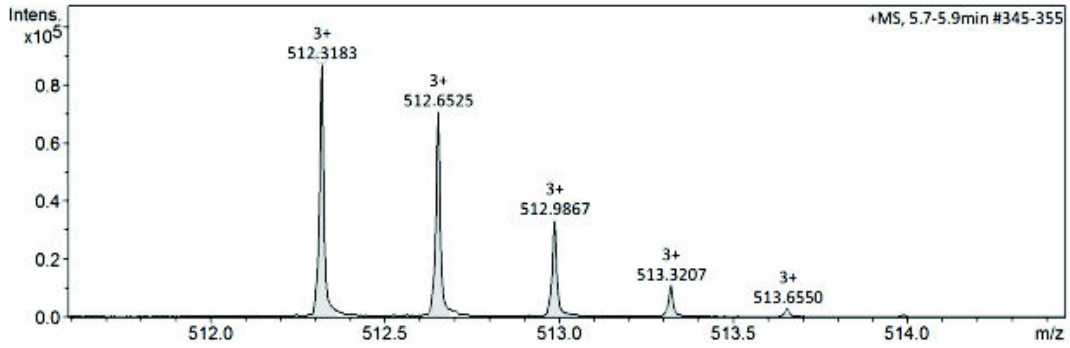

HR-ESI (ESI$^+$ Q-TOF) of compound **4**.

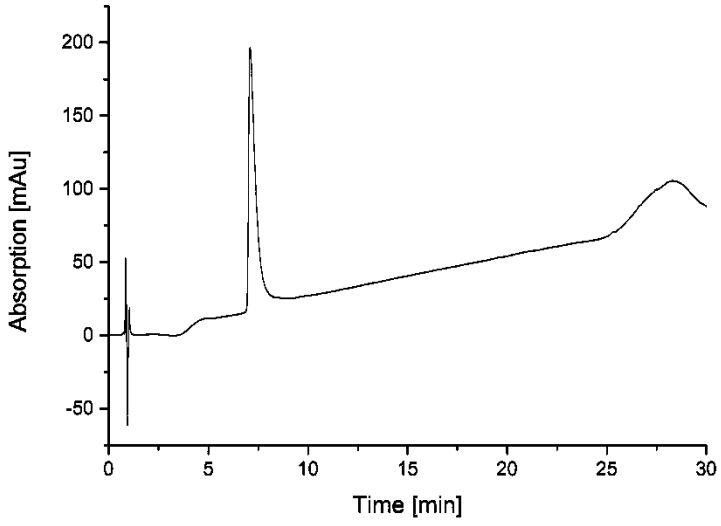

RP-HPLC chromatogram of compound **4** (gradient from 0% to 50% eluent B over 30 min at 25°C).

(**5**)

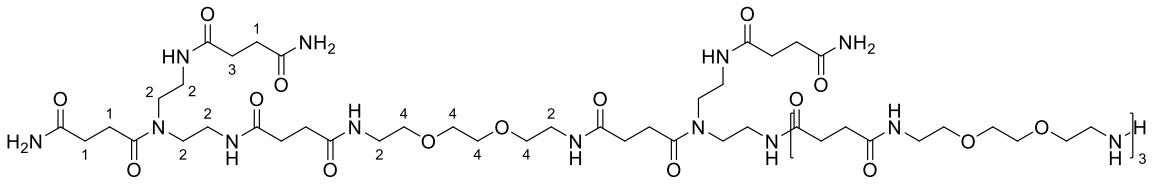

5

Compound **5** was obtained with a yield of 35% after purification by preparative RP-HPLC and lyophilization.

^{1}H-NMR (500 MHz, D_2O) δ [ppm]: 8.49 (s, NH), 3.80-3.59 (m, 32H, H-4), 3.57-3.20 (m, 32H, H-2), 2.71 (m, 4H, H-3) 2.60-2.46 (m, 28H, H-1).

^{13}C-NMR (126 MHz, D_2O) δ [ppm]: 175.73, 175.66, 175.63, 175.58, 175.53, 175.50, 175.47, 108.36, 108.21, 100.86, 70.54, 70.40, 69.80, 39.87, 39.80, 32.00, 31.95, 31.91, 31.87, 31.83, 31.79, 31.70, 31.67, 31.64, 28.94, 28.68.

HR-ESI-MS: calculated mass for $C_{64}H_{118}N_{17}O_{24}$ $[M+3H]^{3+}$ 502.9506, found 502.9499.

RP-HPLC (gradient from 0% to 50% eluent B over 30 min at 25°C):t_r=8.3 min, purity 94%.

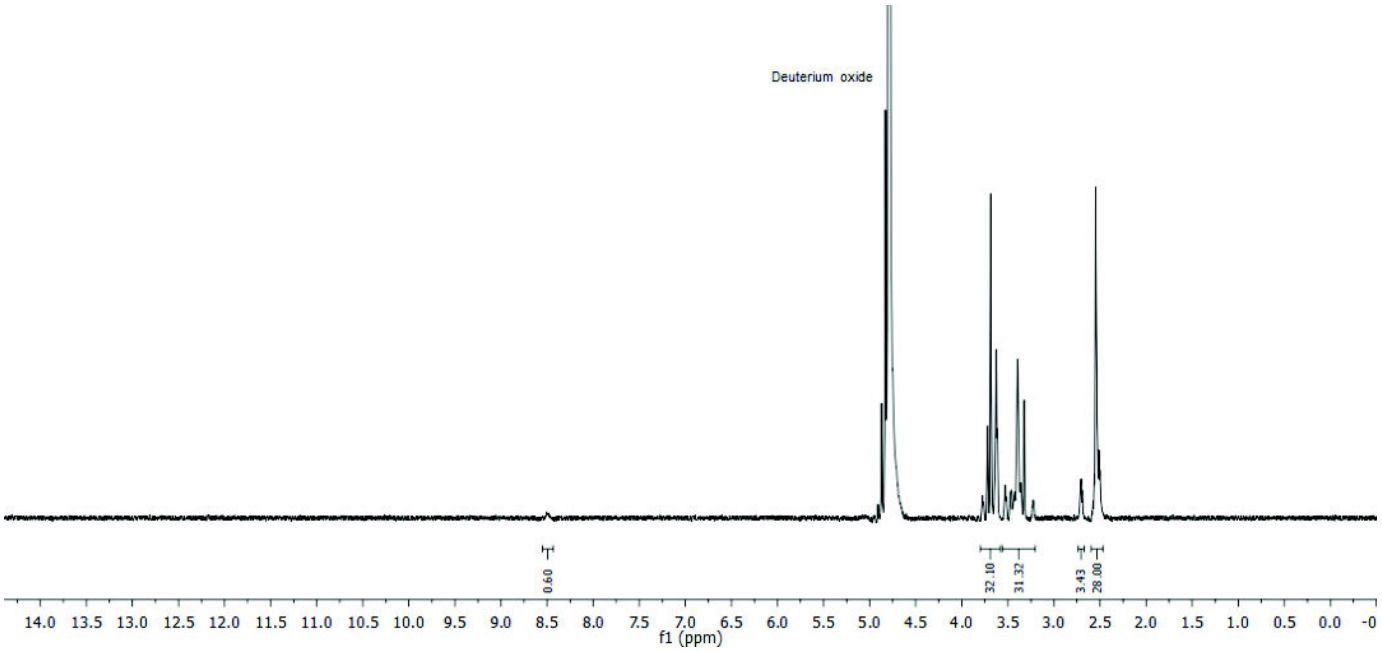

^{1}H-NMR spectrum of compound **5** (500 MHz, D_2O).

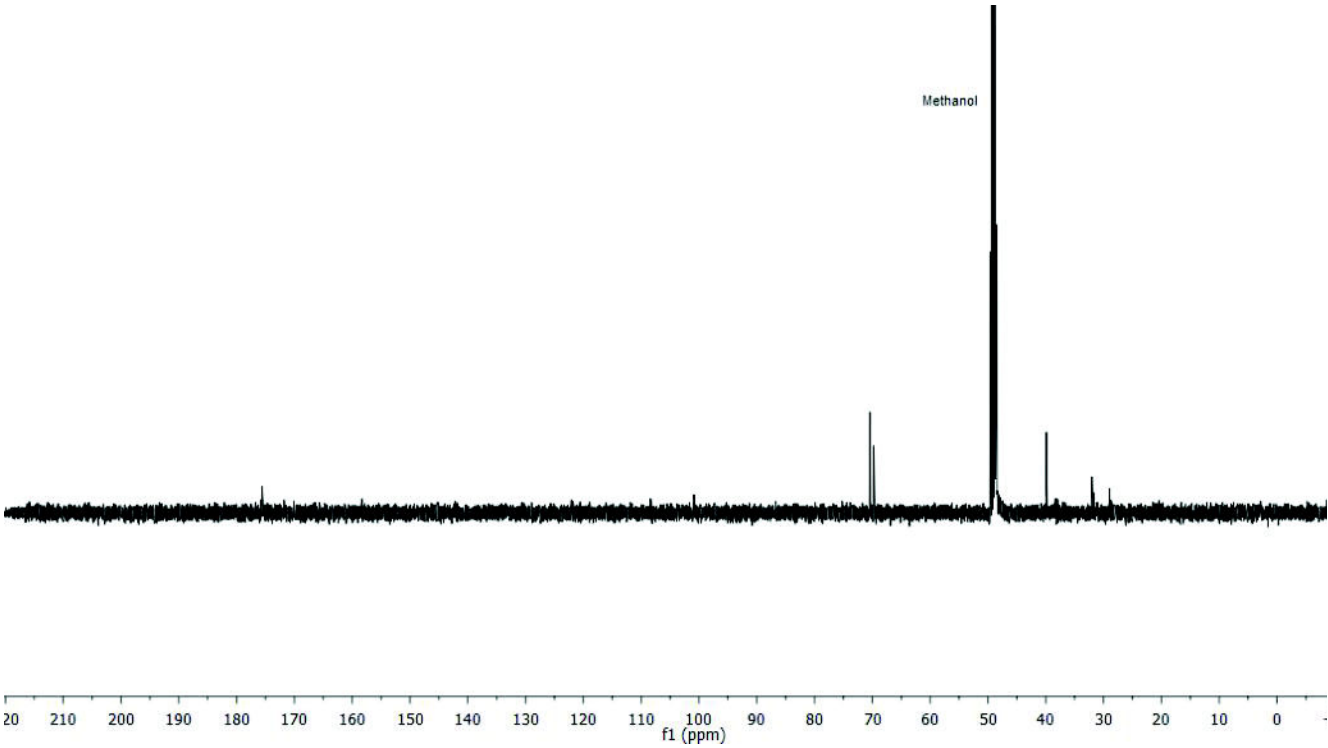

^{13}C-NMR spectrum of compound **5** (126 MHz, D_2O).

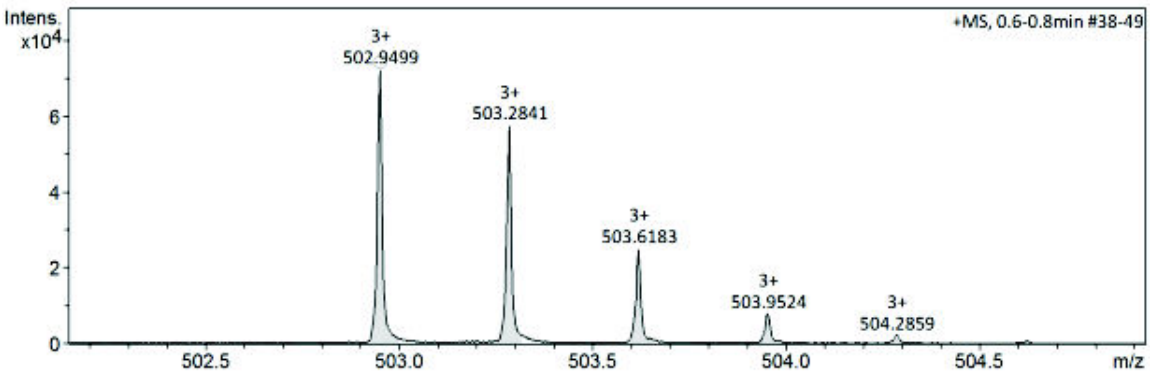

HR-ESI (ESI$^+$ Q-TOF) of compound **5**.

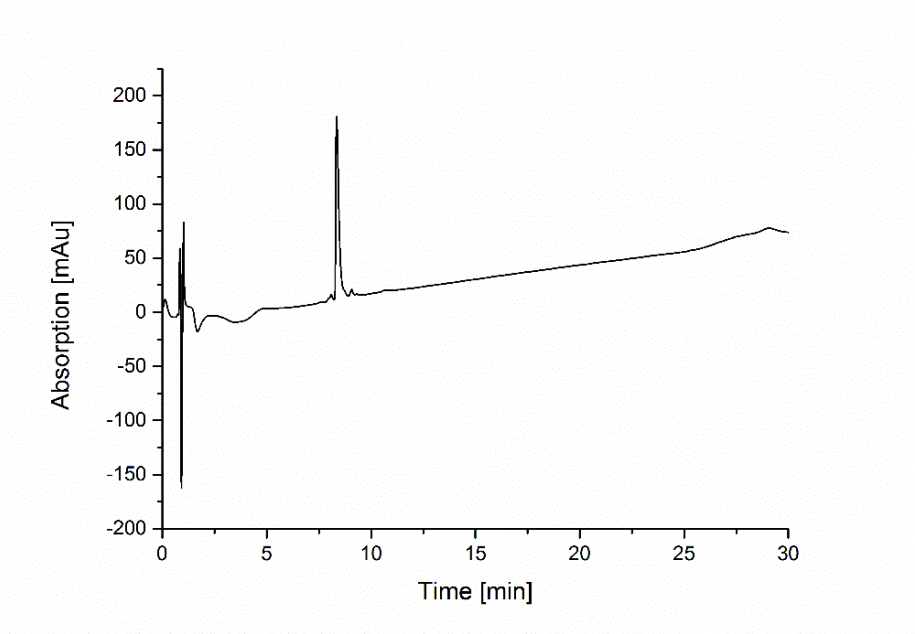

RP-HPLC chromatogram of compound **5** (gradient from 0% to 50% eluent B over 30 min at 25°C).

(**6**) *protected*

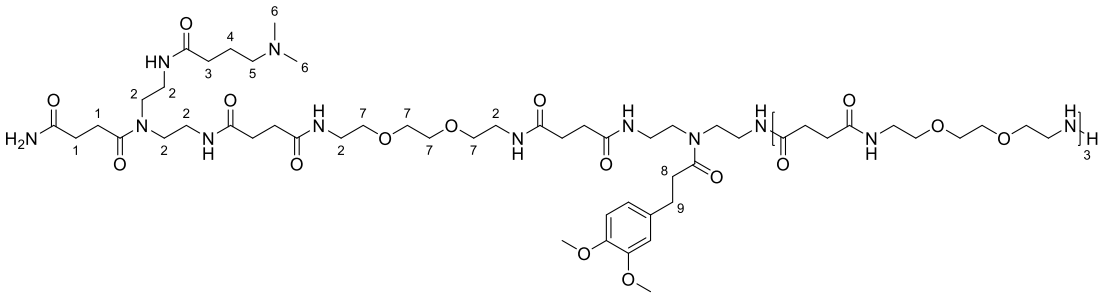

Compound **6** protected was obtained with a yield of 72% after cleavage from solid support and lyophilization.

^{1}H-NMR (500 MHz, D_2O) δ [ppm]: 6.92 (m, 2H, $H_{Aromatic}$), 6.81 (m, 1H, $H_{Aromatic}$), 3.81 (s, 3H, OCH_3), 3.79 (s, 3H, OCH_3), 3.74-3.51 (m, 32H, H-7), 3.50-3.15 (m, 32H, H-2), 3.09 (m, 2H, H-5), 2.85 (m, 8H, 6-H, 9-H), 2.64 (m, 4H, 3-H, 8-H), 2.53-2.25 (m, 24H, 1-H), 1.94 (m, 2H, 4-H).

^{13}C-NMR (126 MHz, D_2O) δ [ppm]: 178.60, 176.60, 175.81, 175.67, 175.61, 175.58, 175.50, 175.46, 175.35, 149.15, 147.73, 134.99, 130.73, 121.84, 120.71, 118.39, 116.08, 115.65, 113.76, 113.33, 113.05, 70.55, 70.39, 69.78, 67.29, 66.81, 57.95, 56.75, 56.67, 48.06, 47.95, 47.77, 45.91, 45.81, 43.62, 40.09, 39.87, 39.25, 39.07, 38.91, 38.31, 38.17, 38.00, 37.90, 35.17, 33.02, 32.90, 31.99, 31.86, 31.75, 31.62, 30.96, 28.94, 28.85, 20.99, 20.94, 15.04.

HR-ESI-MS: calculated mass for $C_{73}H_{131}N_{16}O_{24}$ $[M+3H]^{3+}$ 538.6502, found 538.6499.

RP-HPLC (gradient from 0% to 50% eluent B over 30 min at 25°C):t_r=10.6 min, purity 87%.

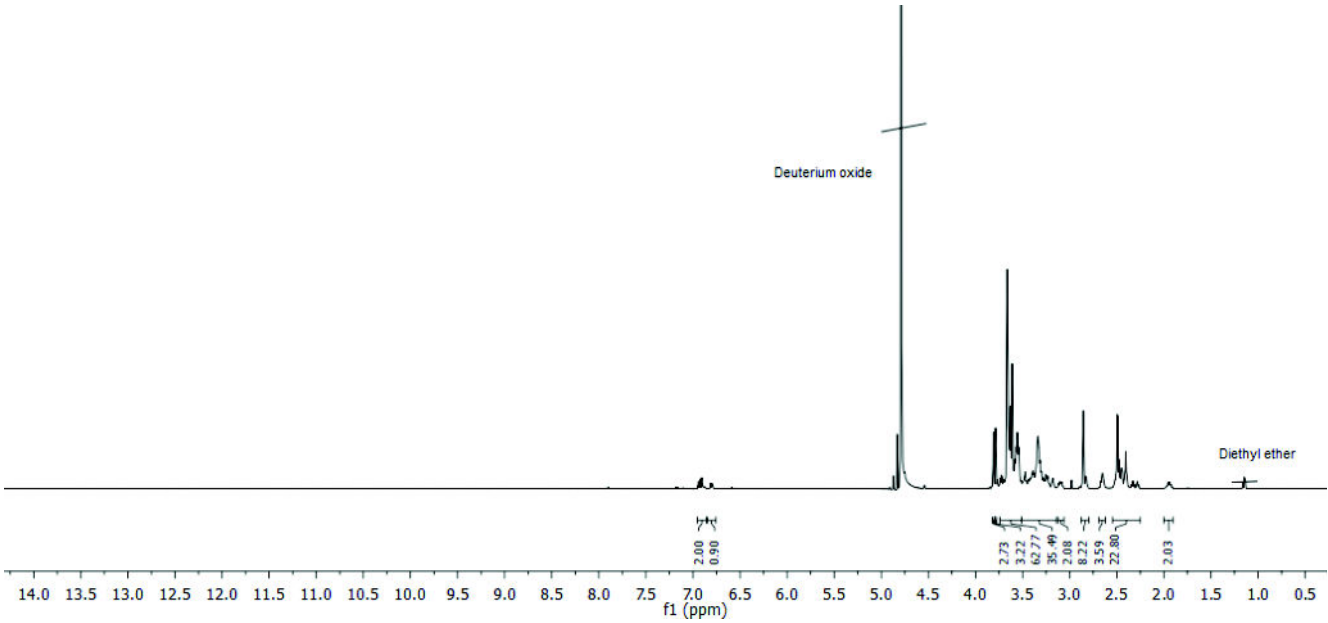

^{1}H-NMR spectrum of compound **6** protected (500 MHz, D_2O).

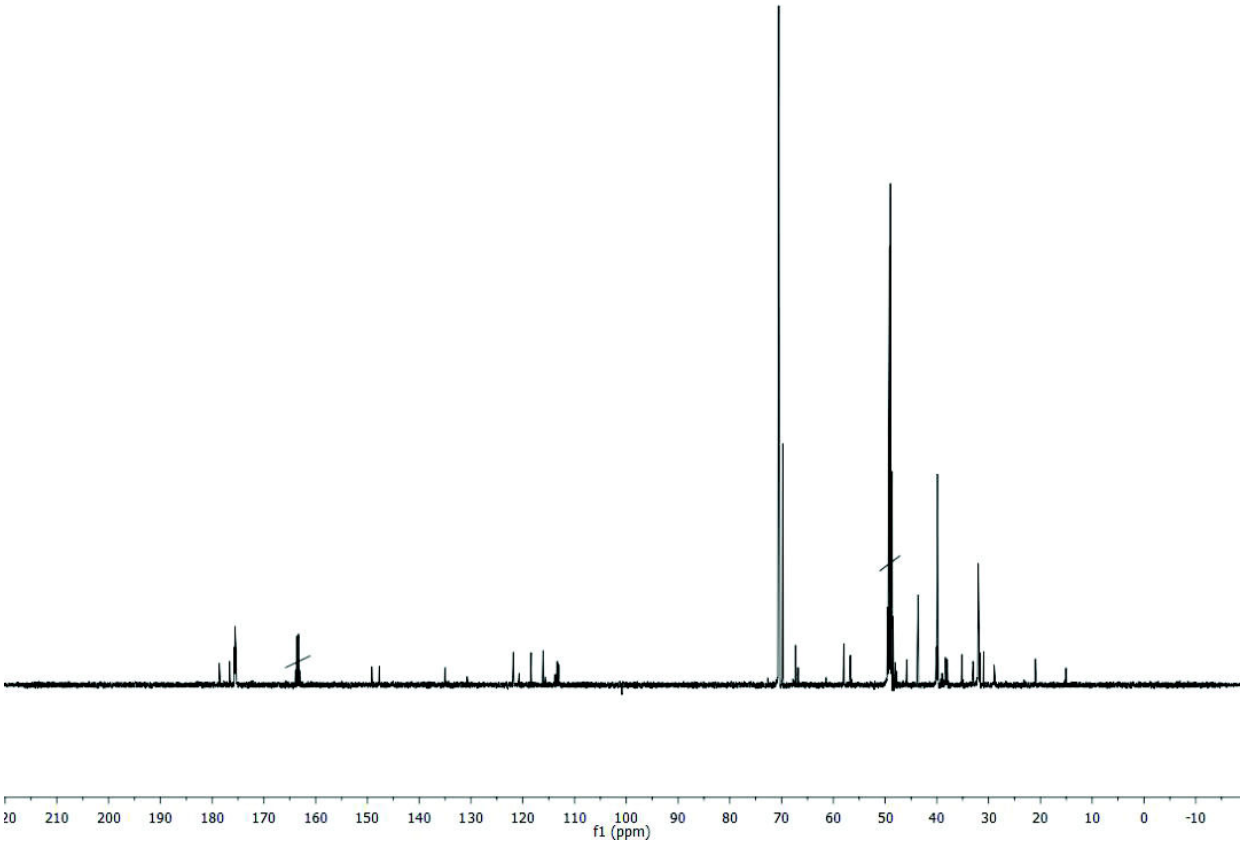

^{13}C-NMR spectrum of compound **6** protected (126 MHz, D_2O).

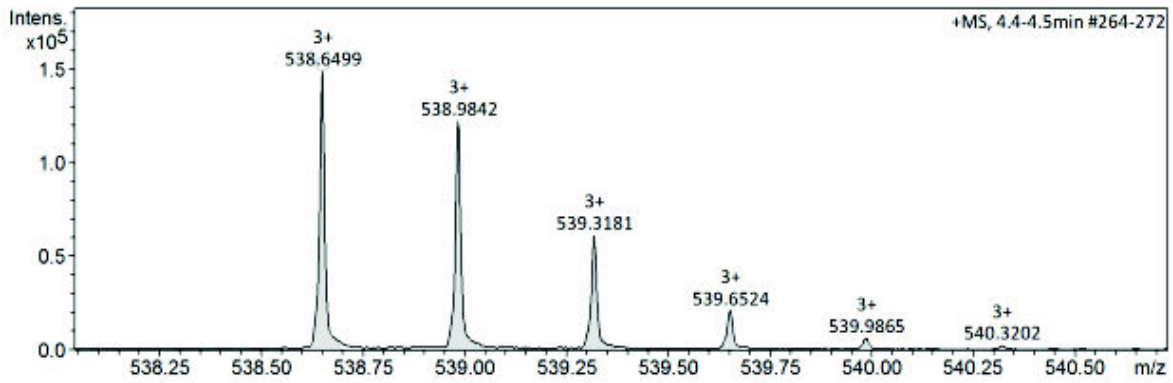

HR-ESI (ESI$^+$ Q-TOF) of compound **6** protected.

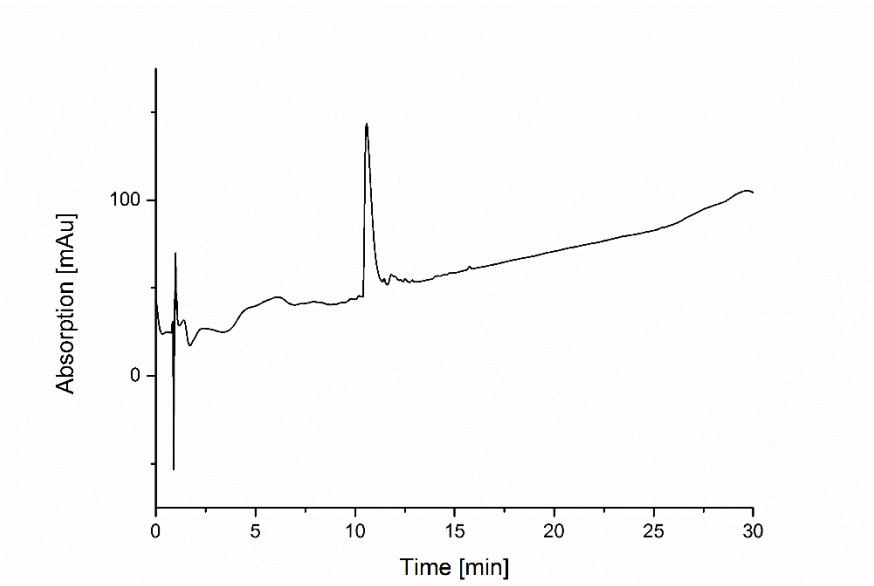

RP-HPLC chromatogram of compound **6** protected (gradient from 0% to 50% eluent B over 30 min at 25°C).

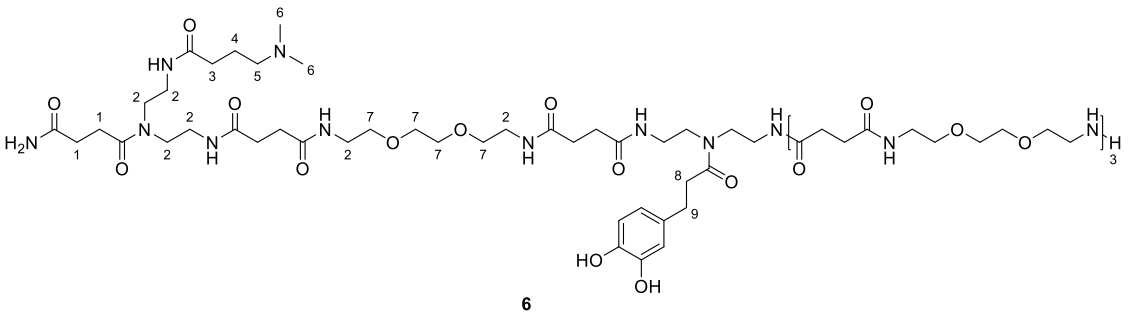

6

(**6**)

Compound **6** was obtained with a yield of 26% after deprotection, purification by preparative RP-HPLC and lyophilization.

^{1}H-NMR (500 MHz, D_2O) δ [ppm]: 6.84 (d, J = 8.0 Hz, 1H, $H_{Aromatic}$), 6.78 (s, 1H, $H_{Aromatic}$), 6.69 (d, J = 7.5 Hz1H, $H_{Aromatic}$), 3.77-3.55 (m, 32H, H-7), 3.53-3.20 (m, 32H, H-2), 3.12 (m, 2H, H-5), 2.88 (m, 6H, H-6,), 2.78 (t, J = 7.3 Hz, 2H, H-9), 2.68 (t, J = 6.7 Hz, 2H, H-3), 2.64 (t, J = 7.3 Hz, 2H, H-8), 2.56-2.30 (m, 24H, H-1), 1.97 (m, 2H, H-4).

^{13}C-NMR (126 MHz, D_2O) δ [ppm]: 180.71, 178.76, 177.92, 177.82, 177.77, 177.72, 177.69, 177.64, 177.62, 177.59, 177.48, 123.52, 119.08, 72.47, 72.34, 71.74, 69.30, 59.83, 50.01, 49.88, 49.68, 47.79, 47.71, 47.64, 45.58, 42.00, 41.82, 41.76, 40.18, 40.06, 39.92, 39.82, 39.80, 37.20, 34.98, 34.85, 33.93, 33.89, 33.86, 33.79, 33.73, 33.68, 33.36, 32.88, 30.90, 30.81, 23.00, 22.94.

HR-ESI-MS: calculated mass for $C_{71}H_{127}N_{16}O_{24}$ $[M+3H]^{3+}$ 529.3064, found 529.3067.

RP-HPLC (gradient from 0% to 50% eluent B over 30 min at 25°C):t_r=8.3 min, purity 97%.

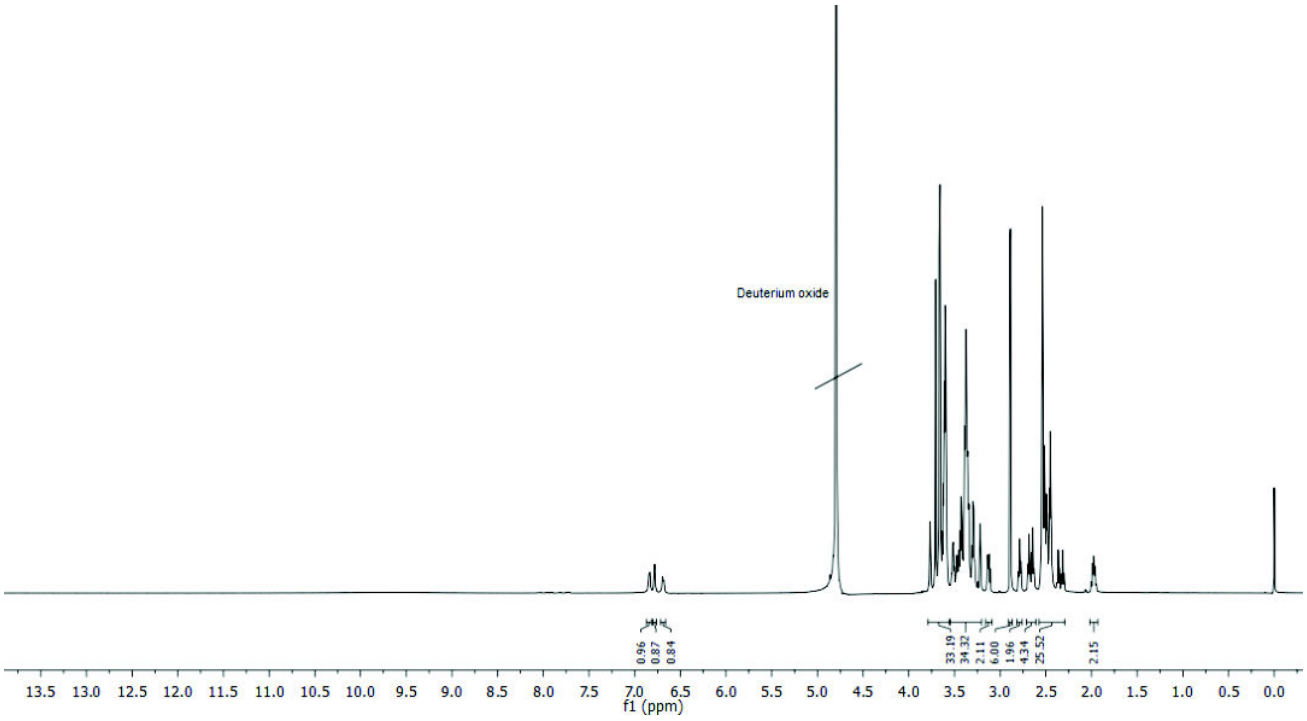

^{1}H-NMR spectrum of compound **6** (600 MHz, D_2O).

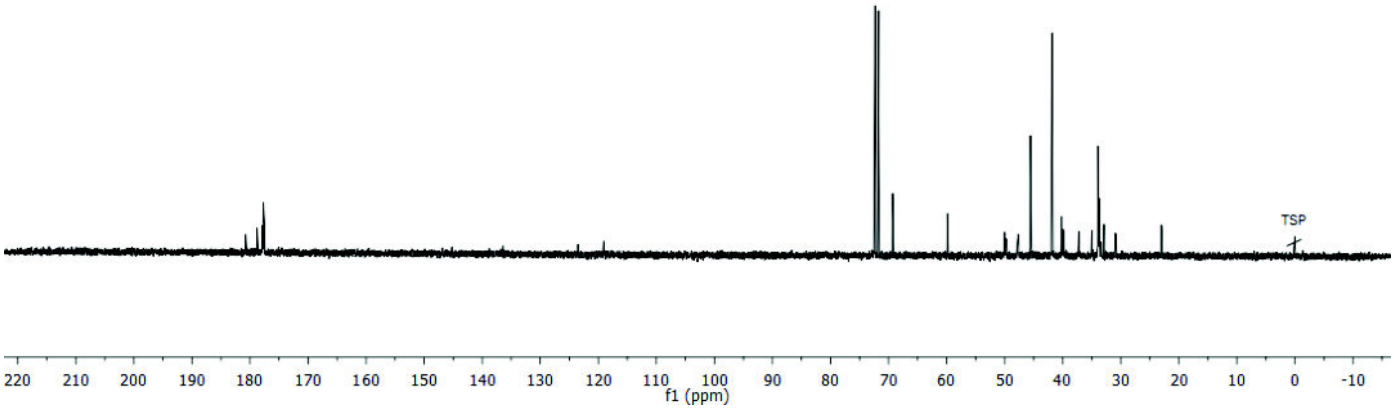

^{13}C-NMR spectrum of compound **6** (126 MHz, D_2O).

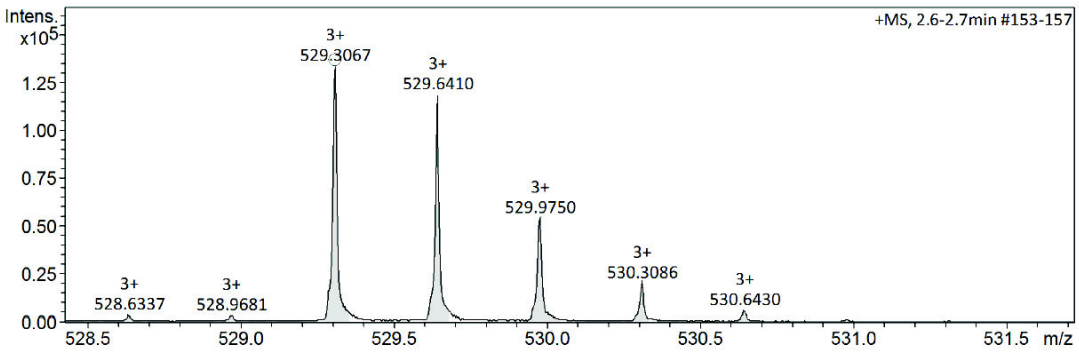

HR-ESI (ESI$^+$ Q-TOF) of compound **6**.

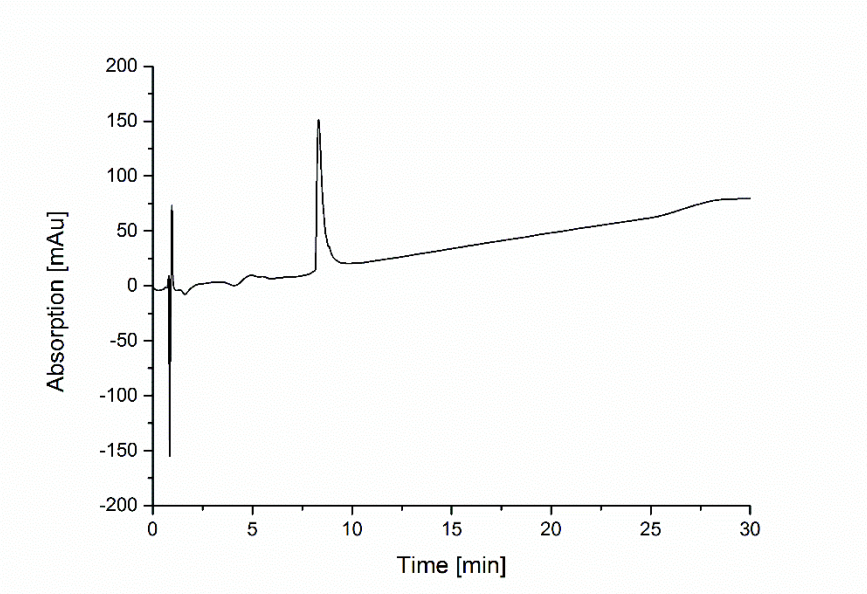

RP-HPLC chromatogram of compound **6** (gradient from 0% to 50% eluent B over 30 min at 25°C).

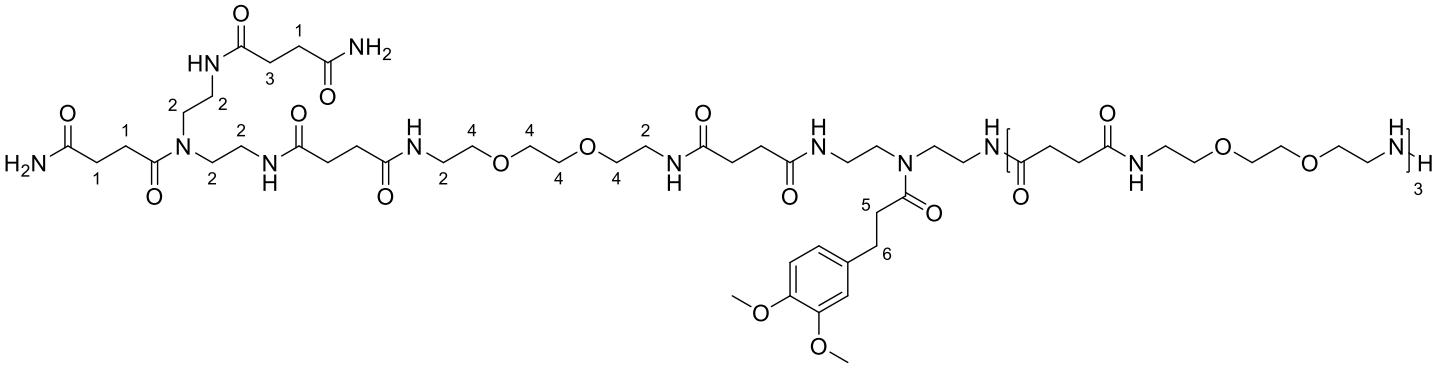

(**7**) *protected*

7 protected was obtained with a yield of 52% after cleavage from solid support and lyophilization.

^{1}H-NMR (500 MHz, D_2O) δ [ppm]: 8.49 (s, NH), 6.98 (d, J = 8.2 Hz, 1H, $H_{Aromatic}$), 6.95 (d, J = 2.0 Hz, 1H, $H_{Aromatic}$), 6.85 (d, J = 8.2 Hz, 2.0 Hz, 1H, $H_{Aromatic}$), 3.85 (s, 3H, OCH_3), 3.83 (s, 3H, OCH_3) 3.77-3.49 (m, 32H, H-4), 3.47-3.20 (m, 32H, H-2), 2.87 (t, J = 7.3 Hz, 2H, H-6), 2.69 (m, 4H, H-3, H-5), 2.62-2.45 (m, 26H, H-1).

^{13}C-NMR (126 MHz, D_2O) δ [ppm]: 178.64, 176.60, 175.67, 175.65, 175.59, 175.56, 175.52, 175.49, 175.45, 175.33, 171.61, 149.16, 147.75, 134.99, 121.84, 113.29, 113.00, 70.57, 70.43, 69.82, 67.33, 56.72, 56.65, 48.07, 46.06, 45.81, 40.11, 39.88, 39.82, 38.31, 38.00, 37.94, 35.21, 31.99, 31.96, 31.92, 31.86, 31.80, 31.74, 31.71, 31.66, 31.24, 31.14, 31.01, 28.93.

HR-ESI-MS: calculated mass for $C_{71}H_{125}N_{16}O_{25}$ $[M+3H]^{3+}$ 533.9662, found 533.9665.

RP-HPLC (gradient from 0% to 50% eluent B over 30 min at 25°C):t_r=10.7 min, purity 97%.

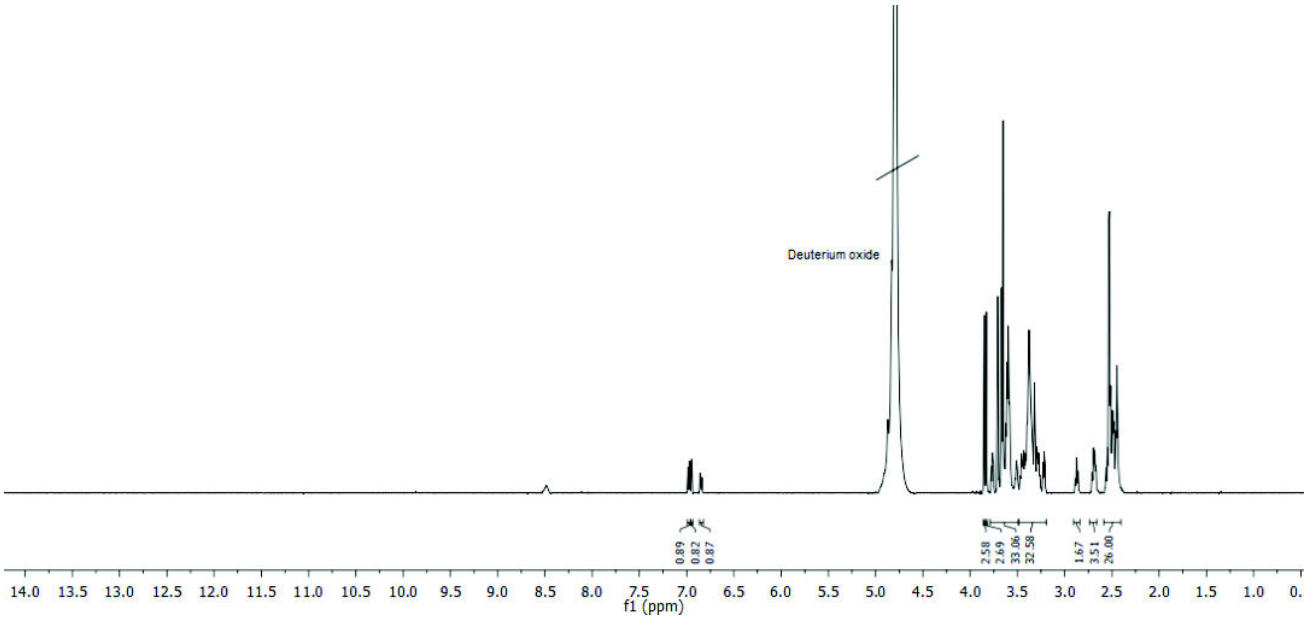

^{1}H-NMR spectrum of compound **7** protected (600 MHz, D_2O).

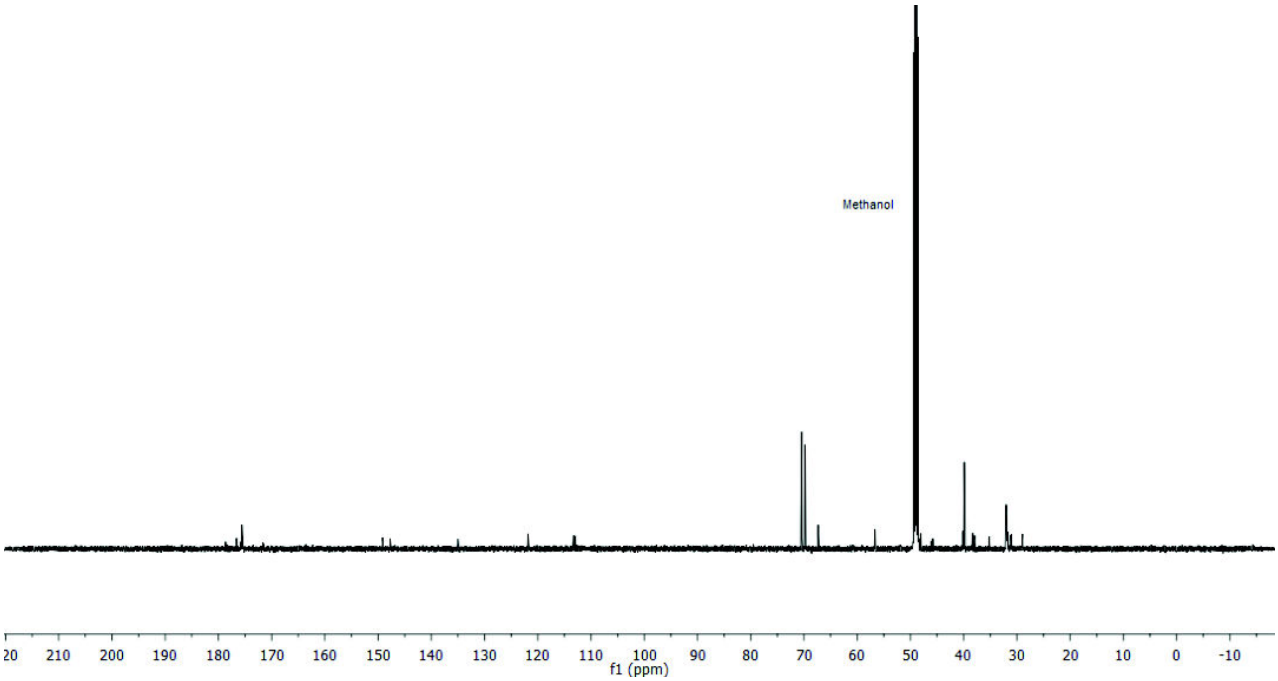

^{13}C-NMR spectrum of compound **7** protected (126 MHz, D_2O).

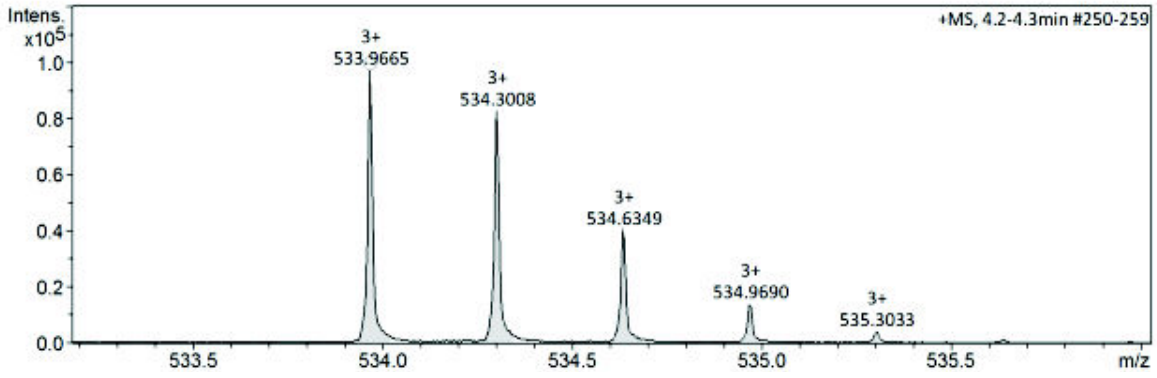

HR-ESI (ESI$^+$ Q-TOF) of compound **7** protected.

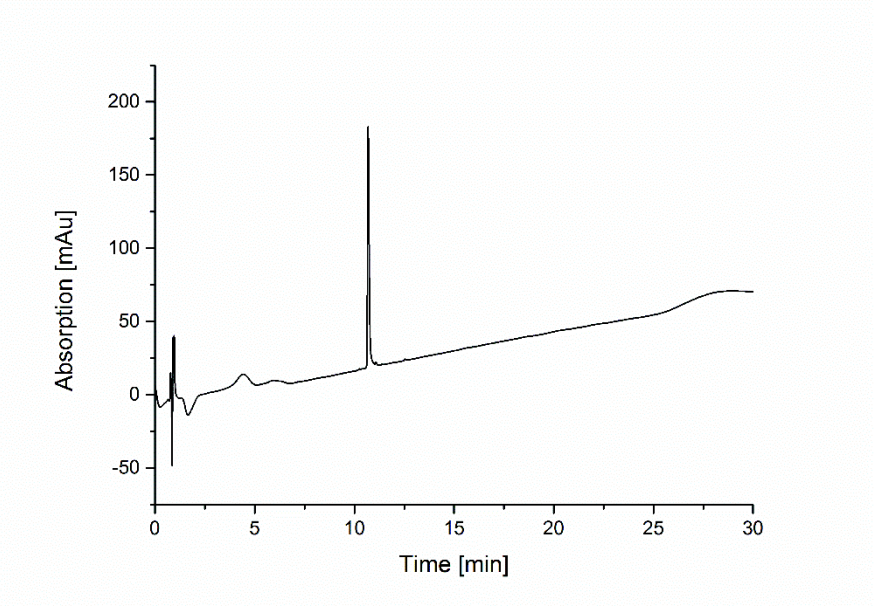

RP-HPLC chromatogram of compound **7** protected (gradient from 0% to 50% eluent B over 30 min at 25°C).

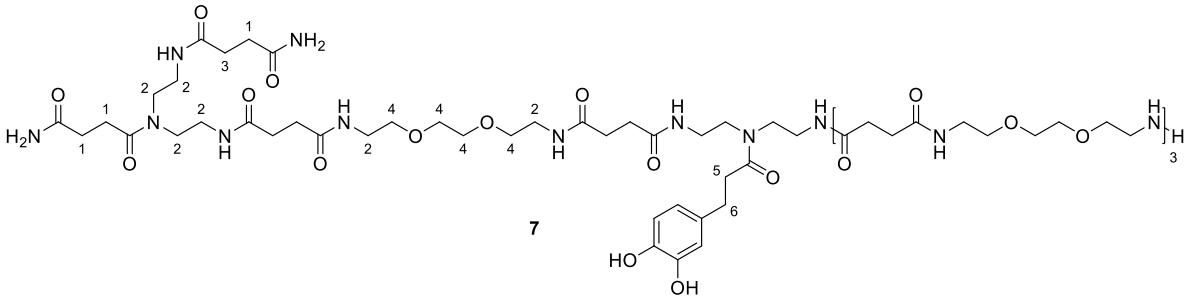

7

(**7**)

Compound **7** was obtained with a yield of 24% after deprotection, purification by preparative RP-HPLC and lyophilization.

^{1}H-NMR (500 MHz, D_2O) δ [ppm]: 8.45 (s, NH), 6.83 (d, J = 8.0 Hz, 1H, $H_{Aromatic}$), 6.77 (d, J = 2.1 Hz, 1H, $H_{Aromatic}$), 6.68 (dd, J = 8.0 Hz, 2.1 Hz, 1H, $H_{Aromatic}$), 3.78-3.56 (m, 32H, H-5), 3.51-3.20 (m, 32H, H-2), 2.79 (t, J = 7.0 Hz, 2H, H-4), 2.66 (m, 4H, H-3, H-6), 2.54-2.43 (m, 26H, H-1).

^{13}C-NMR (126 MHz, D_2O) δ [ppm]: 178.50, 175.91, 175.88, 175.81, 175.74, 175.66, 175.64, 171.96, 171.93, 144.91, 134.45, 117.15, 70.41, 69.81, 67.37, 39.88, 39.81, 38.25, 37.91, 35.23, 31.98, 31.94, 31.91, 31.85, 31.82, 31.76, 31.75, 31.70, 31.61, 31.60, 29.00.

HR-ESI-MS: calculated mass for $C_{69}H_{121}N_{16}O_{25}$ $[M+3H]^{3+}$ 524.6224, found 524.6221.

RP-HPLC (gradient from 0% to 50% eluent B over 30 min at 25°C):t_r=6.5 min, purity 85%.

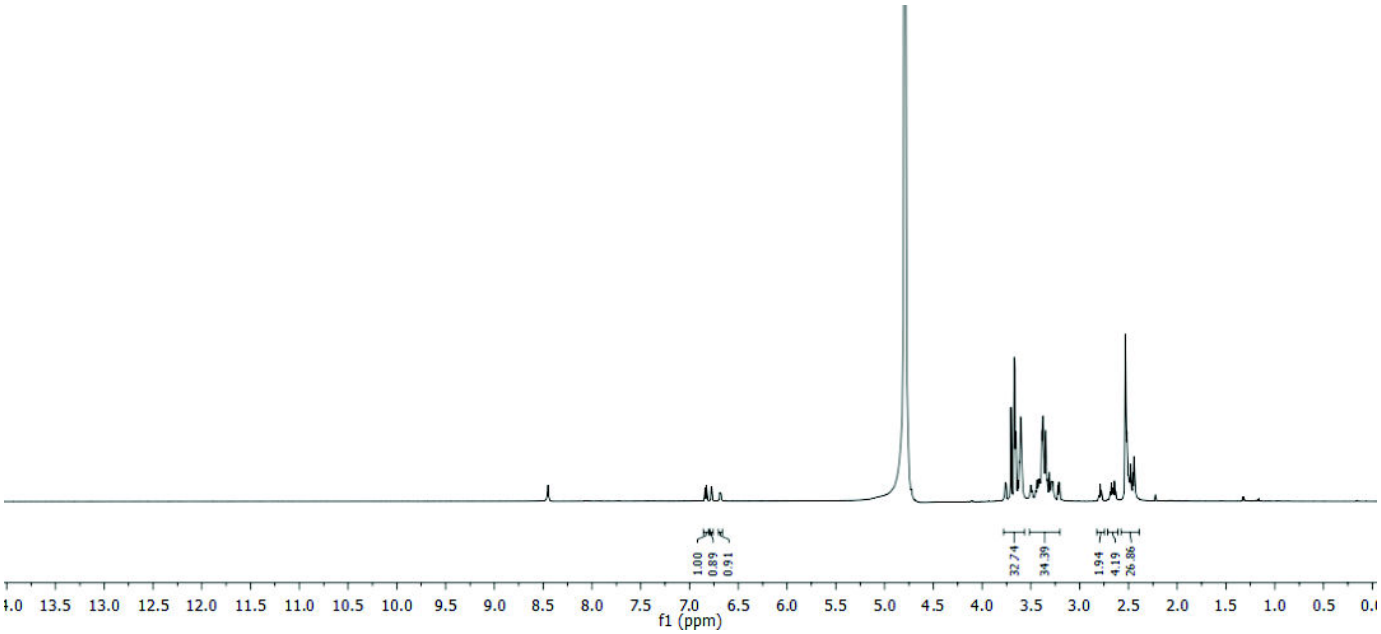

^{1}H-NMR spectrum of compound **7** (600 MHz, D_2O).

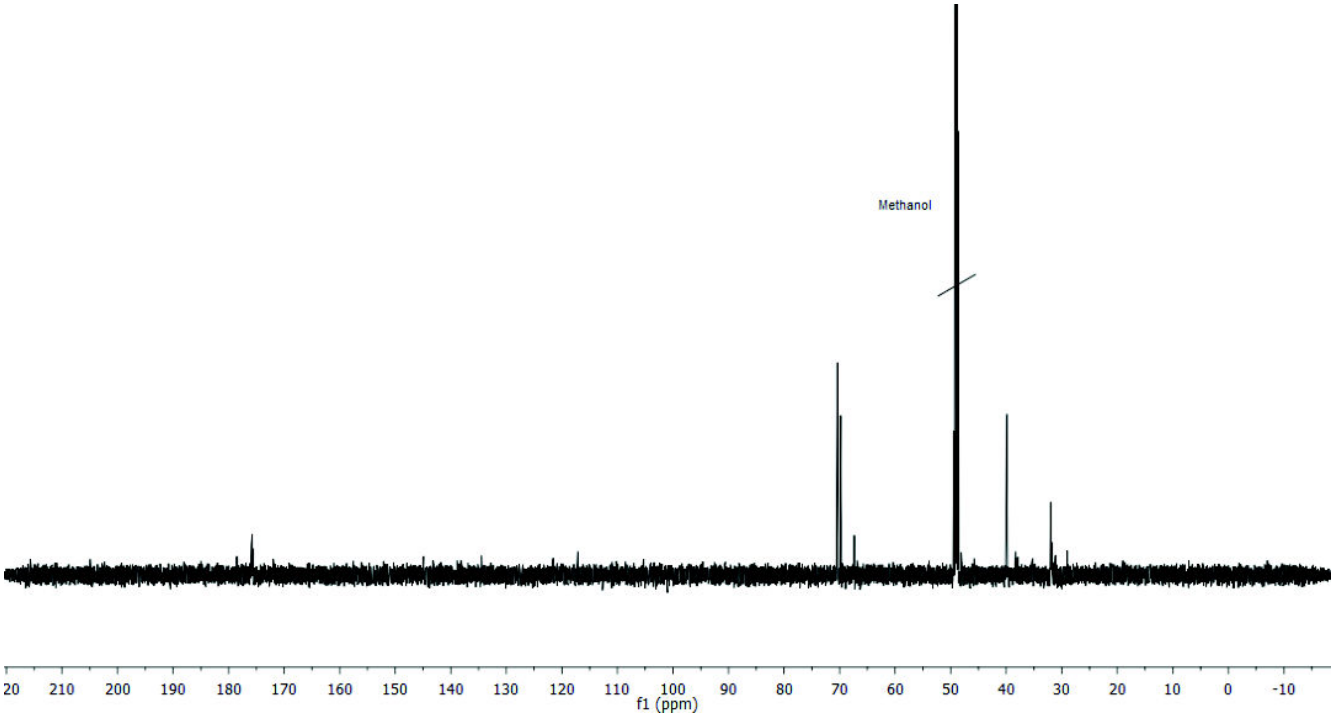

^{13}C-NMR spectrum of compound **7** (126 MHz, D_2O).

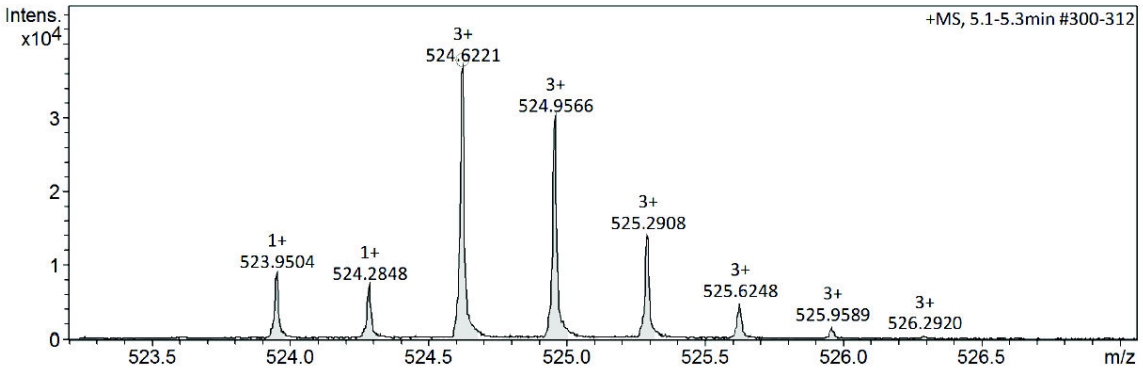

HR-ESI (ESI$^+$ Q-TOF) of compound **7**.

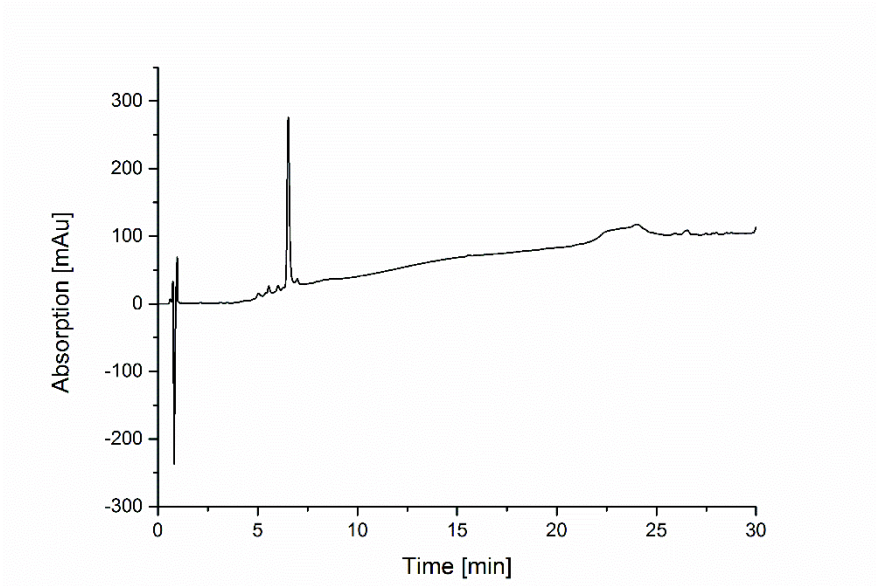

RP-HPLC chromatogram of compound **7** (gradient from 0% to 50% eluent B over 30 min at 25°C).

(**8**)

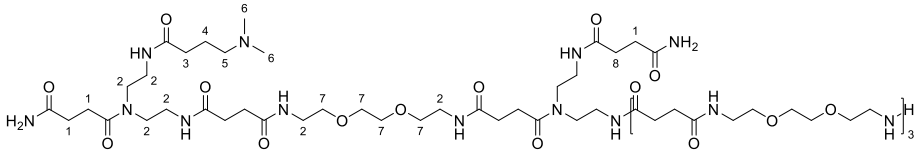

8

Compound **8** was obtained with a yield of 34% after purification by preparative RP-HPLC and lyophilization.

^{1}H-NMR (600 MHz, D_2O) δ [ppm]: 8.48 (s, NH), 3.75-3.56 (m, 32H, H-7), 3.52-3.17 (m, 32H, H-2, Methanol), 3.11 (m, 2H, H-5) 2.86 (m, 6H, H-6), 2.67 (m, 4H, H-3, H-8), 2.55-2.27 (m, 26H, H-1), 1.95 (m, 2H, H-4).

^{13}C-NMR (126 MHz, D_2O) δ [ppm]: 70.58, 70.47, 70.45, 69.89, 69.86, 69.85, 43.63, 40.11, 39.90, 31.99, 31.91, 31.88, 31.84, 31.82, 31.78, 31.63.

Supporting Information

HR-ESI-MS: calculated mass for $C_{66}H_{124}N_{17}O_{23}$ $[M+3H]^{3+}$ 507.6347, found 507.6356.

RP-HPLC (gradient from 0% to 50% eluent B over 30 min at 25°C):t_r=1.2 min, purity 91%.

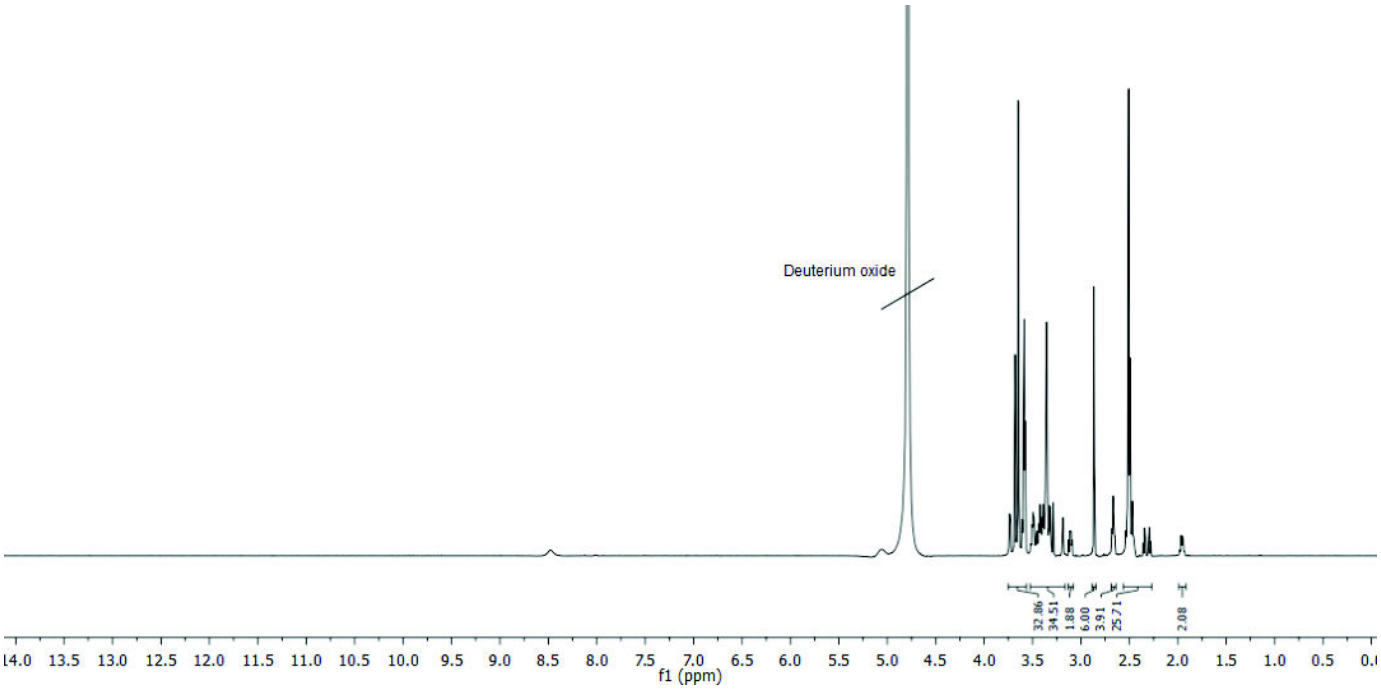

^{1}H-NMR spectrum of compound **8** (500 MHz, D_2O).

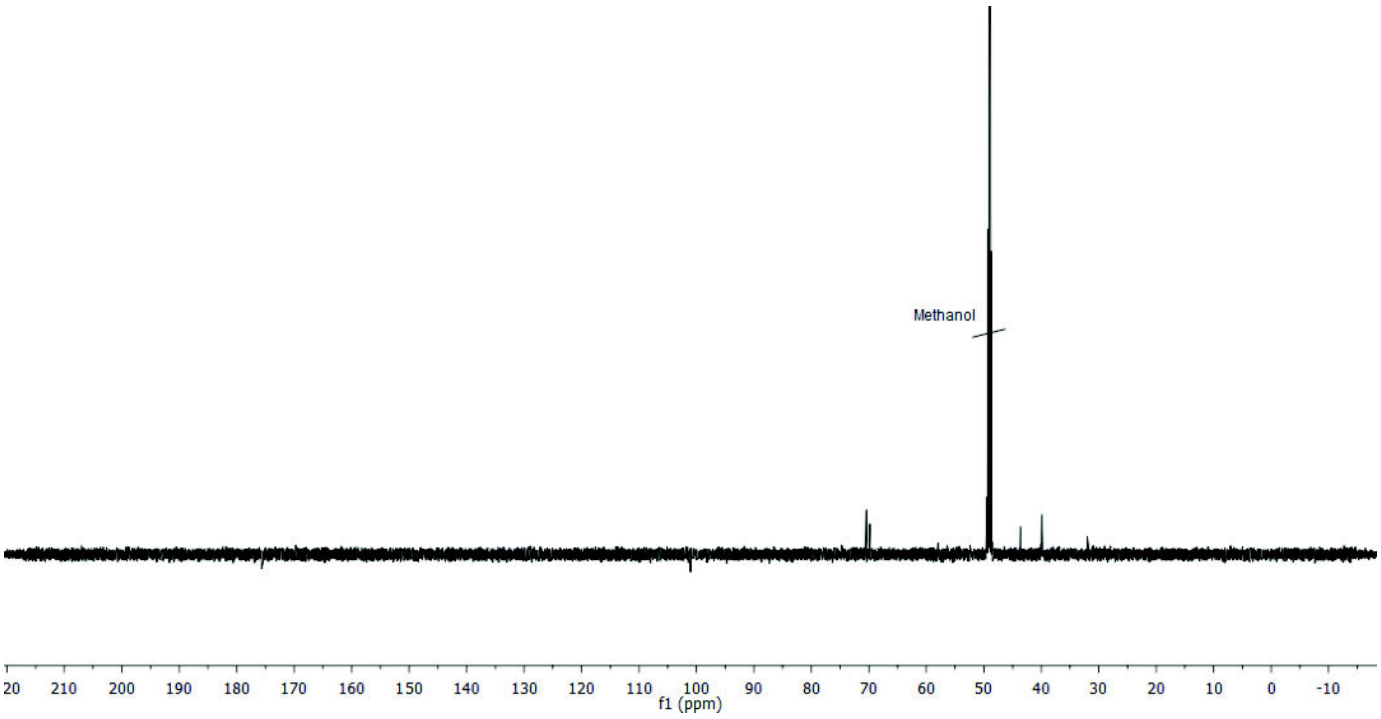

^{13}C-NMR spectrum of compound **8** (126 MHz, D_2O).

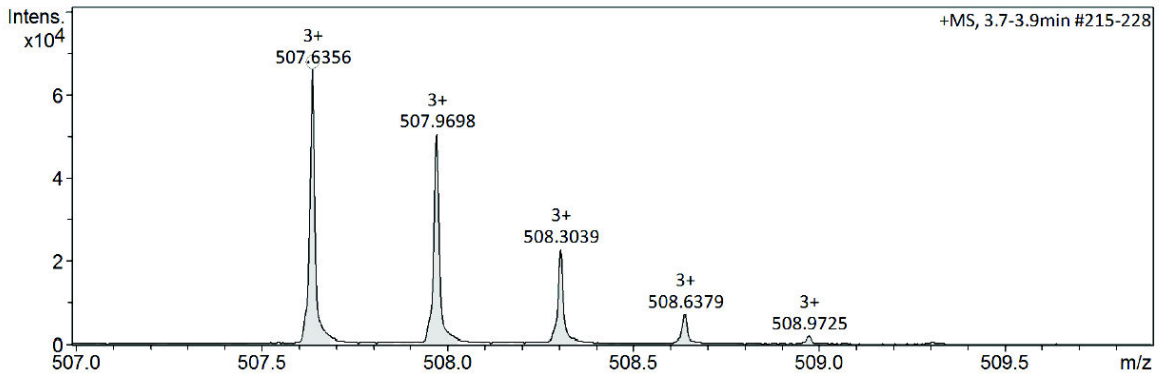

HR-ESI (ESI$^+$ Q-TOF) of compound **8**.

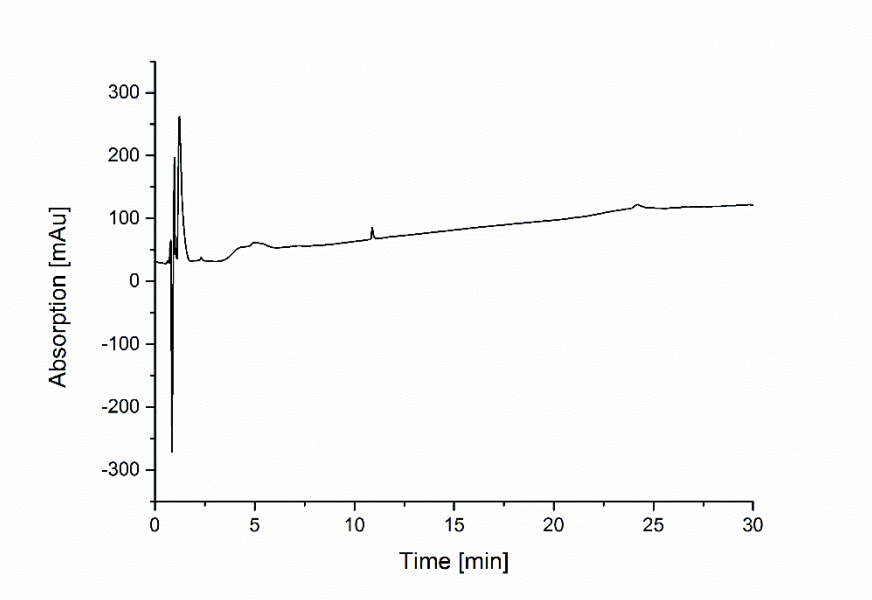

RP-HPLC chromatogram of compound **8** (gradient from 0% to 50% eluent B over 30 min at 25°C).

(**9**) *protected*

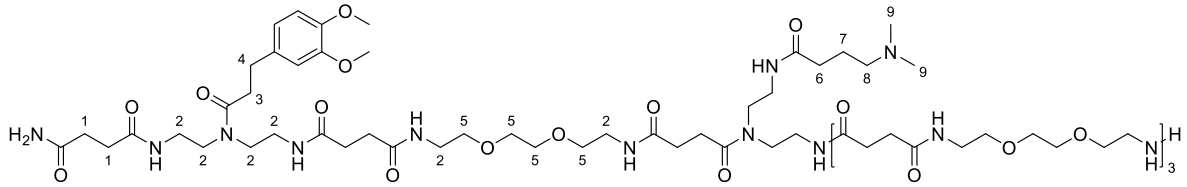

Compound **9** protected was obtained with a yield of 67% after cleavage from solid support and lyophilization.

^{1}H-NMR (500 MHz, D_2O) δ [ppm]: 8.62 (s, NH), 7.05 (d, J = 8.2 Hz, 1H, $H_{Aromatic}$), 7.02 (d, J = 1.9 Hz, 1H, $H_{Aromatic}$), 6.92 (dd, J = 8.2, 1.9 Hz, 1H, $H_{Aromatic}$), 3.91 (s, 3H, OCH_3), 3.89 (s, 3H, OCH_3), 3.85-3.64 (m, 32H, H-5), 3.60-3.26 (m, 32H, H-2), 3.19 (m, 2H, H-8), 2.95 (m, 8H, 4-H, 9-H), 2.75 (m, 4H, 6-H, 3-H), 2.62-2.35 (m, 24H, 1-H), 2.04 (m, 2H, 7-H).

^{13}C-NMR (126 MHz, D_2O) δ [ppm]: 177.88, 176.29, 175.39, 175.36, 175.28, 175.21, 175.16, 175.01, 171.29, 148.70, 147.28, 134.64, 121.50, 112.99, 112.71, 70.12, 69.98, 69.38, 66.91, 57.52, 56.39, 56.32, 47.66, 45.43, 43.24, 39.67, 39.43, 37.92, 37.60, 37.51, 34.68, 32.63, 32.52, 31.60, 31.47, 31.38, 31.20, 30.78, 30.65, 28.58, 20.60, 20.55.

HR-ESI-MS: calculated mass for $C_{73}H_{131}N_{16}O_{24}$ $[M+3H]^{3+}$ 538.6502, found 538.6503.

RP-HPLC (gradient from 0% to 50% eluent B over 30 min at 25°C): t_r=10.6 min, purity 89%.

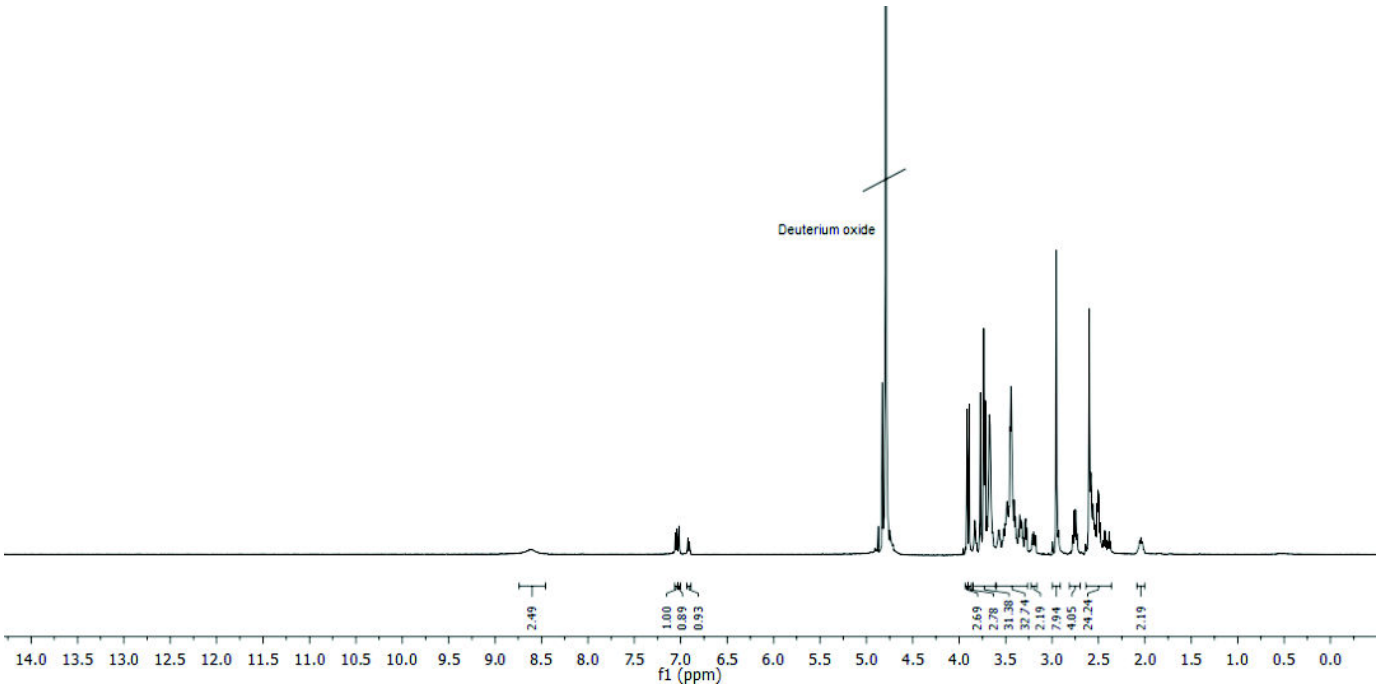

^{1}H-NMR spectrum of compound **9** protected (500 MHz, D_2O).

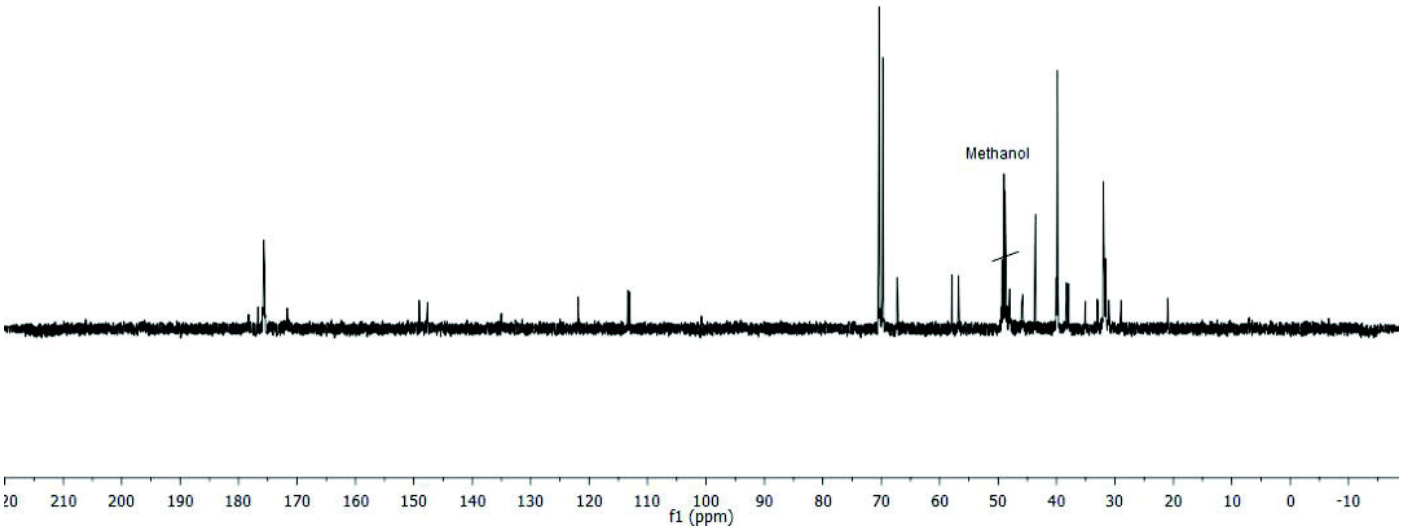

^{13}C-NMR spectrum of compound **9** protected (126 MHz, D_2O).

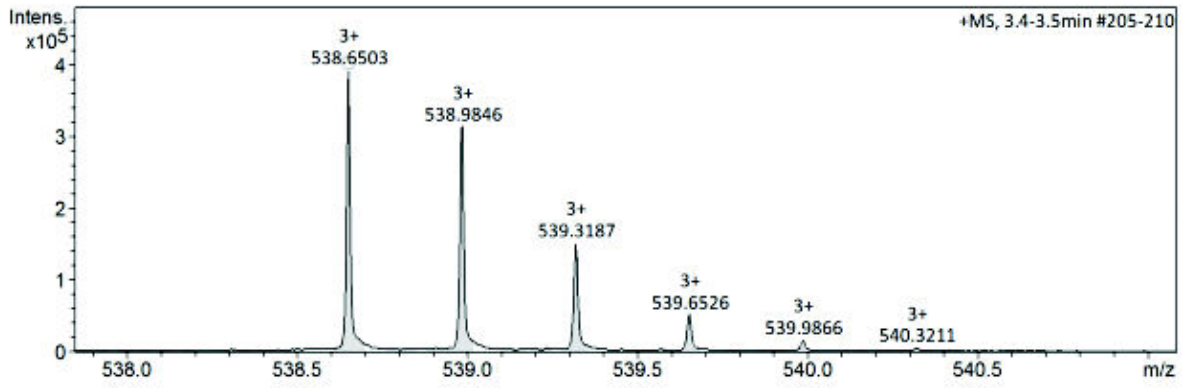

HR-ESI (ESI^+ Q-TOF) of compound **9** protected.

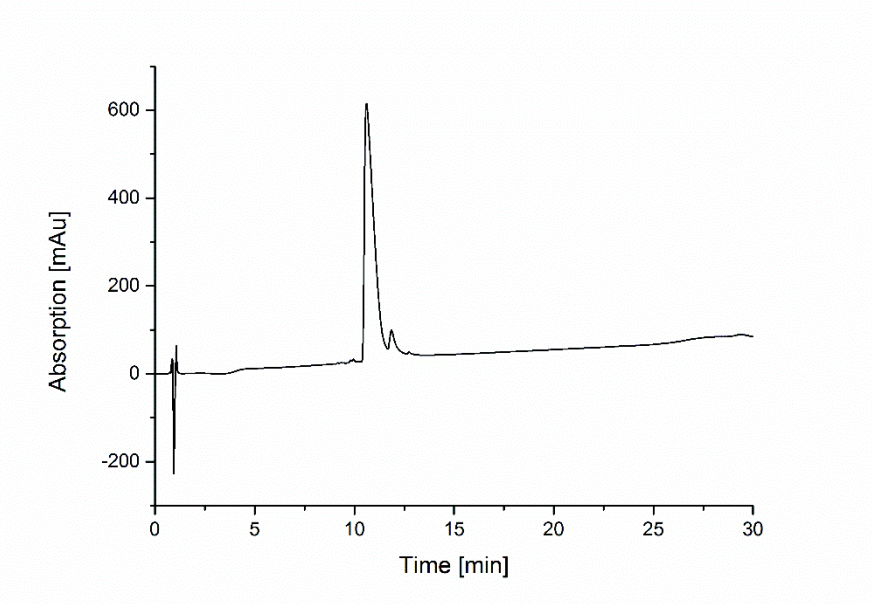

RP-HPLC chromatogram of compound **9** protected (gradient from 0% to 50% eluent B over 30 min at 25°C).

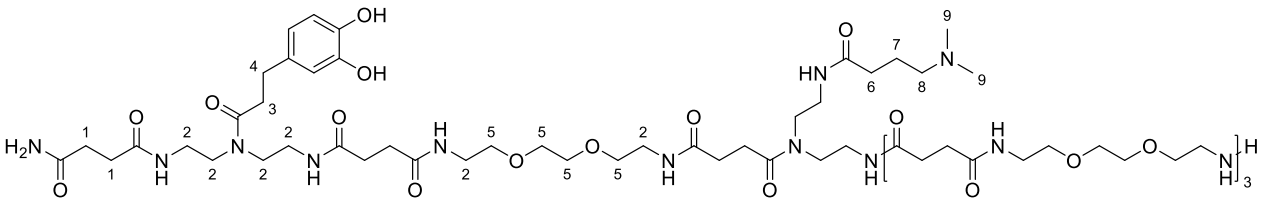

9

(**9**)

Compound **9** was obtained with a yield of 27% after deprotection, purification by preparative RP-HPLC and lyophilization.

^{1}H-NMR (600 MHz, D_2O) δ [ppm]: 8.44 (s, NH), 6.82 (d, J = 8.0 Hz, 1H, $H_{Aromatic}$), 6.76 (s, 1H, $H_{Aromatic}$), 6.67 (d, J = 8.0 HZ, 1H, $H_{Aromatic}$), 3.76-3.55 (m, 32H, H-5), 3.51-3.18 (m, 32H, H-2),

3.11 (t, J = 8.1Hz, 2H, H-8), 2.87 (s, 6H, H-9), 2.77 (t, J = 7.2 Hz, 2H, H-4), 2.65 (m, 4H, H-3, H-6), 2.55-2.28 (m, 24H, H-1), 1.97 (m, 2H, H-7).

^{13}C-NMR (126 MHz, D_2O) δ [ppm]: 175.76, 175.71, 175.64, 175.54, 171.78, 121.52, 117.10, 70.53, 70.39, 69.79, 67.32, 57.93, 46.02, 45.84, 40.08, 39.86, 39.80, 38.02, 37.94, 37.91, 35.20, 33.04, 32.92, 31.99, 31.95, 31.92, 31.86, 31.78, 31.63, 31.40, 31.08, 29.02, 28.97.

HR-ESI-MS: calculated mass for $C_{71}H_{127}N_{16}O_{24}$ $[M+3H]^{3+}$ 529.3064, found 529.3056.

RP-HPLC (gradient from 0% to 50% eluent B over 30 min at 25°C): t_r=6.3 min, purity 97%.

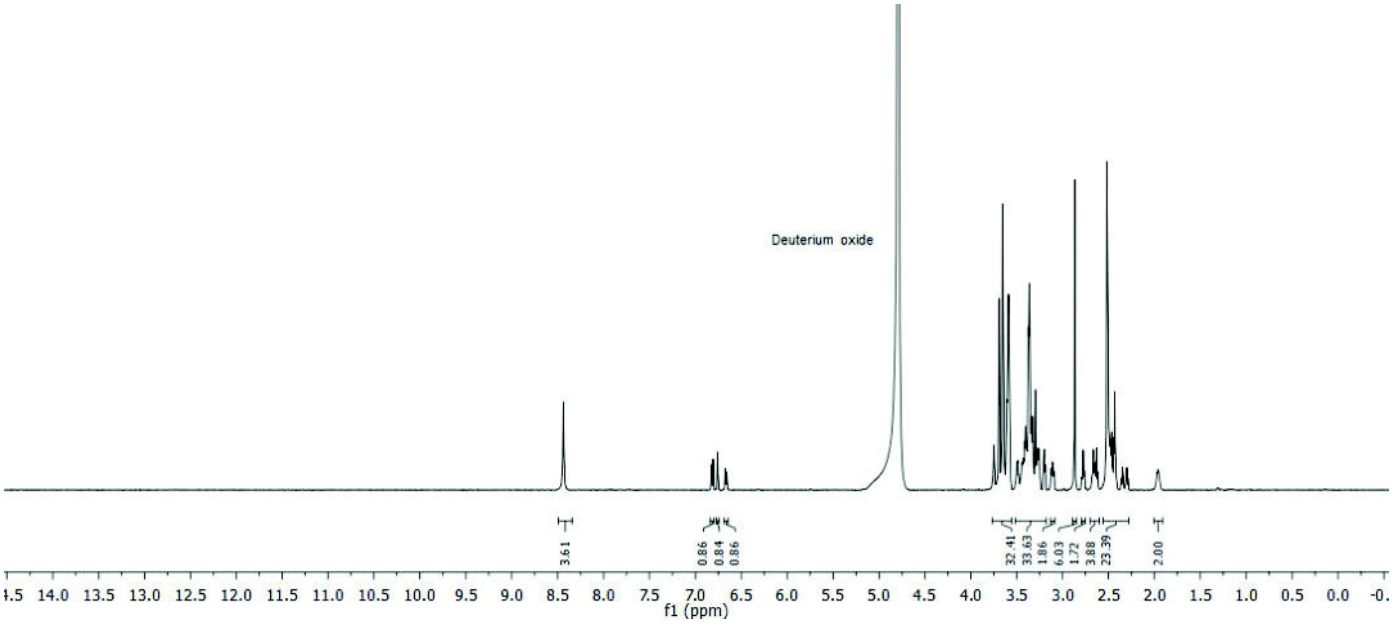

^{1}H-NMR spectrum of compound **9** (500 MHz, D_2O).

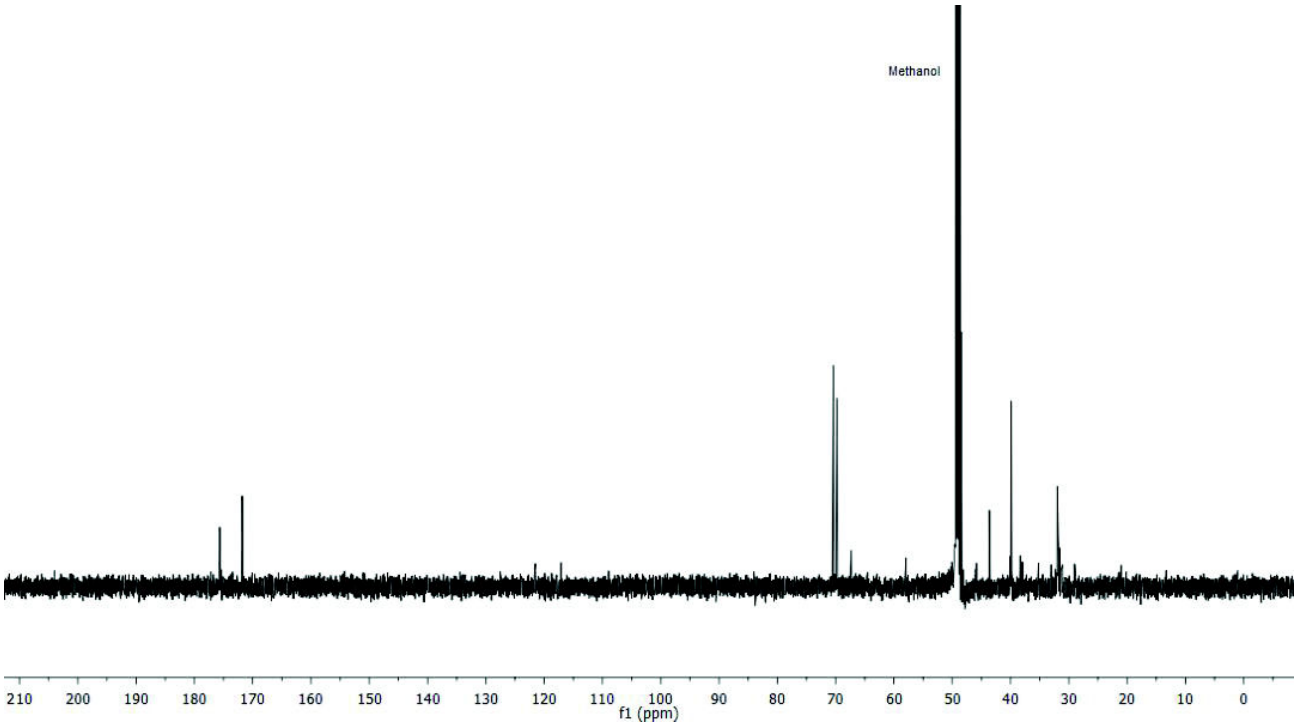

^{13}C-NMR spectrum of compound **9** (126 MHz, D_2O).

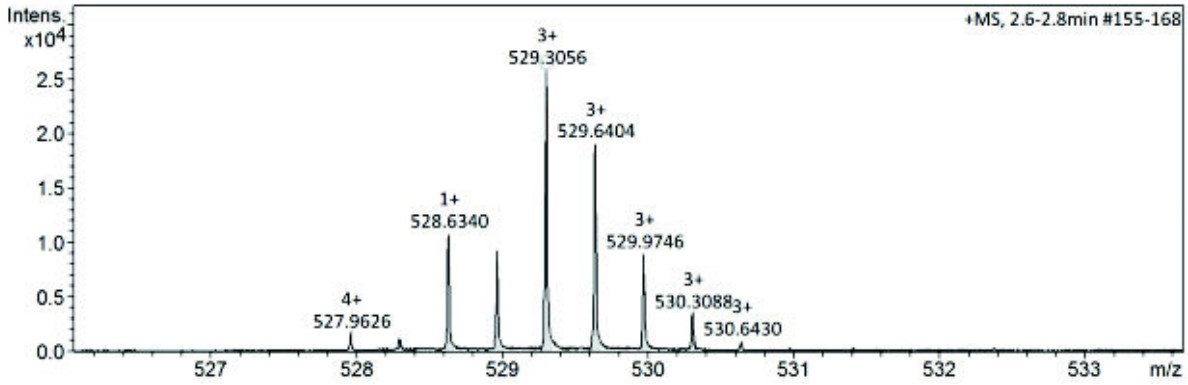

HR-ESI (ESI$^+$ Q-TOF) of compound **9**.

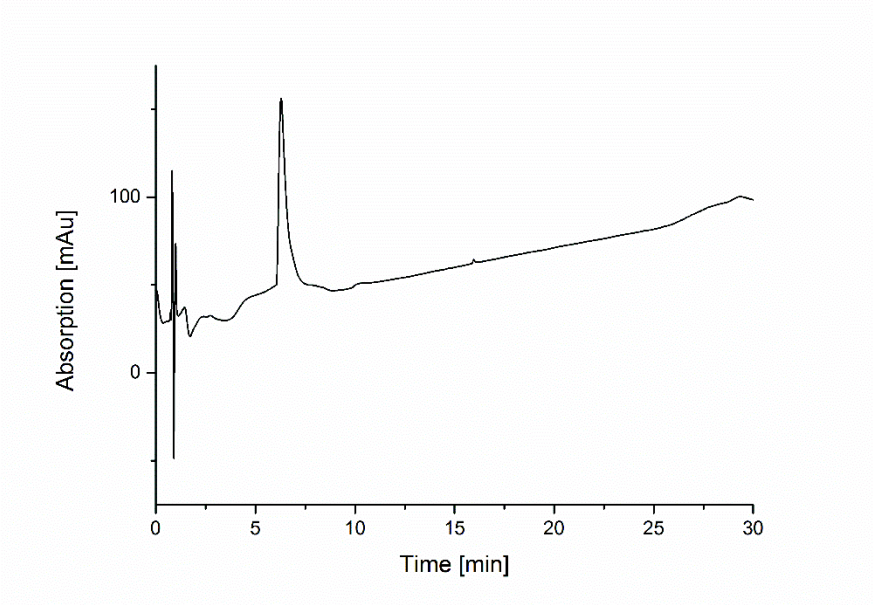

RP-HPLC chromatogram of compound **9** (gradient from 0% to 50% eluent B over 30 min at 25°C).

(**10**) *protected*

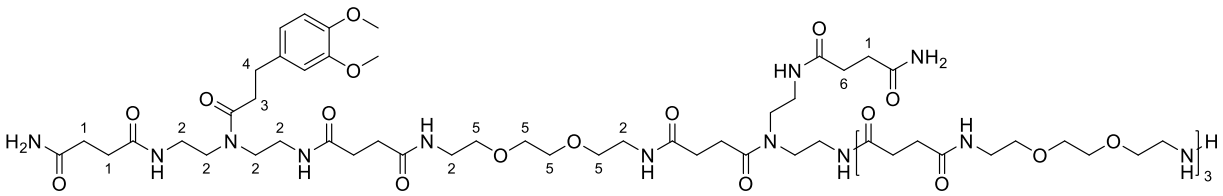

10

Compound **10** protected was obtained with a yield of 61% after cleavage from solid support and lyophilization.

^{1}H-NMR (500 MHz, D_2O) δ [ppm]: 8.45 (s, NH), 7.04 (d, J = 8.2 Hz, 1H, $H_{Aromatic}$), 7.01 (m, 1H, $H_{Aromatic}$), 6.91 (m, 1H, $H_{Aromatic}$), 3.91 (s, 3H, OCH_3), 3.89 (s, 3H, OCH_3), 3.84-3.62 (m, 32H, H-5), 3.58-3.25 (m, 32H, H-2), 2.94 (t, J = 7.2 Hz, 2H, H-4), 2.74 (m, 4H, H-3, H-6), 2.64-2.43 (m, 26H, H-1).

^{13}C-NMR (126 MHz, D_2O) δ [ppm]: 178.00, 177.88, 176.30, 175.43, 175.36, 175.29, 175.25, 175.21, 175.17, 175.03, 148.69, 147.27, 134.63, 121.49, 112.97, 112.69, 70.12, 69.97, 69.40, 69.37, 66.91, 56.38, 56.31, 47.73, 45.75, 45.43, 39.67, 39.46, 39.39, 37.92, 37.59, 37.52, 34.73, 34.68, 31.60, 31.53, 31.50, 31.47, 31.43, 31.39, 31.34, 31.30, 31.24, 31.19, 30.82, 30.78, 30.73, 30.65, 28.60.

HR-ESI-MS: calculated mass for $C_{71}H_{125}N_{16}O_{25}$ $[M+3H]^{3+}$ 533.9662, found 533.9661.

RP-HPLC (gradient from 0% to 50% eluent B over 30 min at 25°C): t_r=11.8 min, purity 98%.

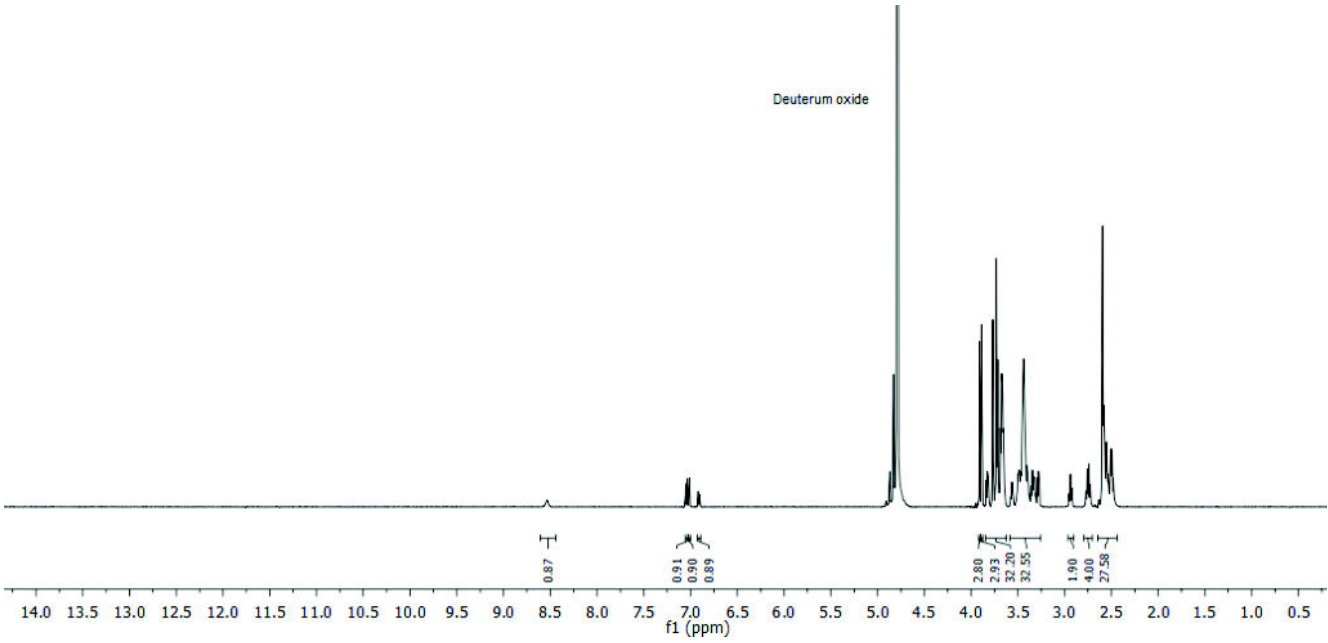

^{1}H-NMR spectrum of compound **10** protected (500 MHz, D_2O).

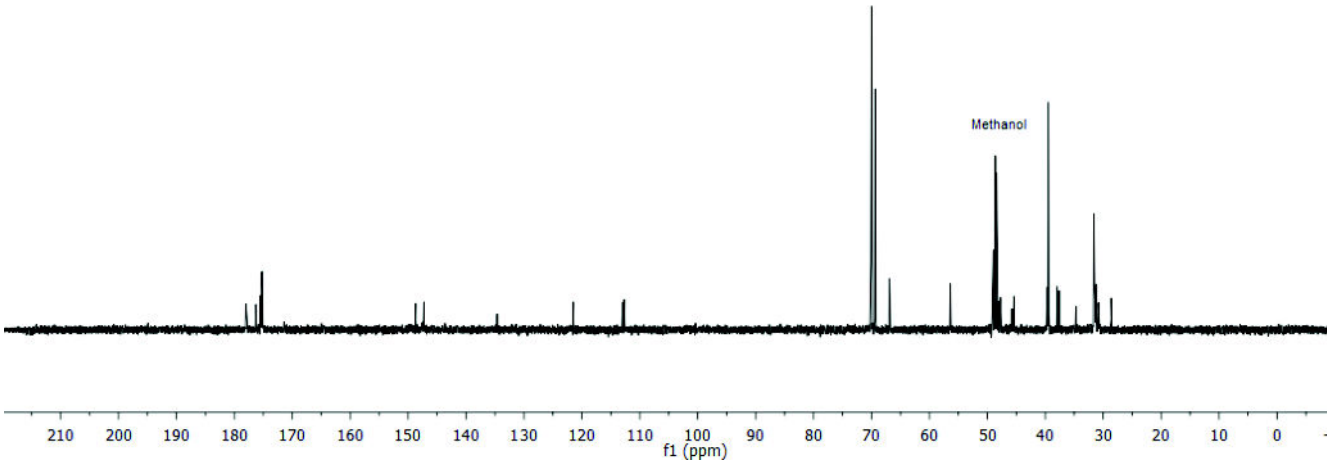

^{13}C-NMR spectrum of compound **10** protected (126 MHz, D_2O).

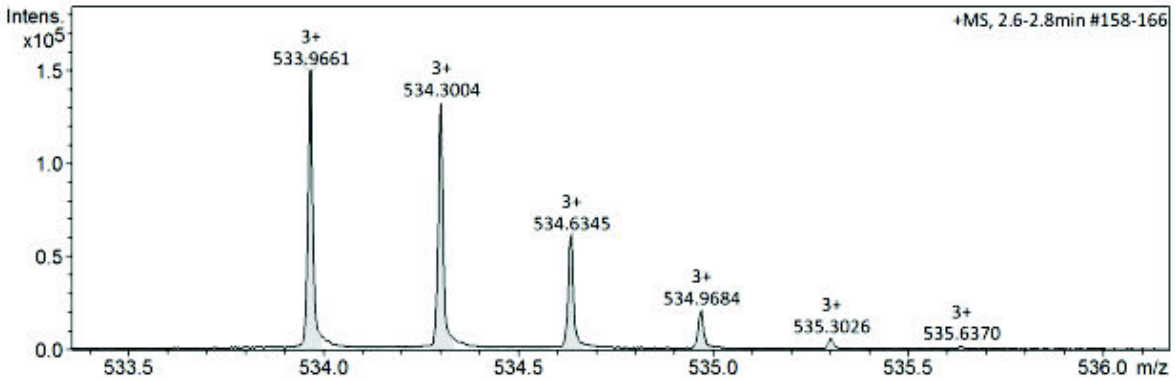

HR-ESI (ESI$^+$ Q-TOF) of compound **10** protected.

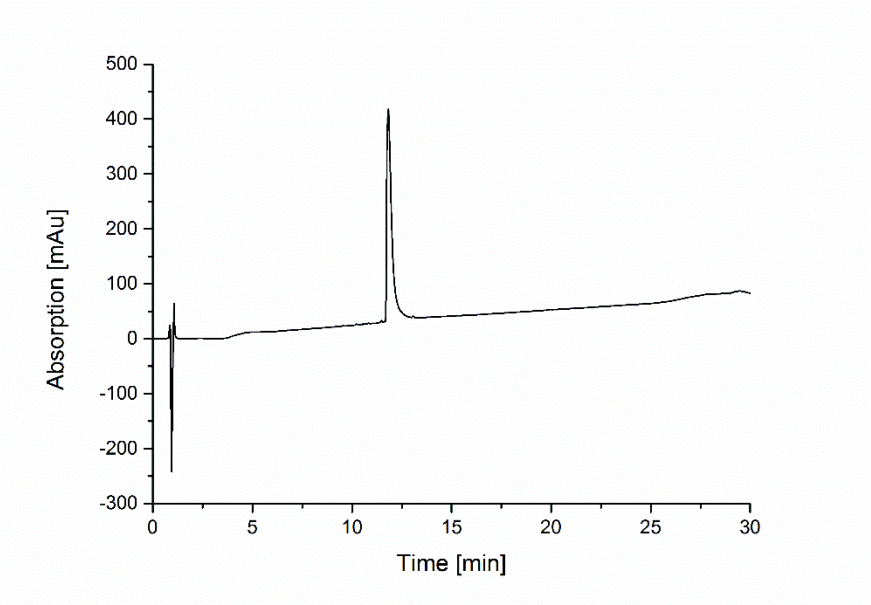

RP-HPLC chromatogram of compound **10** protected (gradient from 0% to 50% eluent B over 30 min at 25°C).

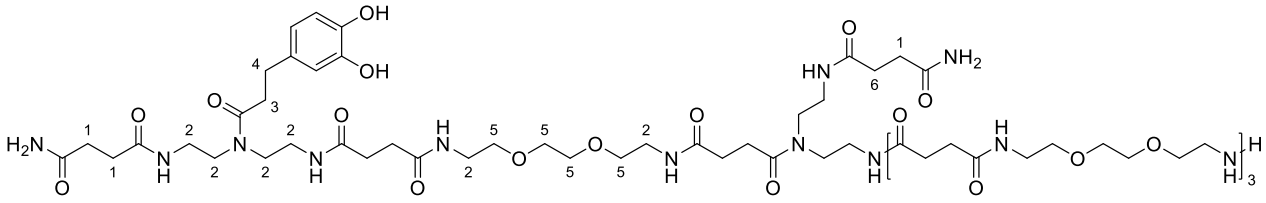

10

(**10**)

Compound **10** was obtained with a yield of 19% after deprotection, purification by preparative RP-HPLC and lyophilization.

^{1}H-NMR (500 MHz, D_2O) δ [ppm]: 8.5 (s, NH), 6.88 (d, J = 8.1 Hz, 1H, $H_{Aromatic}$), 7.82 (d, J = 2.0 Hz, 1H, $H_{Aromatic}$), 6.73 (d, J = 8.1 Hz, 2.0 Hz, 1H, $H_{Aromatic}$), 3.82-3.59 (m, 32H, H-5), 3.57-3.25 (m, 32H, H-2), 2.83 (t, J = 7.1 Hz, 2H, H-4), 2.70 (m, 4H, H-3, H-6), 2.62-2.45 (m, 26H, H-1).

^{13}C-NMR (126 MHz, D_2O) δ [ppm]: 178.01, 177.97, 176.35, 176.33, 175.41, 175.36, 175.32, 175.24, 175.21, 175.15, 144.46, 142.84, 134.05, 121.12, 116.73, 116.68, 70.10, 69.96, 69.38, 69.35, 66.88, 47.70, 45.39, 39.64, 39.43, 39.37, 37.91, 37.88, 37.58, 37.50, 34.76, 34.75, 31.61, 31.57, 31.53, 31.50, 31.45, 31.38, 31.28, 31.22, 30.93, 30.80, 30.75, 30.71, 30.66, 28.58.

HR-ESI-MS: calculated mass for $C_{69}H_{121}N_{16}O_{25}$ $[M+3H]^{3+}$ 524.6224, found 524.6222.

RP-HPLC (gradient from 0% to 50% eluent B over 30 min at 25°C): t_r=9.8 min, purity 89%.

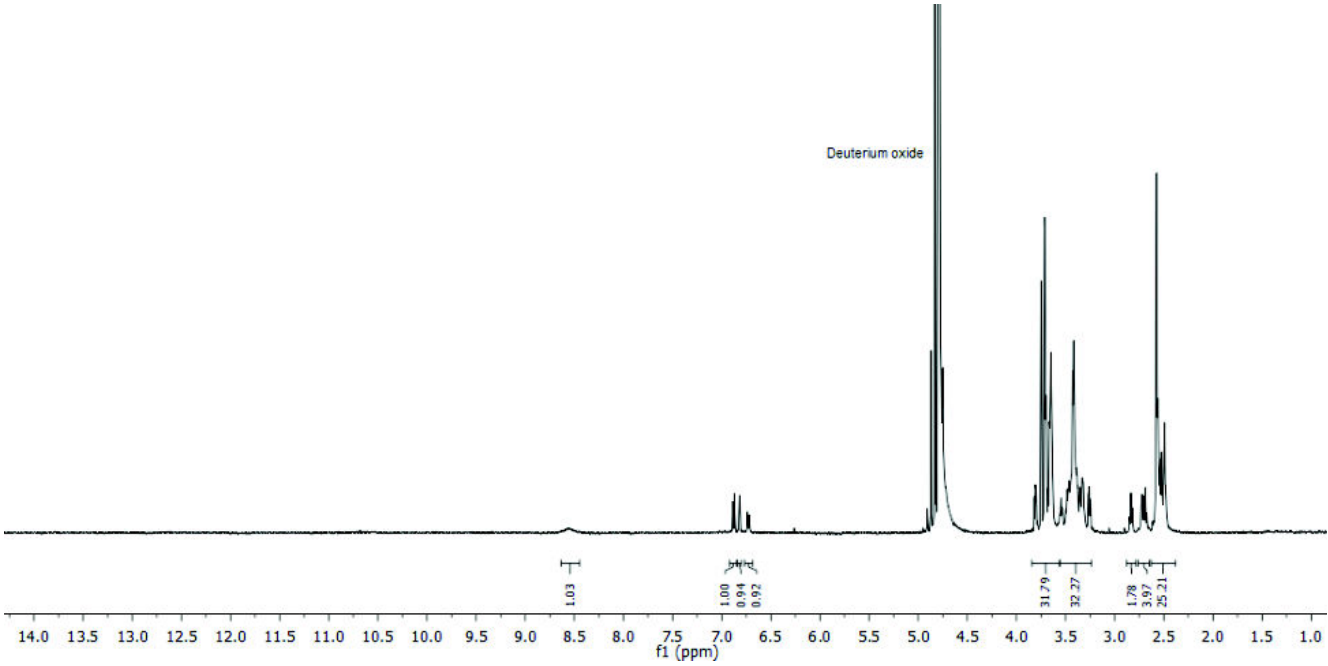

^{1}H-NMR spectrum of compound **10** (500 MHz, D_2O).

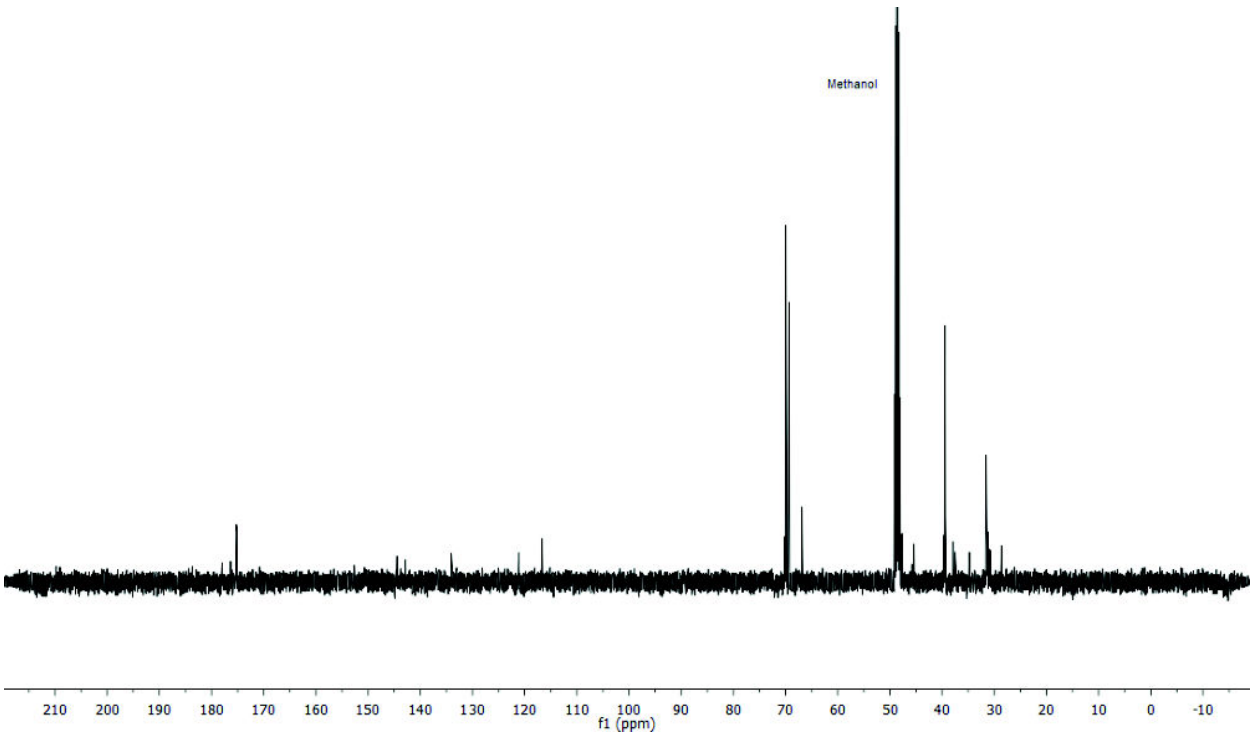

^{13}C-NMR spectrum of compound **10** (126 MHz, D_2O).

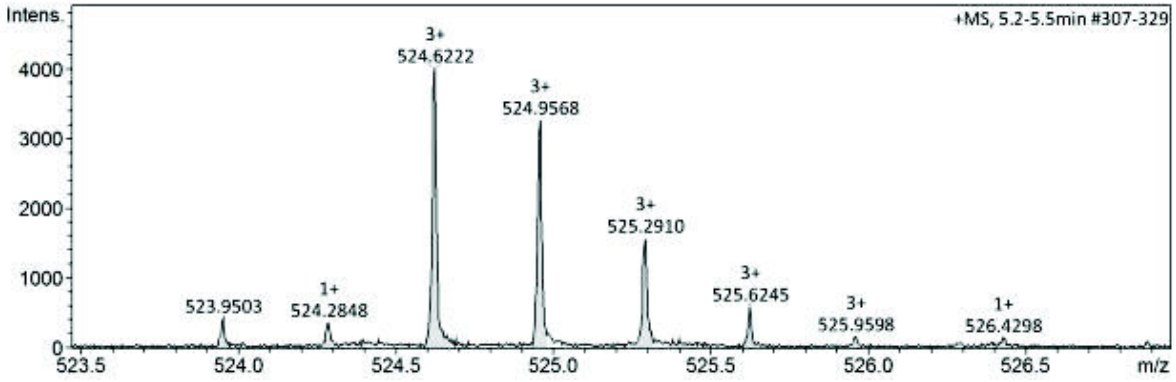

Figure 59: HR-ESI (ESI$^+$ Q-TOF) of compound **10**.

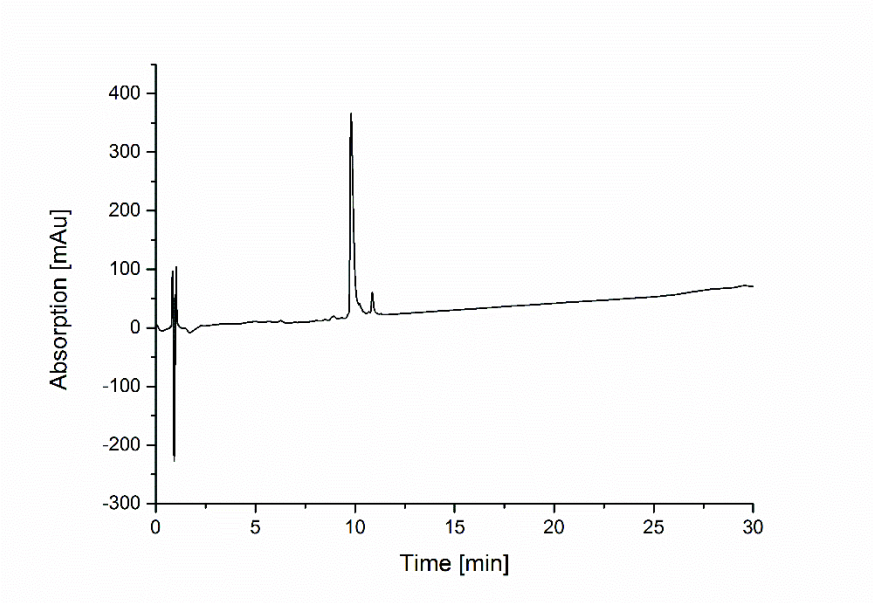

RP-HPLC chromatogram of compound **10** (gradient from 0% to 50% eluent B over 30 min at 25°C).

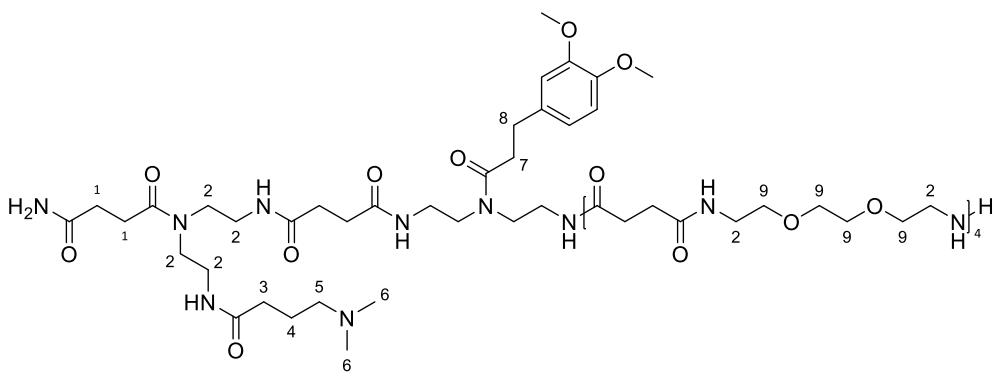

(**11**) *protected*

Supporting Information

Compound **11** protected was obtained with a yield of 72% after cleavage from solid support and lyophilization

^{1}H-NMR (500 MHz, D_2O) δ [ppm]: 8.50 (s, NH), 7.04 (d, J = 8.2 Hz, 1H, $H_{Aromatic}$), 7.01 (d, J = 2.0 Hz, 1H, $H_{Aromatic}$), 6.91 (dd, J = 8.2, 2.0 Hz, 1H, $H_{Aromatic}$), 3.91 (s, 3H, OCH_3), 3.89 (s, 3H, OCH_3), 3.75-3.52 (m, 32H, H-9), 3.49-3.18 (m, 32H, H-2), 3.10 (m, 2H, H-5), 2.86 (m, 8H, 6-H, 8-H), 2.65 (m, 4H, 3-H, 7-H), 2.55-2.27 (m, 24H, 1-H), 1.94 (m, 2H, 4-H).

^{13}C-NMR (126 MHz, D_2O) δ [ppm]: 178.62, 176.66, 175.74, 175.68, 175.66, 175.63, 175.59, 175.56, 175.5, 175.39, 171.46, 149.09, 147.67, 135.01, 121.83, 113.33, 113.07, 70.51, 70.36, 69.75, 67.29, 57.91, 56.77, 56.69, 43.62, 40.05, 39.81, 38.19, 37.95, 37.87, 35.14, 33.01, 32.88, 31.99, 31.95, 31.92, 31.84, 31.77, 31.72, 31.56, 30.93, 28.92, 28.82, 20.94.

HR-ESI-MS: calculated mass for $C_{73}H_{131}N_{16}O_{24}$ $[M+3H]^{3+}$ 538.6502, found 538.6497.

RP-HPLC (gradient from 0% to 50% eluent B over 30 min at 25°C):t_r=11.1 min, purity 92%.

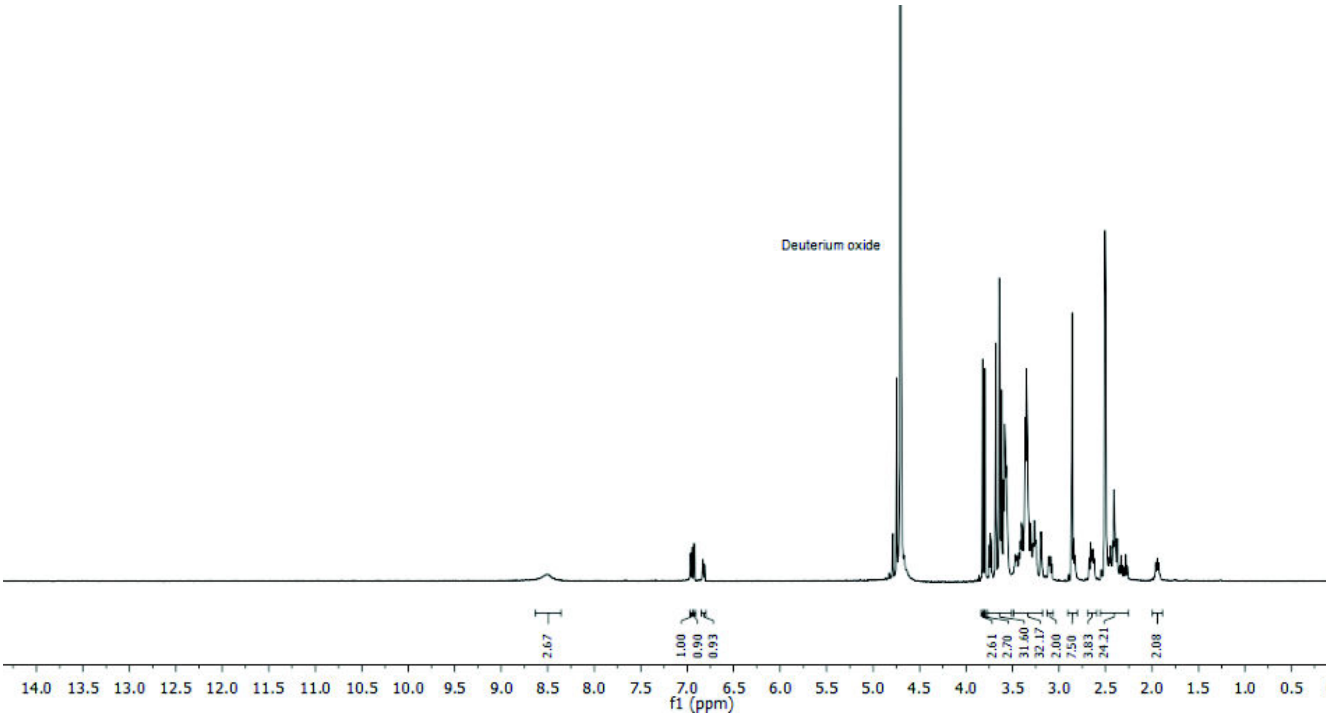

^{1}H-NMR spectrum of compound **11** protected (500 MHz, D_2O).

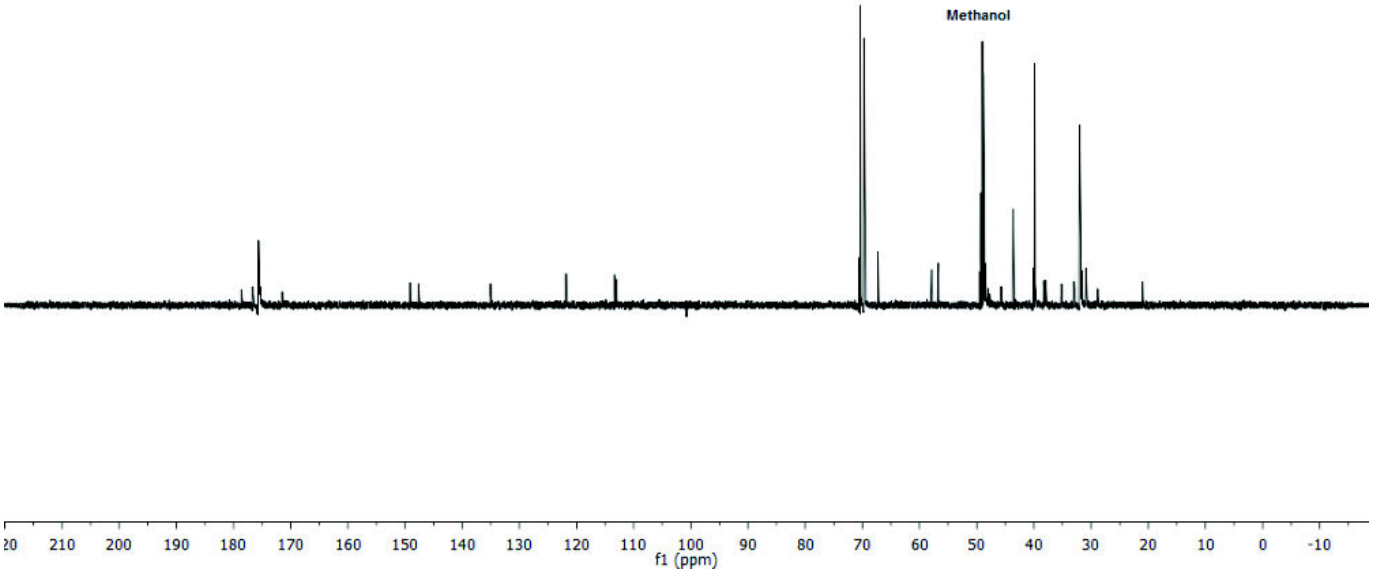

^{13}C-NMR spectrum of compound **11** protected (126 MHz, D_2O).

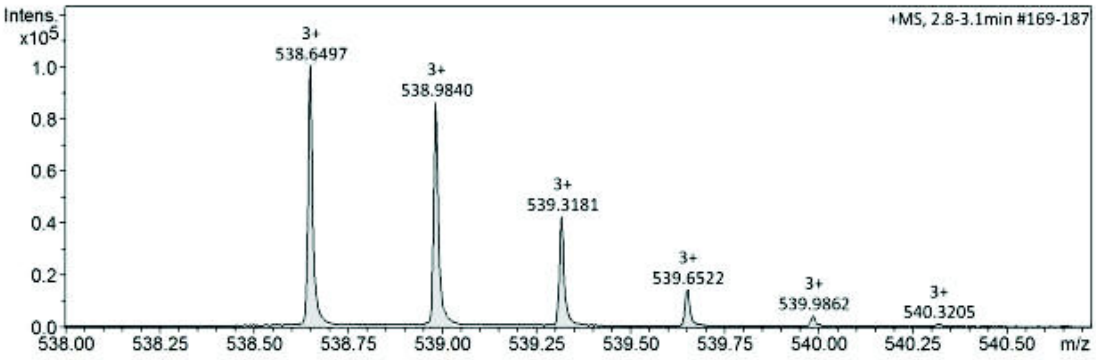

HR-ESI (ESI$^+$ Q-TOF) of compound **11** protected.

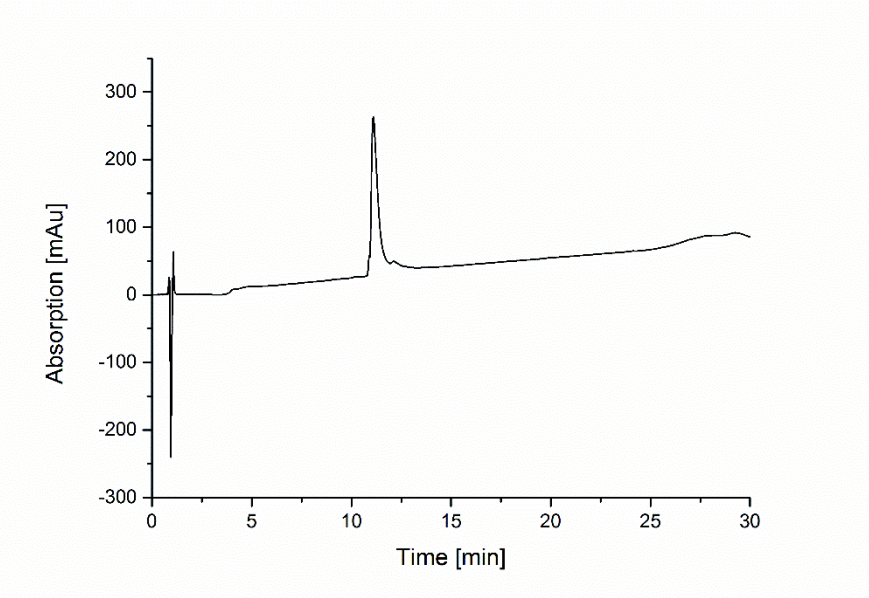

RP-HPLC chromatogram of compound **11** protected (gradient from 0% to 50% eluent B over 30 min at 25°C).

(**11**)

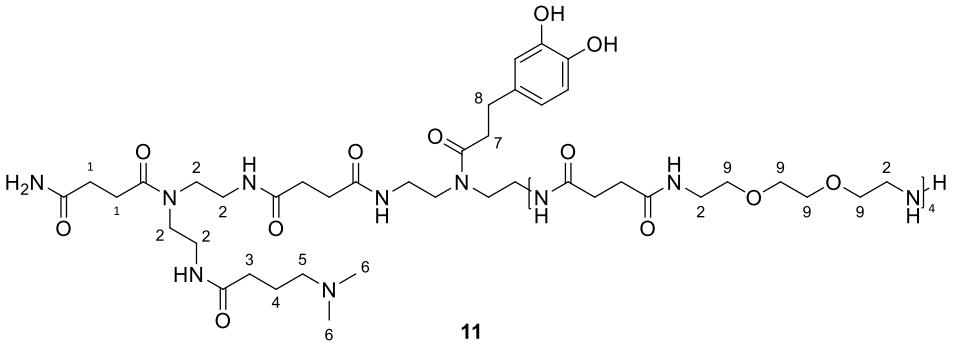

11

Compound **11** was obtained with a yield of 28% after deprotection, purification by preparative RP-HPLC and lyophilization.

^{1}H-NMR (500 MHz, D_2O) δ [ppm]: 8.43 (s, NH), 6.85 (m, 1H, $H_{Aromatic}$), 6.79 (m, 1H, $H_{Aromatic}$), 6.70 (m, 1H, $H_{Aromatic}$), 3.82-3.60 (m, 32H, H-9), 3.59-3.20 (m, 32H, H-2), 3.15 (m, 2H, H-5), 2.91 (s, 6H, H-6), 2.80 (m, 2H, H-8), 2.69 (m, 4H, H-3, H-7), 2.64-2.30 (m, 24H, H-1), 2.01 (m, 2H, 4-H).

^{13}C-NMR (126 MHz, D_2O) δ [ppm]: 178.60, 176.69, 175.73, 175.68, 175.60, 175.54, 175.49, 175.43, 175.39, 175.38, 175.36, 171.57, 144.94, 143.32, 134.42, 121.48, 117.11, 117.06, 70.53, 70.39, 69.78, 67.30, 57.93, 43.62, 40.09, 39.86, 39.79, 38.26, 37.99, 37.90, 35.24, 33.01, 32.89, 31.99, 31.95, 31.91, 31.85, 31.80, 31.75, 31.70, 31.38, 30.94, 28.93, 28.83.

HR-ESI-MS: calculated mass for $C_{71}H_{127}N_{16}O_{24}$ $[M+3H]^{3+}$ 529.3064, found 529.3056.

RP-HPLC (gradient from 0% to 50% eluent B over 30 min at 25°C): t_r=9.5 min, purity 90%.

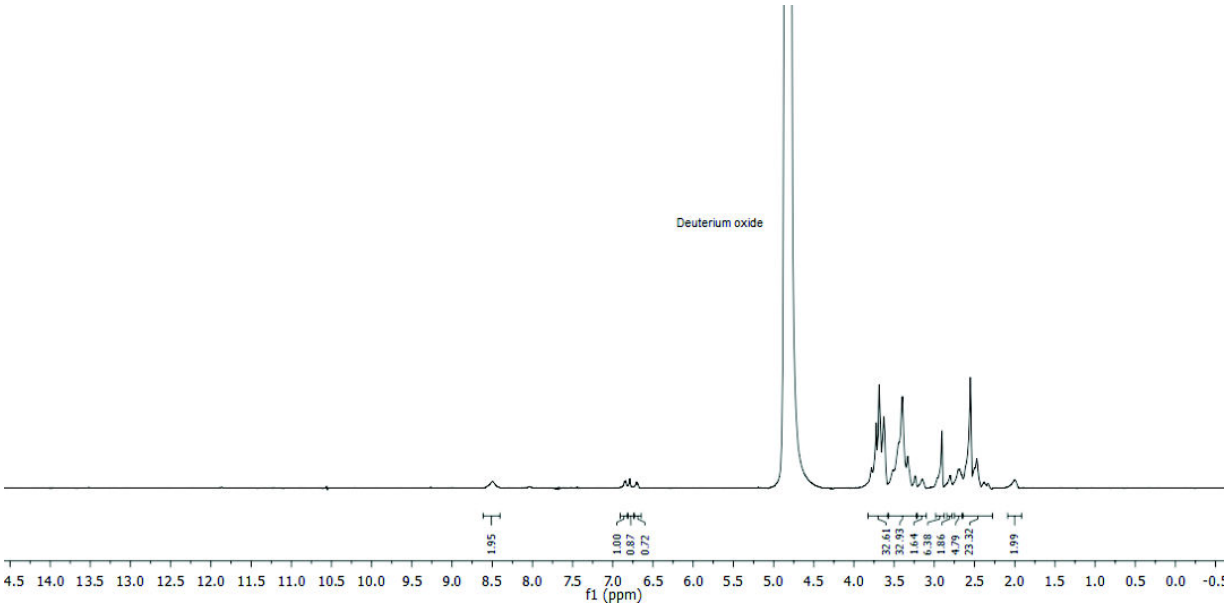

^{1}H-NMR spectrum of compound **11** (500 MHz, D_2O).

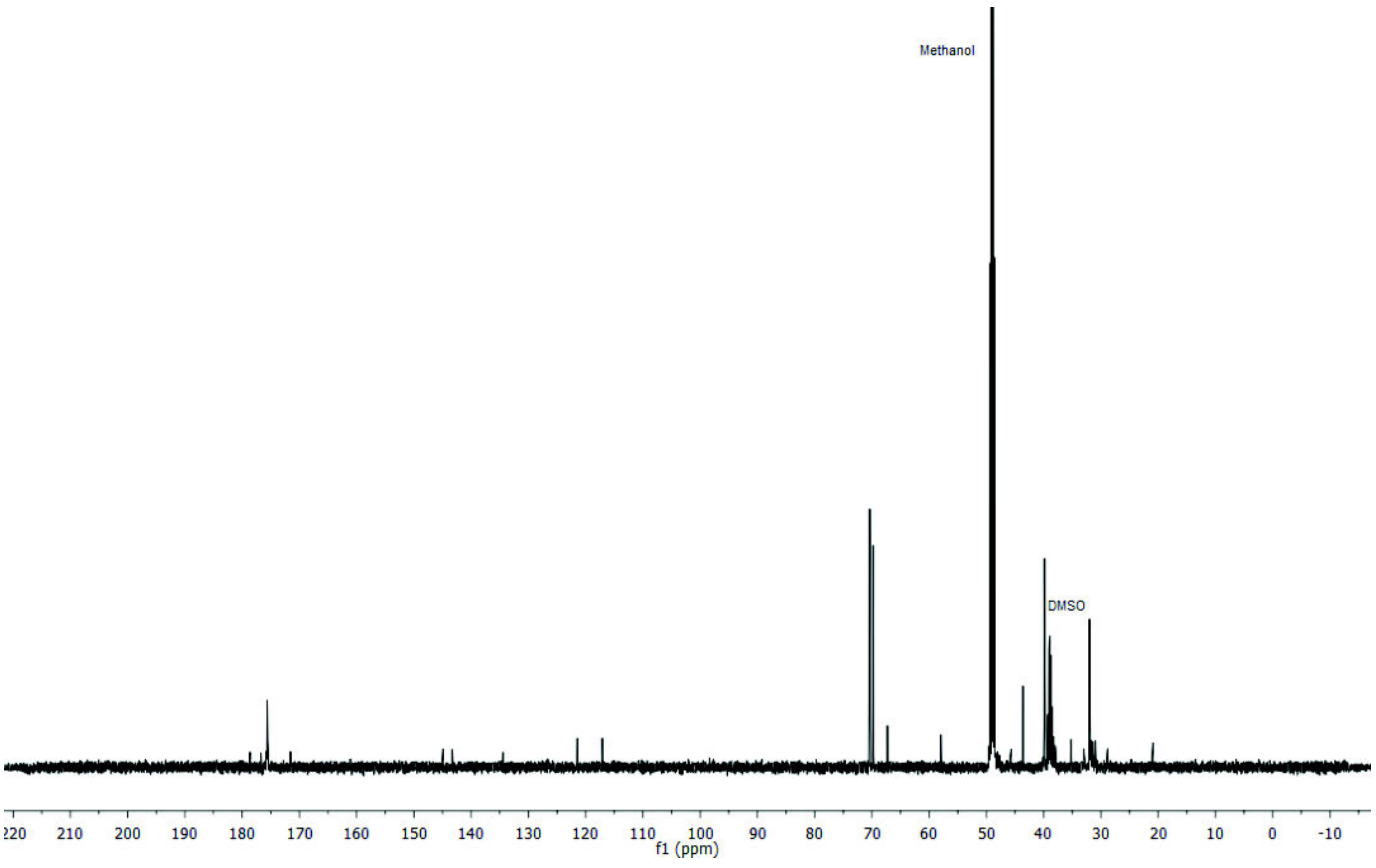

^{13}C-NMR spectrum of compound **11** (126 MHz, D_2O).

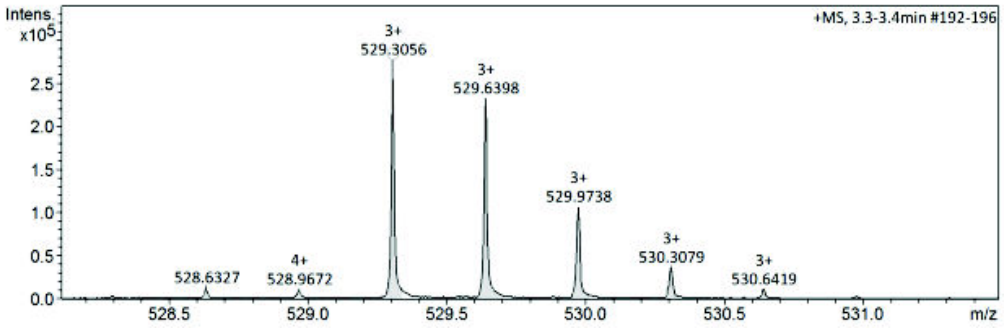

HR-ESI (ESI$^+$ Q-TOF) of compound **11**.

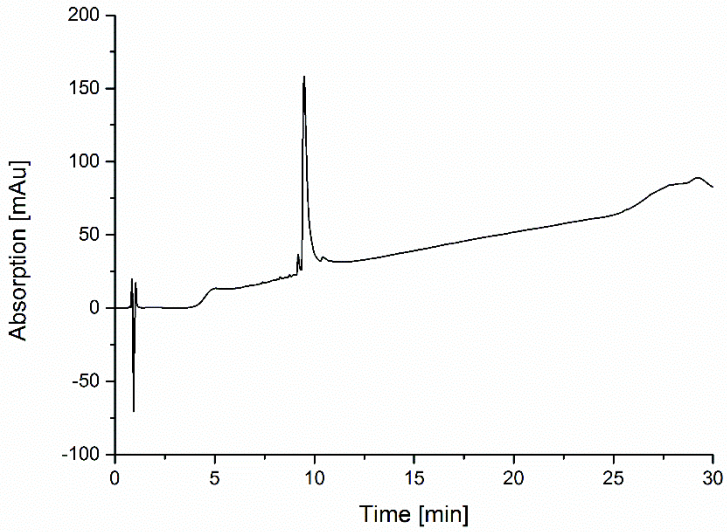

RP-HPLC chromatogram of compound **11** (gradient from 0% to 50% eluent B over 30 min at 25°C)

S5 Determination of SCP Functionalization Degrees

Oligomer Functionalization of PEG-CA-SCPs

For the functionalization of PEG-CA-SCPs with oligomers 1 mL of SCP dispersion is washed with 2-(*N*-morpholino)ethansulfonic acid (MES) buffer with a concentration of 0.1 mol L^{-1} with pH 5 via centrifugation (13500 rpm, 5 min). Afterwards, 200 µL of MES buffer is added to the particles. Additionally, 500 µL of Oligomer in MES buffer is added. The amount of Oligomer was equal to a 10 fold excess in comparison to carboxylic acid groups on the particles (see Table S5). To start the reaction 100 µL of a solution of 1-Ethyl-3-(3-dimethylaminopropyl)carbodiimide hydrochloride (EDC) with concentration 100 mg mL^{-1} in ultrapure water is added. The reaction solution is shaken for 2 h before the reaction solution was removed via centrifugation (13500 rpm, 5 min) and replaced with a fresh reaction solution. After an additional reaction time of 2 h the supernatant is removed and the particle are washed with ultrapure water via centrifugation (13500 rpm, 5 min). The functionalization degree was determined via microscope based TBO titration.

Table S5: Overview over molecular weight and amount of the oligomers that were used per reaction step for PEG-CA-SCP functionalization and the functionalization degree of the particles determined via microscope based TBO titration.

Oligomer	MW [g/mol]	Amount of oligomer per reaction step [mg]	Functionalization degree [%]
1N3N (4)	1650	3.0	88
1C3C (3)	1636	2.9	98
1D3D (5)	1622	2.9	84
1D3C (6)	1584	2.8	86
1N2C (11)	1584	2.8	87
1C3N (10)	1584	2.8	98
1D3C (7)	1570	2.8	98
1C3D (9)	1570	2.8	98
1N3D (8)	1636	2.9	98

Crotonic Acid Titration via UV-VIS Spectroscopy

The determination of carboxylic acid groups on the PEG-CA particles was done in triplicates. 1 mL of SCP dispersion was dried after exchanging the water with ethanol via centrifugation (13500 rpm, 5 min) to determine the amount of particles. To the dried particles 1 mL of TBO (toluidine blue O) solution with a concentration of 0.3125 mmol L^{-1} with a pH of 10-11 was added wrapped in aluminum foil and shaken overnight. After that the solution was centrifuged (13500 rpm, 5 min) and 0.3 mL were taken and diluted to 2 mL with sodium hydroxide solution with pH 10-11. The same procedure was done with a blank where no particles were added in the beginning. The absorption of this solution was measured via UV-VIS spectroscopy and the absorption at 633 nm was used to calculate the functionalization degree using the following equation:

$$D_{CGF} = N_R(1 - A_S/A_E)/W_{Dry}$$

Where D_{CGF} is the carboxylic acid functionalization degree, A_S and A_R are the UV-VIS absorbances of sample and reference, W_{Dry} is the dry weight of 1.0 mL SCPs, N_R is the amount of TBO in the reference in units of µmol.

Determination of oligomer functionalization degree via microscope based TBO titration

Supporting Information

For the determination of functionalization degree of oligomer functionalized SCPs 100 µL of SCP solution was washed via centrifugation (13500 rpm, 5 min) with sodium hydroxide solution pH 10-11. After removing the supernatant 125 µL of TBO solution with 0.3125 mmol L^{-1} were added, wrapped in aluminum foil and shaken overnight. Next, the TBO solution was removed and the particles were washed three times with 1 mL of sodium hydroxide solution with pH 10-11 and afterwards dissolved in 125 µL. The same procedure was done for PEG-CA particles and non-functionalized PEG particles. Next, for all particle solutions the grey value was determined for 20 particles per batch to calculate the functionalization degree as following:

$$D_{OGF} = (1 - (G_N - G_{SCP})/\Delta G_B) * 100$$

Where D_{OGF} is the oligomer functionalization degree, ΔG_B is the difference of grey values between non-functionalized and carboxylic acid functionalized SCPs ($\Delta G_B > 0$), G_N is the average grey value of non-functionalized SCPs and G_{SCP} is the average grey value of oligomer functionalized SCPs.

S6 Determination of the SCPs elastic modulus

Force-indentation measurement with a NanoWizard 2 AFM provided the elastic modulus of the SCPs. A silica bead with a raduis of 2.3 µm was glued with an epoxy glue onto a tipless, non-coated cantilever (spring constant 0.32 N/m; NanoAndMore GmbH). Several force curves were recorded from different particles and analyzed with the novel contact model developed by Glaubitz et al.[5] The model considers deformation of the object at two sites: the indentation site of the AFM probe and at the contact with the solid support. The respective deformation (δ) –force (F) dependence reads:

$$\delta(F) = \left(\frac{3F}{4E} \cdot \frac{1-\upsilon^2}{R_{AFM}^{\frac{1}{2}}}\right)^{\frac{2}{3}} + \left[\frac{3(1-\upsilon^2)\left(F + 6W\pi R_{SCP} + \sqrt{12W\pi R_{SCP}F_c(6W\pi R_{SCP})^2}\right)}{4E \cdot R_{SCP}^{\frac{1}{2}}}\right]^{\frac{2}{3}} - \left[\frac{9W\pi(1-\upsilon^2)}{E}\right]^{\frac{2}{3}} \cdot R_{SCP}^{\frac{1}{3}}$$

where E is the elastic modulus of the indented SCP, R_{SCP} its radius, υ the Poisson ratio of the SCP, W the SCP adhesion energy with the support surface and R_{AFM} the radius of the indenter. The Poisson ration was assumed to be 0.5 (volume conservation upon indentation). E and W were free fit parameters. The elastic moduli of FN SCPs were on the order of 72 kPa and their surface energy varied only marginally between 20 and 30 µJ/m^2 for the different fits.

For all SCPs except for the diamine oligomer (**4**) carrying SCPs the elastic moduli were similar, around 71.9 ± 10.5 kPa. The elastic modulus for the diamine oligomer (**4**) functionalized SCPs was 103 ± 14.4 kPa. The increase in elastic modulus for the diamine carrying SCP is probably the to an extended conformation of the of the oligomer stiffening the PEG network. But overall, the rather low variations of the elastic moduli for the different SCPs are expected due to the low density of

oligomers in the SCP. About 13.5-14.2 wt% of the SCPs material are oligomers. Due to the high SCP swelling degree the oligomer concentration within the SCP network is 11 mmol l^{-1}.

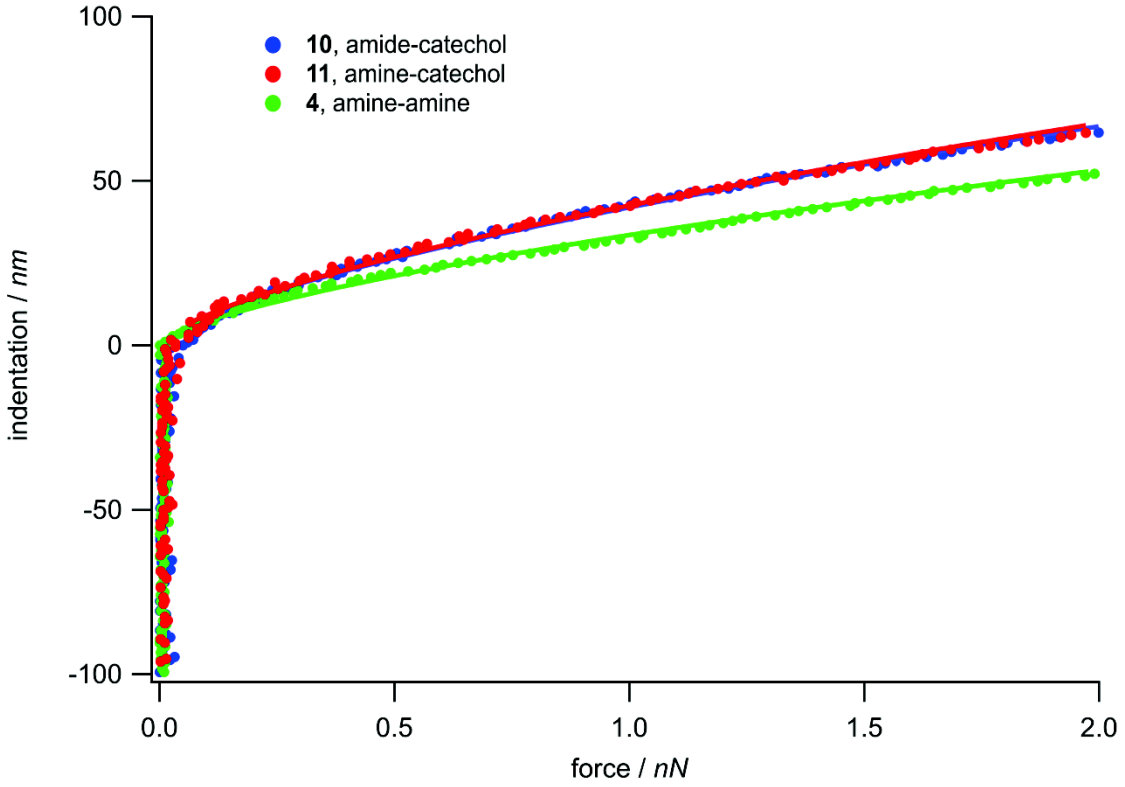

Figure S5 Typical AFM indentation-force curves for the analysis with the contact model developed by Glaubitz et al[5] The solid lines are fits to the data.

S7 Reflection Interference Contrast Microscopy (RICM) measurements

Setup

RICM on an inverted microscope (Olympus IX73) was used to obtain the contact area between the microparticles and a hard glass surface. For illumination a monochromatic (530 nm) collimated LED (Thorlabs, Germany, M530L2-C1) was used. An UPlanFL N 60x/0.90 dry objective (Olympus Corporation, Japan), additional polarizers and a quarter waveplate (Thorlabs, germany) to avoid internal reflections and a monochrome CMOS camera (DMK 33UX174, The Imaging Source Europe GmbH, Germany) were used to image the RICM patterns.

Determination of the Contact Radius

RICM was used to measure the contact radius formed by the SCPs resting on the polymer surface (Figure S2). Polarized light waves reflected from the upper glass surface (I_1) and the surface of the bead (I_2) interact to create an interference image. The intensity at a given position in the image depends on the separation $h(x)$ between the two surfaces: $I(x) = I_1 + I_2 + 2\cdot\mathrm{sqrt}(I_1 \cdot I_2)\cos[2k\cdot h(x) + \pi]$, where $k = 2\pi n/\lambda$, and n and λ are the index of refraction of water and the wavelength of the

monochromatic light, respectively. In order to detect the interference pattern, stray light was reduced by an 'antiflex' technique. This is accomplished by crossed polarizer and analyzer filter with a λ/4-plate placed between the objective lens and the analyzer.[6]

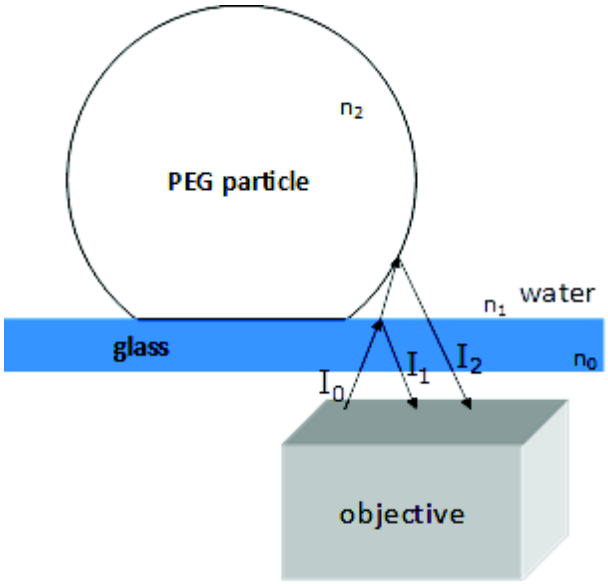

Figure S6: Schematic drawing of the RICM principle.

Correction Factors

For analysis of the RICM patterns correction factors must be determined for finite aperture and geometry effects. To obtain the correction factors, we imaged hard, non-deformable glass beads on a glass surface in RICM mode with a known size and curvature. We recorded 5 glass beads with a diameter in the range of 20-40 µm (polysciences) and extracted the intensity profile. Using the profiles, we reconstructed the shape of the beads and compared it to the known spherical shapes of the glass beads (glass bead radius *R* measured by light microscope), and determined the correction factors, see Pussak et al.[7]

Contact radius determination

To determine the contact radius *a* of the SCP on the polymer surface we reconstructed the height profile of the particles from the RICM images (see Figure S3). This was done by determining the lateral $x(i)$ positions of the i-th minima and maxima by a self-written IgorPro procedure (Wavemetrics, USA). Next, the vertical position $y(i)$ of the maxima and minima were determined by

$$y(i) = \frac{i\lambda}{4n} + c_i ,$$

where n is the refractive index and λ the wavelength. The height profile was then reconstructed by plotting $y(i)$ vs $x(i)$ and fitting the data by a circle equation representing the assumed shape of the SCP:

$$y(x) = y_0 + \sqrt{R^2 - x^2}\ .$$

where R is the independently measured SCP radius and y_0 the vertical shift of the SCP center due to flattening of the SCP upon adhesion. The fit with y_0 as the only free fit parameter intersects with the x-axis and gives the contact radius a.

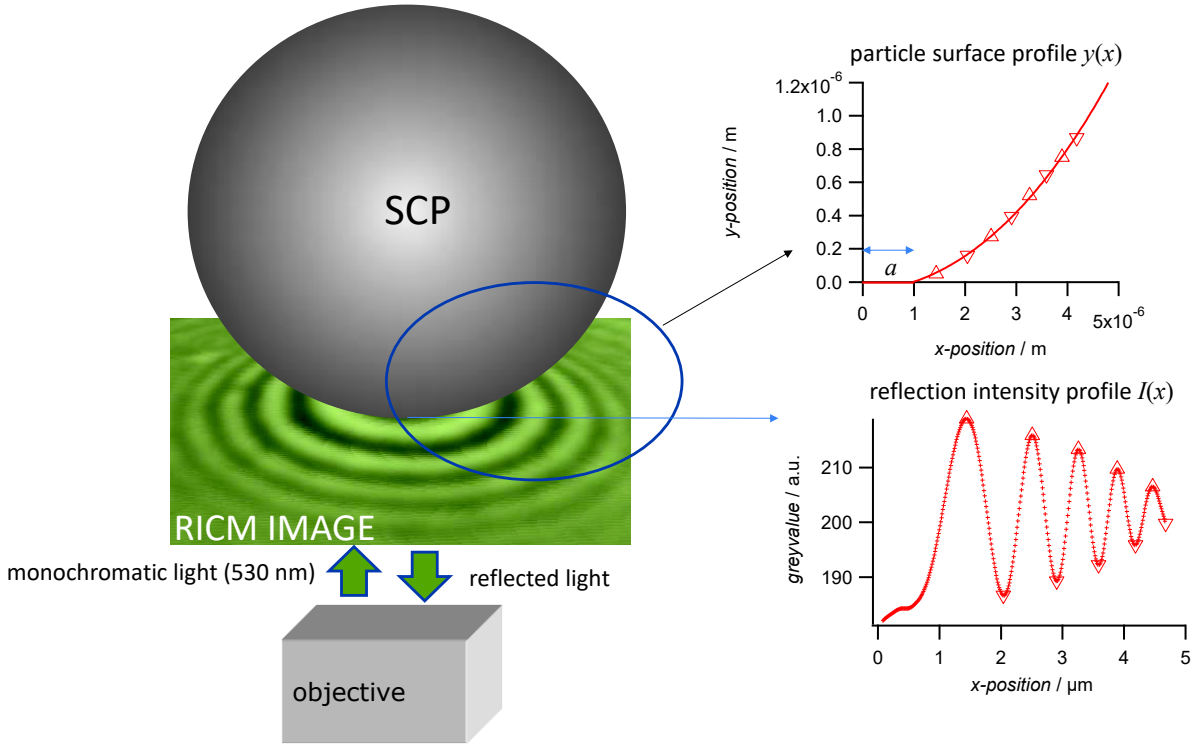

Figure S6 Left: schematic representation of the measurement setup. Bottom right: actual intensity profile of an adherent SCP showing 5 minima and 5 maxima. Top right: reconstructed surface profile of the SCP and the contact radius a at the intersection of the profile at $y = 0$.

S8 Stability of the catechol group

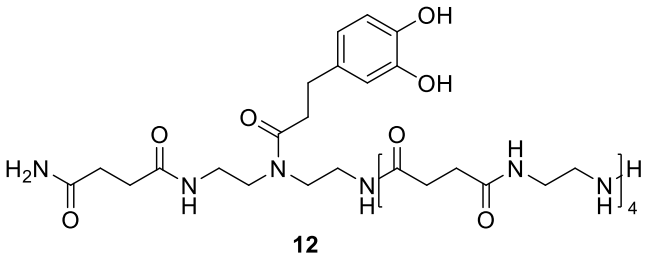

12

Compound **12** was used as a model for the investigation of the catechol stability. For this 1 mg was dissolved in 500 µl water and the mixture was measured via RP-HPLC directly after dissolving and after 12 days.

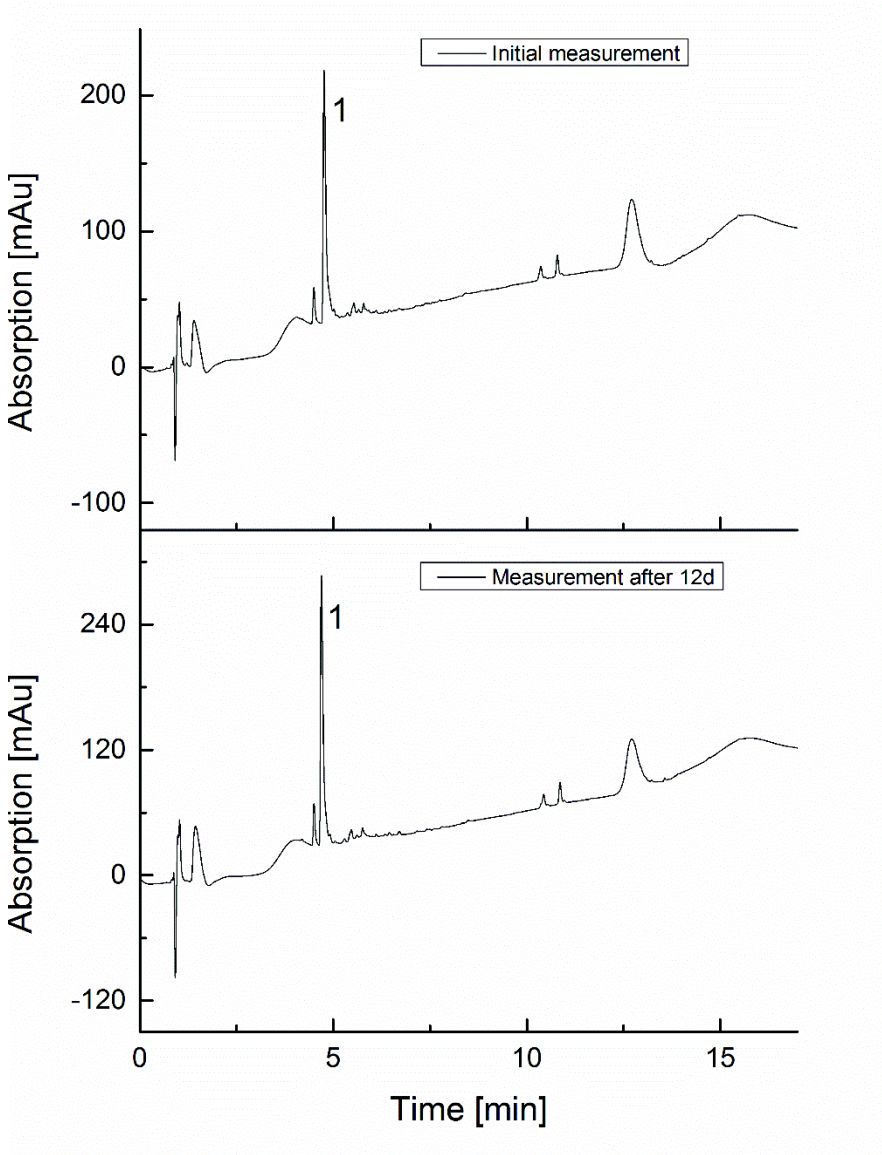

RP-HPLC of compound **12** directly after dissolving and after 12 days. Peak 1 shows compound **12**.

Supporting References

[1] C. Gerke, M. F. Ebbesen, D. Jansen, S. Boden, T. Freichel, L. Hartmann, *Biomacromolecules* **2017**, *18*, 787-796.
[2] D. Pussak, M. Behra, S. Schmidt, L. Hartmann, *Soft Matter* **2012**, *8*, 1664-1672.
[3] S. Schmidt, H. Wang, D. Pussak, S. Mosca, L. Hartmann, *Beilstein Journal of Organic Chemistry* **2015**, *11*, 720-729.
[4] D. Ponader, F. Wojcik, F. Beceren-Braun, J. Dernedde, L. Hartmann, *Biomacromolecules* **2012**, *13*, 1845-1852.
[5] M. Glaubitz, N. Medvedev, D. Pussak, L. Hartmann, s. schmidt, C. A. Helm, M. Delcea, *Soft Matter* **2014**.
[6] L. Limozin, K. Sengupta, *ChemPhysChem* **2009**, *10*, 2752-2768.
[7] D. Pussak, D. Ponader, S. Mosca, S. V. Ruiz, L. Hartmann, S. Schmidt, *Angewandte Chemie International Edition* **2013**, *52*, 6084-6087.

5.2. Temperature switchable glycopolymers and their conformation-dependent binding to receptor targets

Authors: Tanja J. Paul[#], **Alexander K. Strzelczyk**[#], Melina I. Feldhof, Stephan Schmidt

Journal: *Biomacromolecules*

Issue: **2020**, *21*, 7, 2913–2921.

Type of Paper: Full Paper

Impact Factor: 5.680 (2019)

DOI: 10.1021/acs.biomac.0c00676

Own Contribution (first author, equal contribution)

Synthesis of Poly(*N*-isopropylacrylamide-co-*N*-(2-hydroxypropyl) α-$_D$-mannopyranoside acrylamide) and Poly(*N*-isopropylacrylamide-co-*N*-ethyl α-$_D$-mannopyranoside acrylamide) polymers and precursors as well as their characterization with DSC, GPC, ^{1}H-NMR and ATR-FTIR. Determination of lower critical solution temperature and performance of turbidity measurements. Collaborative writing of the paper.

pubs.acs.org/Biomac

Article

Temperature-Switchable Glycopolymers and Their Conformation-Dependent Binding to Receptor Targets

Tanja J. Paul,[#] Alexander K. Strzelczyk,[#] Melina I. Feldhof, and Stephan Schmidt*

Cite This: *Biomacromolecules* 2020, 21, 2913−2921

Read Online

ACCESS | Metrics & More | Article Recommendations | Supporting Information

ABSTRACT: The temperature-dependent binding of copolymers from poly(*N*-isopropylacrylamide) (PNIPAM) and mannose ligands to *Escherichia coli* and concanavalin A (ConA) is determined. Through polymer analogous reactions using poly(*N*-acryloxysuccinimide) and amine-linked mannose residues with different linkers, glycopolymers are prepared with the variation of the mannose density. Quantitative adhesion inhibition assays show the inhibitory potential of the glycopolymers as a function of the mannose/NIPAM ratio and linker type above and below their lower critical solution temperature (LCST). Intriguingly, opposite temperature effects on the binding to *E. coli* and ConA are observed. While the *E. coli* inhibition is stronger above the LCST, the ConA inhibition is, in overall, weaker at elevated temperatures. When going beyond the LCST, the polymers undergo a coil-to-globule transition, forming microphases with surface-enriched hydrophilic sugar moieties exhibiting increased *E. coli* inhibition through steric shielding. However, the formation of such microphases above the LCST renders a fraction of carbohydrate ligands inaccessible,and the polymers remaining in the solution phase then have coil sizes below the minimum binding site spacing of the ConA receptor, explaining reduced ConA inhibition. Overall, these results suggest that the coil-to-globule transition of glycopolymers may induce lower or higher inhibitory potentials due to the adverse effects of steric shielding and carbohydrate ligand accessibility.

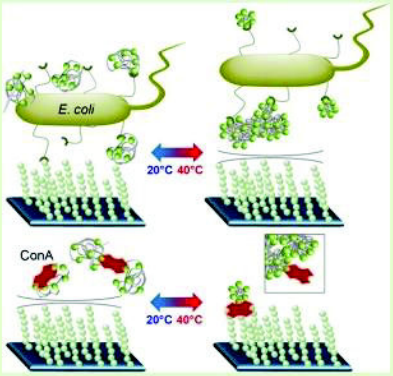

1. INTRODUCTION

Interactions between carbohydrates and proteins at the surface of cells or pathogens control numerous biological processes including infections, fertilization, recognition, or signaling.[1] Lectins, as a class of carbohydrate-binding proteins, decorate the pathogen surface and form complexes with glycans at the cell's glycocalyx, which is a critical step in the development of infectious diseases. The macromolecular glycans involved in these processes interact with the pathogen receptors through multiple weak interactions generating sufficient adhesion across large interfacial areas[2,3] to drive pathogen invasion and disease progression. The ability to suppress such lectin−glycan mediated adhesion processes by multivalent carbohydrate-presenting inhibitors has been proposed as a strategy to fight infections.[4−6] Different glycoconjugates have been developed for this purpose, for example, nanogels,[7] gold nanoparticles,[8,9] and many more, see recent reviews.[10−12] To improve the viability of such inhibitors in practice, being able to increase or decrease their affinity toward pathogens by remote stimulus is desired, for example, to first capture pathogens at a high-affinity state of the glycoconjugate and to release the pathogen afterward for diagnosis by switching to a low-affinity state. Remote stimuli could also reduce side effects, for example, by locally restricting bacterial inhibition/capture to the inflamed tissues. For a controlled drug release, many of such remotely switchable and site specific scaffolds are successfully established.[13] Recent studies also applied this concept to glyco-conjugated thermoresponsive polymers in order to control the interactions with lectins, bacteria, or viruses via temperature stimulus.[14−23] The involved polymers have a lower critical solution temperature (LCST) in the physiological temperature range. They form extended coils below the LCST and attain a collapsed globule conformation above the LCST. It was reasonably assumed that the temperature-controlled coil-to-globule transition affects the presentation of carbohydrate ligands as well as the size of the scaffold and thus controls the binding affinity of the glycoconjugate. However, the literature shows diverging results on how temperature changes affect the affinity. One the one hand, affinities toward single lectins or bacteria were shown to decrease above the LCST,[14−16] whereas other studies showed increasing affinities.[19−23] For example, using linear copolymers composed of *N*-isopropylacrylamide (NIPAM) and mannose derivatives, Pasparakis et al. showed that binding to *E. coli* and their clustering is preferred below the LCST.[14] Using a similar pair of monomers and additional cross-linkers to form

Received: April 30, 2020
Revised: June 12, 2020
Published: June 16, 2020

https://dx.doi.org/10.1021/acs.biomac.0c00676
Biomacromolecules 2020, 21, 2913−2921

microgels, we showed that the binding and clustering of *E. coli* is preferred above the LCST.[19] Other works showed no clear effect of temperature transition on the binding efficiency.[18,24,25]

This work is aimed at investigating the changes in the temperature-dependent affinity of thermosensitive glycopolymers to understand the diverging findings and interpretations in the literature. It could be argued that carbohydrate units become inaccessible at elevated temperatures when linear LCST polymers attain a globule conformation and aggregate to exhibit reduced affinity. On the other hand, the surface presentation of hydrophilic carbohydrate units of such globules might increase above the LCST when the polymer becomes hydrophobic. In addition, the size ratio between the glycopolymer ligands and their targets are shifted by the coil-to-globule transition, which may affect their inhibitory potential due to steric shielding effects.[26] Such steric shielding effects describe the ability of a large inhibitor particle to block the binding between ligands and receptor-decorated surfaces due to the steric screening of binding sites.[27] Furthermore, the multivalent binding to receptor sites could be affected because of the change of the polymer coil size when crossing the LCST, for example, when the coil size falls below the minimum binding site of the receptor. Therefore, here, we systematically vary the compositions of linear PNIPAM/mannose copolymers as well as the linkers between mannose units and the polymer backbone. We study their binding via inhibition assays with concanavalin A (ConA) as a well-known mannose-specific lectin with a minimum binding site distance of 7.2 nm[28] and *E. coli*, a bacteria binding to mannose via monovalent FimH receptors.[29] By choosing these targets with broadly different properties and systematically varying the glycopolymer mannose density and linker type, we aim to elucidate the phase transition effects in glycopolymer binding.

2. EXPERIMENTAL SECTION

2.1. Materials. α-$_D$-mannopyranoside (99%, Acros Organics), β-$_D$-galactose pentaacetate (95%, Fluorochem), acetonitrile (≥99.9%, PanReac AppliChem), *p*-toluenesulfonic acid (98%, Alfa Aesar), sodium methanolate (98%, Alfa Aesar), isopropylamine (99 + %, Alfa Aesar), acetic anhydride (≥98%, VWR Chemicals), *n*-hexane (99%, VWR Chemicals), ethyl acetate (freshly distilled), sodium bicarbonate (100%, Fisher Chemicals), Amberlite-IR120 (Fisher Chemicals), magnesium sulfate (62−70%, Fisher Chemicals), tetrahydrofuran (99.99%, Fisher Chemicals), chloroform (99.97%, Fisher Chemicals), dimethylsulfoxide (99.99%, Fisher Chemicals), allyl alcohol (≥99%, Merck KGaA), trimethylamine (>99.0%, Merck KGaA), acryloyl chloride (96%, Merck KGaA), boron trifluoride diethyl etherate (≥98%, TCI), hydrogen (Air Liquide), and *N*,*N*-dimethylformamide (≥99.8%, Biosolve Chemicals). All other chemicals were obtained from Sigma-Aldrich (Germany).

2.2. Synthesis of *N*-Acryloxysuccinimide (NAS). The synthesis of NAS was carried out according to previously published protocols.[16] In 200 mL of chloroform, *N*-Hydroxysuccinimide (14.4 g, 125 mmol) and triethylamine (22 mL, 155 mmol) were dissolved at 0 °C. Then, acryloyl chloride (10 mL, 125 mmol) was added dropwise under stirring at 0 °C for 30 min. The organic phase was washed three times with a saturated sodium bicarbonate solution and dried over sodium sulfate. The volume was then reduced to 1/3 and NAS was precipitated by the addition of *n*-hexane. The supernatant *n*-hexane was removed under reduced pressure. The remaining yellow oil was dissolved in chloroform. This cycle was repeated until the remaining oil was not soluble in chloroform giving a yield of 18.09 g (88%).^{1}H-NMR (300 MHz, $CDCl_3$) δ 6.74−6.67 (dd,$^3J_{HH}$ = 17.4, 0.8 Hz, 1H, *H1*), δ 6.38−6.27 (dd,$^3J_{HH}$ = 16.6, 10.3 Hz, 1H, *H2*), δ 6.20−6.14 (dd,$^3J_{HH}$ = 10.7, 0.8 Hz, 1H, *H3*), and δ 2.89−2.81 (s, 4H, *H4*−7) (Supporting Information S1).

2.3. Synthesis of Poly(*N*-Acryloxysuccinimide) (PNAS). NAS (15.3 g, 90 mmol) in 140 mL of *N*,*N*-dimethylformamide (DMF) was heated to 80 °C and flushed with nitrogen for 15 min. The polymerization was initiated by the addition of 4,4′-Azobis(4-cyanovaleric acid) (255.6 mg, 0.9 mmol) in 10 mL of DMF. After 20 h, the polymer was precipitated in cold tetrahydrofuran, filtered, and dried under vacuum. A brown solid was obtained (yield 12.21 g, 79%, $\bar{M}_n$ = 15,340 Da).^{1}H-NMR (600 MHz, $CDCl_3$) δ = 12.38−12.14 (s, 1H, *H9*) 3.28−3.00 (s, 1H, *H3*), 2.85−2.74 (s, 4H, *H4*−*7*), and 2.25−1.90 (s, 2H, *H1* + *2*) 1.40−1.33 (s, 3H, *H8*) (Supporting Information S2).

2.4. Synthesis of Glycopolymers. Poly(*N*-acryloxysuccinimide) (1.00 g, 65 μmol) was dissolved in 10 mL of dimethyl sulfoxide (DMSO) and heated to 40 °C. Depending on the Man/Gal functionalization degree, different amounts of amine-functionalized sugar (Supporting Information S4) were added. After 2 h of the reaction, isopropylamine (1.5 mL, 17.7 mmol) was added to react for additional 2 h. The reaction solution was cooled down and diluted with 35 mL of water and dialyzed for 48 h followed by freeze drying. The Supporting Information shows the ^{1}H NMR analysis (Supporting Information S4) and the size exclusion chromatography (Supporting Information S5) of the polymers.

2.5. Phenol Sulfuric Acid (PSA) Method. To determine the glycopolymer Man/Gal functionalization degree, the PSA method was used.[30] At first, a calibration curve was measured using a methyl α-$_D$-mannopyranoside (MeMan) dilution series in water (160, 80, 40, and 20 μM). To 125 μL of each MeMan solution, 125 μL of a 5 wt % phenol solution in water was added and vigorously shaken. Afterward, 625 μL of concentrated sulfuric acid was added, vigorously shaken, and reacted at 30 °C for 30 min. Next, the absorbance at a wavelength of 490 nm was measured. For analyzing the functionalization degree, 125 μL of the polymer solution at a known concentration was used (Supporting Information S6).

2.6. Turbidimetry. Turbidity measurements were performed with a Tepper turbidity photometer using a 1 mW laser at 630−690 nm. Solution (2 mL) of 5 mg mL^{-1} polymer in LBB was poured into a QS quartz cuvette (Hellma Analytics, Müllheim, Germany). After reaching the starting temperature of 20 °C, 0.5 mL of a ConA solution (1 mg mL^{-1}) was added followed by heating and cooling cycles from 20 to 44 °C and back to 20 °C at a temperature rate of 1 °C min^{-1}. To determine the cloud point as an indication for the LCST of the polymers, the measurement was executed without proteins (Supporting Information S9). From the transmission-temperature traces, the onset of the transmission decrease was used to determine the cloud points.

2.7. Mannan Coating. For coating the 96-well plates, mannan from *Saccharomyces cerevisiae* (Sigma-Aldrich) was used. A volume of 120 μL of mannan solution (1.2 mg mL^{-1}) in carbonate buffer (pH 9.5) was filled into each well. The plates were dried at 37 °C overnight followed by washing with PBST (PBS with 0.5 wt % Tween 20, 3 × 120 μL per well).

2.8. GFP-Based Bacterial Adhesion Inhibition Assay. The adhesion assay was carried out according to previously previous protocols.[29] For blocking nonspecific binding, each well was filled with 120 μL of 1 wt % polyvinylalcohol (22,000 g/mol) in PBS at 37 °C followed by shaking at 120 rpm for 1 h. Next, the plates were washed three times with 120 μL of PBST and one time with PBS. Then, a dilution series of the polymers was prepared and added to the well plates. The bacteria suspension (50 μL) at a concentration of 2 mg mL^{-1} (OD = 0.4) was added to the wells, and the plates were incubated for 1 h. at 100 rpm at either 20 or 40 °C. Afterward, the plates were washed three times with 120 μL of PBS and then filled with 100 μL of PBS per well. Finally, the fluorescence intensity of the adhered *E. coli* was detected at 485 nm/535 nm.

2.9. FITC−ConA Adhesion Inhibition Assay. The mannan-coated surfaces were blocked with a 5 wt % solution of bovine serum albumin in carbonate buffer (pH 9.5) by adding 120 μL of a BSA solution into each well and shaking at 120 rpm for 1 h at ambient

https://dx.doi.org/10.1021/acs.biomac.0c00676
Biomacromolecules 2020, 21, 2913−2921

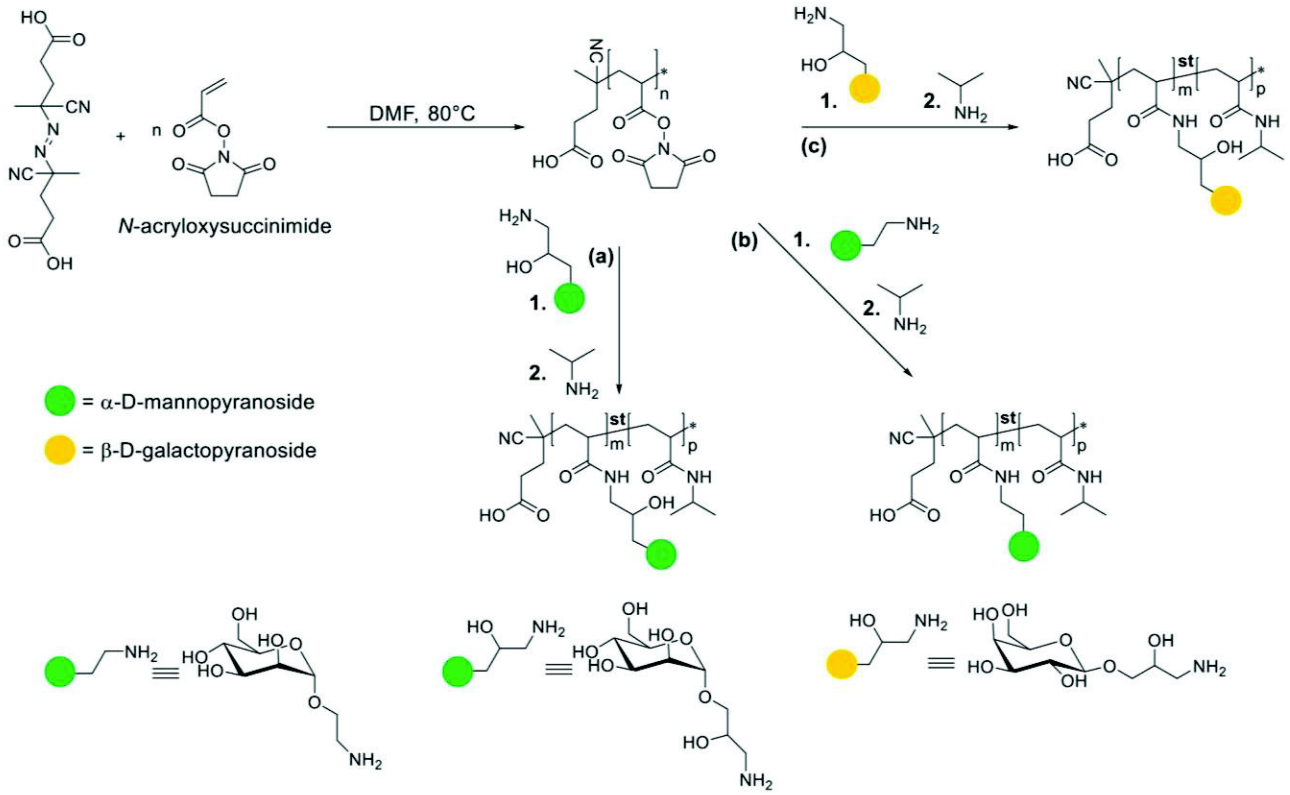

Figure 1. Schematic of the synthesis of active ester and grafting of different sugars. Grafting of (a) **ManHPL**, (b) **ManEL**, and (c) **GalHPL** at different carbohydrate densities on the polymer backbone is followed by the addition of isopropylamine to quench the remaining active esters and to form thermoresponsive NIPAM residues.

temperature. After blocking, the plates were washed three times with 120 μL of PBST and one time with 120 μL of LBB. A dilution series of the polymers was prepared on the mannan-coated, BSA-blocked well plates. A solution of FITC−ConA at a concentration of 0.1 mg mL^{-1} in LBB was prepared. The ConA solution (50 μL) was added to each well, and the plates were incubated for 1 h at 100 rpm either at 20 or at 40 °C. After 1 h, the plates were washed three times with 120 μL of LBB and filled with 100 μL of LBB per well. The fluorescence intensity of the adhered FITC−ConA was determined at 485 nm/535 nm.

3. RESULTS AND DISCUSSION

3.1. Synthesis of Thermoresponsive Glycopolymers.

The key objective of this work is to control the sugar density and linker type in thermoresponsive glycopolymers and to test the effect of these parameters on the inhibition of ConA and *E. coli* FimH receptors. Ten different polymers with varying carbohydrate densities and different linkers were prepared. For straightforward variation of the sugar densities and linker type, a polymer analogous reaction was chosen (Figure 1). By postfunctionalization of a poly(active ester), the NIPAM repeating units and the sugar ligands were introduced. First, the succinimide-based poly(active ester) was synthesized according to a previously published protocol.[16] Using free radical polymerization (FRP) with 4,4′-azobis(4-cyanovaleric acid) as the initiator, an active ester polymer poly(*N*-acryloxysuccinimide) (PNAS) was synthesized. As expected from FRP, PNAS exhibited a dispersity of 1.51 and a number average molecular weight ($\bar{M}_n$) of 15.34 kDa as determined via size exclusion chromatography (SEC) and ^{1}H-NMR. As carbohydrate ligands, varying quantities of 2-aminoethyl-α-$_D$-mannopyranoside (**ManEL**) and 3-amino-2-hydroxypropyl-α-$_D$-mannopyranoside (**ManHPL**) were then reacted with PNAS. The two carbohydrates have different linkers, where the hydroxypropyl (**HPL**) linker can be considered slightly more hydrophilic due to the added hydroxy group as compared to the ethyl (**EL**) linker. In the second reaction step, isopropylamine was added to quench the remaining active esters and to create thermoresponsive NIPAM repeating units.

The incorporation of carbohydrates into the polymers took place with an efficiency of roughly 50% (Supporting Information S4). Because of the presence of hydroxyl groups, it is possible that a fraction of sugar units was grafted to the polymer backbone via ester groups. However, as evidenced by the absence of ester groups in the IR traces (Supporting Information S7), the esters were likely substituted by isopropylamine groups in the second grafting step under basic conditions. With this synthetic route, five glycopolymers bearing **ManHPL** with carbohydrate functionalization degrees from 1 to 97% and three glycopolymers bearing **ManEL** with carbohydrate functionalization degrees from 1 to 5% were produced. As negative controls, two non-Man-presenting polymers were prepared: pure **PNIPAM** without sugar ligands and a galactose-decorated polymer via grafting of 3-amino-2-hydroxypropyl-β-$_D$-galactopyranoside (**GalHPL**). In Table 1, the synthesized polymers are listed and named by the grafted carbohydrate followed by a number representing the functionalization degree, for example, **ManHPL7** signifies 7% Man units compared to NIPAM. The polymer's carbohydrate functionalization degree was determined using a quantitative colorimetric test for sugars (PSA-test).[31,32] In addition, the degree of carbohydrate functionalization was confirmed by AT-FTIR. The glycopolymer molecular weights were determined by considering the $\bar{M}_n$ of PNAS as determined by NMR and the degree of carbohydrate functionalization as determined by

https://dx.doi.org/10.1021/acs.biomac.0c00676
Biomacromolecules 2020, 21, 2913−2921

Table 1. Glycopolymers Functionalized with Different Quantities of Man and Gal, $\bar{M}_n$, Tg, Cloud Point, and Carbohydrate Functionalization Degree are Listed[f]

polymer sample	$\bar{M}_n$ [kDa][a]	Tg [°C][b]	LCST [°C][c]	man/gal functionalization degree [μmol g^{-1}][d]
PNIPAM	10.30	117	32.6	0.0
ManHPL1	10.48	122	35.9	4.2 ± 0.1
ManHPL2	10.65	126	36.8	5.7 ± 0.1
ManHPL7	11.53	126	40.2	23 ± 0.1
ManHPL34	16.24	133	>45[e]	99 ± 0.3
ManHPL97	27.24	123	>45[e]	298 ± 2.2
ManEL1	10.45	125	35.6	3.5 ± 0.1
ManEL2	10.59	128	36.7	6.8 ± 0.1
ManEL5	11.04	129	40.8	14 ± 0.1
GalHPL3	10.83	132	40.8	8.3 ± 0.1

[a]The M_n of the active ester polymer (PNAS) was determined by ^{1}H-NMR. [b]DSC measurements. [c]Turbidimetry measurements. [d]Phenol sulfuric acid assay. [e]No sigmoidal curve, LCST could not be determined. [f]The polymers are named by the sugar type and the functionalization degree in mol %.

the PSA-test. Size exclusion chromatography confirmed the shifts in $\bar{M}_n$ with varying degrees of functionalization because of the higher molecular weight of the carbohydrates compared to isopropylamine. Also, the glass transition temperature (Tg) increased with a higher carbohydrate content (Supporting Information S8), in agreement with the literature.[33] The cloud point of the polymers, as determined by turbidimetry, increased at higher carbohydrate functionalization, in line with previous studies on carbohydrate-functionalized microgels.[19] For **ManHPL97** and **ManHPL34**, no temperature responsive behavior could be observed owing to a high carbohydrate content.

3.2. Aggregation of ConA with Glycopolymers.

Turbidity measurements were conducted to test the temperature dependent binding of the glycopolymers to ConA. ConA exhibits a homotetrameric structure at neutral pH, with four Man-binding sites and a minimum spacing of 7.2 nm.[34] All studies were carried out in lectin-binding buffer (LBB) containing Mn^{2+} and Ca^{2+} to activate the ConA-binding sites.[35−37] Since ConA exhibits four binding sites, it typically forms clusters with multivalent carbohydrates.[28,38] The formation of such ConA−glycopolymer clusters can be studied using turbidimetry in real time, due to the increase of light scattering for increased cluster sizes.[39]

The temperature-dependent cluster formation was tested under a heating/cooling rate of 1 °C min^{-1} between 20 and 44 °C. Without adding ConA, all polymers showed an increase in turbidity above the phase transition temperature as indicated by the cloud point. This can be attributed to the formation of polymer−polymer aggregates (Supporting Information S9a-h). All measurements in the absence of ConA reach the starting turbidity value after cooling back to 20 °C. However, when ConA is added to the measurement cell, the turbidity value does not return to the starting value upon cooling for all Man-bearing polymers (Figure 2). This hysteresis effect can be assigned to ConA−glycopolymer binding and the formation of clusters that dissolve only very slowly below the cloud point. Moreover, this hysteresis effect is stronger for the polymers bearing **ManEL**. This suggests that the more hydrophobic linker leads to slower cluster dissolution. For the non-carbohydrate-bearing polymers **PNIPAm** and **GalHPL3**, the hysteresis effect was not observed (Supporting Information S9). This indicates that the delayed cluster dissolution for Man-bearing polymers is because of the specific binding to ConA. In addition, when inhibiting ConA binding using an excess of MeMan, the hysteresis was significantly reduced confirming specific binding. When the cooling rate was

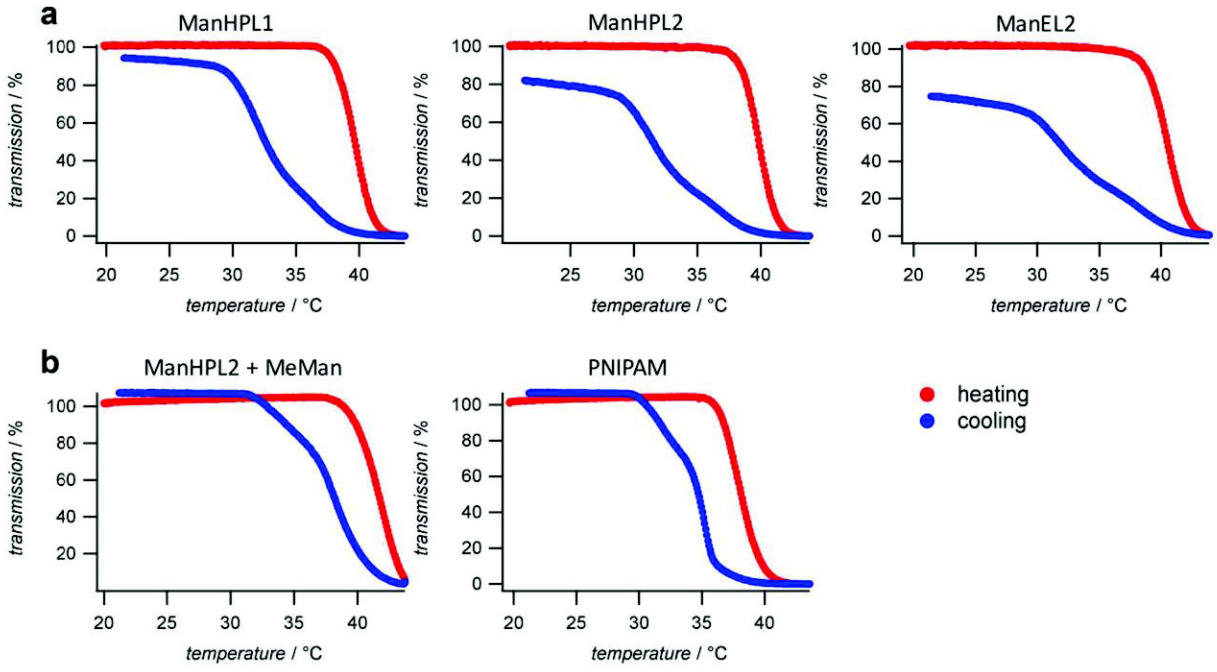

Figure 2. . Turbidity under heating (solid red line) and cooling (solid blue line) at 1 °C min^{-1} of glycopolymer samples in the presence of 0.2 mg mL^{-1} of ConA. (a) Three different Man functionalized polymers are shown. **ManEL2** showed a stronger heating/cooling hysteresis compared to **ManHPL2** as indicated by the lower transmission value after cooling. (b) Negative control samples **PNIPAm** and **GalHPL3** showed a reduced hysteresis. The inhibitor MeMan also led to a reduced hysteresis upon cooling.

https://dx.doi.org/10.1021/acs.biomac.0c00676
Biomacromolecules 2020, 21, 2913−2921

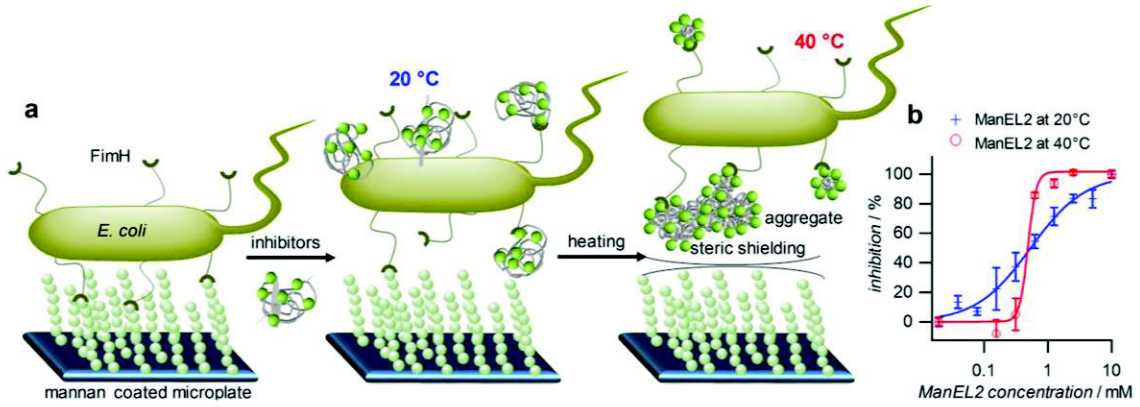

Figure 3. (a) Temperature-dependent inhibition assay of *E. coli* adhesion. GFP-tagged *E. coli* adhere to mannan-coated surfaces. After the addition of the thermoresponsive glycopolymer, the *E. coli* adhesion to the mannan-coated surface is hindered. The glycopolymers form aggregates and show an increased Man surface density above the cloud point. (b) A typical inhibition curve at 20 and 40 °C for **ManEL2**. The full set of inhibition curves is shown in Supporting Information S10.

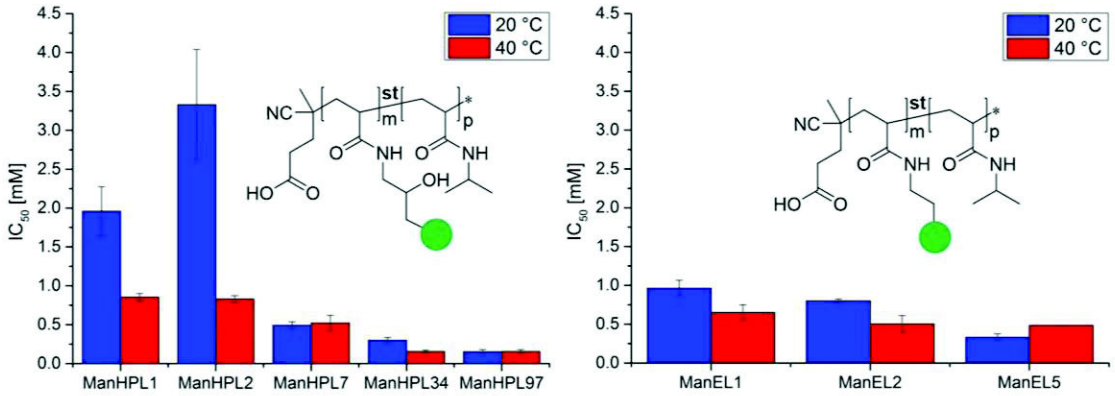

Figure 4. Left: IC_{50} values for the inhibition of *E. coli* adhesion with ManHPL glycopolymers at 20 °C (solid blue bars) and 40 °C (solid red bars). Right: IC_{50} values for ManEL glycopolymers. The IC_{50} values are related to the polymer concentration. All measurements were performed in triplicate, and averaged values and standard deviations are presented.

reduced to 0.1 °C min^{-1}, the starting turbidity value was reached indicating that glycoclusters with Man functionalization degrees up to 2% as tested are not stable below the phase transition temperature but their dissolution is merely delayed (Supporting Information S9k). Overall, these measurements confirm a statistical/additive effect on glycopolymer binding,[39] that is, an increased number of Man units leads to larger and more persistent clustering with ConA. Moreover, the linker chemistry affects the cluster dissolution, where the more hydrophilic linker in **ManHPL** leads to faster dissolution than the more hydrophobic linker in **ManEL**.

3.3. Temperature-Dependent Adhesion Inhibition of *E coli*. The turbidity measurements confirmed the phase behavior of glycopolymers. To understand the phase transition effect on the glycopolymer affinity, a quantitative binding assay is required. Therefore, we carried out adhesion inhibition assays with *E. coli*. These bacteria have evolved hairy adhesive organelles, called pili or fimbriae, allowing the bacteria to adhere to cells via carbohydrate−lectin interactions and cause infections.[40] One of the best characterized adhesive organelles is the type 1 fimbriae, which comprises various protein subunits and the monovalent α-$_D$-mannopyranoside-binding lectin FimH.[41,42]

To evaluate the Man-specific adhesion of the GFP-tagged type 1-fimbriated pKL1162 strain, we used a mannan-coated microtiter plate, added the bacteria, incubated/washed with glycopolymers, and then quantified the number of adhered bacteria using a fluorescent readout (Figure 3). In this manner, glycopolymers compete with the mannan-coated surface for binding to FimH. Therefore, by increasing the concentration of the Man-presenting glycopolymers, a larger inhibition of the bacterial adhesion was achieved as measured by a reduction of the fluorescence signal.[29] From the changes in fluorescence intensity as a function of glycopolymer concentration, the inhibitory concentration at half maximum intensity (IC_{50}) was determined. The IC_{50} value represents the concentration of glycopolymers, where 50% of the bacterial adhesion to the surface was inhibited. If the IC_{50} value is low, the inhibitory potency of the glycopolymers is high and vice versa.

At increased Man functionalization, a stronger adhesion inhibition took place (Figure 4). Furthermore, **GalHPL3** showed only a small inhibition effect due to the low affinity to FimH. Comparing **ManEL** and **ManHPL** with the same Man concentration, it can be seen that the IC_{50} values for **ManEL** are lower. This is likely due to a higher lectin-binding affinity of the hydrophobic linker, which was also observed by Lindhorst and co-workers.[43] For low Man functionalization degrees of less than 5%, an affinity increase is observed for both **ManEL** and **ManHPL** when heating to 40 °C, where **ManHPL** polymers show a stronger temperature response. At elevated Man content larger than 5%, the cloud point was above 40 °C for all polymers, indicating that coil-to-globule transition and glycopolymer aggregate formation did not take place.

https://dx.doi.org/10.1021/acs.biomac.0c00676
Biomacromolecules 2020, 21, 2913−2921

Consequently, no clear temperature dependence on the IC_{50} was observed for these polymers.

A comparison of the Hill coefficients shows the degree of cooperative binding. Cooperative binding is observed when ligand/receptor complex formation between multivalent structures yields a higher binding energy as compared to the sum of energies from single ligand/receptor subunits.[27] A Hill coefficient below 1 represents negative cooperativity, and a value higher than 1 stands for a positive cooperativity effect. For all polymers incorporating less than 5 mol % Man, the Hill coefficient increases above the cloud point, which was below 40 °C for these polymers (Table 2). This could be attributed to the formation of highly multivalent glycopolymer aggregates, which likely show an increased surface presentation of hydrophilic Man units as these polymers aggregate via hydrophobic polymer−polymer contacts. This results in increased sugar surface densities and explains the increased binding cooperativity and reduced IC_{50} values. Furthermore, the glycopolymer aggregates can block additional areas on the bacteria besides the Man-FimH binding sites, that is, steric shielding by these aggregates amplifies the inhibitory potential. The fraction of glycopolymers not incorporated into aggregates above the cloud point still attained a collapsed coil conformation since their LCST likely exceeded, thus showing improved affinity to FimH due to the increased carbohydrate surface density. For polymers with a larger Man functionalization degree (**ManHPL7**, **ManHPL34**, **ManHPL97**, and **ManEL5**), the Hill coefficients tend to decrease at elevated temperatures since their cloud point was not reached, that is, a complete coil-to-globule transition and aggregate formation did not take place.

Table 2. Hill Coefficients from the *E. coli* Adhesion Inhibition Curves

sample	hill coefficient 20 °C	hill coefficient 40 °C
ManHPL1	0.5 ± 0.2	3.1 ± 0.4
ManHPL2	0.4 ± 0.5	2.7 ± 0.2
ManHPL7	1.1 ± 0.1	2.3 ± 0.8
ManHPL34	0.6 ± 0.2	0.3 ± 1.0
ManHPL97	0.4 ± 0.2	0.1 ± 1.6
ManEL1	1.4 ± 0.2	3.3 ± 1.1
ManEL2	1.2 ± 0.4	4.0 ± 2.7
ManEL5	0.1 ± 1.4	0.7 ± 0.1

These results overall showed that the coil-to-globule transition of glycopolymers followed by aggregate formation and steric shielding increased the *E. coli* adhesion inhibition. In particular, polymers with low Man-functionalization degrees showed a large temperature response, most likely due to the high fraction of thermoresponsive repeating units. The inhibitory potential of polymers with hydrophobic linkers (**ManEL**) did not benefit significantly from the coil-to-globule transition since they exhibit strong inhibition in the coiled state below the LCST. In addition, owing to the linker hydrophobicity, the proposed effect of increased surface presentation of sugars on collapsed coils could be reduced compared to **ManHPL**.

3.4. Temperature-Dependent Adhesion Inhibition of ConA. We compared *E. coli* inhibition studies to inhibition studies employing ConA as carbohydrate-binding species (Figure 5). The microplates were again coated with mannan and the IC_{50} values were determined by incubating a glycopolymer concentration series in the presence of fluorescein-labeled ConA.

As observed in the *E. coli* assay, increasing the degree of Man functionalization reduced the IC_{50} values (Figure 6). However, the results from the inhibition assay with ConA show two striking differences compared to the *E. coli* assay. First, the majority of compounds now shows increasing IC_{50} values (weaker inhibition) when increasing the temperature above the cloud point. Second, changing the linker type does not affect the IC_{50} values significantly. Regarding the temperature dependence of the IC_{50} values, it should be noted that ConA offers four binding sites with a minimum spacing of 7.2 nm,[28,34] whereas *E. coli's* FimH receptor has only a single binding site and is positioned with a larger spacing on the bacteria.[44] Dynamic light scattering of the glycopolymers showed that their coil size was around 8 nm at 20 °C (Supporting Information S12). Therefore, the glycopolymers may bind to more than just one ConA binding site, whereas this is not possible when binding to FimH. At elevated temperatures where the polymer forms small globules, such multivalent binding to ConA is not possible leading to reduced affinity and increased IC_{50} values. In addition, an extended coil conformation at 20 °C may increase the accessibility of Man units for small receptors in solution phase (ConA), whereas a large fraction of Man units was rendered inaccessible due to aggregate formation above the cloud point temperature. The presence of microscopic aggregates thus effectively reduced the glycopolymer inhibitory potential for ConA but not for *E. coli* as the bacteria are also of microscopic size, that is, their inhibition benefits less from an excess of low-affinity glycopolymers in solution but more from similar-sized high-

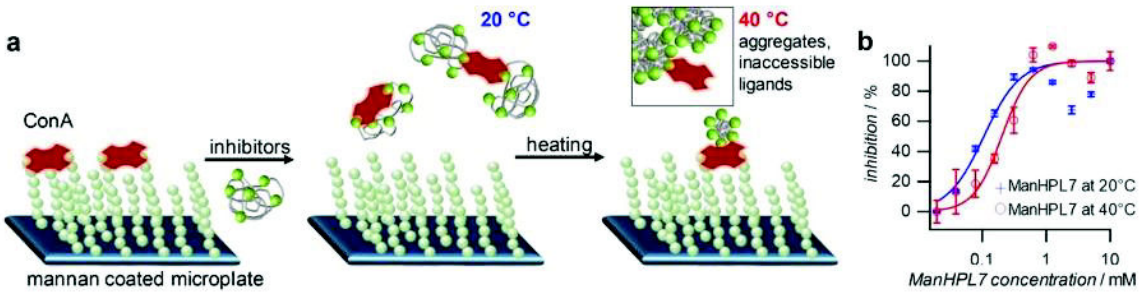

Figure 5. (a) Temperature-dependent inhibition of ConA binding. Below the phase transition temperature, the extended glycopolymer coil can bind to multiple ConA-binding sites resulting in low IC_{50} values, whereas this is not possible in the collapsed state where a large fraction of carbohydrate units is inaccessible due to aggregate formation. (b) A typical inhibition curve at 20 and 40 °C for **ManHPL7**. The full set of inhibition curves is shown in Supporting Information S11.

https://dx.doi.org/10.1021/acs.biomac.0c00676
Biomacromolecules 2020, 21, 2913−2921

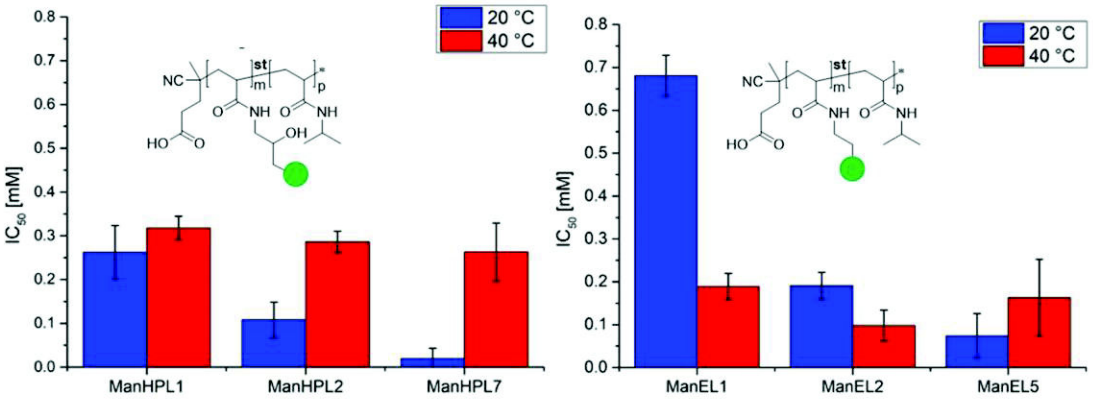

Figure 6. Left: IC_{50} values for the inhibition of ConA with ManHPL glycopolymers at 20 °C (solid blue bars) and 40 °C (solid red bars). Right: IC50 values for ManEL glycopolymers. All measurements were performed in triplicate.

affinity aggregates capable of additional steric shielding.[26] Therefore, the temperature-induced phase transition upon heating resulted in weaker inhibition of ConA but stronger inhibition of *E. coli*. Nevertheless, the proposed increase in affinity in a compact globule state at elevated temperatures due to an increased surface density of Man units should also be present in case of binding to ConA. Therefore, the thermoresponsive binding of the glycooligomers to ConA is mediated by adverse effects: (1) reduced multivalent binding and lower Man accessibility above the LCST and (2) increased binding due to increased surface density of Man in the globule state. These opposing contributions may explain the less obvious temperature trend for inhibiting ConA as compared to inhibiting *E. coli*. This is also reflected in the comparatively small changes of the Hill coefficients at 20 and 40 °C (Table 3).

Table 3. Hill Coefficients from the ConA Inhibition Curves

sample	hill coefficient at 20 °C	hill coefficient at 40 °C
ManHPL1	5.2 ± 1.4	1.8 ± 0.4
ManHPL2	1.8 ± 0.4	3.4 ± 1.0
ManHPL7	2.0 ± 0.7	2.6 ± 1.2
ManEL1	1.7 ± 0.9	3.6 ± 0.8
ManEL2	2.5 ± 0.1	2.7 ± 1.1
ManEL5	3.4 ± 1.1	4.4 ± 0.8

The reduced influence of the linker on inhibiting ConA binding when compared to *E. coli* binding could be explained by structural differences of the binding sites. The ConA binding pocket mainly has hydrophobic amino acids favoring hydrophobic linkers but at the binding pocket's entrance hydrophilic amino acids such as asparagine reside are present.[43,45] These residues may serve as hydrogen bond acceptors for the hydrophilic **HPL** linker or, alternatively, hydrogen bonding bridged by a hydration shell may increase binding to these residues.[46] In addition, such hydration layer-mediated hydrogen bonding is generally less favored at increased temperatures,[47] which reduces the inhibitory potential at elevated temperatures, as observed.

4. CONCLUSIONS

Taken together, the straightforward synthesis of a poly(active ester) followed by grafting of carbohydrates with varying linker hydrophobicity and isopropylamine to induce thermoresponsiveness was carried out. A set of polymers was synthesized with carbohydrate functionalization degrees between 1 and 97% and tested using inhibition assays with ConA and type 1-fimbriated *E. coli* at 20 and 40 °C. For polymers with low functionalization degrees of 1 to 2% reaching the cloud point at around 40 °C, a large shift in affinity was observed. Importantly, the inhibition of *E. coli* was increased under cloud point conditions, whereas the inhibition of ConA had a tendency to decrease at elevated temperatures although the results are not fully consistent in the case of ConA binding. This confirms the contradicting observations by several groups studying the effect of temperature-induced coil-to-globule transition on glycopolymer-binding affinities. We propose that the enhanced inhibition of *E. coli* binding is driven by an enhanced presentation of carbohydrate units in the collapsed state where the glycopolymers form micrometer-sized high-affinity aggregates capable of steric shielding. ConA binding is reduced above the LCST because of reduced multivalent binding and reduced accessibility of the Man units compared to the extended coil state below the phase transition temperature. This suggests that small receptor targets such as single lectins in the solution phase are bound strongly by nonaggregated multivalent glycopolymers in the extended coil conformation, whereas the inhibition of large targets with surface-anchored receptors having access only to the exterior of polymer coils (bacteria and viruses) benefits from the increased surface density of ligands and steric shielding of polymer aggregates above the phase transition temperature. Overall, these results shed light on the conformation-dependent binding of glycopolymers and provide the blueprint for the design of switchable ligand-presenting polymers for biomedical applications.

■ ASSOCIATED CONTENT

Supporting Information

The Supporting Information is available free of charge at https://pubs.acs.org/doi/10.1021/acs.biomac.0c00676.

Chemical analysis, polymer characterization, IC_{50} curves, DLS measurements, turbidity traces, and details on instrumentation, buffers, and media (PDF)

■ AUTHOR INFORMATION

Corresponding Author

Stephan Schmidt − *Institute of Organic and Macromolecular Chemistry, Heinrich-Heine-University Düsseldorf, Dusseldorf*

https://dx.doi.org/10.1021/acs.biomac.0c00676
Biomacromolecules 2020, 21, 2913−2921

40225, Germany; orcid.org/0000-0002-4357-304X; Email: stephan.schmidt@hhu.de

Authors

Tanja J. Paul − *Institute of Organic and Macromolecular Chemistry, Heinrich-Heine-University Düsseldorf, Dusseldorf 40225, Germany*

Alexander K. Strzelczyk − *Institute of Organic and Macromolecular Chemistry, Heinrich-Heine-University Düsseldorf, Dusseldorf 40225, Germany*

Melina I. Feldhof − *Institute of Organic and Macromolecular Chemistry, Heinrich-Heine-University Düsseldorf, Dusseldorf 40225, Germany*

Complete contact information is available at: https://pubs.acs.org/10.1021/acs.biomac.0c00676

Author Contributions

#T.J.P. and A.K.S. contributed equally to this paper.

Notes

The authors declare no competing financial interest.

■ ACKNOWLEDGMENTS

The authors thank Maria Breuer for performing the NMR measurements and Stephanie Scheelen for performing the SEC measurements. The authors acknowledge funding from the German Research foundation (DFG) in the project SCHM 2748/5-1.

■ REFERENCES

(1) Reitsma, S.; Slaaf, D. W.; Vink, H.; van Zandvoort, M. A.; oude Egbrink, M. G. A. The endothelial glycocalyx: composition, functions, and visualization. *Pflugers Arch.* **2007**, *454*, 345−359.

(2) Schmidt, S.; Paul, T. J.; Strzelczyk, A. K. Interactive Polymer Gels as Biomimetic Sensors for Carbohydrate Interactions and Capture−Release Devices for Pathogens. *Macromol. Chem. Phys.* **2019**, *220*, 1900323.

(3) Jacobi, F.; Camaleno de la Calle, A.; Boden, S.; Grafmuller, A.; Hartmann, L.; Schmidt, S. Multivalent Binding of Precision Glycooligomers on Soft Glycocalyx Mimicking Hydrogels. *Biomacromolecules* **2018**, *19*, 3479−3488.

(4) Ofek, I.; Hasty, D. L.; Sharon, N. Anti-adhesion therapy of bacterial diseases: prospects and problems. *FEMS. Immunol. Med. Microbiol.* **2003**, *38*, 181−191.

(5) Kiessling, L. L.; Grim, J. C. Glycopolymer probes of signal transduction. *Chem. Soc. Rev.* **2013**, *42*, 4476−4491.

(6) Hudak, J. E.; Bertozzi, C. R. Glycotherapy: new advances inspire a reemergence of glycans in medicine. *Chem. Biol.* **2014**, *21*, 16−37.

(7) Steinhilber, D.; Seiffert, S.; Heyman, J. A.; Paulus, F.; Weitz, D. A.; Haag, R. Hyperbranched polyglycerols on the nanometer and micrometer scale. *Biomaterials* **2011**, *32*, 1311−1316.

(8) Papp, I.; Sieben, C.; Ludwig, K.; Roskamp, M.; Bottcher, C.; Schlecht, S.; Herrmann, A.; Haag, R. Inhibition of influenza virus infection by multivalent sialic-acid-functionalized gold nanoparticles. *Small* **2010**, *6*, 2900−2906.

(9) Li, M. H.; Choi, S. K.; Leroueil, P. R.; Baker, J. R., Jr. Evaluating binding avidities of populations of heterogeneous multivalent ligand-functionalized nanoparticles. *ACS Nano* **2014**, *8*, 5600−5609.

(10) Bernardi, A.; Jimenez-Barbero, J.; Casnati, A.; De Castro, C.; Darbre, T.; Fieschi, F.; Finne, J.; Funken, H.; Jaeger, K. E.; Lahmann, M.; Lindhorst, T. K.; Marradi, M.; Messner, P.; Molinaro, A.; Murphy, P. V.; Nativi, C.; Oscarson, S.; Penades, S.; Peri, F.; Pieters, R. J.; Renaudet, O.; Reymond, J. L.; Richichi, B.; Rojo, J.; Sansone, F.; Schaffer, C.; Turnbull, W. B.; Velasco-Torrijos, T.; Vidal, S.; Vincent, S.; Wennekes, T.; Zuilhof, H.; Imberty, A. Multivalent glycoconjugates as anti-pathogenic agents. *Chem. Soc. Rev.* **2013**, *42*, 4709−4727.

(11) Bhatia, S.; Camacho, L. C.; Haag, R. Pathogen Inhibition by Multivalent Ligand Architectures. *J. Am. Chem. Soc.* **2016**, *138*, 8654−8666.

(12) Muller, C.; Despras, G.; Lindhorst, T. K. Organizing multivalency in carbohydrate recognition. *Chem. Soc. Rev.* **2016**, *45*, 3275−3302.

(13) Stuart, M. A.; Huck, W. T.; Genzer, J.; Muller, M.; Ober, C.; Stamm, M.; Sukhorukov, G. B.; Szleifer, I.; Tsukruk, V. V.; Urban, M.; Winnik, F.; Zauscher, S.; Luzinov, I.; Minko, S. Emerging applications of stimuli-responsive polymer materials. *Nat. Mater.* **2010**, *9*, 101−113.

(14) Pasparakis, G.; Cockayne, A.; Alexander, C. Control of bacterial aggregation by thermoresponsive glycopolymers. *J. Am. Chem. Soc.* **2007**, *129*, 11014−11015.

(15) Mahon, C. S.; Wildsmith, G. C.; Haksar, D.; de Poel, E.; Beekman, J. M.; Pieters, R. J.; Webb, M. E.; Turnbull, W. B. A 'catch-and-release' receptor for the cholera toxin. *Faraday Discuss.* **2019**, *219*, 112−127.

(16) Dalier, F.; Eghiaian, F.; Scheuring, S.; Marie, E.; Tribet, C. Temperature-Switchable Control of Ligand Display on Adlayers of Mixed Poly(lysine)-g-(PEO) and Poly(lysine)-g-(ligand-modified poly-N-isopropylacrylamide). *Biomacromolecules* **2016**, *17*, 1727−1736.

(17) Tang, J. S. J.; Rosencrantz, S.; Tepper, L.; Chea, S.; Klopzig, S.; Kruger-Genge, A.; Storsberg, J.; Rosencrantz, R. R. Functional Glyco-Nanogels for Multivalent Interaction with Lectins. *Molecules* **2019**, *24*, 22.

(18) Siirila, J.; Hietala, S.; Ekholm, F. S.; Tenhu, H. Glucose and Maltose Surface-Functionalized Thermoresponsive Poly(N-Vinylcaprolactam) Nanogels. *Biomacromolecules* **2020**, *21*, 955−965.

(19) Paul, T. J.; Rubel, S.; Hildebrandt, M.; Strzelczyk, A. K.; Spormann, C.; Lindhorst, T. K.; Schmidt, S. Thermosensitive Display of Carbohydrate Ligands on Microgels for Switchable Binding of Proteins and Bacteria. *ACS. Appl. Mater. Interfaces* **2019**, *11*, 26674−26683.

(20) Vasani, R. B.; Janardanan, N.; Prieto-Simon, B.; Cifuentes-Rius, A.; Bradley, S. J.; Moore, E.; Kraus, T.; Voelcker, N. H. Microwave Heating of Poly(N-isopropylacrylamide)-Conjugated Gold Nanoparticles for Temperature-Controlled Display of Concanavalin A. *ACS. Appl. Mater. Interfaces* **2015**, *7*, 27755−27764.

(21) Wang, Y.; Kotsuchibashi, Y.; Liu, Y.; Narain, R. Study of bacterial adhesion on biomimetic temperature responsive glycopolymer surfaces. *ACS. Appl. Mater. Interfaces* **2015**, *7*, 1652−1661.

(22) Won, S.; Hindmarsh, S.; Gibson, M. I. Triggerable Multivalent Glyconanoparticles for Probing Carbohydrate-Carbohydrate Interactions. *ACS Macro. Lett.* **2018**, *7*, 178−183.

(23) Won, S.; Richards, S. J.; Walker, M.; Gibson, M. I. Externally controllable glycan presentation on nanoparticle surfaces to modulate lectin recognition. *Nanoscale Horiz.* **2017**, *2*, 106−109.

(24) Hoshino, Y.; Nakamoto, M.; Miura, Y. Control of protein-binding kinetics on synthetic polymer nanoparticles by tuning flexibility and inducing conformation changes of polymer chains. *J. Am. Chem. Soc.* **2012**, *134*, 15209−15212.

(25) Tang, J. S. J.; Rosencrantz, S.; Tepper, L.; Chea, S.; Klöpzig, S.; Krüger-Genge, A.; Storsberg, J.; Rosencrantz, R. R. Functional Glyco-Nanogels for Multivalent Interaction with Lectins. *Molecules* **2019**, *24*, 1865.

(26) Vonnemann, J.; Liese, S.; Kuehne, C.; Ludwig, K.; Dernedde, J.; Bottcher, C.; Netz, R. R.; Haag, R. Size dependence of steric shielding and multivalency effects for globular binding inhibitors. *J. Am. Chem. Soc.* **2015**, *137*, 2572−2579.

(27) Mammen, M.; Choi, S. K.; Whitesides, G. M. Polyvalent interactions in biological systems: Implications for design and use of multivalent ligands and inhibitors. *Angew. Chem. Int. Ed.* **1998**, *37*, 2755−2794.

(28) Wittmann, V. Structural investigation of multivalent carbohydrate-protein interactions using synthetic biomolecules. *Curr. Opin. Chem. Biol.* **2013**, *17*, 982−989.

(29) Hartmann, M.; Horst, A. K.; Klemm, P.; Lindhorst, T. K. A kit for the investigation of live Escherichia coli cell adhesion to glycosylated surfaces. *Chem. Commun.* **2010**, *46*, 330−332.
(30) Gerchakov, S. M.; Hatcher, P. G. Improved Technique for Analysis of Carbohydrates in Sediments. *Limnol. Oceanogr. Lett.* **1972**, *17*, 938−943.
(31) DuBois, M.; Gilles, K. A.; Hamilton, J. K.; Rebers, P. A.; Smith, F. Colorimetric Method for Determination of Sugars and Related Substances. *Anal. Chem.* **1956**, *28*, 350−356.
(32) Boden, S.; Wagner, K. G.; Karg, M.; Hartmann, L. Presenting Precision Glycomacromolecules on Gold Nanoparticles for Increased Lectin Binding. *Polymer* **2017**, *9*, 716.
(33) Bordegé, V.; Muñoz-Bonilla, A.; León, O.; Sánchez-Chaves, M.; Cuervo-Rodríguez, R.; Fernández-García, M. Glycopolymers with glucosamine pendant groups: Copolymerization, physico-chemical and interaction properties. *React. Funct. Polym.* **2011**, *71*, 1−10.
(34) Wittmann, V.; Pieters, R. J. Bridging lectin binding sites by multivalent carbohydrates. *Chem. Soc. Rev.* **2013**, *42*, 4492−4503.
(35) Becker, J. W.; Reeke, G. N., Jr.; Cunningham, B. A.; Edelman, G. M. New evidence on the location of the saccharide-binding site of concanavalin A. *Nature* **1976**, *259*, 406−409.
(36) Bryce, R. A.; Hillier, I. H.; Naismith, J. H. Carbohydrate-protein recognition: molecular dynamics simulations and free energy analysis of oligosaccharide binding to concanavalin A. *Biophys. J.* **2001**, *81*, 1373−1388.
(37) Dam, T. K.; Brewer, C. F. Thermodynamic studies of lectin-carbohydrate interactions by isothermal titration calorimetry. *Chem. Rev.* **2002**, *102*, 387−430.
(38) Lundquist, J. J.; Toone, E. J. The cluster glycoside effect. *Chem. Rev.* **2002**, *102*, 555−578.
(39) Gestwicki, J. E.; Cairo, C. W.; Strong, L. E.; Oetjen, K. A.; Kiessling, L. L. Influencing receptor-ligand binding mechanisms with multivalent ligand architecture. *J. Am. Chem. Soc.* **2002**, *124*, 14922−14933.
(40) Sperling, O.; Fuchs, A.; Lindhorst, T. K. Evaluation of the carbohydrate recognition domain of the bacterial adhesin FimH: Design, synthesis and binding properties of mannoside ligands. *Org. Biomol. Chem.* **2006**, *4*, 3913−3922.
(41) Knight, S. D.; Bouckaert, J. Structure, function, and assembly of type 1 fimbriae. *Topics Curr. Chem.* **2009**, *288*, 67−107.
(42) Cecioni, S.; Imberty, A.; Vidal, S. Glycomimetics versus multivalent glycoconjugates for the design of high affinity lectin ligands. *Chem. Rev.* **2015**, *115*, 525−561.
(43) Igde, S.; Roblitz, S.; Muller, A.; Kolbe, K.; Boden, S.; Fessele, C.; Lindhorst, T. K.; Weber, M.; Hartmann, L. Linear Precision Glycomacromolecules with Varying Interligand Spacing and Linker Functionalities Binding to Concanavalin A and the Bacterial Lectin FimH. *Macromol. Biosci.* **2017**, *17*, 1700198.
(44) Mortezaei, N.; Singh, B.; Zakrisson, J.; Bullitt, E.; Andersson, M. Biomechanical and structural features of CS2 fimbriae of enterotoxigenic Escherichia coli. *Biophys. J.* **2015**, *109*, 49−56.
(45) Sanders, D. A.; Moothoo, D. N.; Raftery, J.; Howard, A. J.; Helliwell, J. R.; Naismith, J. H. The 1.2 A resolution structure of the Con A-dimannose complex. *J. Mol. Biol.* **2001**, *310*, 875−884.
(46) Loris, R.; Stas, P. P.; Wyns, L. Conserved waters in legume lectin crystal structures. The importance of bound water for the sequence-structure relationship within the legume lectin family. *J. Biol. Chem.* **1994**, *269*, 26722−26733.
(47) Lemieux, R. U. How Water Provides the Impetus for Molecular Recognition in Aqueous Solution. *Acc. Chem. Res.* **1996**, *29*, 373−380.

https://dx.doi.org/10.1021/acs.biomac.0c00676
Biomacromolecules 2020, 21, 2913−2921

Supporting Information

Temperature switchable glycopolymers and their conformation-dependent binding to receptor targets

Tanja J. Paul[‡], Alexander K. Strzelczyk[‡], Melina I. Feldhof, and Stephan Schmidt[*]

[1]Institute of Organic and Macromolecular Chemistry, Heinrich-Heine-University Düsseldorf, Universitätsstraße 1, 40225 Dusseldorf, Germany,

Email: Stephan Schmidt – stephan.schmidt@hhu.de

Contents

S1 Synthesis of *N*-acryloxysuccinimide

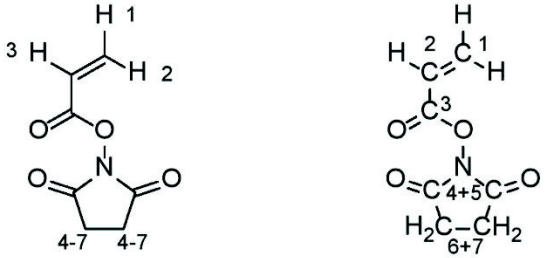

Scheme S1: Structure of monomer *N*-acryloxysuccinimide with numbering of protons (left) and carbons (right).

^{1}H-NMR (600 MHz, $CDCl_3$) δ 6.74 - 6.67 (dd, $^{3}J_{HH}$ = 17.4, 0.8 Hz, 1H, *H1*), δ 6.38 - 6.27 (dd, $^{3}J_{HH}$ = 16.6, 10.3 Hz, 1H, *H2*), δ 6.20 - 6.14 (dd, $^{3}J_{HH}$ = 10.7, 0.8 Hz, 1H, *H3*), δ 2.89 - 2.81 (s, 4H, *H4-7*).

^{13}C-NMR (600 MHz, $CDCl_3$) δ 169,17 ($C_{quart.}$, 1C, *C3*), δ 161,18 ppm ($C_{quart.}$, 2C, *C4+5*), δ 136,33 (CH_2, 1C, *C1*), δ 123,08 (CH, 1C, *C2*), δ 25,75 (CH_2, 2C, *C6+7*).

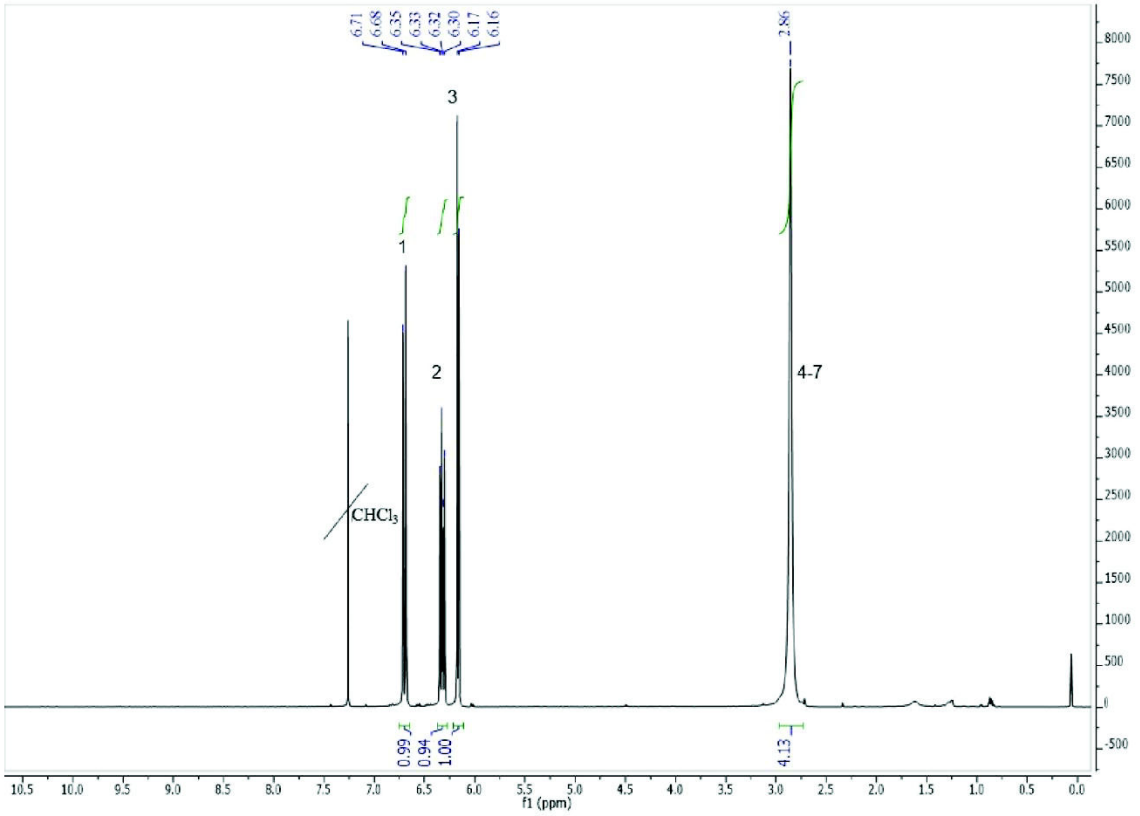

Figure S1a: ^{1}H-NMR (600 MHz, $CDCl_3$) of NAS.

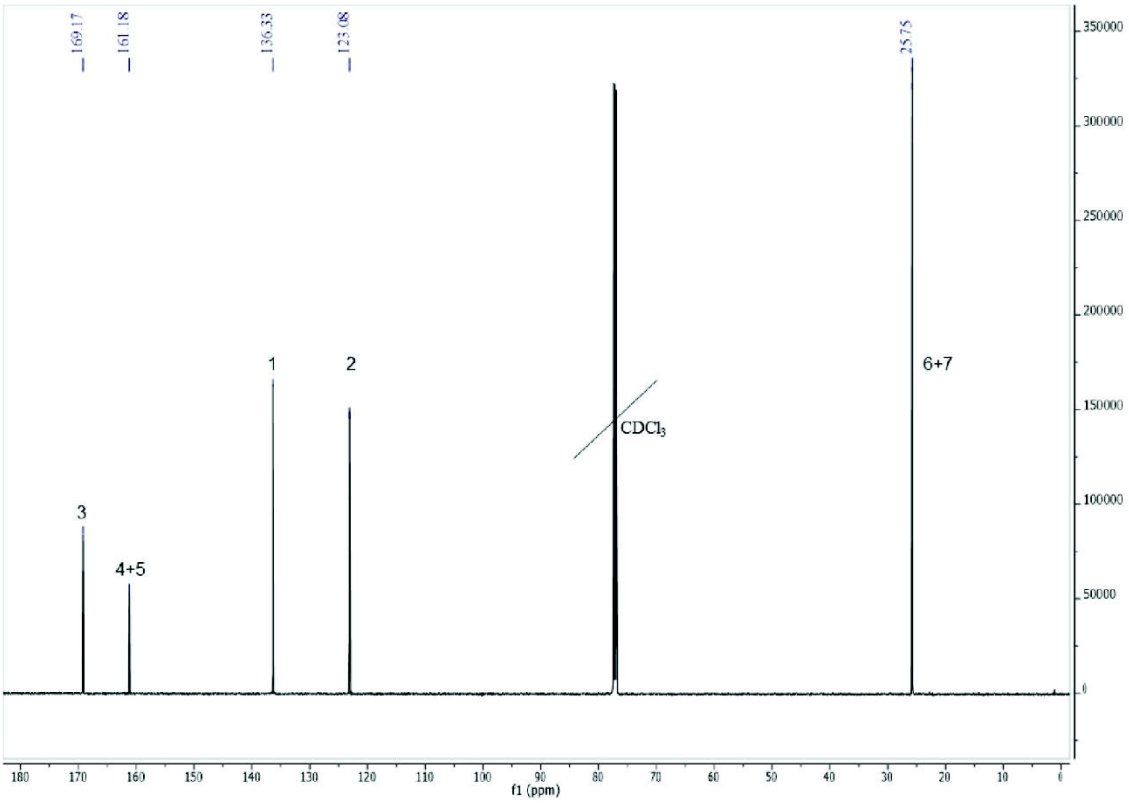

Figure S1b: ^{13}C-NMR (600 MHz, $CDCl_3$) of NAS.

S2 Synthesis of polymer precursor poly (*N*-acryloxysuccinimide)

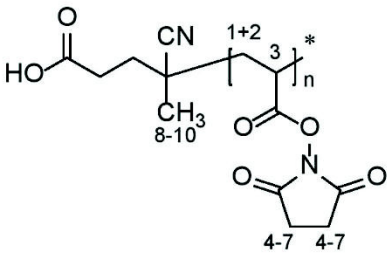

Scheme S2: Structure of polymer precursor poly (*N*-acryloxysuccinimide).

^{1}H-NMR (600 MHz, $CDCl_3$) δ 3.28 - 3.00 (s, 90H, *H3*), δ 2.85 - 2.74 (s, 360H, *H4-7*), δ 2.25 - 1.90 (s, 180H, *H1+2*) δ 1.40 - 1.33 (s, 3H, *H8-10*).

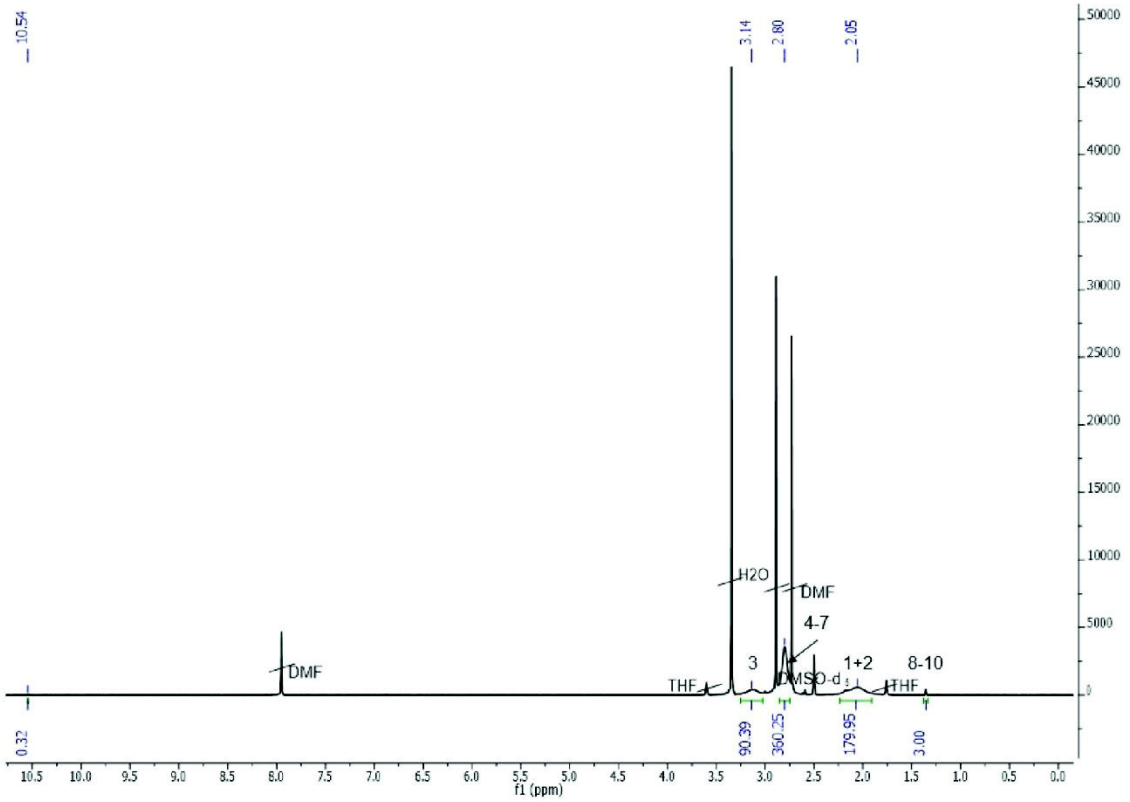

Figure S2: ^{1}H-NMR (600 MHz, $CDCl_3$) of PNAS.

S3 Synthesis of carbohydrate ligands with different linkers

Synthesis of 3-amino-2-hydroxypropyl-linker functionalized ligands

Synthesis of 1,2,3,4,6-penta-*O*-acetyl-α-D-mannopyranoside

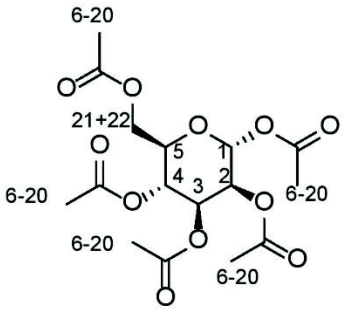

Scheme S3a: Structure of 1,2,3,4,6-penta-*O*-acetyl-α-D-mannopyranoside.

α-D-mannose (30.0 g, 166.6 mmol) was dissolved in 500 mL acetonitrile at 0 °C. Then *p*-toluenesulfonic acid (3.18 g, 18.5 mmol) was added and the solution was flushed with nitrogen for 20 min and over the next 20 min acetic anhydride (100 mL, 1.1 mole) was added and the solution was stirred at room temperature for 48 h. Afterwards the solvent was removed and the residue was dissolved in 600 mL ethyl acetate and washed with saturated sodium

bicarbonate solution, water and dried over magnesium sulfate. Solvent was removed under reduced pressure and the product was dried under vacuum (yield: 64.2 g, 99%).

^{1}H-NMR (600 MHz, $CDCl_3$) δ 6.11 - 5.83 (dd, $^{3}J_{HH}$ = 67.2, 1.8 Hz 1H, *H1*), δ 5.50 - 5.09 (m, 3H, *H2-4*), δ 4.34 - 4.24 (m, 1H, *H5*), δ 4.18 - 3.75 (m, 2H, *H21+22*), δ 2.23 - 2.20 (s, 3H, *H6-20*), δ 2.18 - 2.15 (d, $^{3}J_{HH}$ = 2.4 Hz, 3H, *H6-20*), δ 2.09 - 2.07 (s, 3H, *H6-20*), δ 2.06 - 2.02 (s, 3H, *H6-20*), δ 2.02 - 1.96 (s, 3H, *H6-20*).

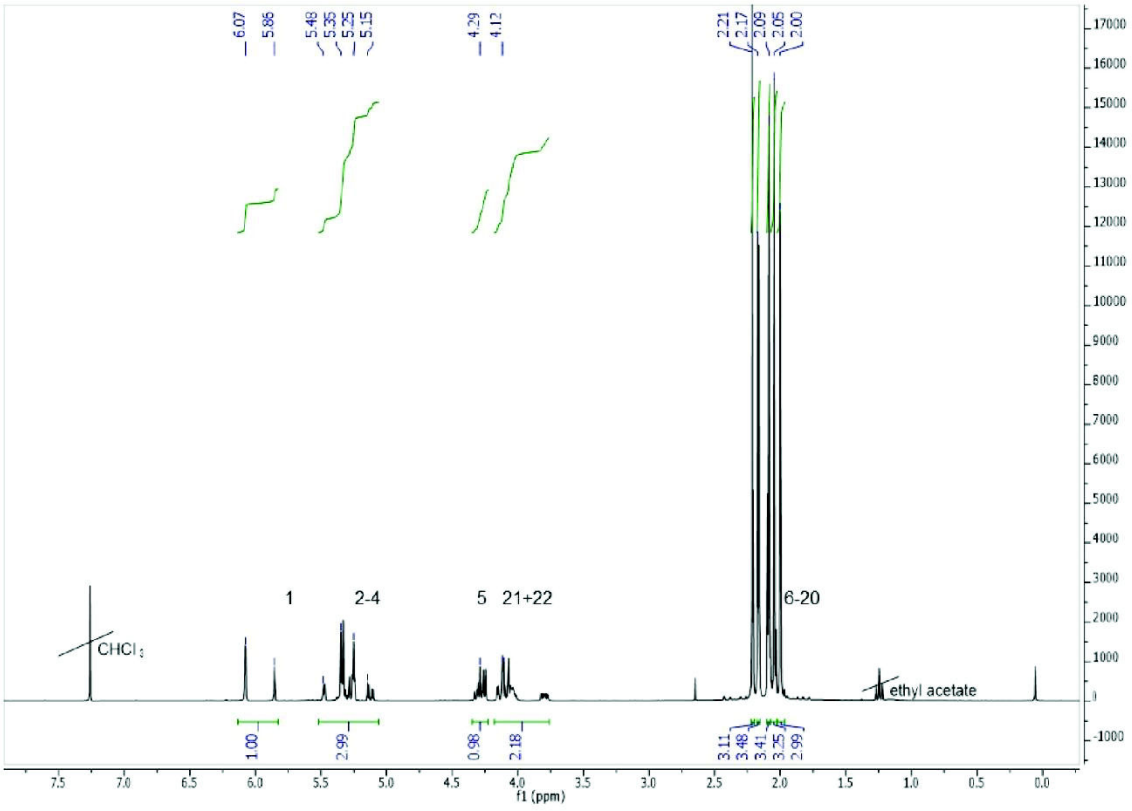

Figure S3a: ^{1}H-NMR (600 MHz, $CDCl_3$) 1,2,3,4,6-penta-*O*-acetyl-α-D-mannopyranoside.

Synthesis of allyl-2,3,4,6-tetra-*O*-acetyl-α-D-mannopyranoside and allyl-2,3,4,6-tetra-*O*-acetyl-β-D-galactopyranoside

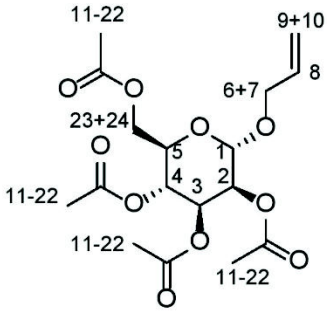

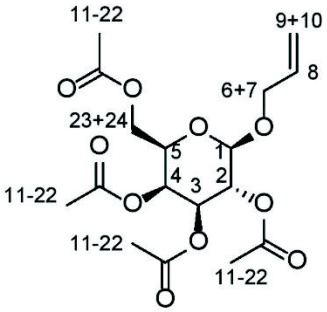

Scheme S3b: Structures of allyl-2,3,4,6-tetra-*O*-acetyl-α-D-mannopyranoside (left) and allyl-2,3,4,6-tetra-*O*-acetyl-β-D-galactopyranoside (right).

The synthesis was done according to literature.[1] The protected sugar (25.5 g, 65.4 mmol) was dissolved in 410 mL dichloromethane before allyl alcohol (25 mL, 360.9 mmol) was added. After 30 min of flushing with nitrogen at 0 °C boron trifluoride diethyl etherate (250 mL, 1.97 mol) was added dropwise over 15 min and the solution was then stirred for 72 h at room temperature. Afterwards the solution was poured into 1000 mL of ice water. The organic phase was washed with saturated sodium bicarbonate, water and dried over magnesium sulfate. Solvent was removed and product was purified via column chromatography using n-hexane:ethyl acetate (1:1) (yield mannose: 15.99 g, 63%; galactose 17.75 g, 69%).

^{1}H-NMR allyl-2,3,4,6-tetra-*O*-acetyl-α-D-mannopyranoside: (600 MHz, $CDCl_3$) δ 5.93 - 5.86 (tdd, $^3J_{HH}$ = 11.3, 5.3, 0.9 Hz, 1H, *H8*), δ 5.38 - 5.35 (dd, $^3J_{HH}$ = 10.0, 3.5 Hz, 1H, *H4*), δ 5.33 - 5.26 (m, 2H, *H9+10*), δ 5.26 - 5.22 (m, 2H, *H2+3*), δ 4.88 - 4.85 (d, $^3J_{HH}$ = 1.7 Hz, 1H, *H1*), δ 4.30 - 4.26 (dd, $^3J_{HH}$ = 12.1, 5.3 Hz, 1H, *H23+24*), δ 4.21 - 4.16 (ddt, $^3J_{HH}$ = 12.8, 5.3, 1.4 Hz, 1H, *H5*), δ 4.12 - 4.08 (dd, $^3J_{HH}$ = 12.3, 2.4 Hz, 1H, *H23+24*), δ 4.05 - 3.99 (m, 2H, *H6+7*), δ 2.17 - 2.14 (s, 3H, *H11-22*), δ 2.12 - 2.09 (s, 3H, *H11-22*), δ 2.05 - 2.03 (s, 3H, *H11-22*), δ 2.00 - 1.97 (s, 3H, *H11-22*).

^{1}H-NMR allyl-2,3,4,6-tetra-*O*-acetyl-β-D-galactopyranoside (600 MHz, $CDCl_3$) δ 5.90 - 5.80 (td, $^3J_{HH}$ = 11.3, 4.9 Hz, 1H, *H8*), δ 5.48 - 5.40 (dd, $^3J_{HH}$ = 3.7, 1.0 Hz, 1H, *H1*), δ 5.39 - 5.32 (m, 1H, *H3*), δ 5.31 - 5.25 (dd, $^3J_{HH}$ = 17.2, 1.4 Hz, 1H, *H2*), δ 5.22 - 5.18 (dd, $^3J_{HH}$ = 10.4, 1.1 Hz, 1H, *H5*), δ 5.15 - 4.97 (m, 2H, *H9+10*), δ 4.25 - 4.19 (t, $^3J_{HH}$ = 6.4 Hz, 1H, *H4*), δ 4.19 - 4.13 (dd, $^3J_{HH}$ = 13.0, 5.1 Hz, 1H, *H23+24*), δ 4.13 - 4.03 (m, 2H, *H6+7*), δ 4.03 - 3.96 (dd, $^3J_{HH}$ = 13.1, 6.1 Hz, 1H, *H23+24*), δ 2.14 - 2.11 (s, 3H, *H11-22*), δ 2.08 - 2.04 (s, 3H, *H11-22*), δ 2.04 - 2.01 (s, 3H, *H11-22*), δ 1.97 - 1.94 (s, 3H, *H11-22*).

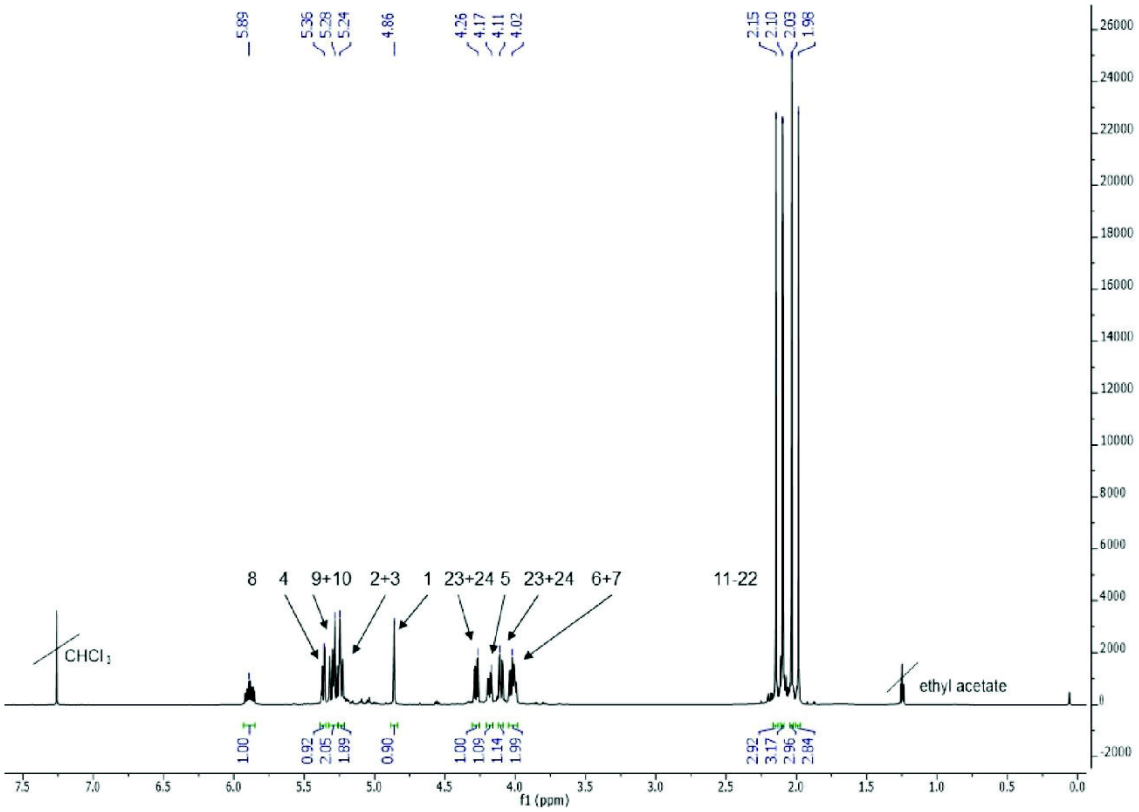

Figure S3b: ^{1}H-NMR (600 MHz, $CDCl_3$) allyl-2,3,4,6-tetra-*O*-acetyl-α-D-mannopyranoside.

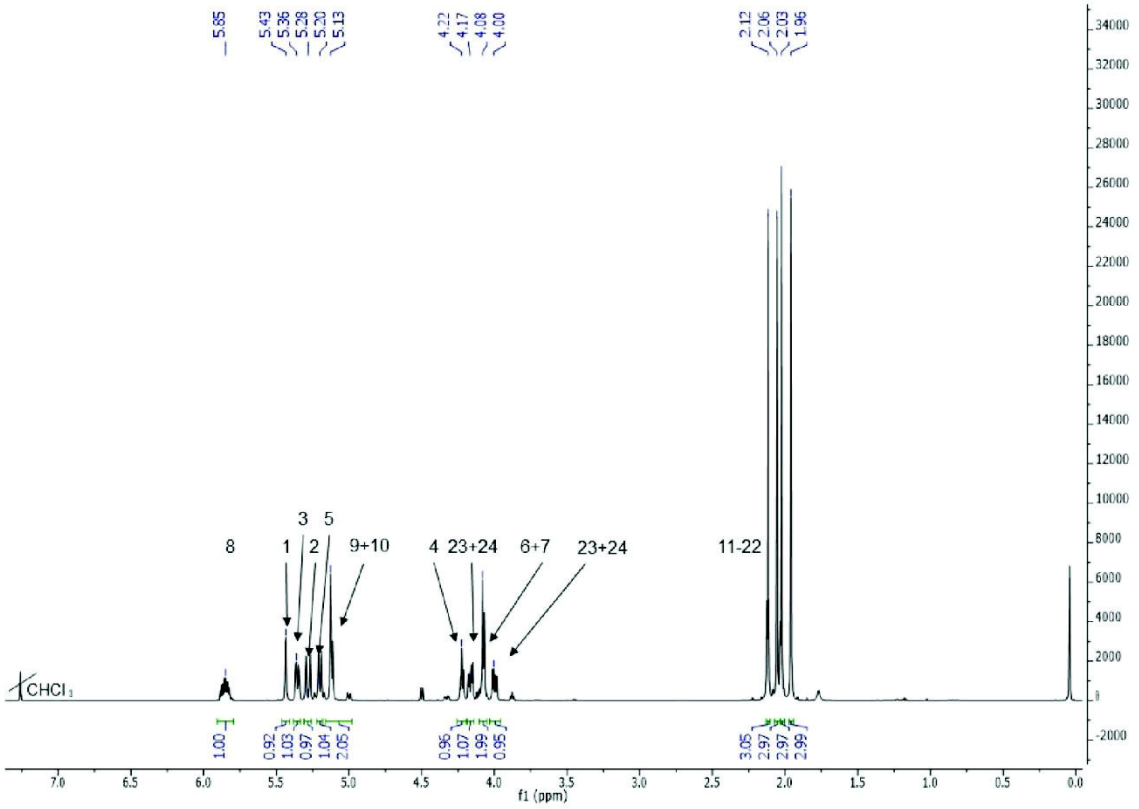

Figure S3c: ^{1}H-NMR (600 MHz, $CDCl_3$) allyl-2,3,4,6-tetra-*O*-acetyl-α-D-galactopyranoside.

Synthesis of 2',3'-epoxypropyl-2,3,4,6-tetra-*O*-acetyl-α-D-mannopyranoside and 2',3'-epoxypropyl-2,3,4,6-tetra-*O*-acetyl-β-D-galactopyranoside

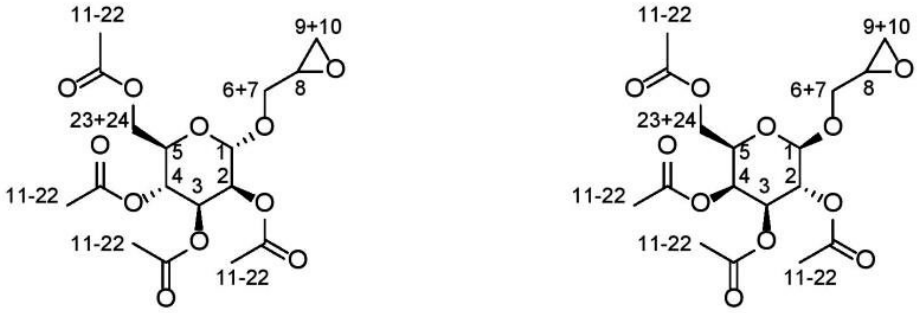

Scheme S3c: Structures of 2',3'-epoxypropyl-2,3,4,6-tetra-*O*-acetyl-α-D-mannopyranoside (left) and 2',3'-epoxypropyl-2,3,4,6-tetra-*O*-acetyl-β-D-galactopyranoside (right).

The allyl-functionalized sugar (15.5 g, 40 mmol) was dissolved in 300 mL dichloromethane and flushed with nitrogen. Then *m*-chloroperoxybenzoic acid (14 g, 81.2 mmol) was added and the solution was stirred for 48 h. After that additional *m*-chloroperoxybenzoic acid (4.24 g, 24.2 mmol) was added and stirred for another 24 h. After that 20 ml of dichloromethane was added and washed with saturated sodium bicarbonate before dried with sodium sulfate. Solvent was removed under reduced pressure and product was purified via column chromatography using n-hexane:ethyl acetate (3:2) (yield mannose: 10.1 g, 63%; galactose: 9.86 g, 61%).

^{1}H-NMR 2',3'-epoxypropyl-2,3,4,6-tetra-*O*-acetyl-α-D-mannopyranoside (600 MHz, $CDCl_3$) δ 5.39 - 5.33 (m, 1H, *H4*), δ 5.32 - 5.26 (m, 2H, *H2+3*), δ 4.93 - 4.84 (dd, $^3J_{HH}$ = 34.3, 1.6 Hz, 1H, *H1*), δ 4.30 - 4.26 (m, 1H, *H5*), δ 4.14 - 4.10 (m, 1H, *H23+24*), δ 4.07 - 4.02 (m, 1H, *H23+24*), δ 3.92 - 3.79 (ddd, $^3J_{HH}$ = 57.3, 11.9, 3.0 Hz, 1H, *H6+7*), δ 3.59 - 3.52 (ddd, $^3J_{HH}$ = 25.0, 11.7, 5.6 Hz, 1H, *H6+7*), δ 3.22 - 3.18 (m, 1H, *H8*), δ 2.85 - 2.82 (m, 1H, *H9+10*), δ 2.65 - 2.62 (m, 1H, *H9+10*), δ 2.18 - 2.14 (s, 3H, *H11-22*), δ 2.11 - 2.08 (s, 3H, *H11-22*), δ 2.06 - 2.03 (s, 3H, *H11-22*), δ 2.02 - 1.98 (s, 3H, *H11-22*).

^{1}H-NMR 2',3'-epoxypropyl-2,3,4,6-tetra-*O*-acetyl-β-D-galactopyranoside (600 MHz, $CDCl_3$) δ 5.48 - 5.42 (m, 1H, *H1*), δ 5.39 - 5.33 (m, 1H, *H3*), δ 5.20 - 5.14 (dd, $^3J_{HH}$ = 17.2, 3.7 Hz, 1H, *H2*), δ 5.14 - 5.11 (m, 1H, *H4*), δ 4.30 - 4.25 (ddt, $^3J_{HH}$ = 6.7, 3.3, 1.2 Hz, 1H, *H5*), δ 4.13 - 4.05 (m, 2H, *H23+24*), δ 3.92 - 3.79 (ddd, $^3J_{HH}$ = 55.5, 11.8, 3.0 Hz, 1H, *H6+7*), δ 3.64 - 3.46 (ddd, $^3J_{HH}$ = 82.8, 12.2, 5.4 Hz, 1H, *H6+7*), δ 3.20 - 3.12 (m, 1H, *H8*), δ 2.84 - 2.77 (dd, $^3J_{HH}$ = 10.2, 4.8 Hz, 1H, *H9+10*), δ 2.69 - 2.58 (ddd, $^3J_{HH}$ = 46.4, 5.3, 2.7 Hz, 1H, *H9+10*), δ 2.16 - 2.12 (d, $^3J_{HH}$ = 1.8 Hz, 3H, *H11-22*), δ 2.10 - 2.06 (d, $^3J_{HH}$ = 2.9 Hz, 3H, *H11-22*), δ 2.04 - 2.02 (s, 3H, *H11-22*), δ 2.00 - 1.97 (s, 3H, *H11-22*).

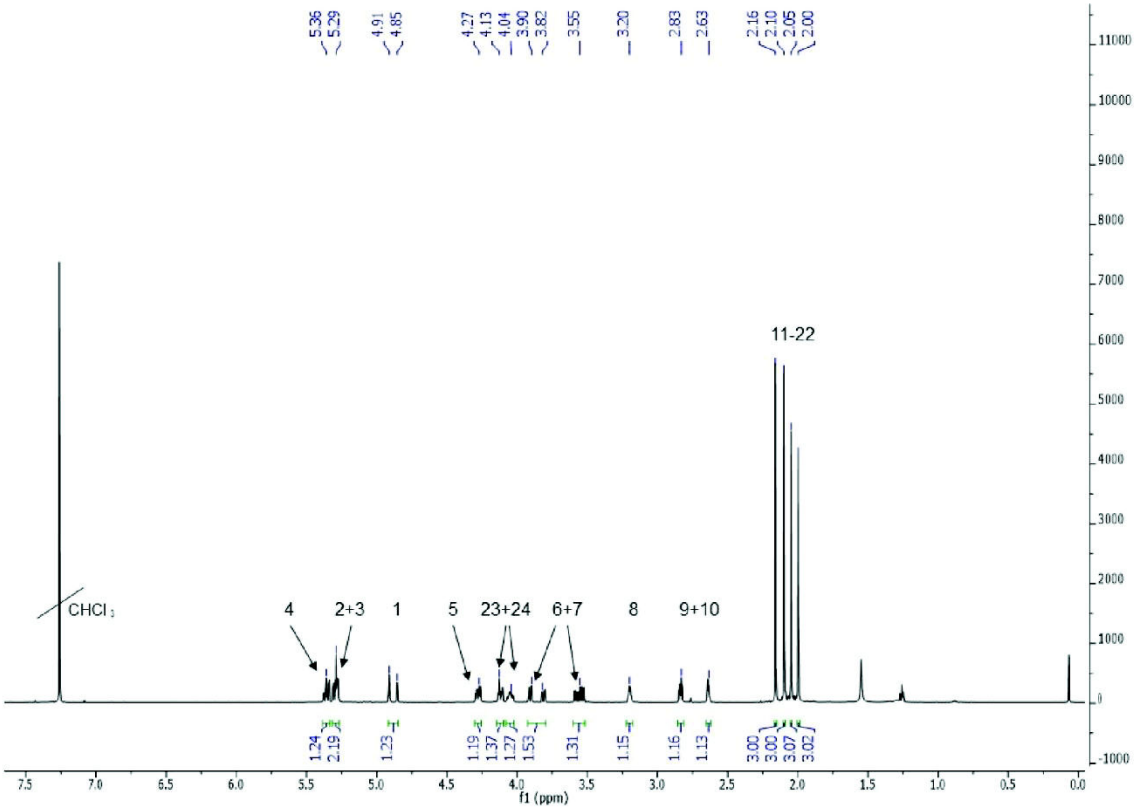

Figure S3d: ^{1}H-NMR (600 MHz, $CDCl_3$) 2',3'-epoxypropyl-2,3,4,6-tetra-*O*-acetyl-α-D-mannopyranoside.

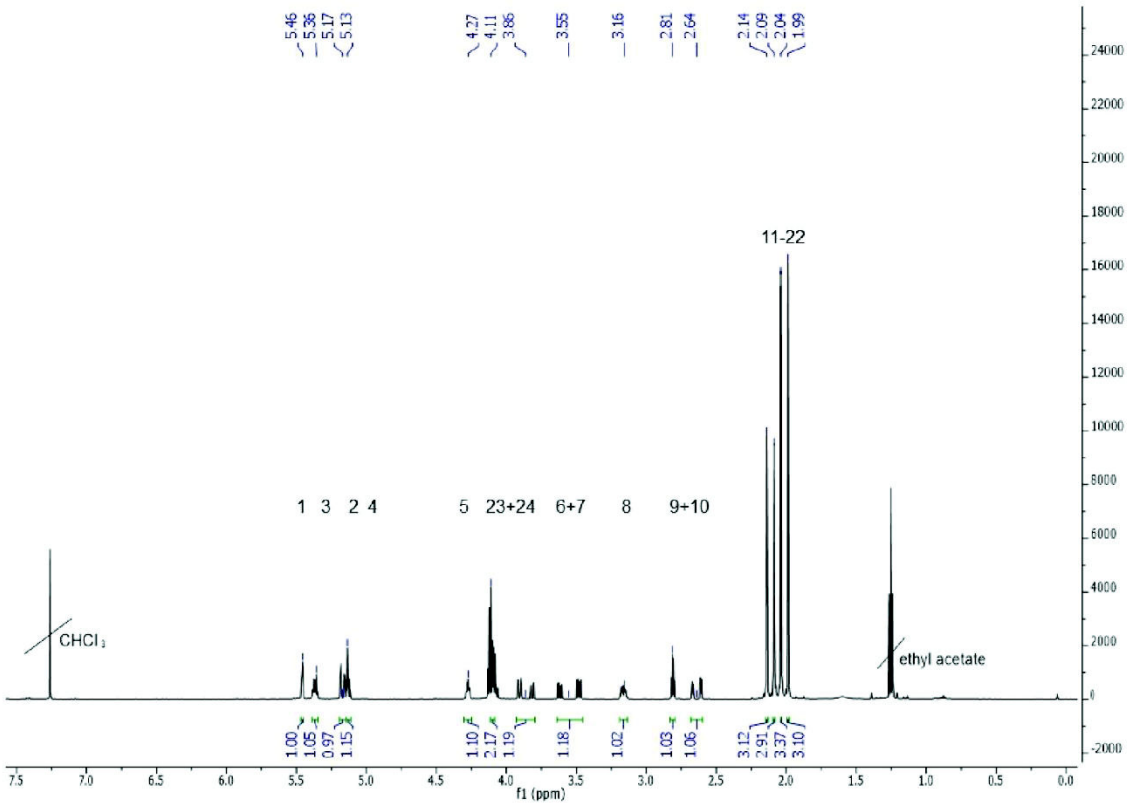

Figure S3d: ^{1}H-NMR (600 MHz, $CDCl_3$) 2',3'-epoxypropyl-2,3,4,6-tetra-*O*-acetyl-α-D-galactopyranoside.

Synthesis of 3-amino-2-hydroxypropyl-α-D-mannopyranoside and 3-amino-2-hydroxypropyl-β-D-galactopyranoside

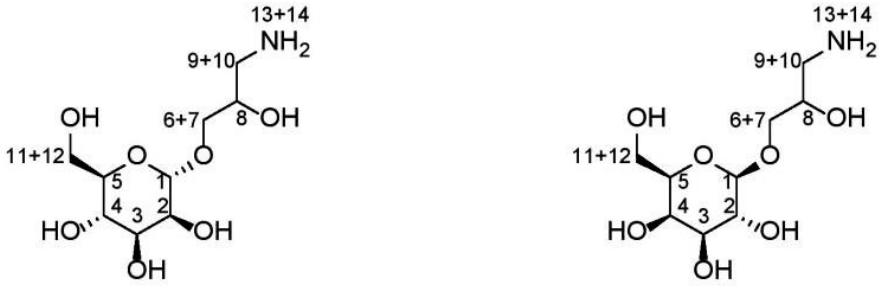

Scheme S3d: 3-amino-2-hydroxypropyl-α-D-mannopyranoside (left) and 3-amino-2-hydroxypropyl-β-D-galactopyranoside (right).

The epoxy-functionalized sugar (9.7 g, 24.2 mmol) was dissolved in 3 mL acetonitrile. After dissolving the sugar ammonia solution (25%, 21 mL) was added and stirred for 72 h. After that the solvent was removed under vacuum and the residue was dissolved in acetone, precipitated in diethyl ether, filtered and dried under vacuum (yield mannose: 5.16 g, 85%; galactose: 3.71 g, 61%).

^{1}H-NMR 3-amino-2-hydroxypropyl-α-D-mannopyranoside (600 MHz, CD_3OD) δ 4.80 - 4.76 (s, 1H, *H1*), δ 3.87 - 3.81 (m, 3H, *H8-10*), δ 3.76 - 3.68 (dd, $^3J_{HH}$ = 12.4, 1.5 Hz, 3H, *H2+6+7*), δ 3.63 - 3.58 (m, 1H, *H4*), δ 3.56 - 3.51 (m, 1H, *H3*), δ 3.47 - 3.42 (m, 1H, *H5*), δ 2.95 - 2.68 (m, 2H, *H11+12*), δ 1.91 - 1.89 (s, 1H, *H13+14*),

^{1}H-NMR 3-amino-2-hydroxypropyl-β-D-galactopyranoside (600 MHz, CD_3OD) δ 4.85 - 4.83 (s, 1H, *H1*), δ 3.84 - 3.65 (m, 8H, *H2-4+6-10*), δ 3.91 - 3.77 (td, $^3J_{HH}$ = 10.3, 3.4 Hz 1H, *H5*), δ 2.99 - 2.77 (m, 2H, *H11+12*), δ 1.91 - 1.88 (s, 2H, *H13+14*).

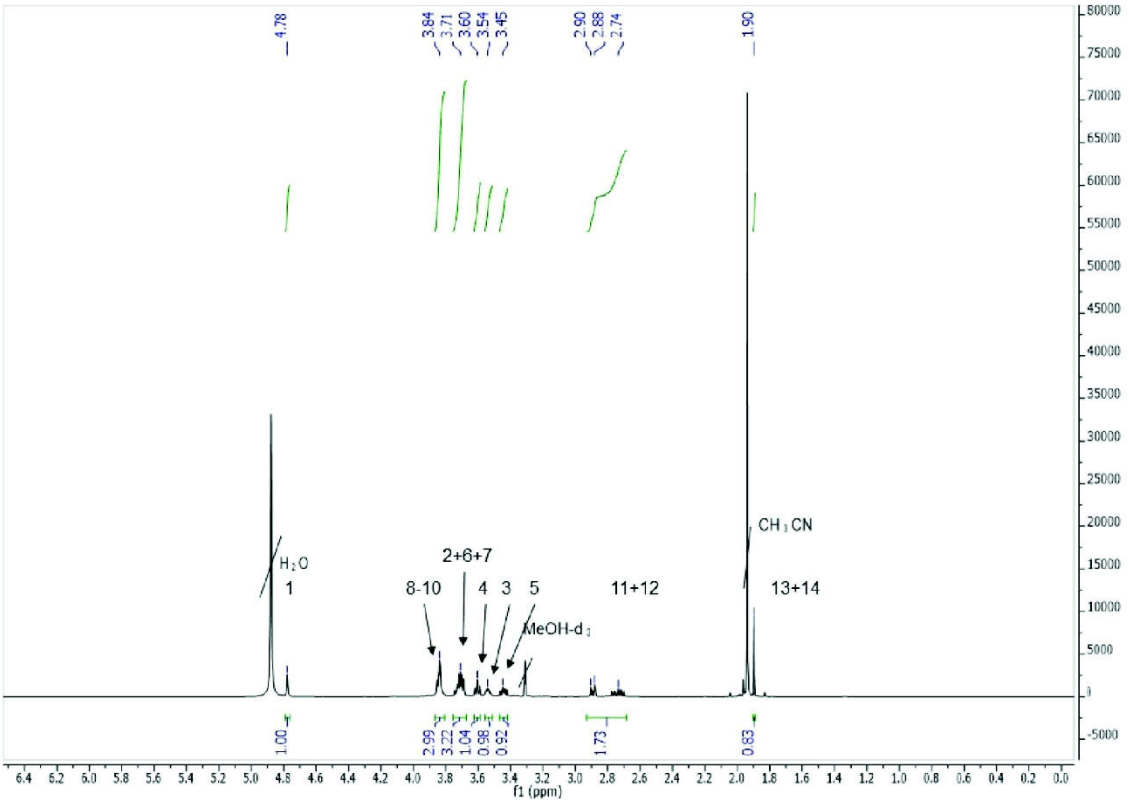

Figure S3e: ^{1}H-NMR (600 MHz, CD_3OD) 3-amino-2-hydroxypropyl-α-$_D$-mannopyranoside.

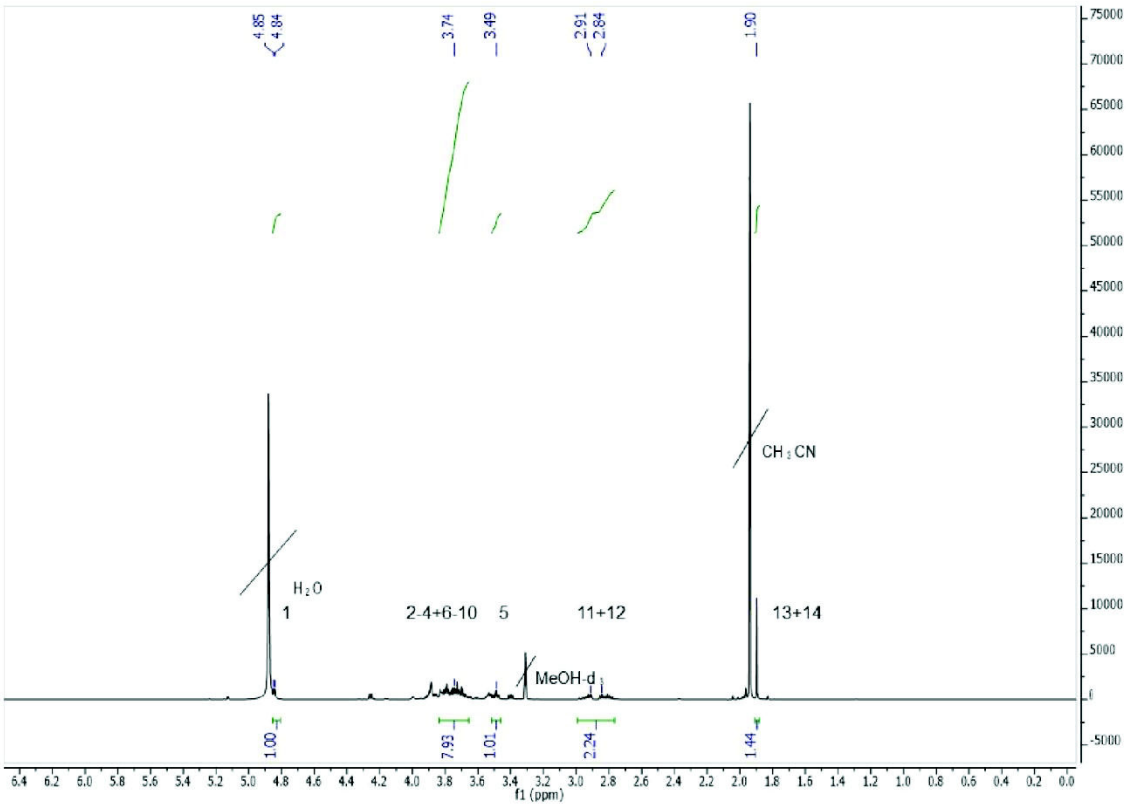

Figure S3f: ^{1}H-NMR (600 MHz, CD_3OD) 3-amino-2-hydroxypropyl-α-$_D$-galactopyranoside.

Synthesis of ethyl-linker functionalized ligand

Synthesis of 2-aminoethyl-α-D-mannopyranoside

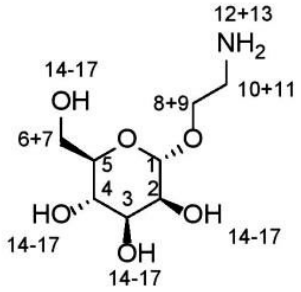

Scheme S3e: 2-aminoethyl-α-D-mannopyranoside.

2-azidoethyl-2,3,4,6-tetra-*O*-acetyl-α-D-mannopyranose was synthesized according to literature.[2] 0.2 M sodium methoxide in methanol solution (8 mL) was added to 2-azidoethyl-2,3,4,6-tetra-*O*-acetyl α-D-mannopyranose (1.5 g, 3.6 mmol) and shaken for 48 h. Afterwards Amberlite-IR120® was added until pH6 was reached. Afterwards, Amberlite-IR120 was filtered off and methanol was added to the filtrate up to a volume of 25 mL. Then palladium on charcoal (10wt%, 106.5 mg, 1 mmol) was added and the solution was flushed three times with hydrogen. The solution was stirred for 24 h under hydrogen atmosphere, filtered and dried under vacuum giving 0.68 g product (yield: 84%).

^{1}H-NMR (600 MHz, DMSO-d_6) δ 4.63 - 4.57 (dd, $^3J_{HH}$ = 8.9, 1.4 Hz, 1H, *H1*), δ 3.66 - 3.62 (dd, $^3J_{HH}$ = 11.6, 2.1 Hz, 1H, *H14-16*), δ 3.62 - 3.59 (dd $^3J_{HH}$ = 3.5, 1.7 Hz, 1H, *H14+16*), δ 3.59 - 3.54 (m, 1H, *H14-16*), δ 3.49 - 3.45 (dd, $^3J_{HH}$ = 8.9, 3.4 Hz, 1H, *H17*), δ 3.45 - 2.41 (dd, $^3J_{HH}$ = 11.6, 6.1 Hz, 1H, *H2*), δ 3.39 - 3.28 (m, 3H, *H3-7+12+13*), δ 3.17 - 3.16 (s, 4H, *H3-7+12+13*), δ 2.77 - 2.63 (o, $^3J_{HH}$ = 6.1 Hz, 2H, *H8+9*), δ 1.85 - 1.78 (s, 2H, *H10+11*).

S4 Synthesis of Poly(*N*-isopropylacrylamide-co-*N*-(2-hydroxypropyl) α-D-mannopyranoside acrylamide) and Poly(*N*-isopropylacrylamide-co-*N*-ethyl α-D-mannopyranoside acrylamide)

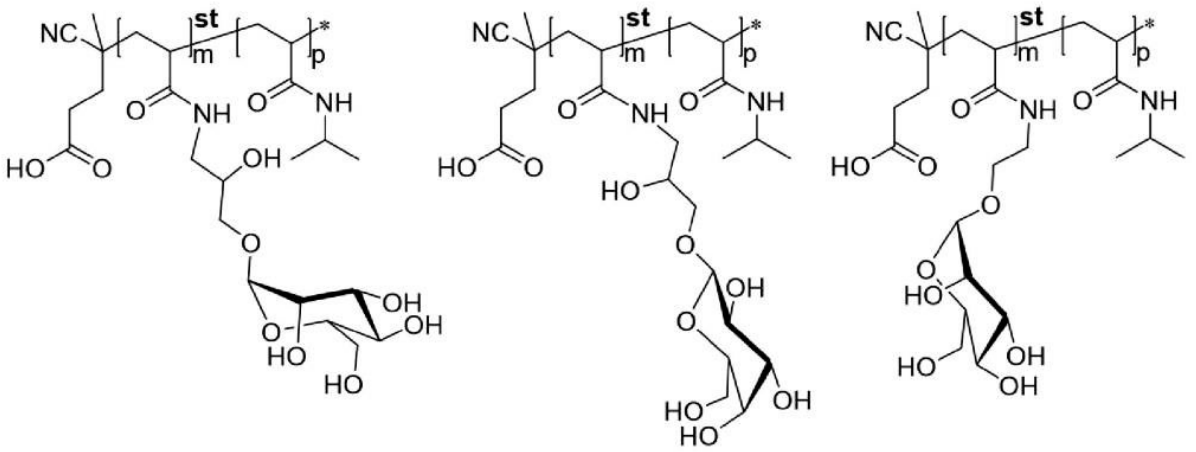

Scheme S4a: General structures of Poly(*N*-isopropylacrylamide-co-*N*-(2-hydroxypropyl) α-D-mannopyranoside acrylamide) (left), Poly(*N*-isopropylacrylamide-co-*N*-ethyl α-D-mannopyranoside acrylamide) (right) and Poly(*N*-isopropylacrylamide-co-*N*-(2-hydroxypropyl) α-D-galactopyranoside acrylamide) (middle) polymers.

Table S4a: Amount of sugar added during polymer functionalization and reaction yield after dialysis.

*for **GalHPL3** 3-amino-2-hydroxypropyl-β-D-galactopyranose was used.

Polymer	Amount of sugar added [mg]		Yield	
	3-amino-2-hydroxypropyl-α-D-mannopyranose*	2-aminoethyl-α-D-mannopyrannose	[mg]	[%]
Man0	---	---	452	67
ManHPL1	60	---	438	64
ManHPL2	120	---	435	63
ManHPL7	150	---	540	74
ManHPL34	1600	---	855	81
ManHPL97	3200	---	1358	80
ManEL1	---	26	415	61
ManEL2	---	53	421	61
ManEL5	---	132	441	61
GalHPL3	150	---	456	63

Molecular weight of PNAS was calculated from ^{1}H-NMR spectroscopy giving a $\bar{M}_n$ = 15340 g mol^{-1}, divided by the molecular weight of the monomer giving a number of repeating units of 90. The ratio of the anomeric hydrogen integral at the carbohydrate in comparison to the backbone CH-group integral gave similar results to the colorimetric carbohydrate assay (PSA method). The PSA functionalization degrees were used due to higher accuracy of the method. By multiplication of functionalization degrees with number of repeating units and molecular weight of the monomers the molecular weights were calculated.

Table S4b: Funtionalization degrees determined by ^{1}H-NMR-spectroscopy and phenol sulphuric acid (PSA) method and the molecular weight calculated from PSA methods functionalization degree.

Polymer	Results		
	Functionalization degree (^{1}H-NMR) [%]	Functionalization degree (PSA) [%]	Molecular weight (PSA) [g mol^{-1}]
Man0	0	0	10300
ManHPL1	1.3	1.4	10480
ManHPL2	1.8	1.9	10650
ManHPL7	7.4	7.5	11525
ManHPL34	31.1	33.6	16240
ManHPL97	89.3	96.9	27770
ManEL1	1.3	1.1	10450
ManEL2	2.8	2.2	10600
ManEL5	4.2	4.6	11040
GalHPL3	2.6	2.7	10825

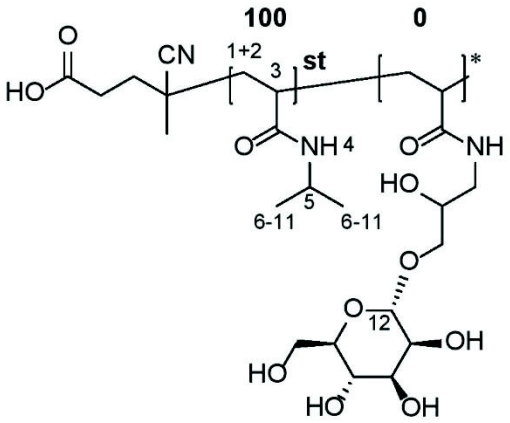

Scheme S4b: Structure of **PNIPAM**. Bold numbers showing functionalization degree.

^{1}H-NMR **PNIPAM** (600 MHz, $CDCl_3$) δ 7.15 - 5.90 (s, 1H, *H4*), δ 4.15 - 3.90 (s, 1H, *H5*), δ 2.32 - 1.96 (s, 1H, *H3*) δ 1.95 - 1.30 (s, 2H, *H1+2*), δ 1.28 - 0.94 (s, 6H, *H6-11*).

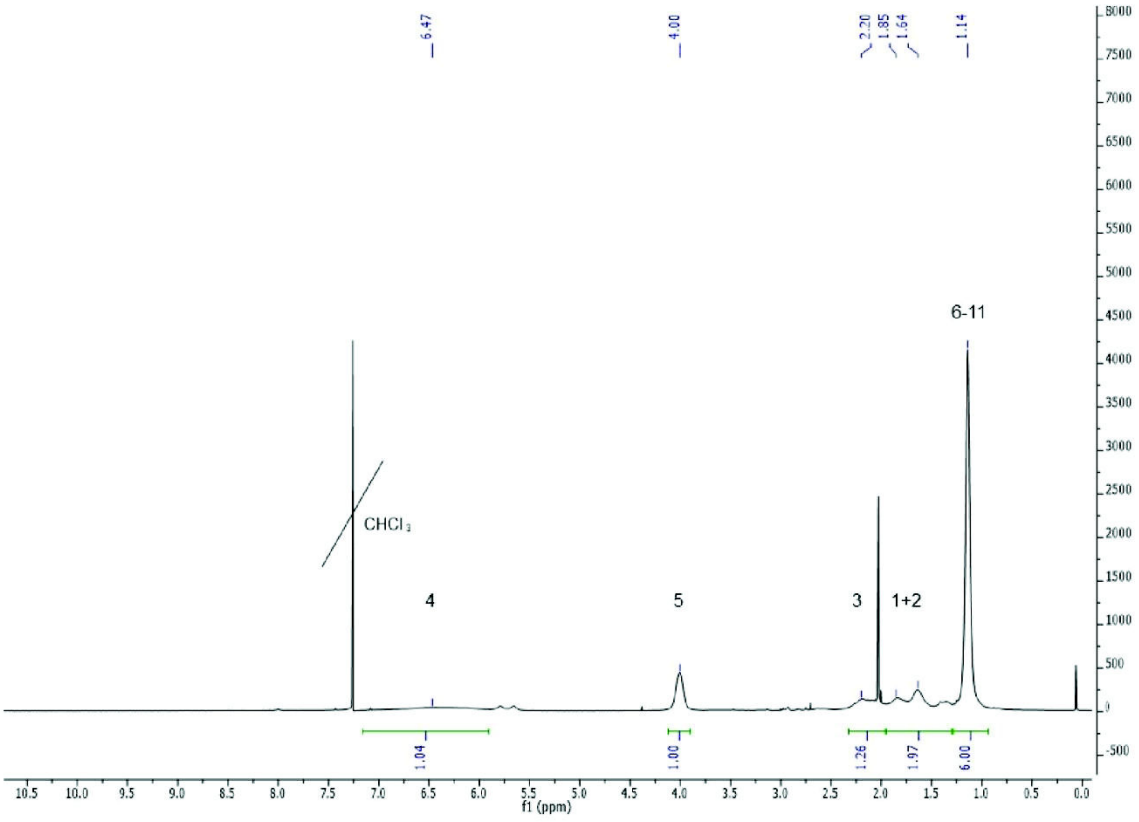

Figure S4a: ^{1}H-NMR (600 MHz, $CDCl_3$) of **PNIPAM**.

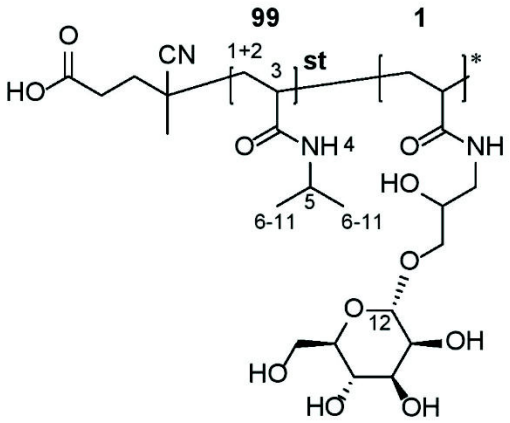

Scheme S4c: Structure of **ManHPL1**. Bold numbers showing functionalization degree.

^{1}H-NMR **ManHPL1** (600 MHz, $CDCl_3$) δ 7.14 - 6.03 (s, 1H, *H4*) δ 4.97 - 4.85 (s, 1H, *H12*), δ 4.07 - 3.95 (s, 75H, *H5*) δ 2.32 - 1.99 (s, 76H, *H3*), δ 1.93 - 1.55 (s, 152H, *H1+2*), δ 1.31 - 0.94 (s, 305H, *H6-11*).

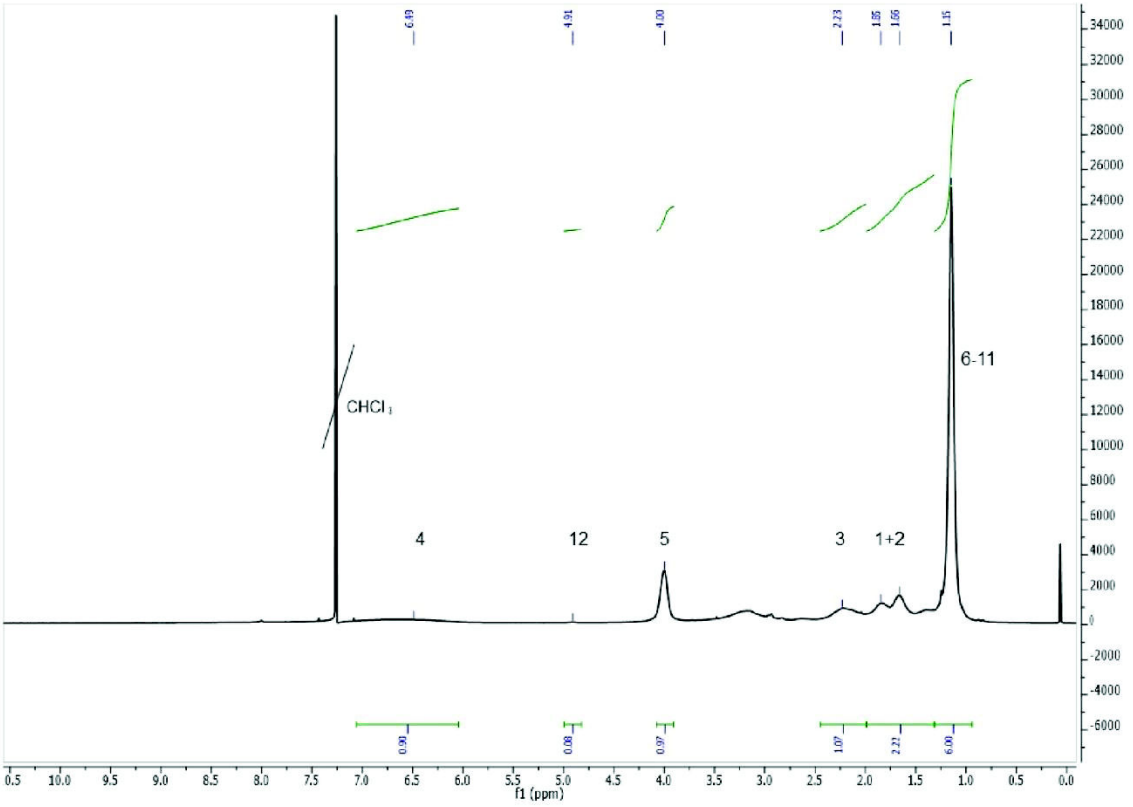

Figure S4b: ^{1}H-NMR (600 MHz, $CDCl_3$) of **ManHPL1**.

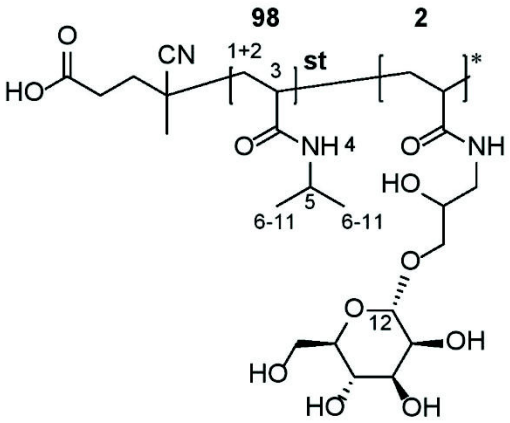

Scheme S4d: Structure of **ManHPL2**. Bold numbers showing functionalization degree.

^{1}H-NMR **ManHPL2** (600 MHz, $CDCl_3$) δ 7.03 - 5.57 (s, 55H, *H4*), δ 4.92 - 4.86 (s, 1H, *H12*), δ 4.07 - 3.92 (s, 56H, *H5*) δ 2.65 - 1.98 (s, 55H, *H3*), δ 1.95 - 1.25 (s, 111H, *H1+2*), δ 1.19 - 1.03 (s, 334H, *H6-11*).

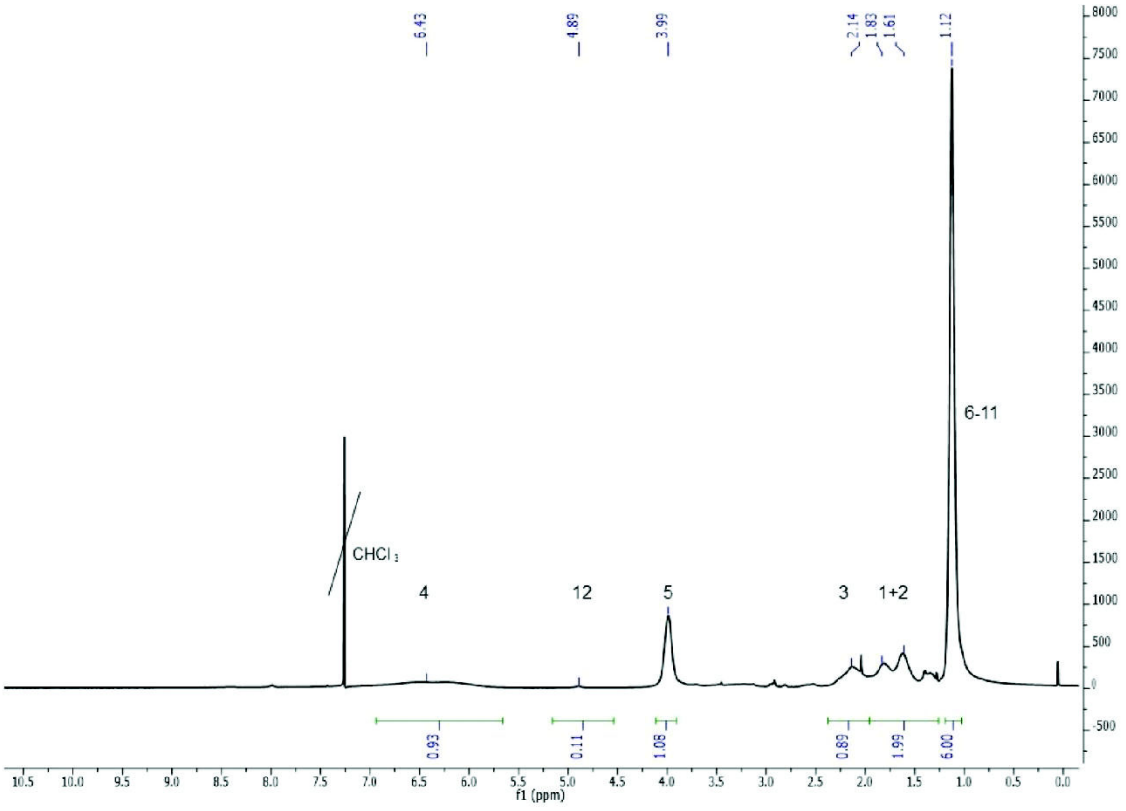

Figure S4c: ^{1}H-NMR (600 MHz, $CDCl_3$) of **ManHPL2**.

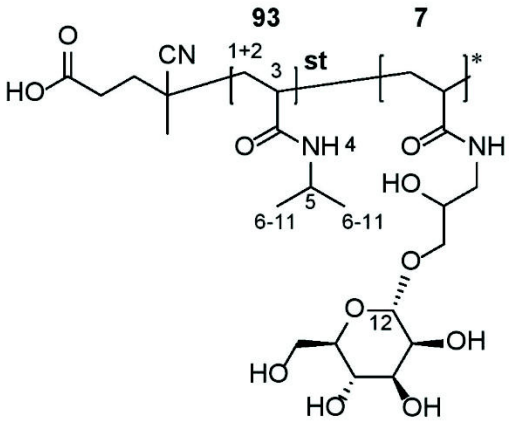

Scheme S4e: Structure of **ManHPL7**. Bold numbers showing functionalization degree.

^{1}H-NMR **ManHPL7** (600 MHz, $CDCl_3$) δ 6.95 - 5.68 (s, 14H, *H4*), δ 4.95 - 4.83 (s, 1H, *H12*), δ 4.07 - 3.92 (s, 14H, *H5*) δ 2.40 - 1.92 (s, 14H, *H3*), δ 1.91 - 1.25 (s, 28H, *H1+2*), δ 1.17 - 0.98 (s, 84H, *H6-11*).

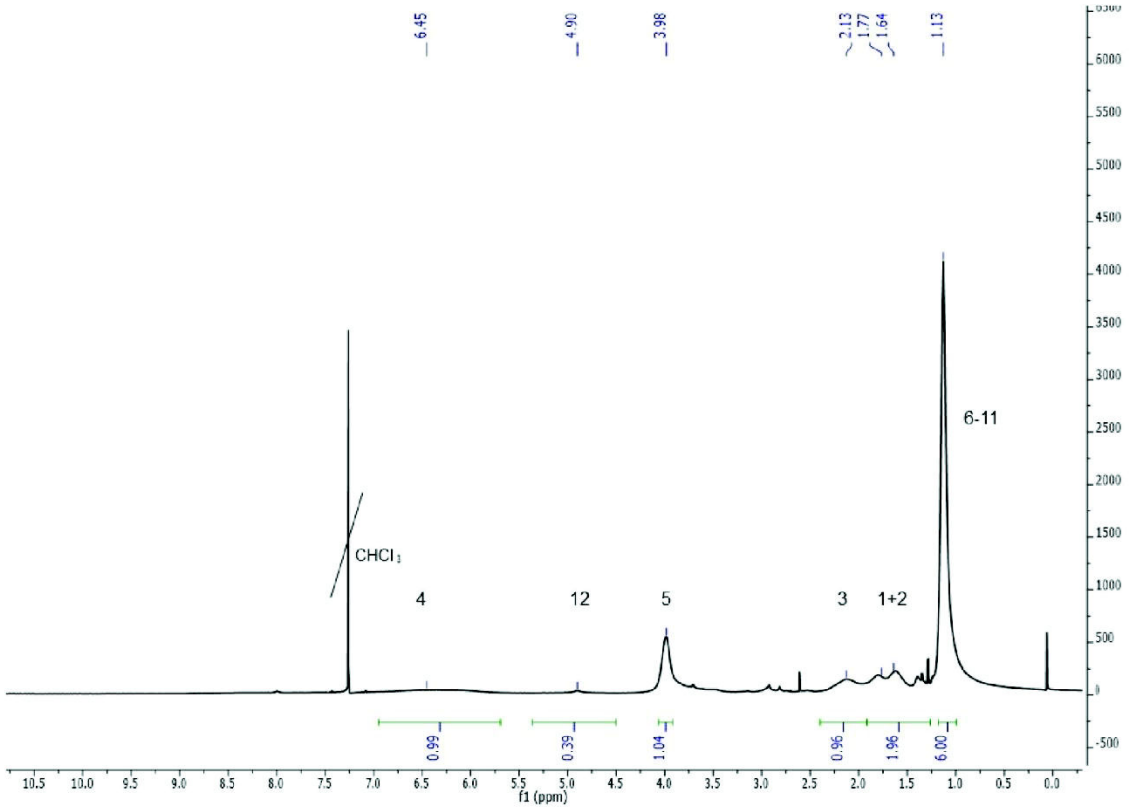

Figure S4d: ^{1}H-NMR (600 MHz, $CDCl_3$) of **ManHPL7**.

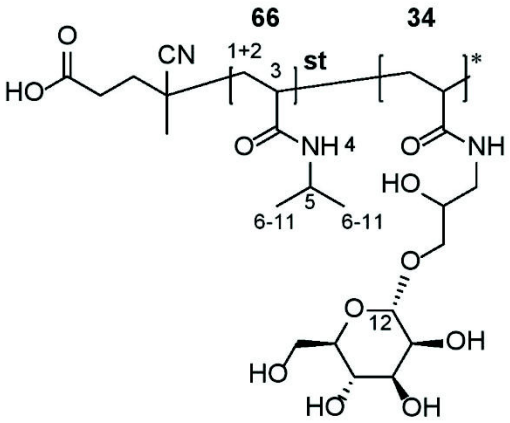

Scheme S4f: Structure of **ManHPL34**. Bold numbers showing functionalization degree.

^{1}H-NMR **ManHPL34** (600 MHz, D_2O) δ 4.91 - 4.88 (s, 1H, *H12*), δ 2.37 - 1.87 (s, 3H, *H3*), δ 1.85 - 1.40 (s, 5H, *H1+2*) δ 1.25 - 0.80 (s, 6H, *H6-11*).

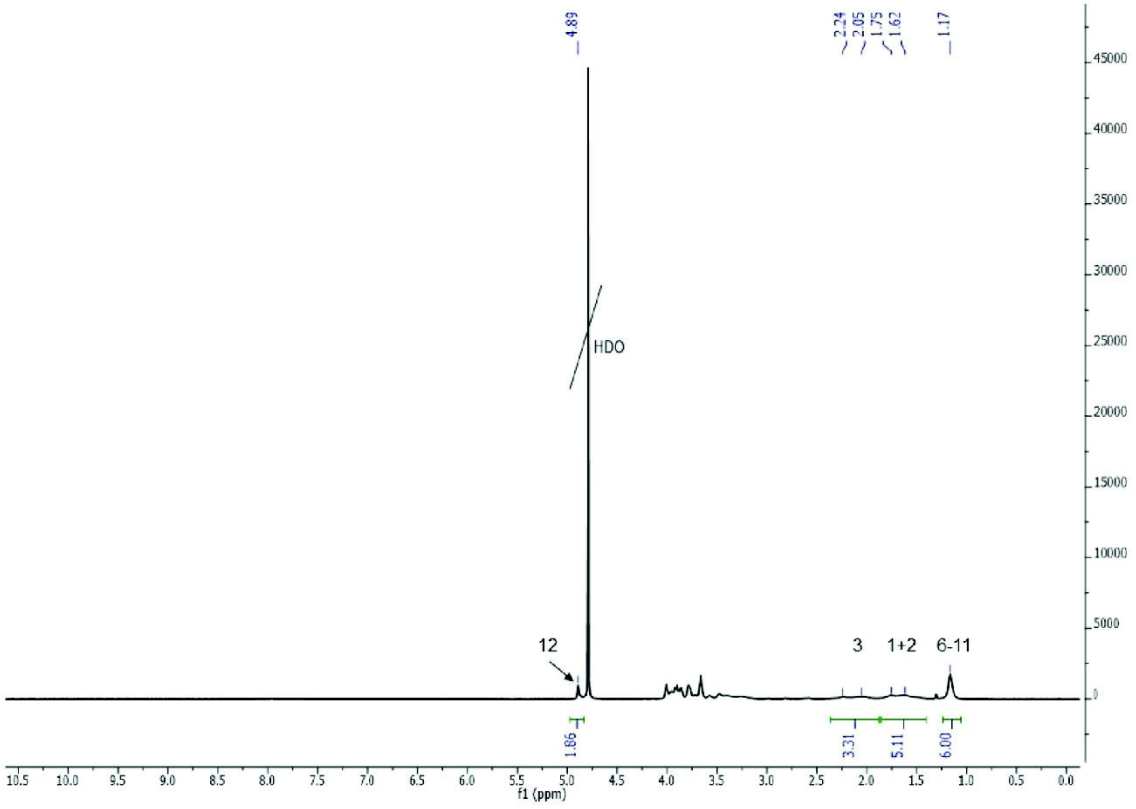

Figure S4e: ^{1}H-NMR (600 MHz, D_2O) of **ManHPL34**.

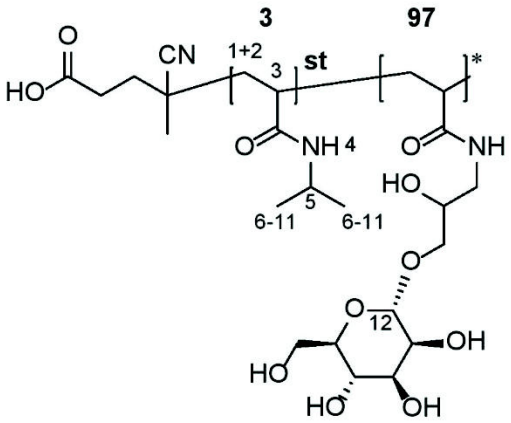

Scheme S4g: Structure of **ManHPL97**. Bold numbers showing functionalization degree.

^{1}H-NMR **ManHPL97** (600 MHz, D_2O) δ 4.95 - 4.85 (s, 1H, *H12*), δ 2.60 - 1.96 (s, 1.18H, *H3*), δ 1.95 - 1.25 (s, 2.14H, *H1+2*) δ 1.18 - 1.12 (s, 0.12H, *H6-11*).

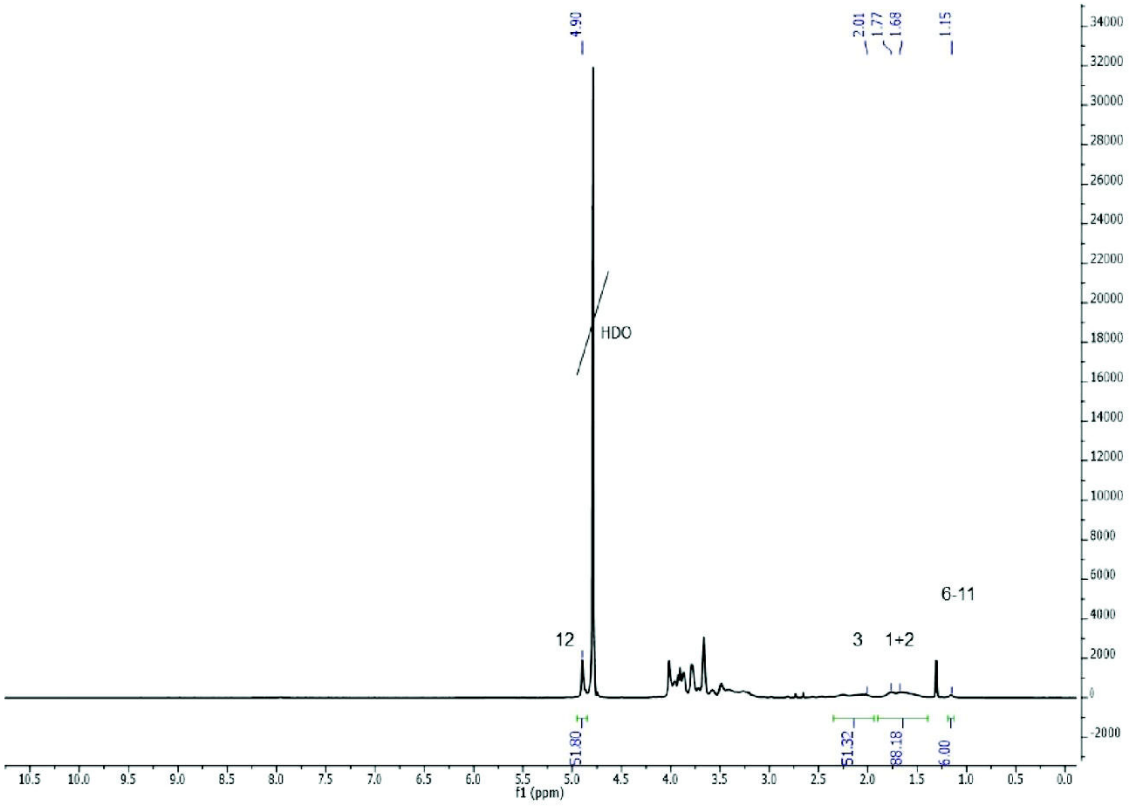

Figure S4f: ^{1}H-NMR (600 MHz, D_2O) of **ManHPL97**.

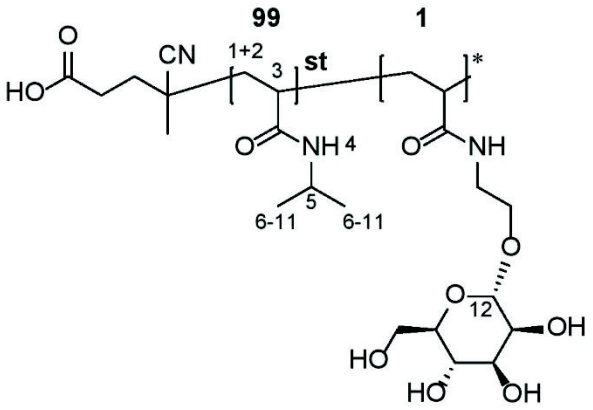

Scheme S4h: Structure of **ManEL1**. Bold numbers showing functionalization degree.

^{1}H-NMR **ManEL1** (600 MHz, $CDCl_3$) δ 7.10 - 5.85 (s, 75H, *H4*), δ 4.90 - 4.85 (s, 1H, *H12*), δ 4.07 - 3.91 (s, 77H, *H5*) δ 2.40 - 1.95 (s, 79H, *H3*), δ 1.90 - 1.30 (s, 158H, *H1+2*), δ 1.24 - 0.95 (s, 463H, *H6-11*).

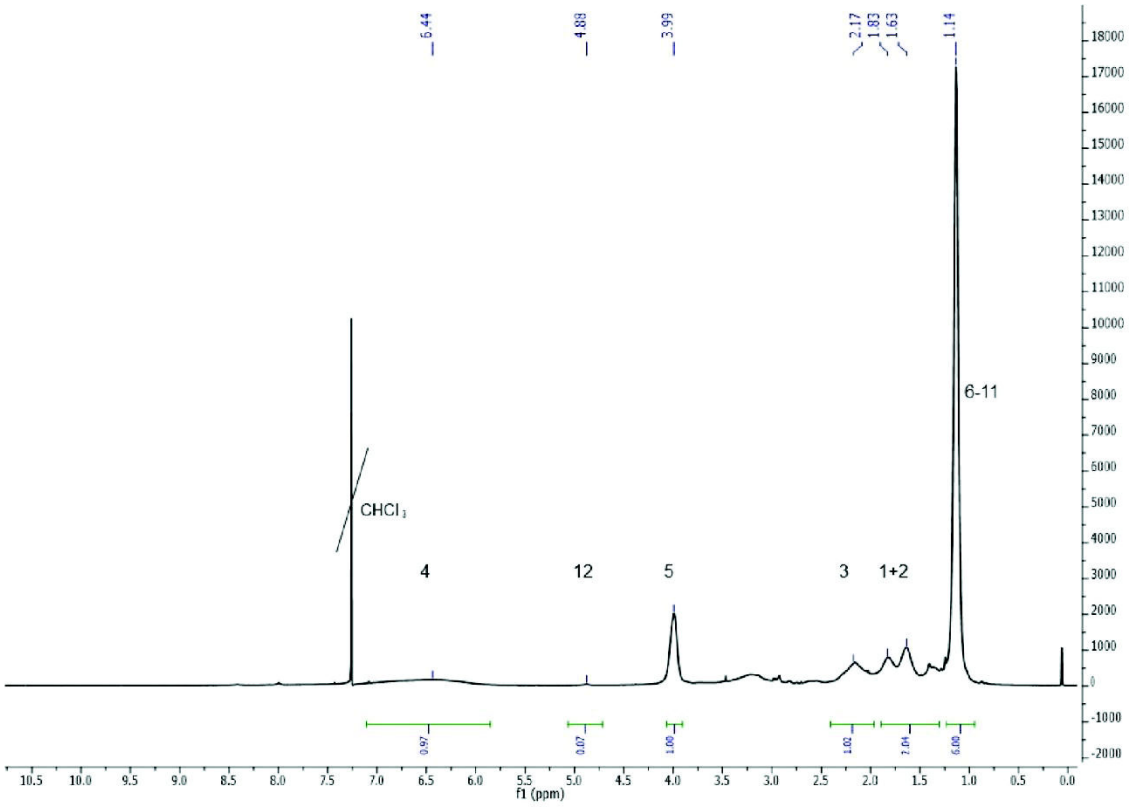

Figure S4g: ^{1}H-NMR (600 MHz, $CDCl_3$) of **ManEL1**.

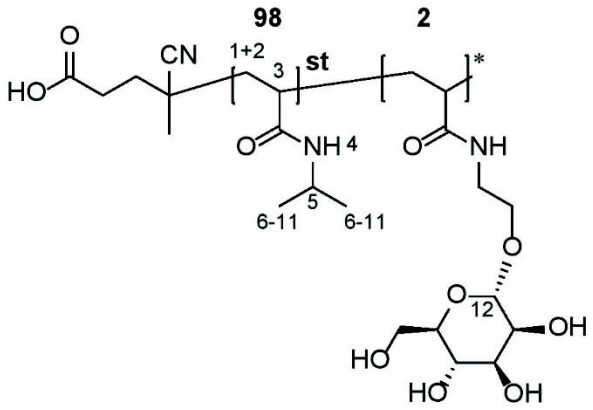

Scheme S4i: Structure of **ManEL2**. Bold numbers showing functionalization degree.

^{1}H-NMR **ManEL2** (600 MHz, $CDCl_3$) δ 7.00 - 6.05 (s, 32H, *H4*), δ 4.91 - 4.87 (s, 1H, *H12*), δ 4.20 - 3.82 (s, 40H, *H5*) δ 2.40 - 1.98 (s, 35H, *H3*), δ 2.00 - 1.31 (s, 72H, *H1+2*), δ 1.30 - 0.75 (s, 203H, *H6-11*).

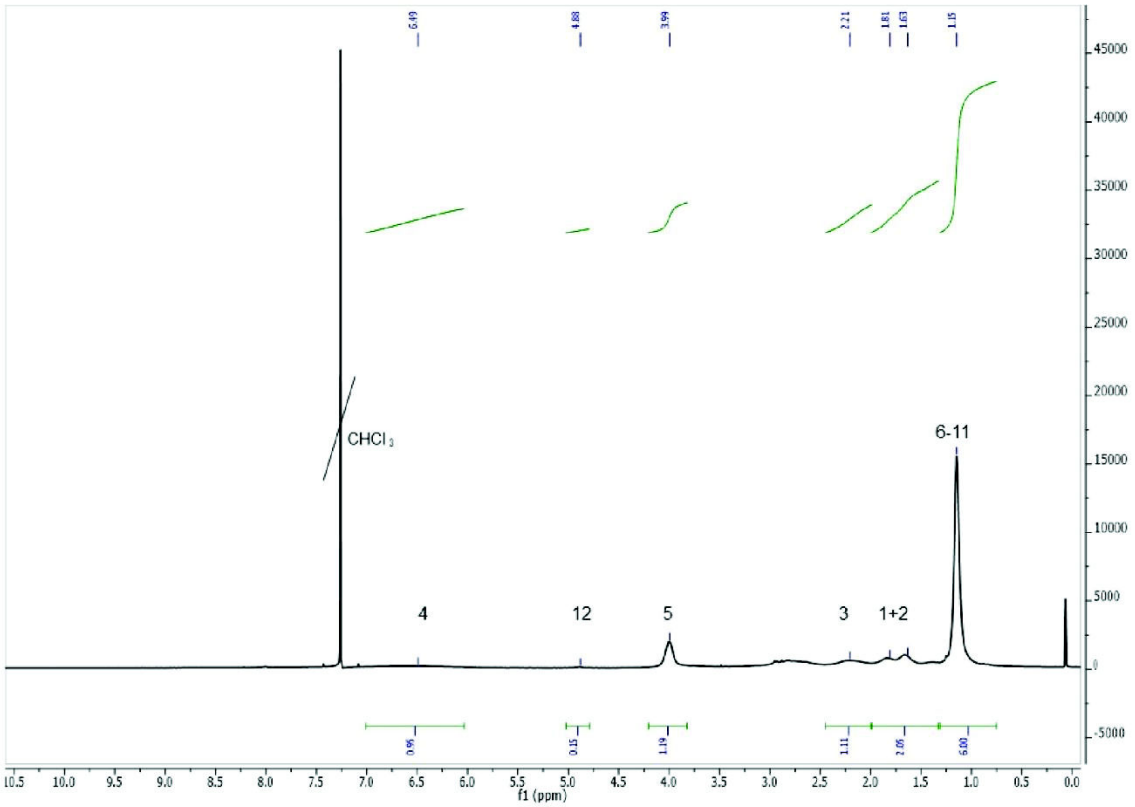

Figure S4h: ^{1}H-NMR (600 MHz, $CDCl_3$) of **ManEL2**.

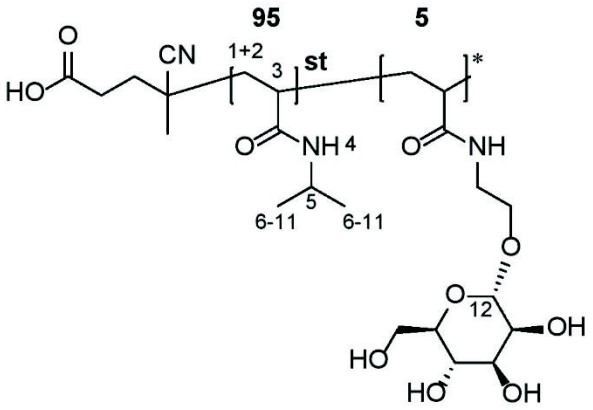

Scheme S4j: Structure of **ManEL5**. Bold numbers showing functionalization degree.

^{1}H-NMR **ManEL5** (600 MHz, $CDCl_3$) δ 6.97 - 5.68 (s, 24H, *H4*), δ 4.90 - 4.84 (s, 1H, *H12*), δ 4.09 - 3.87 (s, 29H, *H5*) δ 2.66 - 1.98 (s, 24H, *H3*), δ 1.95 - 1.25 (s, 48H, *H1+2*), δ 1.20 - 0.96 (s, 149H, *H6-11*).

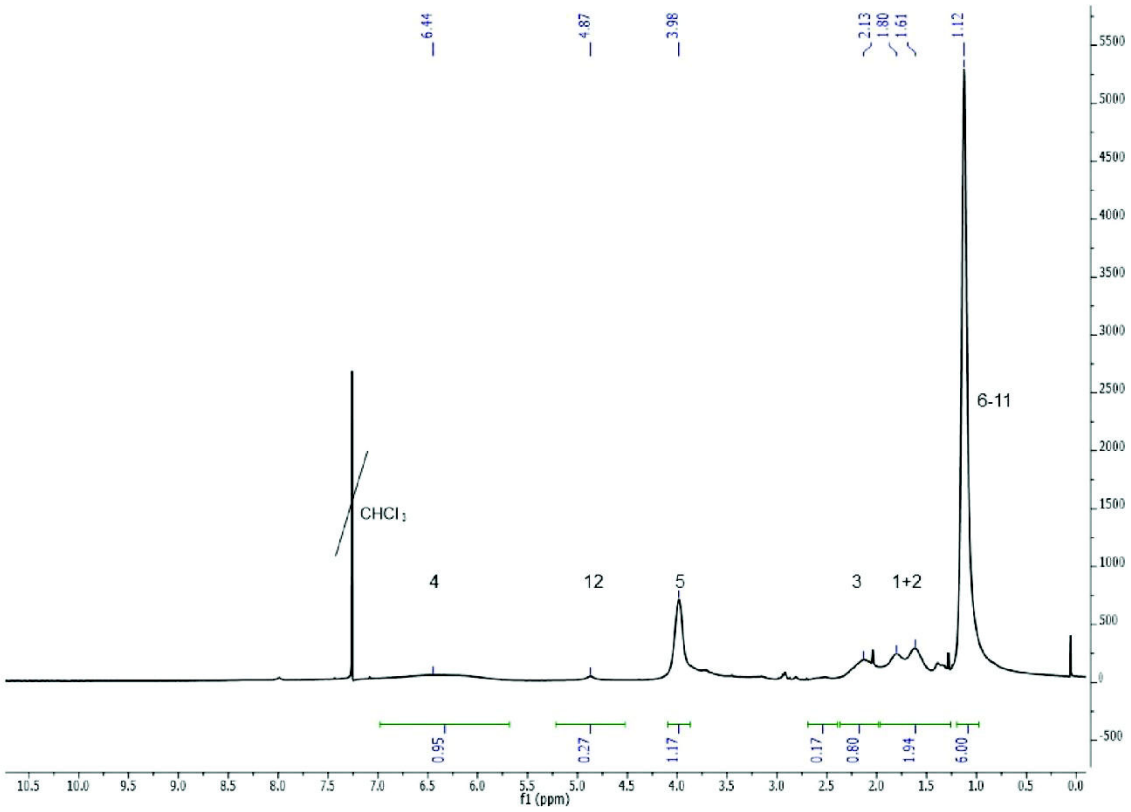

Figure S4i: ^{1}H-NMR (600 MHz, $CDCl_3$) of **ManEL5**.

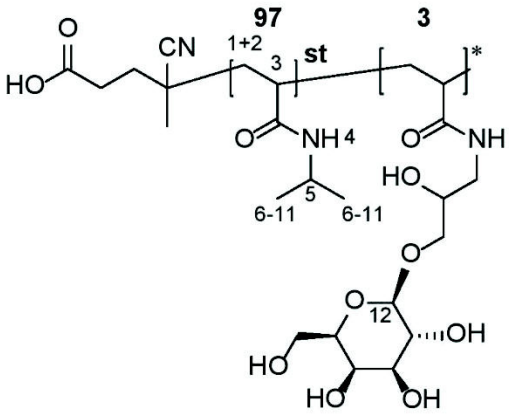

Scheme S4k: Structure of **GalHPL3**. Bold numbers showing functionalization degree.

^{1}H-NMR **GalHPL3** (600 MHz, $CDCl_3$) δ 6.79 - 5.82 (s, 22H, *H4*), δ 4.97 - 4.90 (s, 1H, *H12*), δ 4.06 - 3.90 (s, 31H, *H5*) δ 2.72 - 1.95 (s, 30H, *H3*), δ 1.91 - 1.25 (s, 51H, *H1+2*), δ 1.17 - 1.05 (s, 151H, *H6-11*).

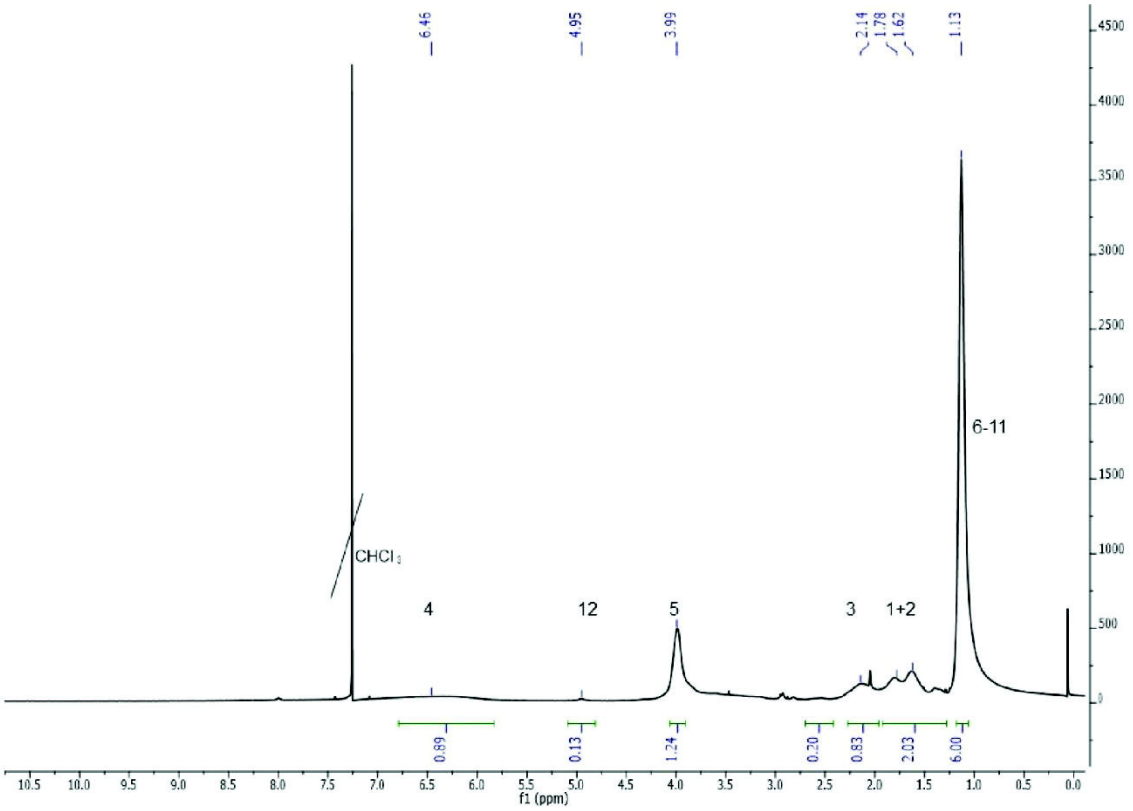

Figure S4j: ^{1}H-NMR (600 MHz, $CDCl_3$) of **GalHPL3**.

S5 Size exclusion chromatography

ManHPL34 and **ManHPL97** were insoluble in DMF, therefore, no SEC measurements were executed for these samples. Having only polystyrene standard at hand and without suitable Marc-Houwink parameters, the SEC measurements were done for determination of Đ-values and not for molecular weight. These measurements show that carbohydrate ligand does not act as intermolecular bridges between two polymer backbones. The molecular weight was calculated using number of repeating units from PNAS determined via ^{1}H-NMR spectroscopy and PSA test for determining the amount of incorporated carbohydrate.

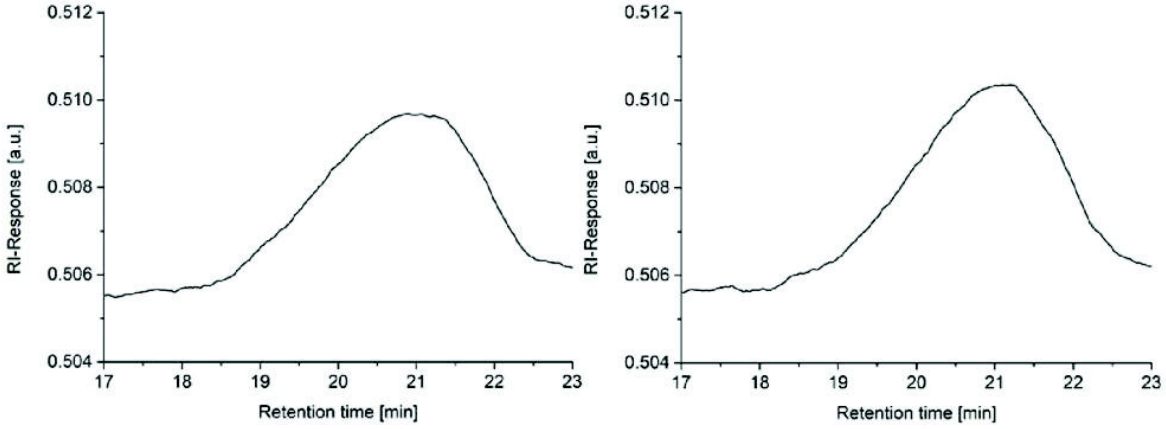

Figure S5a: Size exclusion chromatographies of polymer precursor poly(N-acryloxysuccinimide) (left) and negative control **PNIPAM** (right).

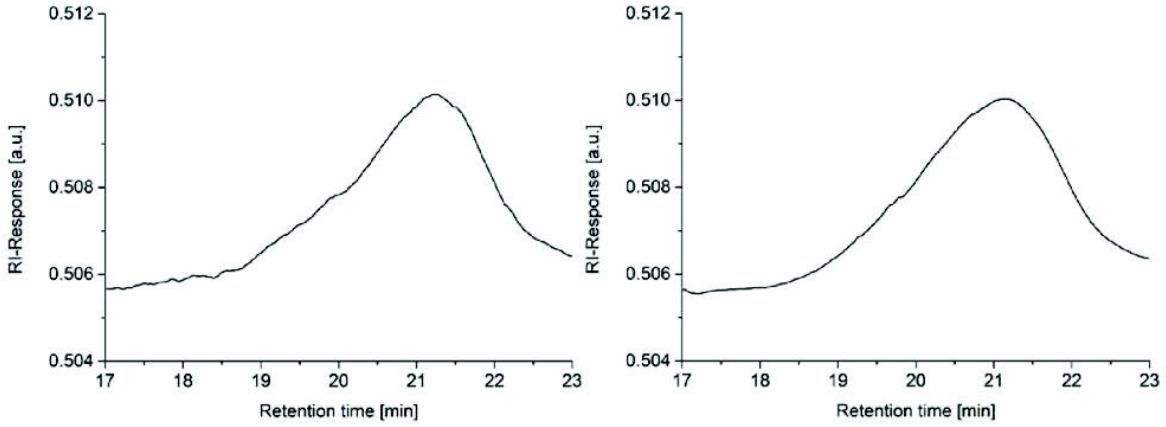

Figure S5b: Size exclusion chromatographies of glycopolymers **ManHPL1** (left) and **ManHPL2** (right).

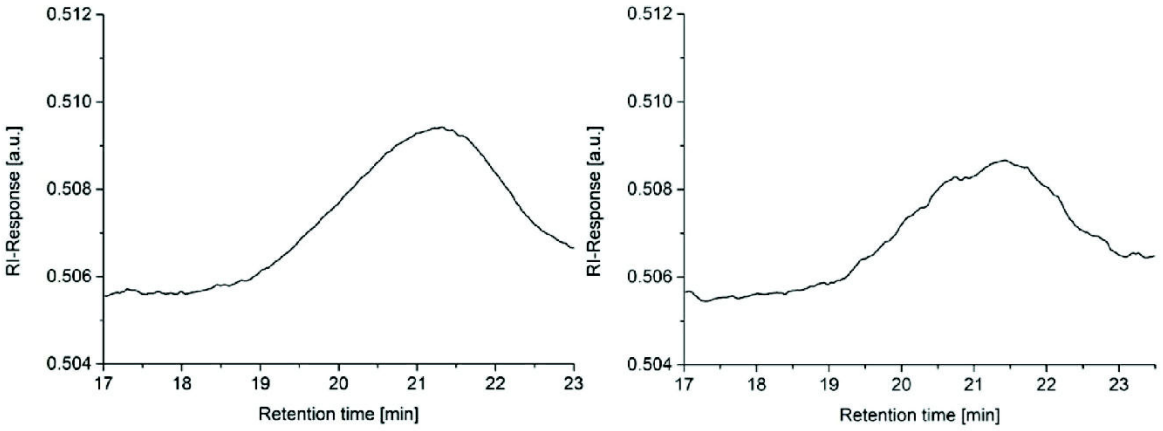

Figure S5c: Size exclusion chromatographies of glycopolymer **ManHPL7** (left) and negative binding control **GalHPL3** (right).

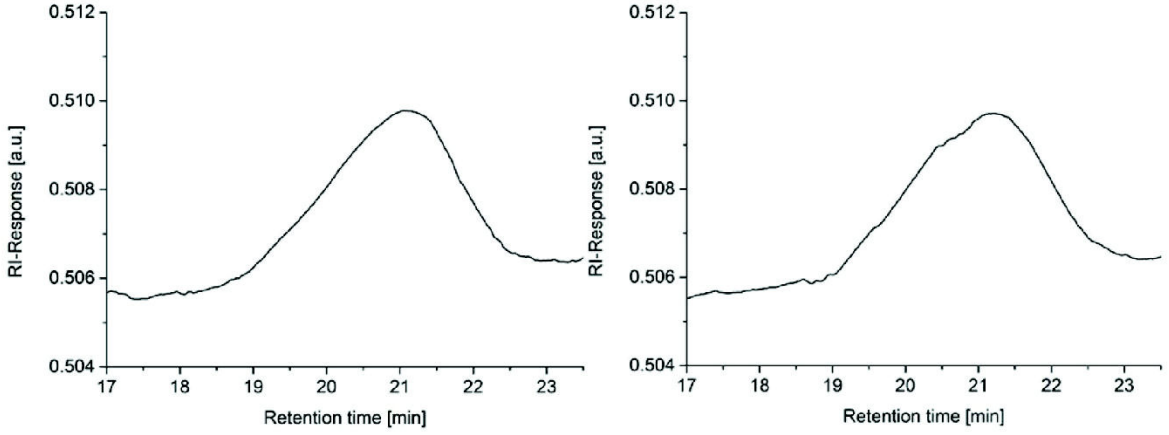

Figure S5d: Size exclusion chromatographies of glycopolymers **ManEL1** (left) and **ManEL2** (right).

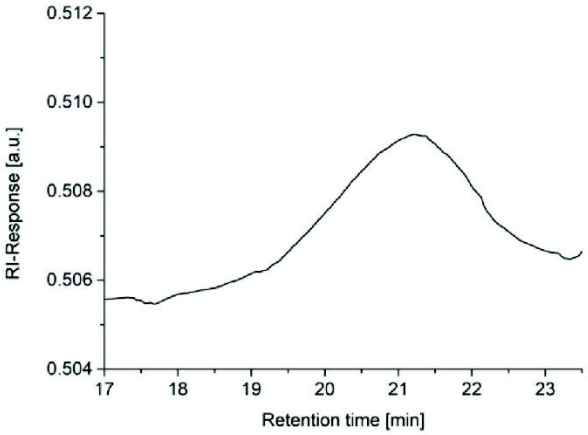

Figure S5e: Size exclusion chromatography of glycopolymer **ManEL5**.

S6 Phenol sulfuric acid method (PSA)

For analysis of the polymer samples to 125 µL of polymer solution with a specific concentration depending on the expected functionalization degree of the polymer (see Table S6) was used. Procedure for polymer sample was the same as for the calibration curve.

Table S6: For sulfuric acid phenol method used concentration of polymer concentration based on the expected functionalization degree.

Polymer	Amount of polymer used [mg mL^{-1}]
PNIPAM	5.84
ManHPL1	5.83
ManHPL2	2.75
ManHPL7	0.62
ManHPL34	0.22
ManHPL97	0.12
ManEL1	5.74
ManEL2	2.66
ManEL5	1.26
GalHPL3	2.92

S7 ATR-FTIR Spectroscopy

To show the successful functionalization of PNAS with isopropyl amine to **PNIPAM** ATR-FTIR measurements were executed. Comparison of both measurements (see **Figure S7a**) show an increase in υ(NH) and a loss of υ(CO-O-R) indicating a successful functionalization.

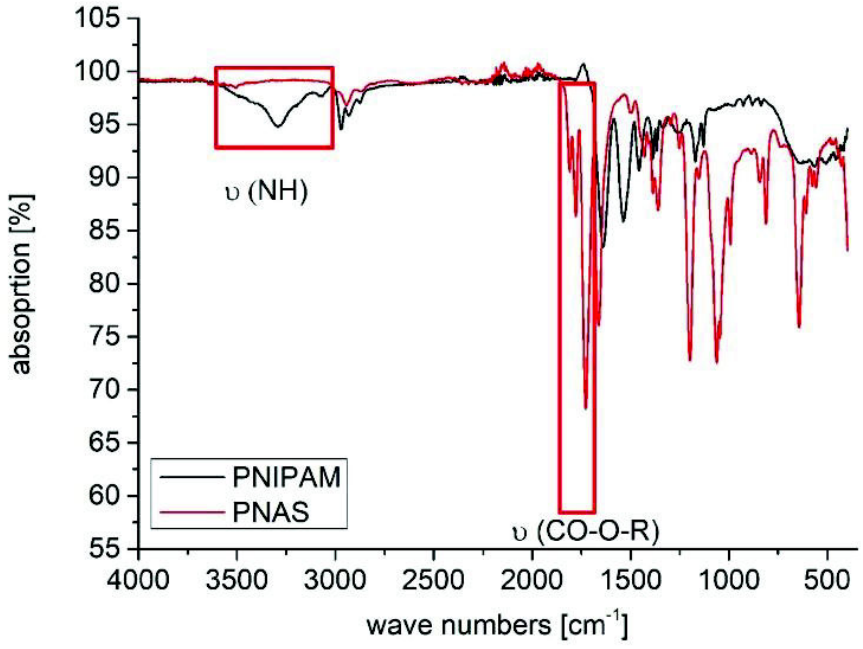

Figure S7a: Comparison of ATR-FTIR measurement of **PNIPAM** and PNAS.

As an indication of the successful functionalization of PNAS with isopropyl amine and carbohydrate ligands ATR-FTIR measurements were executed. Comparison of ATR-FTIR

measurements of **PNIPAM** and **ManHPL** glycopolymers (see **Figure S7b**) show a decrease in amide vibrations and an increase in carbohydrate vibrations.

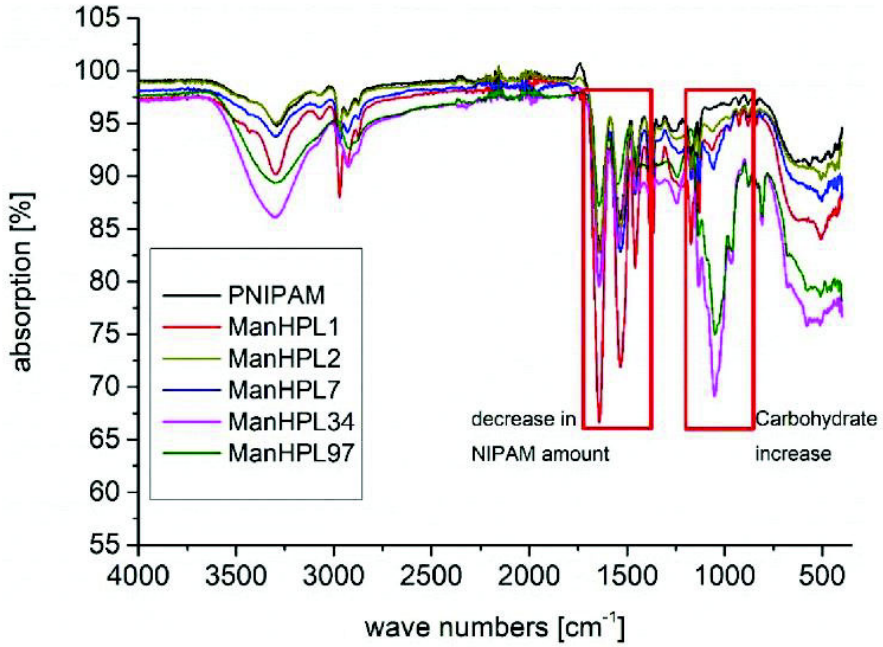

Figure S7b: Comparison of ATR-FTIR measurement of **PNIPAM** and **ManHPL** glycopolymers.

Magnification of wave number range 1250-2000 cm^{-1} (see **Figure S7c**) show that in the area of expected ester vibration no signal is visible for ManHPL glycopolymers. Therefore, no Carbohydrate unit is linked to the polymer backbone by an ester bond.

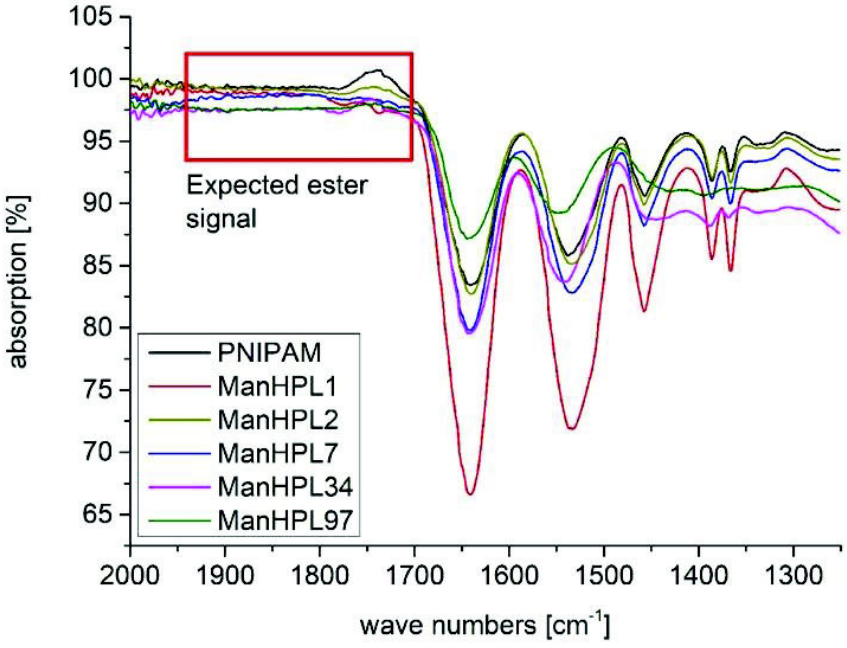

Figure S7c: Magnification of ATR-FTIR measurement of **PNIPAM** and **ManHPL** glycopolymers from wave numbers 1250-2000 cm^{-1}.

Comparison of ManEL glycopolymers (see **Figure S7d**) show and confirm an increase in carbohydrate vibrations at increasing functionalization degree and a decrease in amide vibrations.

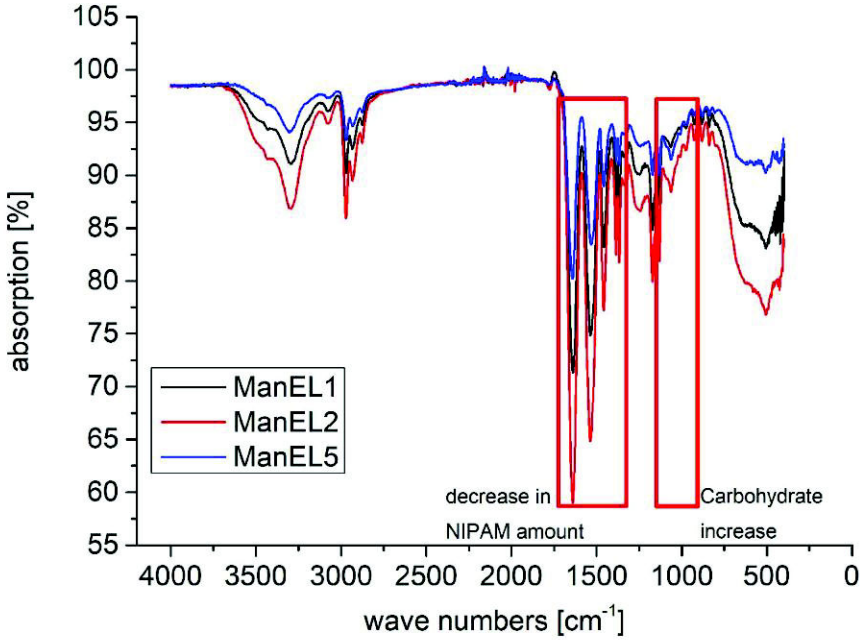

Figure S7d: Comparison of ATR-FTIR measurement of **ManEL** glycopolymers.

Magnification of wave number range 1250-2000 cm^{-1} (see **Figure S7e**) show that in the area of expected ester vibration no signal is visible for ManEL glycopolymers. Therefore, no Carbohydrate unit is linked to the polymer backbone by an ester bond.

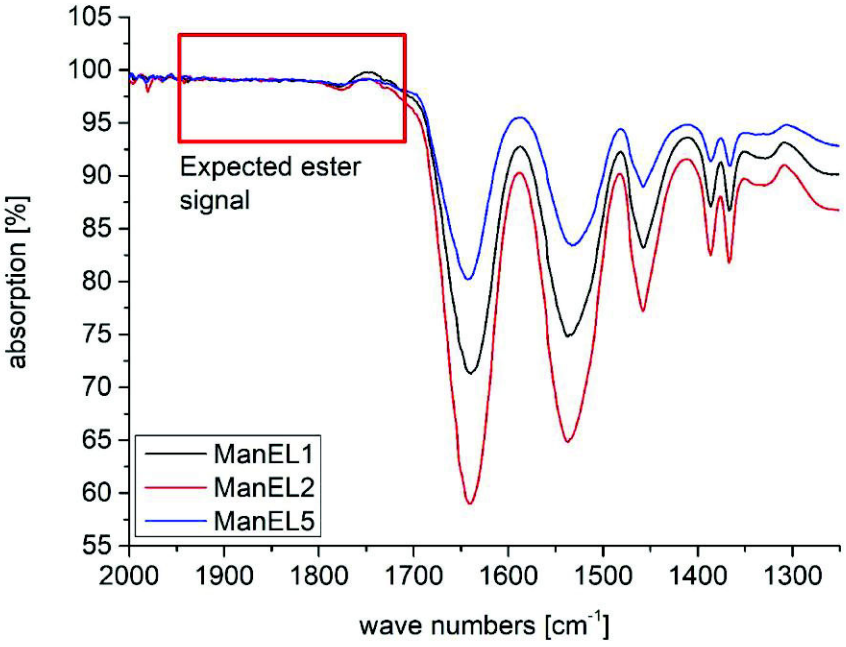

Figure S7e: Magnification of ATR-FTIR measurement of **PNIPAM** and **ManHPL** glycopolymers from wave numbers 1250-2000 cm^{-1}.

S8 Differential scanning calorimetry (DSC)

Below the DSC measurements are shown. Nine heating/cooling segments were done during the measurement. The segments were done as following: Heating segment 1 (black), cooling segment 1 (red), Heating segment 2 (blue), cooling segment 2 (magenta), Heating segment 3 (olive), cooling segment 3 (navy blue), Heating segment 4 (violet), cooling segment 4 (purple), Heating segment 5 (brown). The first heating segment was done to remove solvent leftovers and therefore, the measurements end with a heating segment. T_g was determined by the average values of turning points during the heating segments.

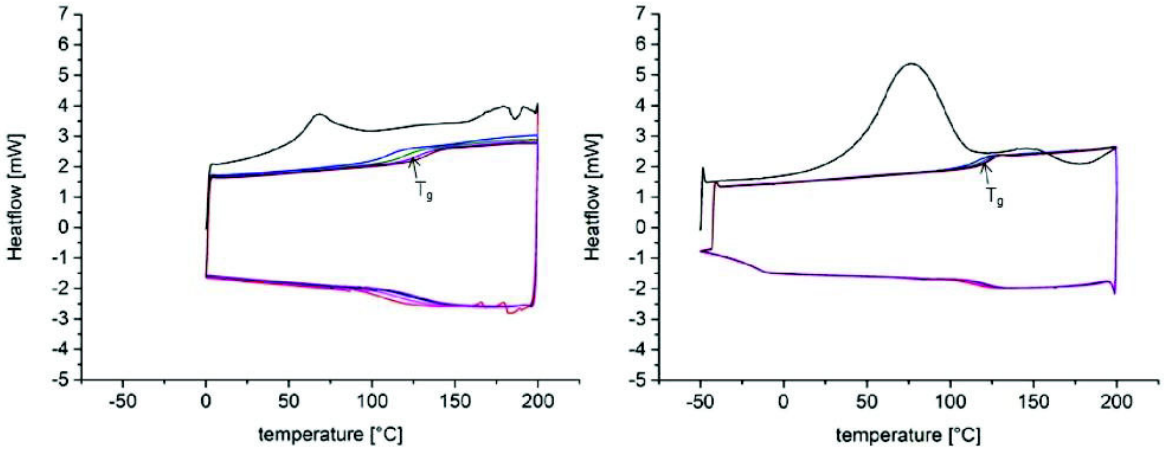

Figure S8a: DSC measurements of polymer precursor PNAS (left) and negative control **PNIPAM** (right).

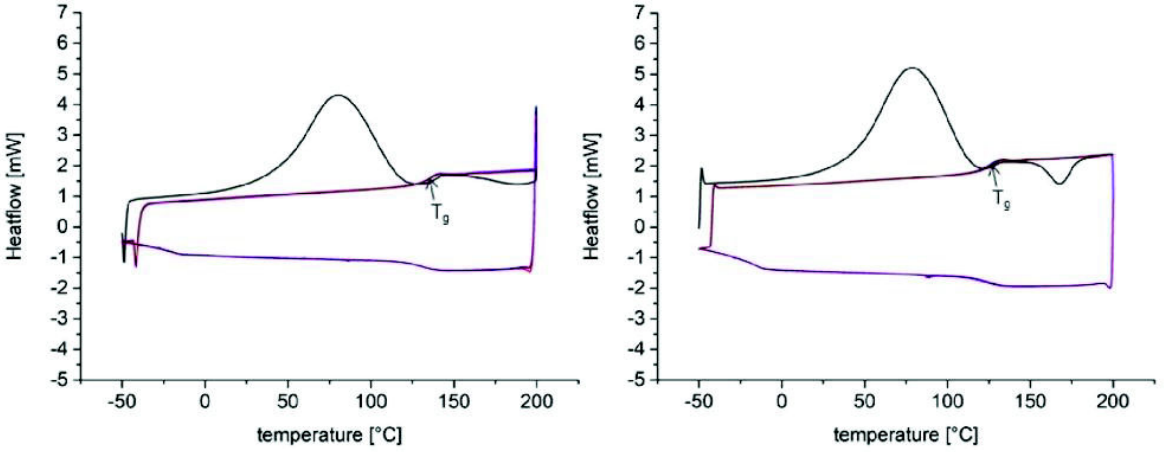

Figure S8b: DSC measurements of non-binding control **GalHPL3** (left) and glycopolymer **ManHPL1** (right).

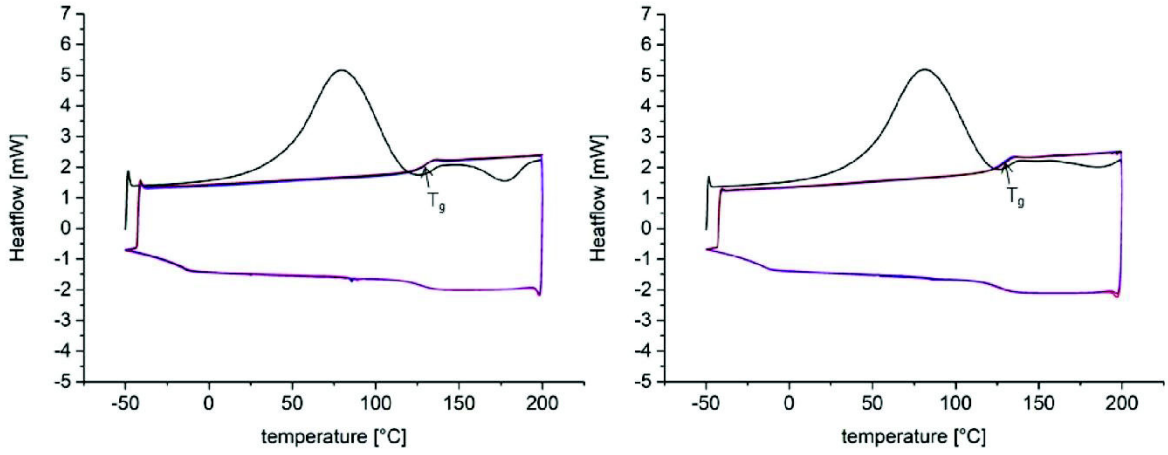

Figure S8c: DSC measurements of glycopolymer **ManHPL2** (left) and glycopolymer **ManHPL7** (right).

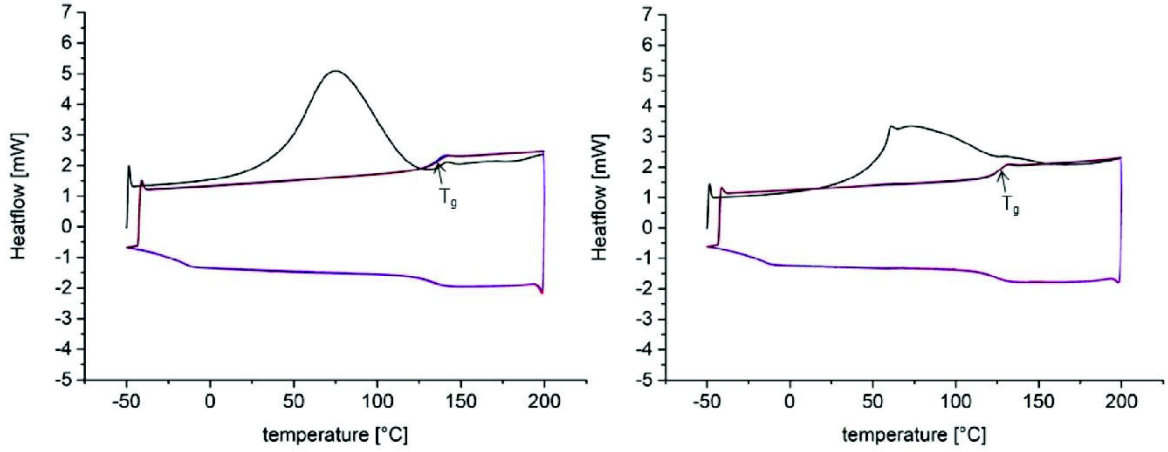

Figure S8d: DSC measurements of glycopolymer **ManHPL34** (left) and glycopolymer **ManHPL97** (right).

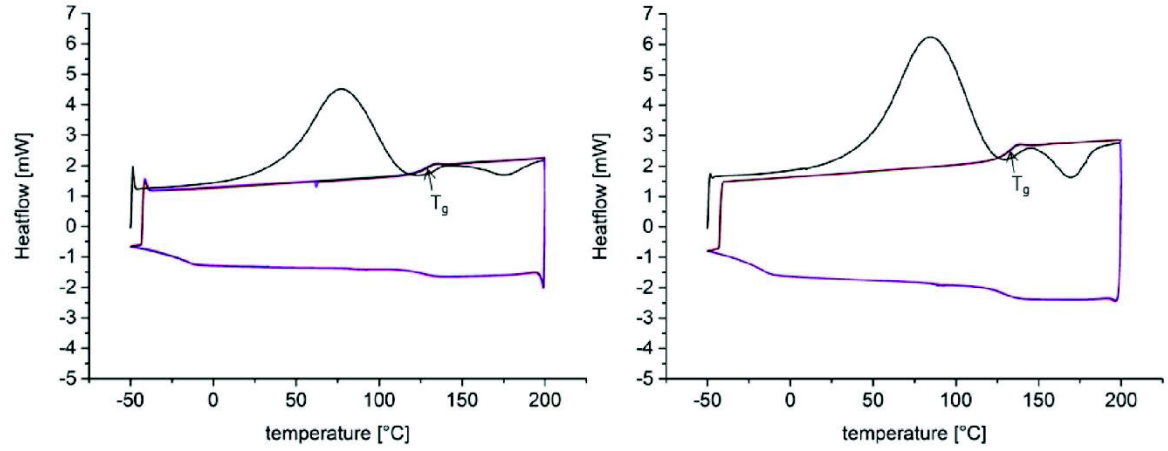

Figure S8e: DSC measurements of glycopolymer **ManEL1** (left) and glycopolymer **ManEL2** (right).

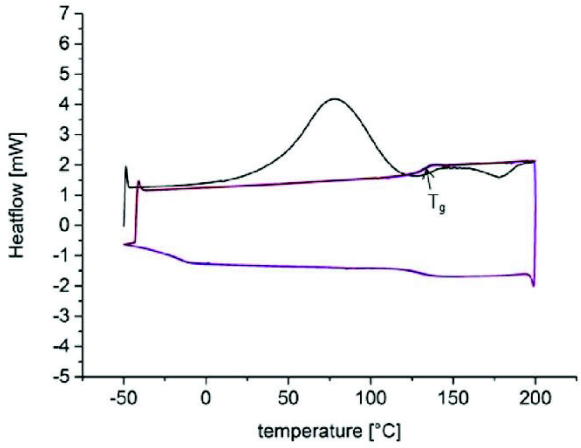

Figure S8f: DSC measurement of glycopolymer **ManEL5.**

S9 Turbidimetry studies

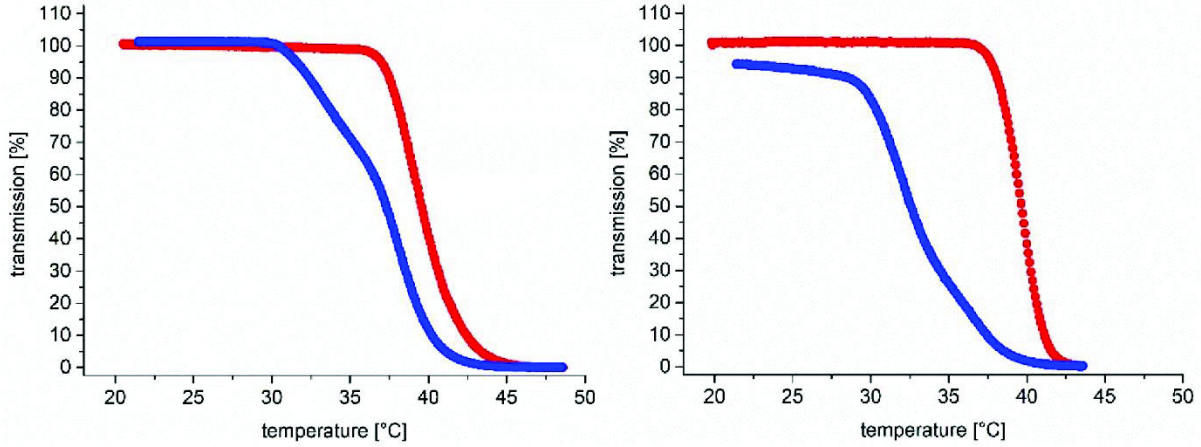

Figure S9a: Turbidity measurements of **ManHPL1** with a polymer concentration of 5 mg mL^{-1} in LBB. left: without ConA, right: with ConA. Red lines denote heating cycle. Blue line denotes cooling cycle.

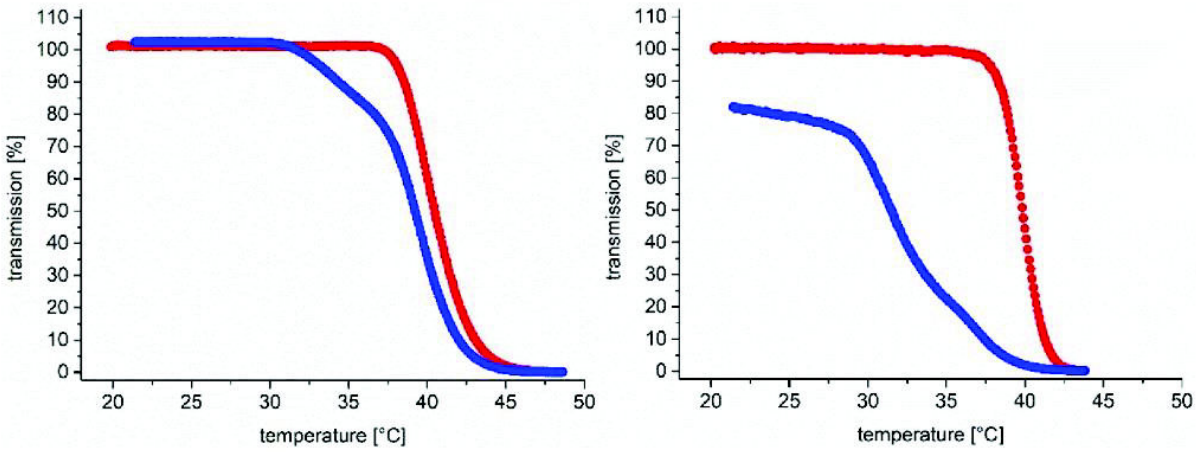

Figure S9b: Turbidity measurement of **ManHPL2** with a polymer concentration of 5 mg mL^{-1}in LBB, left: without ConA, right: with ConA.

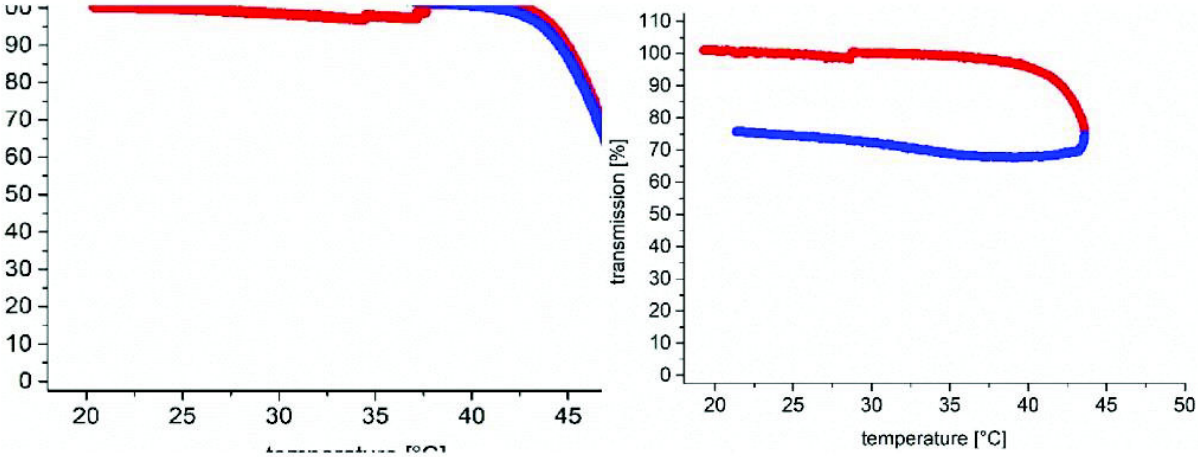

Figure S9c: Turbidity measurements of **ManHPL7** with a polymer concentration of 5 mg mL^{-1}in LBB, left: without ConA, right: with ConA.

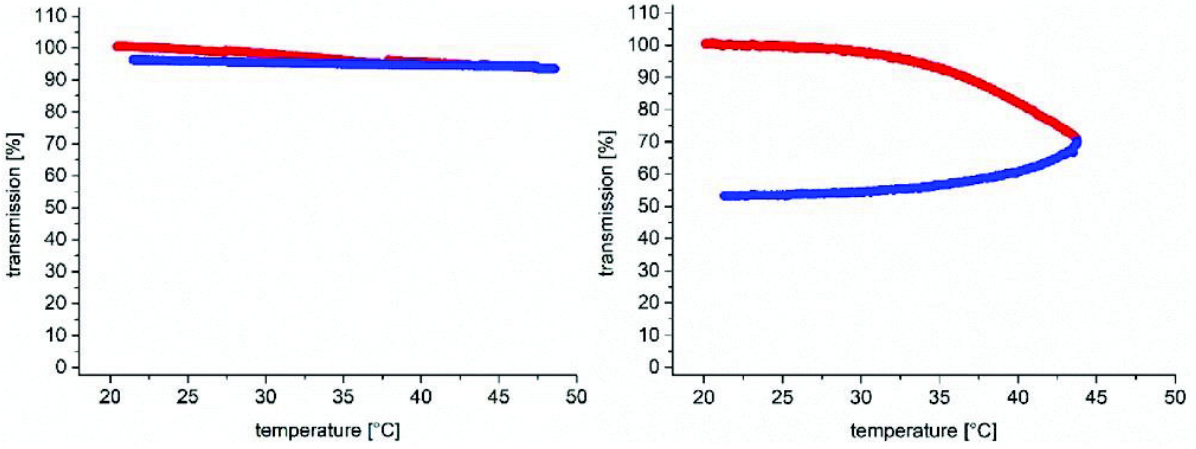

Figure S9d: Turbidity measurements of **ManHPL34** with a polymer concentration of 5 mg mL^{-1} in LBB, left: without ConA, right: with ConA.

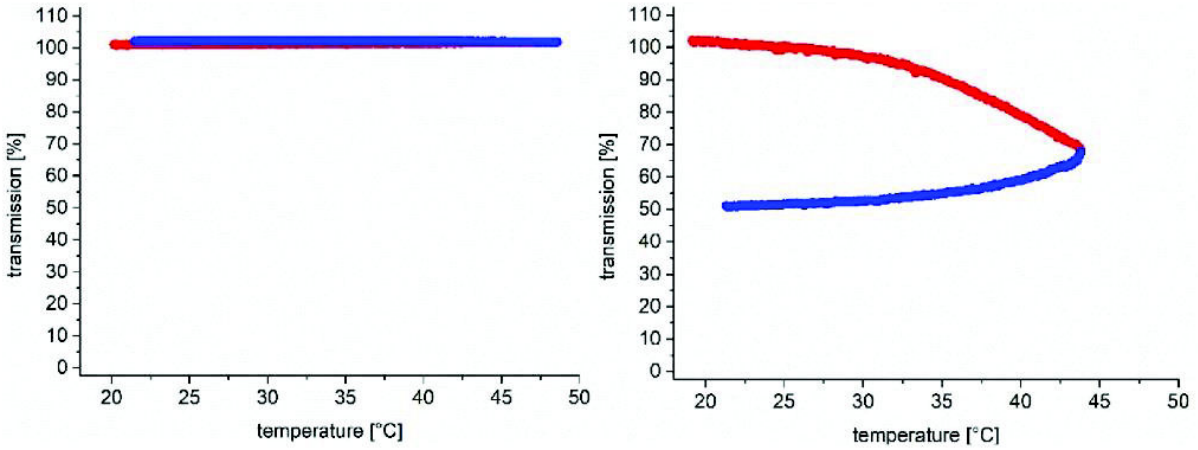

Figure S9e: Turbidity measurements of **ManHPL97** with a polymer concentration of 5 mg mL^{-1} in LBB, left: without ConA, right: with ConA.

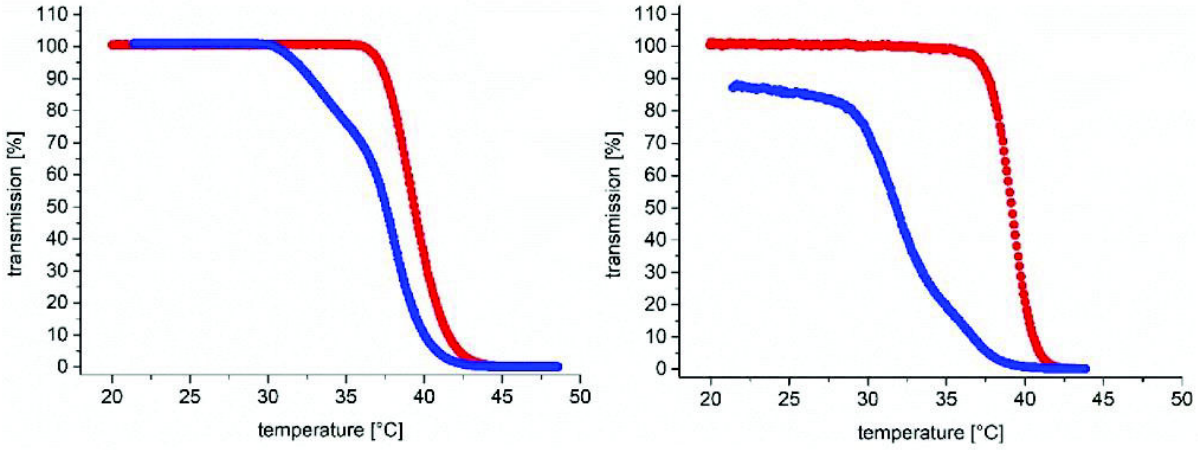

Figure S9f: Turbidity measurements of **ManEL1** with a polymer concentration of 5 mg mL^{-1} in LBB, left: without ConA, right: with ConA.

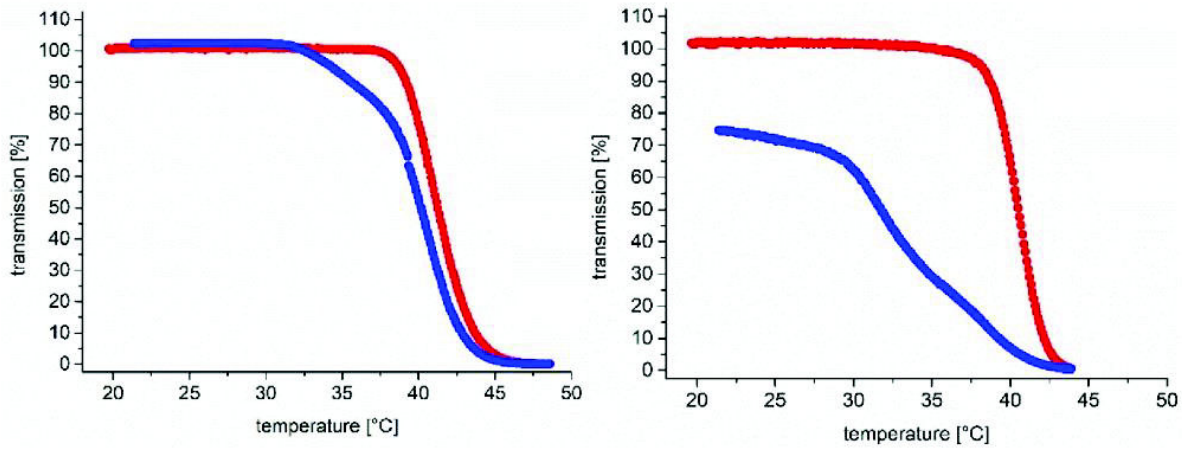

Figure S9g: Turbidity measurement of **ManEL2** with a polymer concentration of 5 mg mL^{-1} in LBB, left: without ConA, right: with ConA.

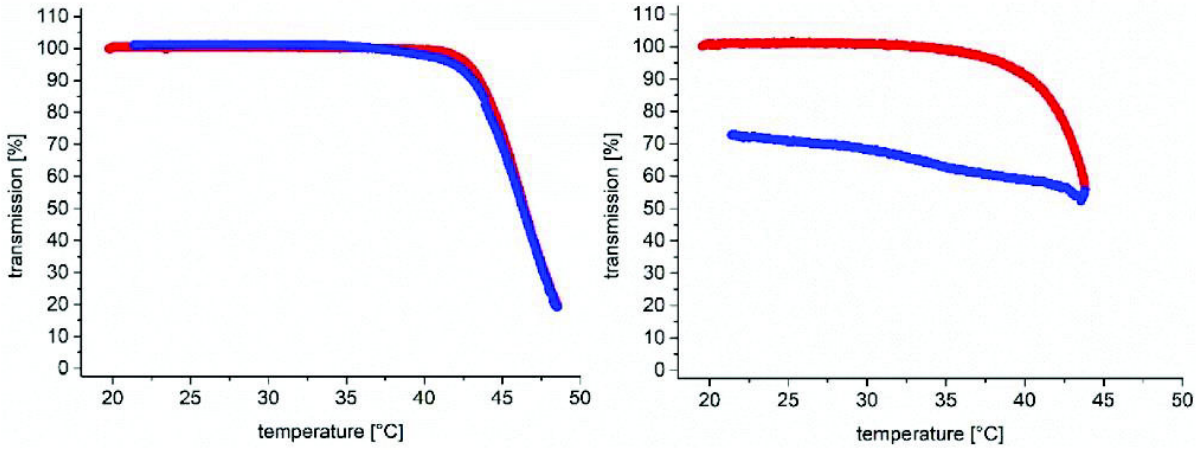

Figure S9h: Turbidity measurement of **ManEL5** with a polymer concentration of 5 mg mL^{-1} in LBB, left: without ConA, right: with ConA.

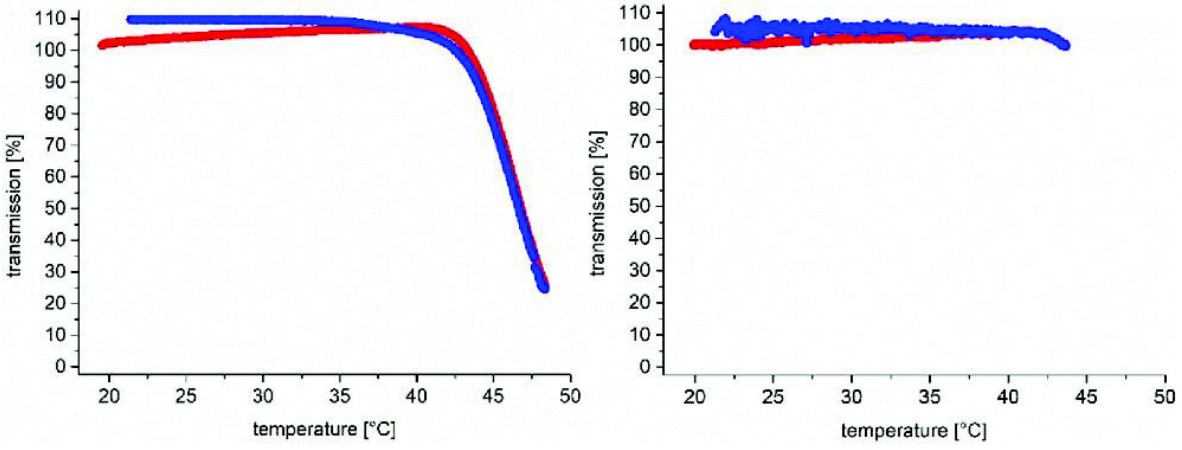

Figure S9i: Turbidity measurements of **GalHPL3** with a polymer concentration of 5 mg mL^{-1} in LBB, left: without ConA, right: with ConA.

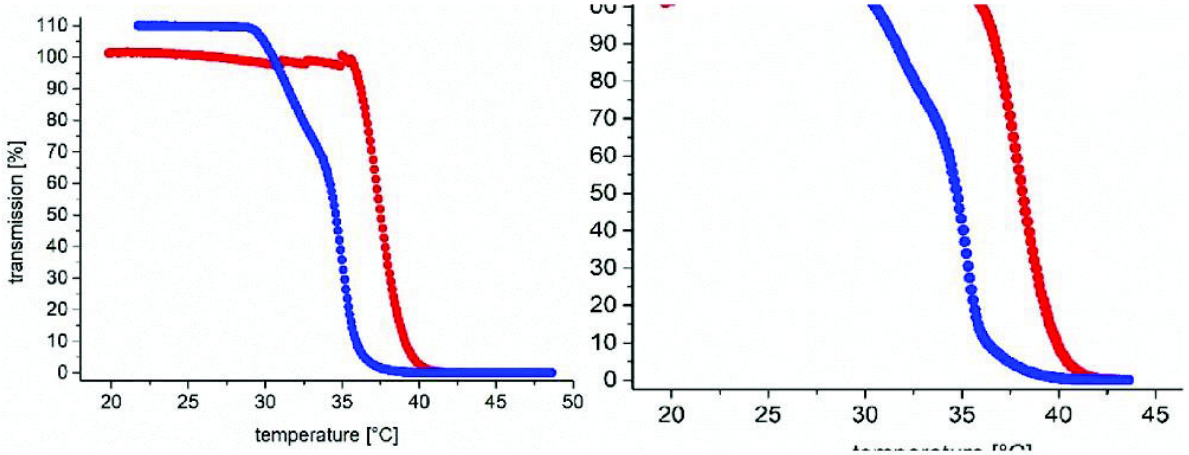

Figure S9j: Turbidity measurements of **PNIPAM** with a polymer concentration of 5 mg mL^{-1} in LBB, left: without ConA, right: with ConA.

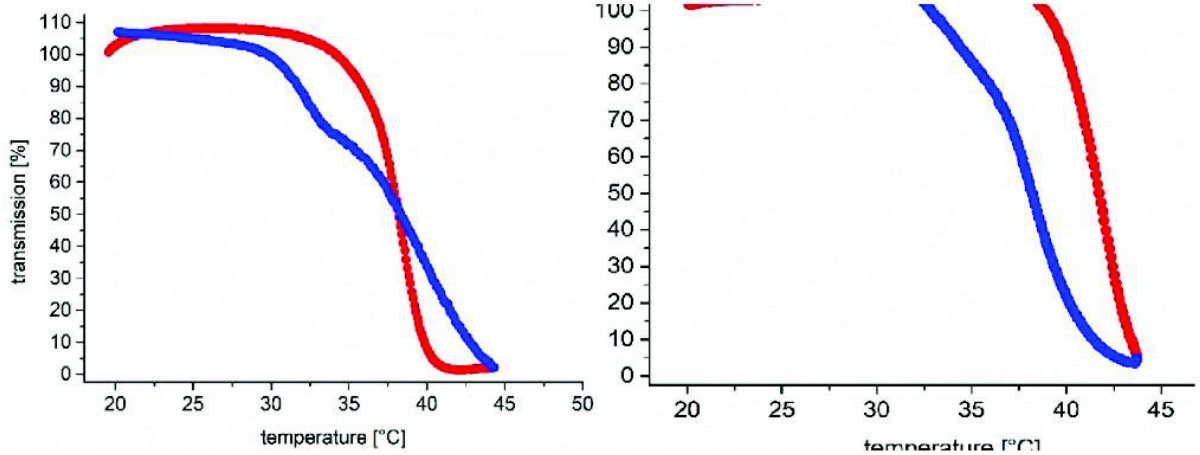

Figure S9k: Turbidity measurement of **ManHPL2** with a polymer concentration of 5 mg mL^{-1} in LBB, left: with ConA at a heating rate of 0.1 °C min^{-1}, right with ConA and 10 mM MeMan.

S10 Temperature dependent adhesion inhibition of *E. coli*

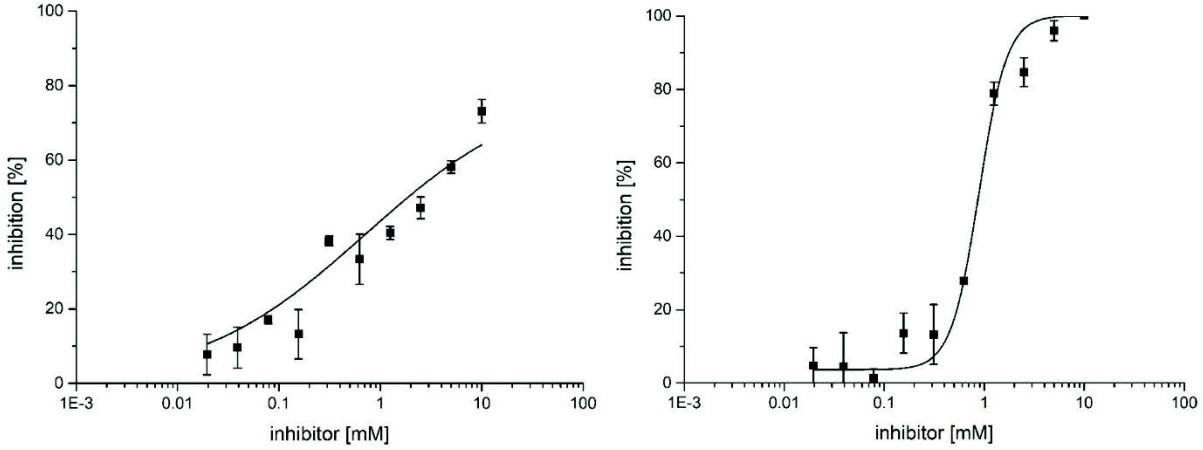

Figure S10a: Representative inhibition curves obtained in testing of **ManHPL1**. The curves result from one experiment and the depicted standard deviations from triplicate determinations on one plate, left: 20 °C, right: 40 °C.

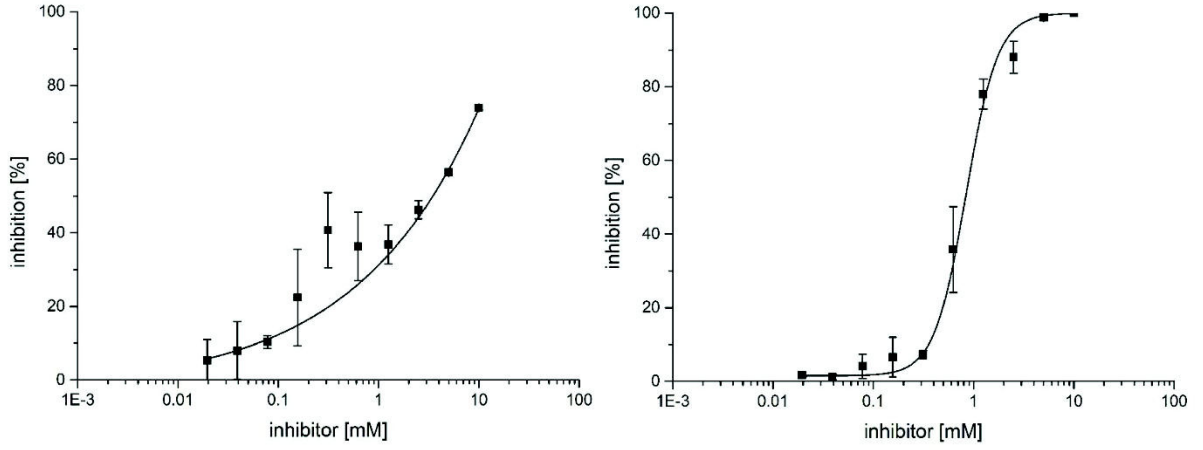

Figure S10b: Representative inhibition curves obtained in testing of **ManHPL2**. The curves result from one experiment and the depicted standard deviations from triplicate determinations on one plate, left: 20 °C, right: 40 °C.

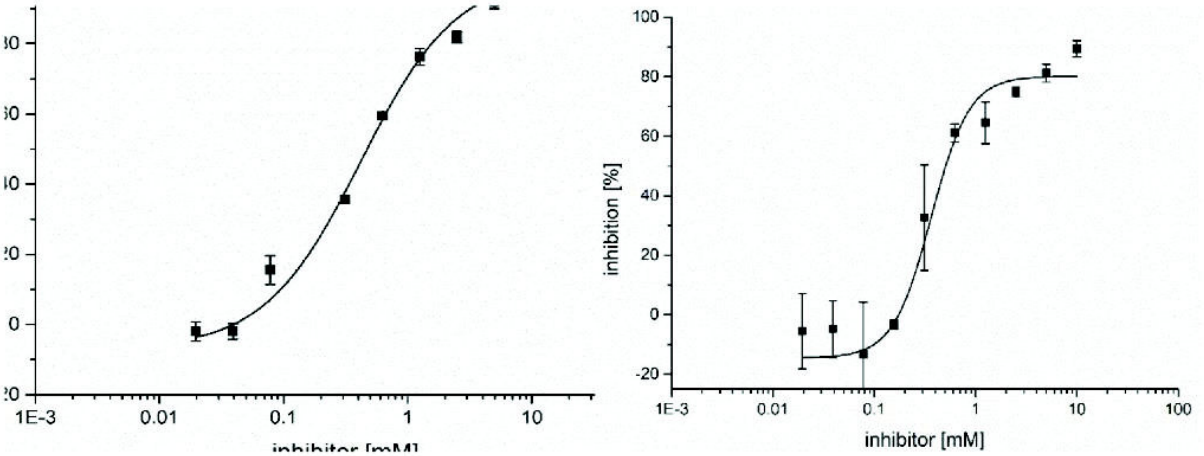

Figure S10c: Representative inhibition curves obtained in testing of **ManHPL7**. The curves result from one experiment and the depicted standard deviations from triplicate determinations on one plate, left: 20 °C, right: 40 °C.

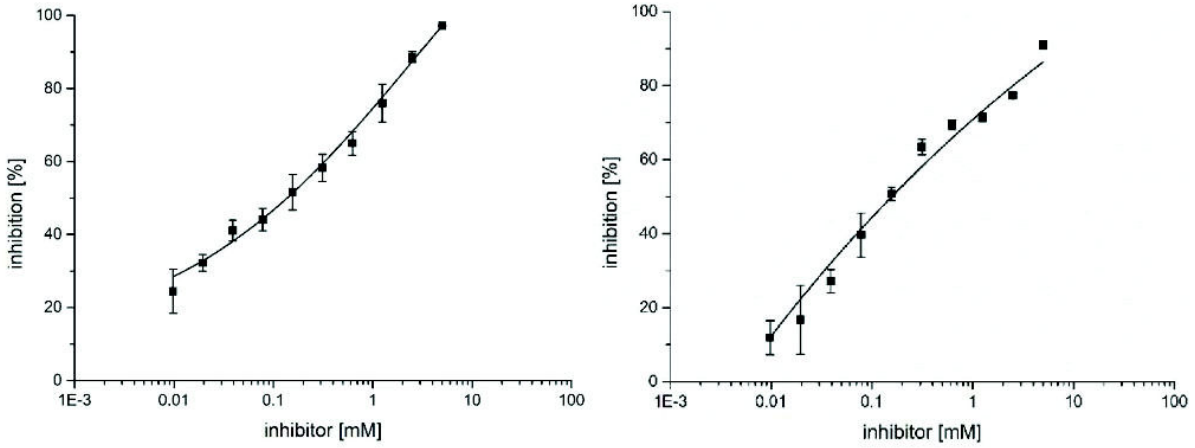

Figure S10d: Representative inhibition curves obtained in testing of **ManHPL97**. The curves result from one experiment and the depicted standard deviations from triplicate determinations on one plate, left: 20 °C, right: 40 °C.

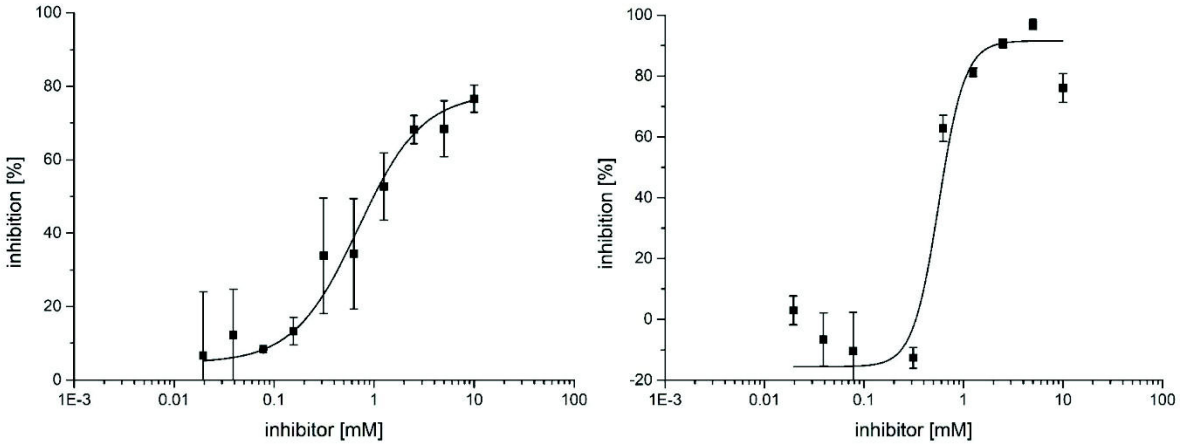

Figure S10e: Representative inhibition curves obtained in testing of **ManEL1**. The curves result from one experiment and the depicted standard deviations from triplicate determinations on one plate, left: 20 °C, right: 40 °C.

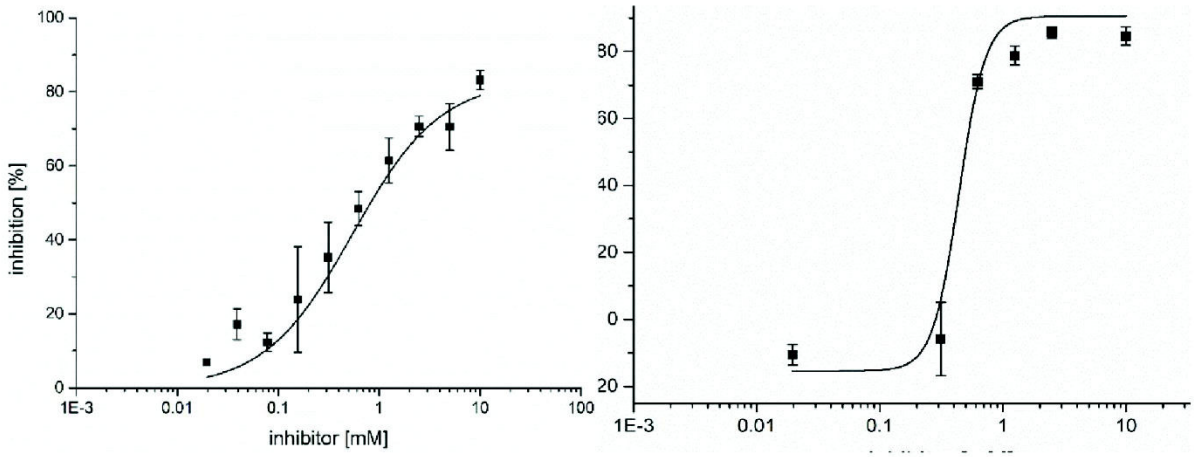

Figure S9f: Representative inhibition curves obtained in testing of **ManEL2**. The curves result from one experiment and the depicted standard deviations from triplicate determinations on one plate, left: 20 °C, right: 40 °C.

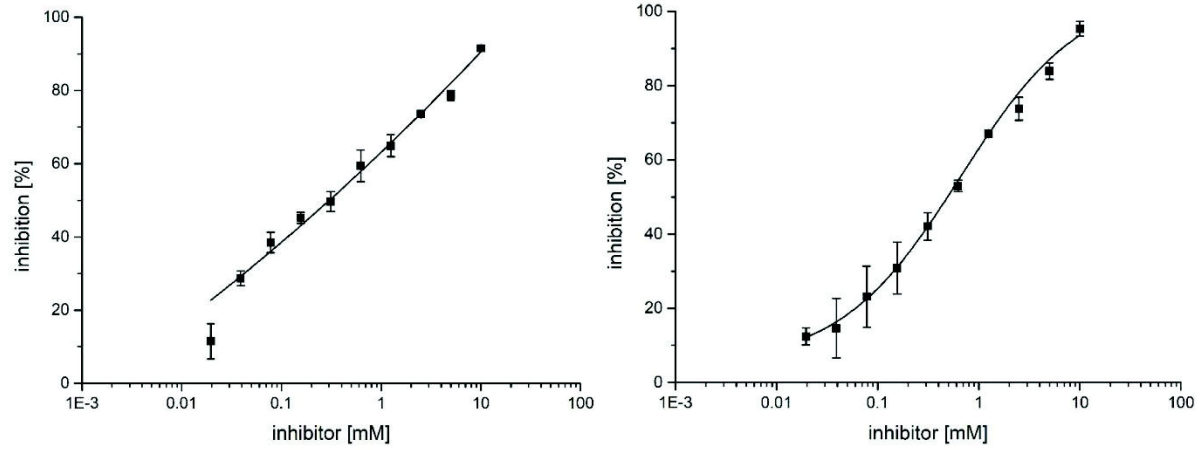

Figure S10g: Representative inhibition curves obtained in testing of **ManEL5**. The curves result from one experiment and the depicted standard deviations from triplicate determinations on one plate, left: 20 °C, right: 40 °C.

S11 Temperature dependent adhesion inhibition of ConA

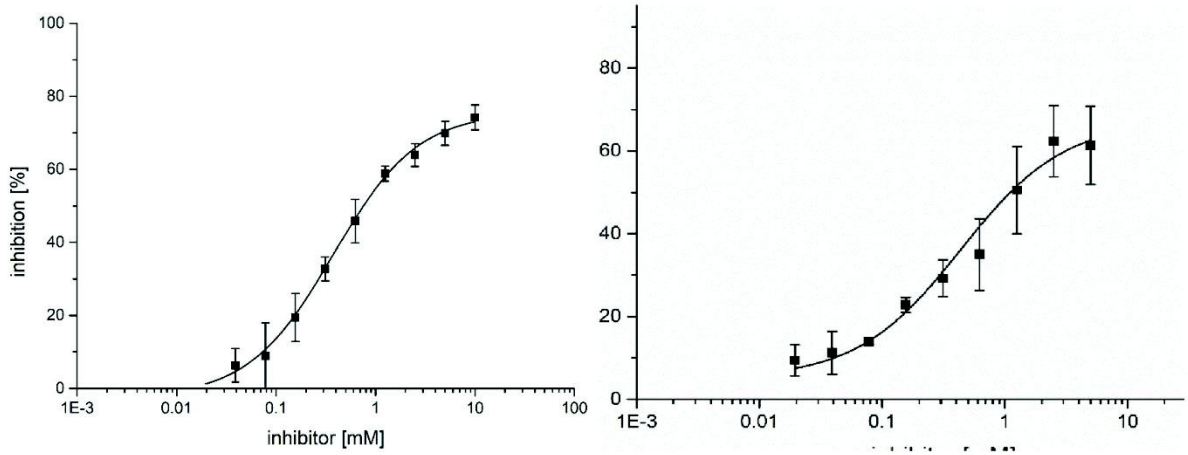

Figure S11a: Representative inhibition curves of ConA obtained in testing of **PNIPAM**. The curves result from one experiment and the depicted standard deviations from triplicate determinations on one plate, left: 20 °C, right: 40 °C.

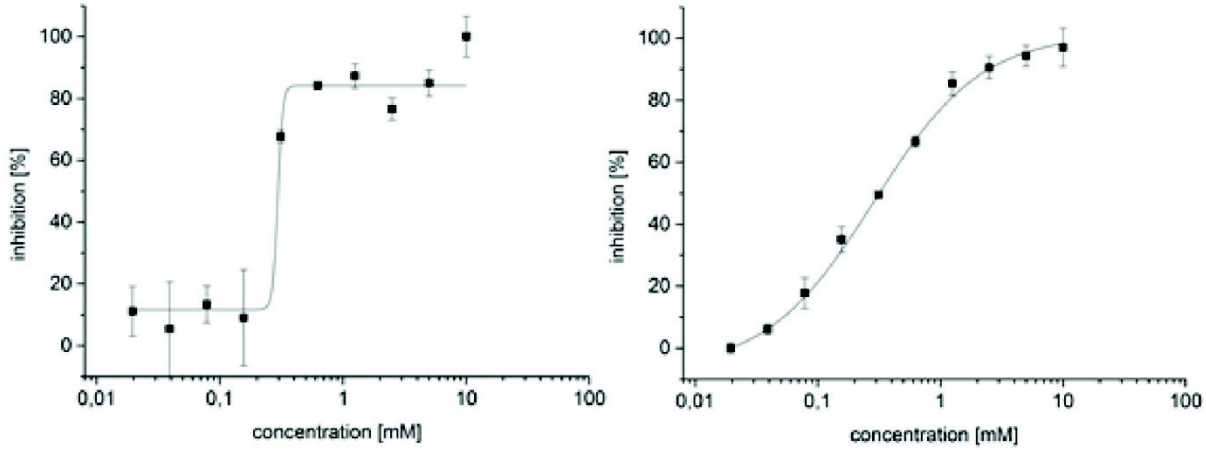

Figure S11b: Representative inhibition curves of ConA obtained in testing of **ManHPL1**. The curves result from one experiment and the depicted standard deviations from triplicate determinations on one plate, left: 20 °C, right: 40 °C.

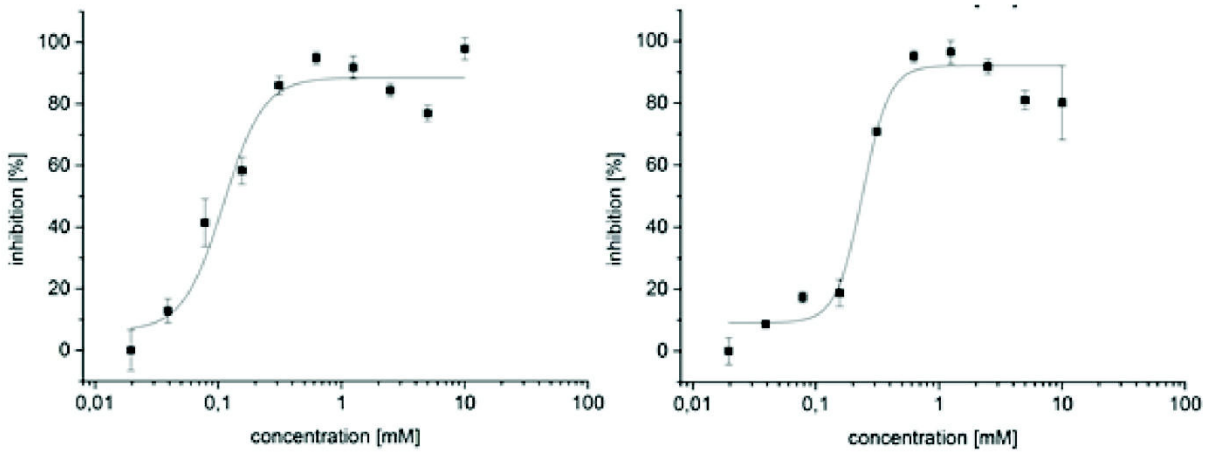

Figure S11c: Representative inhibition curves of ConA obtained in testing of **ManHPL2**. The curves result from one experiment and the depicted standard deviations from triplicate determinations on one plate, left: 20 °C, right: 40 °C.

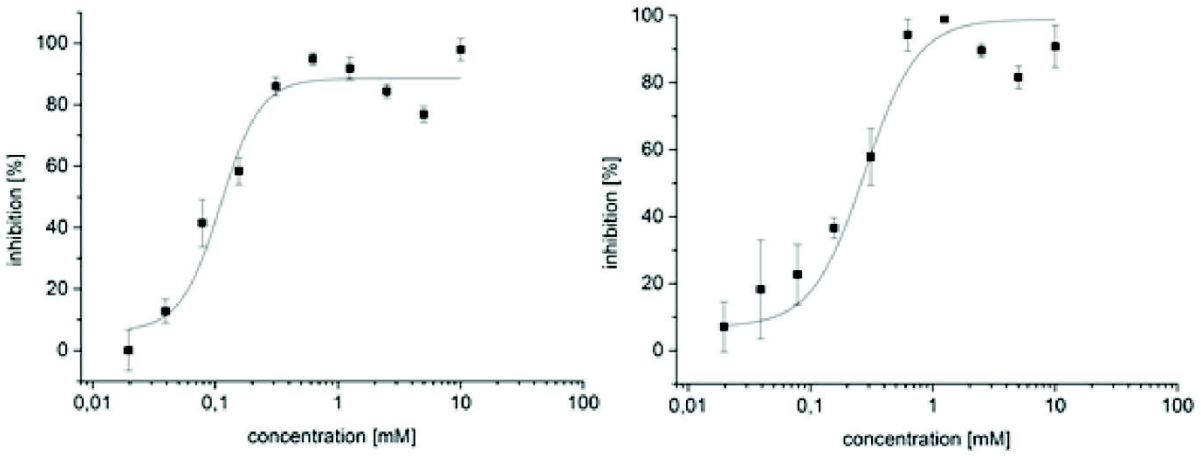

Figure S11d: Representative inhibition curves of ConA obtained in testing of **ManHPL7**. The curves result from one experiment and the depicted standard deviations from triplicate determinations on one plate, left: 20 °C, right: 40 °C.

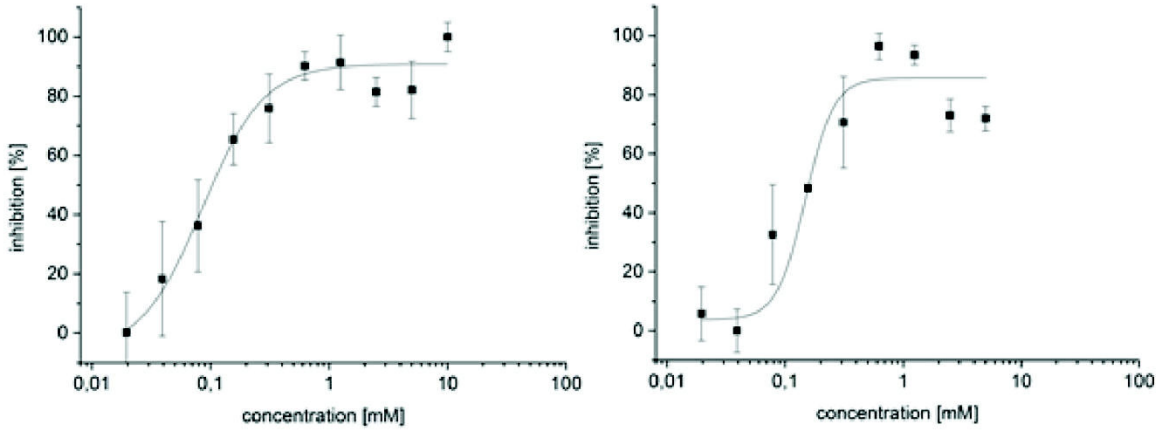

Figure S10e: Representative inhibition curves of ConA obtained in testing of **ManEL1**. The curves result from one experiment and the depicted standard deviations from triplicate determinations on one plate, left: 20 °C, right: 40 °C.

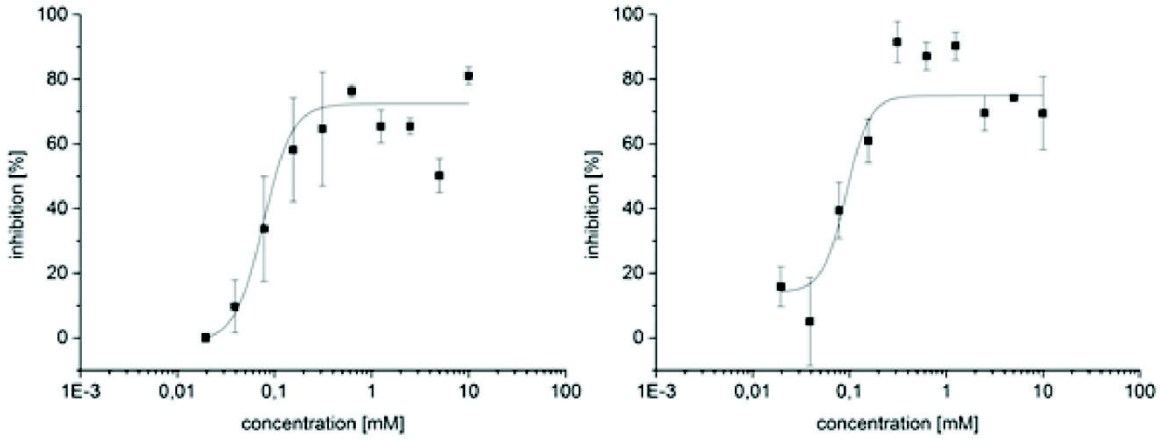

Figure S11f: Representative inhibition curves of ConA obtained in testing of **ManEL2**. The curves result from one experiment and the depicted standard deviations from triplicate determinations on one plate, left: 20 °C, right: 40 °C.

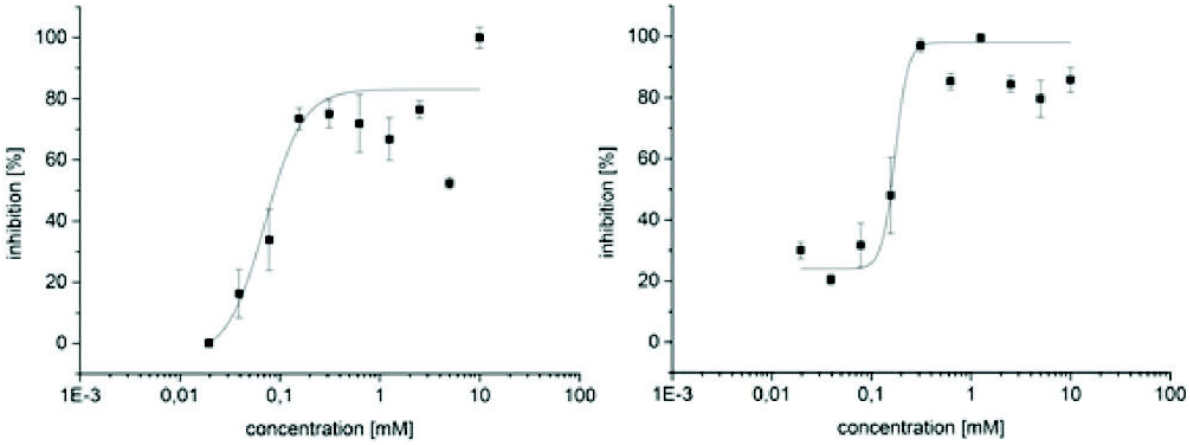

Figure S11g: Representative inhibition curves of ConA obtained in testing of **ManEL5**. The curves result from one experiment and the depicted standard deviations from triplicate determinations on one plate, left: 20 °C, right: 40 °C.

S12 Dynamic light scattering of the glycopolymers

Table S12: Hydrodynamic diameters as measured on a Malvern Nano ZS, scattering angle 173°C, temperature 20°C, the dispersity was calculated from the cumulant Γ / μ^2.

polymer	hydrodynamic diameter	dispersity (DLS)
ManHPL1	7.9	0.36
ManHPL2	7.3	0.33
ManEL1	8.3	0.38
ManEL2	8.0	0.37
ManHPL34	7.9	0.33
ManHPL97	7.6	0.30

S13 Instrumentation

Nuclear Magnetic Resonance Spectroscopy (NMR)

^{1}H-NMR and ^{13}C-NMR (600 MHz) were measured on a Bruker AVANCE III 600 (Bremen, Germany). As internal standard chemical shifts were referenced to the residual non-deuterated solvents ($CDCl_3$: ^{1}H 7.26, ^{13}C 77.16, D_2O: ^{1}H 4.79, DMSO-d_6: ^{1}H 2.50). All chemical shifts are reported in delta (δ) expressed in parts per million (ppm). The following abbreviations were used to indicate multiplicities: s = singlet, d = doublet, t = triplet, m = multiplet.

Size exclusion chromatography (SEC)

SEC measurements were performed using a ViscotekGPCmax VE2001 system. The System has a column set compromising one TSK HHR-H, 100 Å pore size and 10 µm particle size, 800 × 5.0 mm [Length × ID]pre-column and two Viskotek TSK GMHHR-M linear, 10 µm particle

size, 300 × 8.0 mm [Length × ID]columns. The columns were constantly heated to a temperature of 60 °C. N,N-Dimethylformamide (0.05 M LiBr) was used as eluent at a flow rate of 1 mL min^{-1}. For detection a Viscotek VE 3500 RIdetector was used. The system was calibrated with polystyrene standards of a molecular range from 1280 g mol^{-1} to 1373000 g mol^{-1}.

ATR-FTIR Spectroscopy

For ATR-FTIR spectroscopy measurements a NICOLET 6700 ATR-FTIR spectrometer from Thermo Scientific was used. For each measurement a background measurement was executed that was subtracted from the sample measurement.

Freeze Dryer

An Alpha 1-4 LD plus instrument from Martin Christ Freeze Dryers GmbH (Osterrode, Germany) was used for lyophilization of all polymer samples. The main drying method was set to -54 °C and 0.1 mbar.

UV-Vis Spectroscopy

On a dual-trace spectrometer Specord® 210 Plus from *Analytik Jena AG* (Jena, Germany) all UV-Vis measurements were performed at 25 °C. Using Win ASPECT PLUS software the instrument was operated. Protein concentration measurements were performed in a cuvette QX quartz cuvette (d = 1 cm, V = 3.5 mL) from Hellma Anayltics (Mühlheim, Germany). For determination of sugar concentration the absorption from 350-550 nm was measured. Using the absorption and a calibration curve the concentration of carbohydrates was calculated.

Dynamic differential scanning calorimetry (DSC)

Dynamic differential scanning calorimetry (differential scanning calorimetry, DSC) was performed on a DSC 3 equipped with a FRS 5/5+ Sensor, an IntraCooler Julabo FT900 and a GC005 Gas controller of the company Mettler Toledo. Aluminum crucible with a volume of 40 µL without pin were used for the measurements. The heating and cooling rates were 15 K min^{-1} with a total of nine segments each in a temperature range from -50 °C to 200 °C.

Microplate reader

All adhesion inhibition measurements were performed on a CLARIOstar® microplate reader from BMG LABTECH (Freiburg, Germany) at ambient temperature. Using the BMG Mars

software the measurements were evaluated. For all measurements F-bottom 96 black well plates from Greiner BIO-ONE were used.

S14 Buffer and Media

LB-Medium (PKL1162)

12.5 g of LB Broth (Miller) (powder microbial growth medium) were dissolved in 500 mL ultrapure water. The powder contains tryptone (5.0 g), sodium chloride (5.0 g) and yeast extract (2.5 g). Afterwards the solution was sterilized for 30 min at 121 °C and cooled to room temperature. 50.0 mg of ampicillin and 25.0 mg of chloramphenicol were added.

PBS buffer

Five tablets of phosphate buffered saline was dissolved in 1 L of ultrapure water. The final concentrations of the buffer were 0.01 M phosphate buffer, 0.0027 M potassium chloride and 0.137 M sodium chloride. The pH was checked with a potentiometer and set to 7.4.

LBB buffer

Lectin binding buffer (LBB) was used for all measurements with Concanavalin A. Lectin binding buffer contains 10 mM HEPES ((4-(2-hydroxyethyl)-1-piperazineethanesulfonic acid) as buffering agent, which was adjusted to a pH of 7.4 with 1 M NaOH. Thereafter, calcium chloride (1 mM) and manganese chloride (1 mM) and sodium chloride (50 mM) were dissolved in the solution. To prevent bacterial growth in the buffer sodium azide was added to a final concentration of 0.05 wt%

Carbonate-buffer solution

For the carbonate-buffer solution 1.59 g sodium carbonate and 2.52 g sodium hydrogen carbonate were dissolved in 1 of ultrapure water. Afterwards the pH was adjusted to pH 9.5.

Bacterial culture

E. coli PKL 1162 were grown in LB medium (PKL 1162) overnight in a sterilized test tube, which was covered with aluminum foil at 37 °C. The tubes were shaken with a speed of 140 rpm to guarantee a constant mixing of the solution.

1. J. A. Himanen and P. M. Pihko, *Eur. J. Org. Chem.*, 2012, DOI: 10.1002/ejoc.201200277, 3765-3780.
2. W. Hayes, H. M. I. Osborn, S. D. Osborne, R. A. Rastall and B. Romagnoli, *Tetrahedron*, 2003, **59**, 7983-7996.

5.3. Quantifying thermo-switchable carbohydrate mediated interactions via soft colloidal probe adhesion studies

Authors: **Alexander K. Strzelczyk**, Tanja J. Paul, Stephan Schmidt

Journal: *Macromolecular Bioscience*.

Issue: Manuscript accepted

Type of Paper: Full Paper

Impact Factor: 2.895 (2019)

Own Contribution (first author)

Synthesis of Poly (*N*-isopropylacrylamide-co-*N*-(2-hydroxypropyl) α-$_D$-mannopyranoside acrylamide) and Poly (*N*-isopropylacrylamide-co-*N*-ethyl α-$_D$-mannopyranoside acrylamide) polymers as well as their characterization with DSC, GPC, ^{1}H-NMR and ATR-FTIR. Synthesis of poly (ethylene glycol) based SCPs and functionalization with thermoresponsive polymers as well as characterization of elastic modulus and functionalization degree. Measurement of adhesion energies. Writing of the paper.

Quantifying thermo-switchable carbohydrate mediated interactions via soft colloidal probe adhesion studies

*Alexander Klaus Strzelczyk, Tanja Janine Paul and Stephan Schmidt**

A. K. Strzelczyk, Tanja Janine Paul, Jun. Prof. Dr. S. Schmidt

Institute of Organic and Macromolecular Chemistry, Heinrich-Heine-University Düsseldorf, Universitatsstraße 1, 40225 Dusseldorf, Germany,

* E-mail: stephan.schmidt@hhu.de

Keywords

biomimetic hydrogel, biointerface, elastic solids, contact mechanics, PEG, soft colloidal probe; RICM, responsive polymer, interactive material

Abstract

Thermosensitive polymers enable externally controllable biomolecular interactions but hysteresis effects hamper the reversibility and repeated use of these materials. To quantify the temperature-dependent interactions and hysteresis effects an optical adhesion assay based on PEG microgels (soft colloidal probes, SCPs) on mannose binding concanavalin A (ConA) surfaces is used. A series of thermoresponsive glycopolymers is synthesized varying the carbohydrate type, their density and linker type and then grafted to the SCPs. The carbohydrate mediated adhesion is influenced by the density of sugar ligands and increased above the lower critical solution temperature (LCST) of the glycopolymer. Importantly, a strong hysteresis was observed, i.e. cooling back below the LCST did not reduce the adhesion back to the initial value before heating. The hysteresis was stronger for hydrophobic linkers and for low carbohydrate functionalization degrees suggesting insufficient reswelling of the polymers due to hydrophobic interactions. The results are confirmed by studying the adhesion of *E. coli* to the SCPs, where an enhanced capture of the bacteria was observed above the LCST while the detachment upon cooling was not possible. Overall, the quantitative data on the switchable adhesion of specifically binding polymers may provide potential avenues for the design of the next generation interactive biomaterials.

Introduction

Stimuli responsive polymers provide avenues toward smart, interactive materials with a broad range of potential applications, e.g. in sensing, as actuators, in tissue engineering, in controlled drug release, and many more.[1],[2] Stimuli responsive polymers that enable the remote activation or deactivation of specific ligand-receptor interactions are being developed to facilitate site specific drug carriers, externally controlled binding to proteins, or capture / release of pathogens.[3-8] Most of these systems rely on thermoresponsive polymers undergoing a coil-to-globule transition in the physiological temperature range, thereby shifting the affinity of linked biomolecules, e.g. by varying their accessibility to control their specific binding. Thermoresponsive polymers with a lower critical solution temperature (LCST) between 30-40°C are most frequently used for such applications, where poly (*N*-isopropyl acrylamide) (PNIPAM), poly (*N*-vinyl caprolactam) or poly(oligoethylene glycols) are well-known examples.[9] As bioligands conjugated to such LCST polymers, carbohydrates have recently gained attention since they dominate biomolecular interactions on the cellular level and drive numerous physiological processes in the healthy or diseased state.[10] For example, carbohydrate binding proteins, so called

lectins, mediate cell adhesion, communication, fertilization, or pathogen invasion.[11,12] To target carbohydrate binding pathogens or lectins directly, responsive carbohydrate-ligand presenting polymers are being employed in microgels,[13-15] on nanoparticle surfaces,[16-18] 2D-surface coatings,[4] and linear or branched polymers.[19-22]

Although for most of these materials a temperature controllable shift of affinity was achieved, the cause for this behavior and the molecular details are not well understood. For example, when increasing the temperature above the LCST, some studies found that the affinity increased,[15,16,23] whereas other studies obtained decreasing carbohydrate binding affinities.[4,19,20] In addition, the use of these materials is often motivated by being able to remotely "switch" the ligand-receptor interaction on and off, implying reversible ligand-receptor complex formation and dissociation. However, such reversible binding of LCST polymers was rarely shown and typically limited to LCST polymer coatings without specific adhesion motifs targeting receptors.[24-26] Furthermore, the shifts in binding affinity via temperature change were usually indirectly quantified detecting the amount of bound binding partners (e.g. by fluorescence microscopy or SPR) but not via direct interaction energy measurements. Therefore, here we use so called soft colloidal probe (SCP) adhesion studies, to directly measure the specific interactions of carbohydrate ligands on an LCST polymer. The overall aim is to quantify the change in specific receptor binding when increasing the temperature above the LCST and to test whether these changes are reversible by cooling down below the LCST.

In this work, the SCP method employs soft poly(ethylene glycol) microgels that are functionalized with copolymers composed of PNIPAM and mannose or, respectively, galactose, repeat units (Figure 1). As binding partner for the polymers, we use concanavalin A (ConA), a mannose-specific lectin, coated on a glass slide. The SCP approach mimics soft contacts between bio-interfaces and allows sensitive measurements of adhesion energies based on weak carbohydrate interactions.[27],[28],[29] When adhering on the ConA coated glass surface, the carbohydrate functionalized SCPs deform due to their soft gel-like structure.[30,31] The mechanical deformation can be related to the Johnson-Kendall-Roberts (JKR) model of adhesion:[32-34]

$$a^3 = 6\pi\, W_{adh} R^2 / E_{eff} \quad (1)$$

with the contact radius a, the SCP radius R, the adhesion Energy W_{adh} and the effective elastic modulus E_{eff}=[4E/3(1-ν^2)], with the Poisson ratio ν and the elastic modulus E of the SCP. The straightforward optical detection of the contact radius a, and SCP radius R via

reflection interference contrast microscopy (RICM) allows for the consistent analysis of the SCP adhesion energies as a function of temperature. Furthermore, the findings obtained from the SCP model system are compared to a bacteria binding assay, where the adhesion of type 1 fimbriated *E. coli* to the thermoresponsive polymers is quantified by fluorescence microscopy.

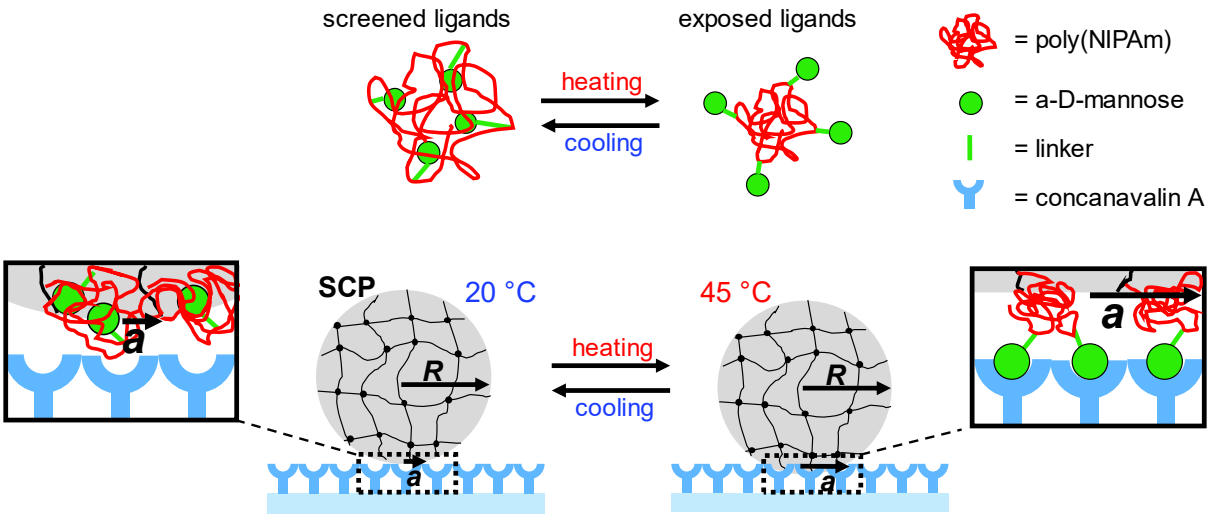

Figure 1 The SCP adhesion assay with thermoresponsive glycopolymers grafted onto the SCP network. The SCP radius *R* and contact radius *a* are read out by optical microscopy to calculate the adhesion energy with the JKR-model of adhesion (see eq.1). It is expected that a temperature stimulus exposes or hides the carbohydrate units and leads to a change in adhesion energy. Previous work on carbohydrate decorated LCST polymers suggest an increase in binding at elevated temperature.[35]

2. Results and Discussion

2.1. Synthesis of ligand bearing polymers

The overall aim of this work is the analysis of carbohydrate interactions on a soft, thermoresponsive scaffold via SCPs. Additionally, the influence of different linkers between the sugar-ligands and the scaffold were analyzed. The preparation of the thermoresponsive glycopolymers is based on the functionalization of a poly(active ester) (Figure 2). Free radical polymerization in DMF gives poly(*N*-acryloxysucinimide) with active ester groups enabling the conjugation of carbohydrate ligands and isopropyl amine, where the latter gives thermoresponsive NIPAM repeat units. To be able to bind the thermoresponsive glycopolymers to SCPs by carbodiimide coupling, the

poly(*N*-acryloxysucinimide) precursor was synthesized with 4,4'Azobis(4-cyanovaleric acid) giving carboxylic acid end groups. The poly(active ester) was functionalized with sugar-ligand first, followed by isopropyl amine. The carbohydrate ligands were prepared with two different amine linkers at the anomeric position, a 2-hydroxypropyl (**HP**) and, respectively, an ethyl (**E**) linker. During the functionalization it was observed that the amount of carbohydrates incorporated to the polymer was only half compared to the amount available for coupling. This can be explained by side reactions via the hydroxyl groups present in the sugar-ligand competing with the amine during the reaction. The hydroxyl-linked carbohydrate ligands were cleaved off during isopropyl amine coupling due the excess of the basic compound. This proves to be advantageous for the preparation of bioactive glycopolymers since the carbohydrates are strictly linked via their anomeric position. The carbohydrate functionalizing degree was quantified via the sulfuric acid phenol test.[36] Nine different polymers were synthesized containing different amounts of ligands between 0% and 97% for polymers, see Table 1. A galactose containing polymer was synthesized with a ligand functionalization degree of 2.7% as a negative control sample. By functionalizing the carboxylic end groups of all polymers, as incorporated by the initiator, with ethylene diamine in an additional step, grafting of the polymers onto the SCPs via the amine group was enabled.

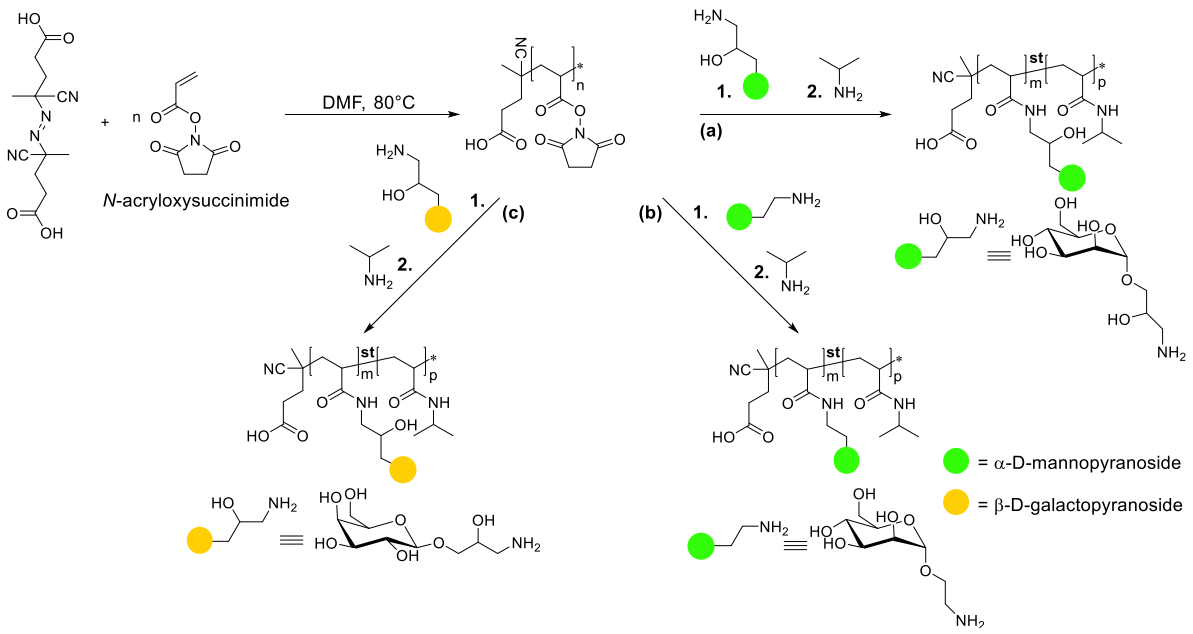

Figure 2 Synthesis route toward ligand bearing thermoresponsive polymers. Glycopolymer functionalized with a) 2-hydroxypropyl linked mannose, b) ethyl linked mannose, c) 2-hydroxypropyl linked galactose. The carboxylic acid end groups of the polymers are used as residues for the grafting of the polymers on the SCPs.

Table 1 List of the glycopolymers, showing the molecular weight (MW), dispersity ($Đ_M$), the functionalization degree and the LCST as measured via turbidimetry.

Polymer	MW [g mol^{-1}]	$Đ_M$	functionalization degree [%]	LCST [°C]
Man0	10300	1.47	0	32.6
Man(HP)1.4	10500	1.47	1.4	35.9
Man(HP)1.9	10650	1.43	1.9	36.8
Man(HP)7.5	11500	1.44	7.5	40.2
Man(HP)97	27800	n.a.	97	n.a.
Man(E)1.1	10400	1.39	1.1	35.6
Man(E)2.2	10600	1.46	2.2	36.7
Man(E)4.6	11000	1.46	4.6	40.8
Gal(HP)2.7	10800	1.39	2.7	40.8

2.2 The LCST behavior of the glycopolymers in solution.

The thermosensitivity of the polymers was assessed by turbidity measurements. With an increasing carbohydrate functionalization degree, the LCST increases (Figure 3). This is expected from the hydrophilic moieties conjugated to PNIPAM. The only polymer that does not show any phase transition is Man(HP)97 since it bears not enough thermoresponsive NIPAM units. The linker chemistry appears to have no effect on the LCST, the more hydrophilic HP-linker and the more hydrophobic E-linker show similar LCST values.

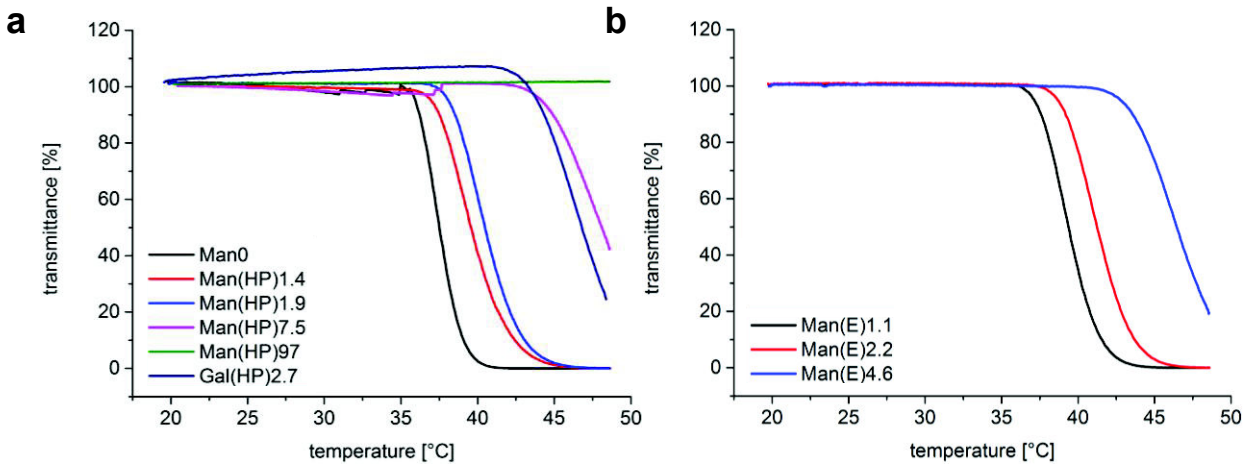

Figure 3 Turbidity measurements from 20°C to 50°C of the synthesized polymers. a) polymers with hydrophilic the HP-linker, b) polymers with the E-linker. Increasing the mannose functionalization degree shifts the phase transition to larger temperatures.

2.3 Synthesis of SCPs and functionalization with thermoresponsive ligand bearing polymers

Polyethylene glycol based SCPs were synthesized by UV-initiated crosslinking of poly(ethylene glycol diacrylamide) (PEGdAAm) microdroplets in aqueous solution containing 1 M sodium sulfate to facilitate the liquid-liquid phase separation of PEGdAAm (Figure 4).[30] To introduce functional groups into the PEG network of the SCPs, crotonic acid was grafted by UV irradiation in presence of benzophenone.[37] The crotonic acid functionalization degree was 90 µmol per gram PEG-SCPs, which corresponds to roughly seven crotonic acid residues in a 10x10x10 nm^3 volume of the SCP scaffold, as calculated from the SCP elastic modulus as an estimate for the swelling degree.[38] The glycopolymers were grafted onto the SCPs by coupling the amine end groups of the polymers to crotonic acid at the SCPs via carbodiimide chemistry. To quantify the polymer functionalization degree, a TBO titration was conducted using a microscope-based readout, giving functionalization degrees above 95% for all grafting reactions. The elastic moduli of the SCPs were determined by AFM force-indentation measurements. To evaluate the temperature effect on adhesion the JKR model (eq. 1) the SCPs elastic moduli were determined at 20°C and 45°C. Between the different samples and temperatures the elastic moduli varied between 40 kPa and 60 kPa, as is expected from previous studies.[39]

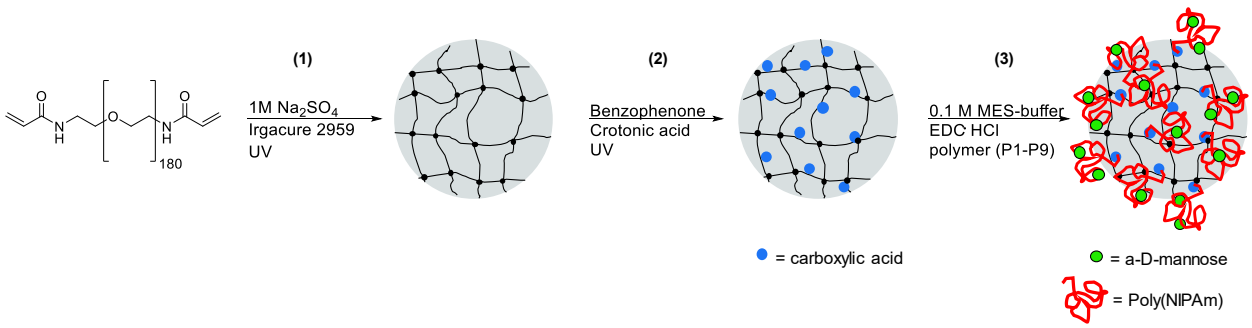

Figure 4 The synthesis of PEG based SCPs using UV irradiation (1) followed by UV mediated functionalization with crotonic acid using benzophenone (2) for further functionalization and polymer functionalization using carbodiimide chemistry (3) to obtain thermoresponsive SCPs for adhesion measurements.

2.4 Quantifying thermo-switchable adhesion on ConA surfaces

To study the temperature-dependent interactions of the glycopolymers, we determine the adhesion of the SCPs on ConA coated glass slides. ConA is a well-known model system for carbohydrate binding studies, which binds to mannose but not to galactose.[40,41] To form stable ConA coatings, we used epoxy functionalized glass slides as described previously.[42] All preparation steps were done at pH 7.4, where ConA attains a tetrameric structure with four mannose binding sites at a minimum spacing of 7.2 nm. The tetrameric structure ensures that each ConA molecule at the glass surface has binding sites facing the solution and are available for binding.

After adding the SCPs to the ConA slides they sediment and make contact to the ConA surface (Figure 5). The SCPs form distinct contact areas with the glass slide that can be visualized by RICM, where a dark area in the center of the particles signifies the contact area. The evaluation of the newton fringes in the RICM images give the contact radii and SCP radii required for JKR analysis. Each measurement consisted of the following temperature cycle: first adhesion measurements at 20°C, second measurements after heating to at 45°C, third measurements after cooling to 20°C. To confirm that the adhesion was due to specific interaction between mannose and ConA, α-$_D$-mannopyranoside (MeMan) was added to reach a concentration of 2 mM in the measurement cell (final measurement step). MeMan competes with the glycopolymer at the SCPs for binding sites, thus a reduction of the contact area after MeMan addition confirmed the specific SCP-surface interaction.

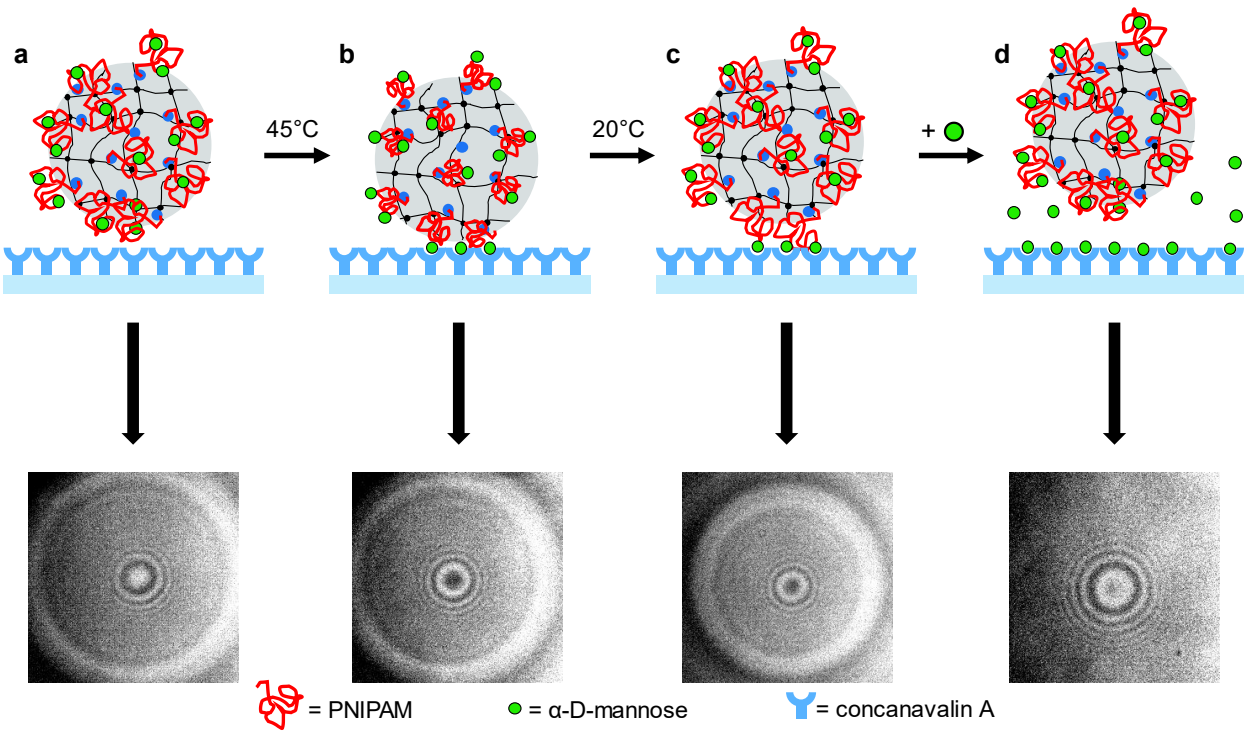

Figure 5 Schematic presentation of a measurement cycle starting 20°C and equilibration for 30 min (a) followed by heating to 45°C and equilibration for 60 min (b) before cooling down to 20°C again and equilibration for another 30 min (c) before MeMan was added and equilibrated for 30 min to prove the specificity of the sugar-protein interaction (d). Exemplary images for each step are show for an SCP functionalized with Man(HP)7.5 (bottom). For each step twenty SCP contact areas are imaged to calculate the adhesion energies.

To estimate the amount of specific and non-specific adhesion we first compared the adhesion energies of the control samples (Figure 6). **Man0** contains no sugar but is essentially PNIPAM, thus is fully thermoresponsive. **Man(HP)97** contains virtually only mannose and is not thermoresponsive. **Gal(HP)2.7** should be thermoresponsive, but does not bind to the ConA surface. The results of the adhesion assay confirmed these expectations. **Man(HP)97** showed, no temperature response but largest adhesion due to mannose-ConA binding, which could be inhibited upon MeMan addition. **Gal(HP)2.7** and **Man0** showed no change in adhesion upon MeMan addition since their interaction with the surface was not due to specific binding. Both polymers also showed no temperature response, suggesting, that the hydrophobicity shift of PNIPAM when crossing the LCST does not affect the interaction with the surface. This could be due to the comparatively low amount of grafted polymer in the SCPs. In addition, in the hydrophobic state of the

polymers above the LCST they more likely interact with each other in the PEG network, but not with the surface. Overall, there was a clear adhesion energy difference between the mannose functionalized polymer **Man(HP)97** and **Gal(HP)2.7** and **Man0**. The comparatively large non-specific adhesion for **Man0** (pure PNIPAM) was reduced when introducing carbohydrates in the polymer chain as can be seen from the strong reduction in adhesion after inhibiting **Man(HP)97**.

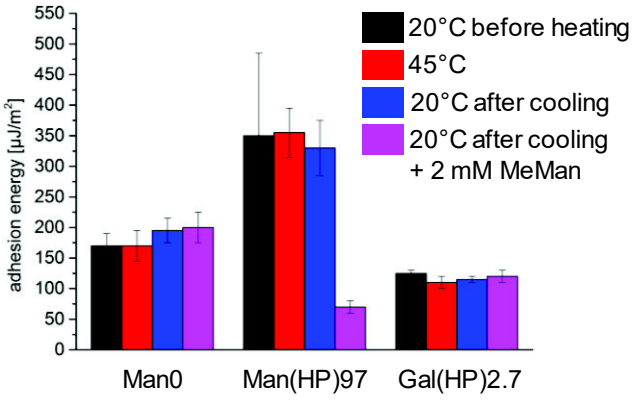

Figure 6 Temperature-dependent adhesion energies at 20°C (black), 45°C (red), after cooling back to 20°C (blue) and after MeMan addition (pink) for control polymers Man0 without ligand, Man(HP)97 lacking thermoresponsivity and Gal(HP)2.7 with nonbinding galactose.

For the mannose bearing thermoresponsive polymers with the hydrophilic linker **Man(HP)1.4**, **Man(HP)1.9** and **Man(HP)7.5** (Figure 7a) the adhesion was strongly thermoresponsive. All polymers showed no adhesion after MeMan addition. Thus, their surface interaction was largely driven by specific binding. Additionally, these polymers showed an increase in adhesion from 20°C to 45°C, presumably due to the collapse of hydrophobic polymer chains, followed by enrichment of the hydrophilic mannose units at the polymer globule surface and reduced steric repulsion. Moreover, with mannose functionalization degree the initial adhesion at 20°C decreases from 50 µJ m^{-2} for **Man(HP)1.4** down to 0 µJ m^{-2} for **Man(HP)7.5**. This suggests, that a rather low density of mannose was sufficient to saturate the binding sites at the ConA surface. Indeed, due to the large spacing of ConA binding sites (~7.2 nm) there is an excess of glycopolymer competing for the binding sites, as it was estimated that in an SCP volume of 10x10x10 nm^3 on average seven grafted polymers were present. On the other hand, upon heating to 45°C higher adhesion energies from 110 µJ/m^2 to 150 µJ/m^2 for **Man(HP)1.4** and

Man(HP)7.5, were observed, indicating that more sugar ligands lead to a higher interaction. Also the highly mannose functionalized polymer **Man(HP)97** achieves significantly larger adhesion energies. This could be explained by additional subsite binding at the ConA binding pocket occurring for multivalent structures with closely arranged mannose residues leading to increased adhesion.[42-44] Importantly, cooling the measurement cell back to 20°C did achieve a reduction of adhesion energies but the initial values obtained before heating were not reached. The adhesion energy decrease appeared to be stronger for polymers containing more sugars suggesting that the polymer re-swelling to the original conformation is increased in case more hydrophilic residues were incorporated. Possibly the specific interactions with the ConA surface lead to a strong hysteresis effect that keep the polymers "locked" in the adhered state with the surface.[15]

Polymers with the hydrophobic linker **Man(E)1.1**, **Man(E)2.2** and **Man(E)4.6** (Figure 7b) generally show larger adhesion at 20°C compared to the polymers with the hydrophilic linker and no clear response upon temperature change. In the ConA binding pocket many hydrophobic amino acids are present thus the hydrophobic linker is favored.[45,46] However, the increased polymer hydrophobicity above the LCST in the collapsed polymer globule might render the mannose units with hydrophobic linker inaccessible resulting in lower adhesion energy. Such decreasing interactions above the LCST of mannose functionalized PNIPAM for bacteria and glucose polymers was reported before.[20] Only **Man(E)4.6** showed an increase in adhesion above the LCST. It could be argued here that the collapse to a compact globule was not as strong due to the increased amount of hydrophilic mannose units rendering the ligands accessible above the LCST. Alternatively, since the **Man(E)1.1** and **Man(E)2.2** were the polymers with the lowest degree of functionalization and having the more hydrophobic linker their overall adhesion might be dominated by non-specific interactions, similar to the pure PNIPAM chains. Therefore, SCPs functionalized with **Man(E)1.1** or **Man(E)2.2** behave similar as compared to SCPs functionalized with **Man0**. After cooling down from 45°C back to 20°C **Man(E)4.6** and **Man(E)2.2** did not show a decrease in adhesion energy, possibly due to slow re-swelling of the polymer chains as observed for the **HP**-linked polymers.

All in all, the strong hysteresis of the adhesion measurements with ConA surfaces suggests that persistent polymer-surface contacts were formed, possibly reinforced by ConA-polymer entanglements. In addition, the hydration barrier of the SCP scaffold (PEG) and ConA coating normally preventing adhesion might be removed above the LCST due to the

elevated temperature and the strong adhesion, which was primed by ligand-receptor binding leading to irreversible nonspecific binding.[47] A possible means to reduce the hysteresis and to achieve reversible adhesion could the taking control of duration an intensity of the temperature stimulus, e.g. by using light in combination with metallic nanoparticles to trigger the temperature stimulus.[17,18] In addition, to maintain the hydration barrier at the polymer scaffold zwitterionic polymer scaffolds could be used.[48]

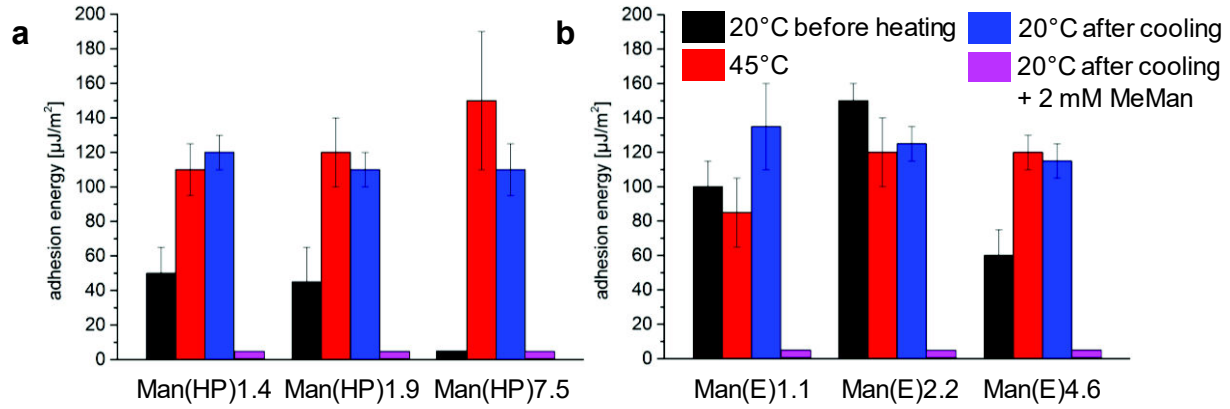

Figure 7 Temperature-dependent adhesion energies at 20°C (black), to 45°C (red), cooled back to 20°C (blue) and after addition of MeMan (pink). (a) Mannose bearing polymers with the hydrophilic linker (HP) and (b) polymers with the hydrophobic linker (E). Bars without errors indicate non-adhering SCPs (W_{adh} = 0 µJ m^{-2})

2.5 E. coli binding assay.

To study the switchable adhesion of the polymers to a natural system, we used *E. coli* with mannose binding FimH receptors at their fimbriae. Fluorescence images were taken of SCPs after incubation with green fluorescent protein (GFP) tagged *E. coli* (Figure 8). Non-binding SCPs decorated with **Gal2.7** and **Man0** as well as SCPs functionalized with **Man1.9** and **Man7.5** were incubated with bacteria for 1 h below and above the LCST before taking fluorescence images. **Man0** and **Gal2.7** were not binding as expected. For **Man1.9** the bacteria bind below the LCST and to a stronger degree above the LCST, whereas for **Man7.5** the binding was only observed above the LCST. These findings are quite similar to the adhesion measurements on ConA surfaces. However, a reduction in *E. coli* adhesion was not observed when cooling down the mannose functionalized SCPs to 20°C. We suspect, that the prolonged incubation above the LCST enabled entanglements between the polymer network and bacterial fimbriae which might hinder detachment of the bacteria.

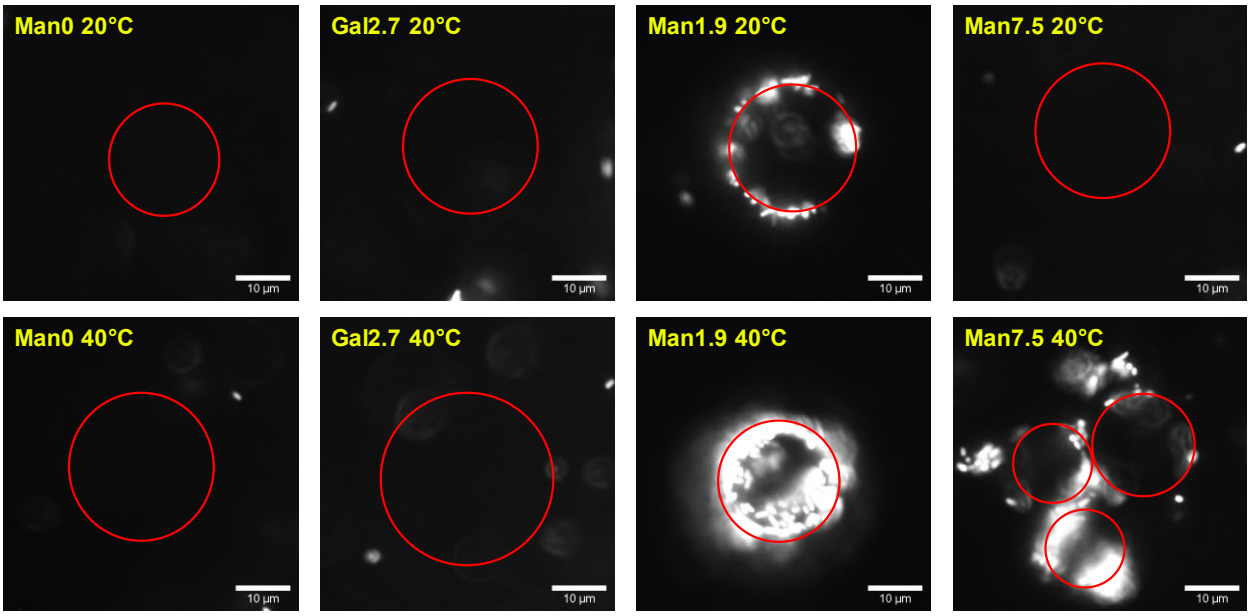

Figure 8 Fluorescence microscope measurements with polymer bearing particles and GFP-tagged *E. coli* at 20°C (top) and 40°C (bottom). For negative control samples Man0 and Gal2.7 no binding to bacteria was observed at both temperatures. Man(HP)1.9 showed an increase in number of bound bacteria above the LCST whereas Man(HP)7.5 showed no-binding at 20°C and binding at 40°C. Red circles indicate the SCP location taken from transmitted light images taken prior to fluorescence microscopy imaging.

3. Experimental Section

Materials: α-$_D$-mannopyranoside (99%, Acros Organics), β-$_D$-galactose pentaacetate (95%, Fluorochem) acetonitrile (≥99.9%, Panreac AppliChem) p-Toluenesulfonic acid (98%, Alfa Aesar), acetic anhydride (≥98%, VWR Chemicals), ethyl acetate (distilled), sodium bicarbonate (100%, Fisher Chemicals), magnesium sulfate (62-70%, Fisher Chemicals), allyl alcohol (≥99%, Merck KGaA), boron trifluoride diethyl etherate (≥98%, TCI), *n*-hexane (99%, VWR Chemicals), sodium methanolate (98%, Alfa Aesar), Amberlite-IR120® (Fisher Chemicals), hydrogen (Air Liquide), tetrahydrofuran (99.99%, Fisher Chemicals), chloroform (99.97%, Fisher Chemicals), trimethylamine (>99.0%, Merck KGaA), acryloyl chloride (96%, Merck KGaA) *N,N*-dimethylformamide (≥99.8%, Biosolve-Chemicals), dimethylsulfoxide (99.99%, Fisher Chemicals) isopropylamine (99+%, Alfa Aesar), sodium sulfate (99.5%, Fisher Chemicals), Benzophenone (99%, Acros Organics), Polyethylene glycol diacrylate (M.W. 8000, Alfa Aesar), 1-Ethyl-3-(3-dimethylaminopropyl)carbodiimid-hydrochlorid (≥99%, Carl Roth). All other chemicals were obtained from Sigma-Aldrich (Germany). All water used here was produced by

purification system with a resistivity higher than 18.2 MΩ·cm at 25 °C and UV treatment to break down organic impurities.

Synthesis of Poly(N-acryloxysuccinimide):N-Acryloxysuccinimide (15.3 g, 90 mmol) was dissolved in 140 mL *N,N*-dimethylformamide, heated to 80°C and flushed with nitrogen for 15 min. To initiate the polymerization 4,4'-Azobis(4-cyanovaleric acid) (255.6 mg, 0.9 mmol) dissolved in 10 mL DMF was added to the preheated solution. After reacting for 20 h at 80°C the polymer was precipitated in cold tetrahydrofuran, filtered and dried under vacuum. A brown solid was obtained (yield 12.21 g, 79%, M_n = 15340 Da). ^{1}H-NMR (600 MHz, Chloroform-*d*) δ 12.38 - 12.14 (s, 1H, *H9*) δ 3.28 - 3.00 (s, 1H, *H3*), δ 2.85 - 2.74 (s, 4H, *H4-7*), δ 2.25 - 1.90 (s, 2H, *H1+2*) δ 1.40 - 1.33 (s, 3H, *H8*), (supporting information S1).

Synthesis of Poly(N-isopropylacrylamide-co-N-(2-hydroxypropyl) α-$_D$-mannopyranoside acrylamide) and Poly(N-isopropylacrylamide-co-N-ethyl α-$_D$-mannopyranoside acrylamide): Poly(*N*-acryloxysuccinimide) (1 g, 65 µmol) was dissolved in 10 mL dimethyl sulfoxide and heated to 40°C. Depending on the sugar functionalization degree different amounts of amine functionalized sugars were added (supporting information S2). After reacting for 2 h Isopropylamine (1.5 mL, 17.7 mmol) was added and stirred for 2 h. The reaction solution was cooled down and diluted with 35 mL of water and dialyzed for 48 h. The remaining solution was freeze dried. In the next step 24 µmol of polymer were dissolved in 10 mL 0.1 M MES-buffer pH 5.0 containing 32.5 mM EDC·HCl and 48 mM ethylenediamine and reacted for 2 h. Afterward the solution was dialyzed in water for 48 h and freeze dried. NMR and GPC showed that the molecular weight of the polymers was between 10.3 and 27.8 kDa depending on the mannose functionalization degree (supporting information S3-S6) The functionalization degree was determined via the sulfuric acid phenol test.[49]

Soft colloidal probe (SCP) preparation: SCPs were synthesized by crosslinking a dispersion of the macromonomer poly(ethylene glycol diacrylamide) (PEGdAAm) in aqueous solution as previously described.[50] Sodium sulfate (1.42 g, 0.01 mol) is dissolved in 10 mL water. The photo initiator Irgacure 2959 (2.1 mg, 5.4 µmol) and PEGdAAm (Mn = 8000 Da) (50 mg, 6.3 µmol) were added followed by vigorous shaking. The obtained dispersion was then photopolymerized under UV light for 90 s (HiLite, Kulzer GmbH, Germany). The SCPs were washed with water via several centrifugation cycles. The diameter of received particles was between 10-70 µm. Next, crotonic acid was grafted

onto the SCPs. Briefly, water was exchanged by ethanol, then benzophenone (250 mg, 1.4 mmol) and crotonic acid (1.5 g, 17.7 mmol) were added and the dispersion was flushed with nitrogen for 60 s followed by UV irradiation for 1080 s. The particles were washed with ethanol and water to remove all reactants. In the final step, the glycopolymers with amine end groups were coupled with crotonic acid on the SCPs in 0.1 M MES buffer pH 5.5 containing 32.5 mM EDC·HCl and 0.225 mM polymer followed by washing with water.

SCP mechanical characterization: AFM force indentation studies with a NanoWizard 2 system (JPK instruments AG, Berlin, Germany) were performed to determine the elastic moduli of the SCPs. As AFM probe a glass bead with a diameter of 4.6 µm was glued with an epoxy glue onto a tipless, non-coated cantilever (spring constant 0.32 N/m; CSC12, NanoAndMore GmbH). Several force curves were recorded for the different SCPs at 20°C and 45°C and analyzed with an appropriate contact model developed by Glaubitz et al. (supporting information S7).[39]

Surface preparation: Round glass coverslips (25 mm #1, Menzel Gläser, Germany) were cleaned in a mixture of ammonia, hydrogen peroxide (30%) and water (1:1:5) at 70°C for 20 min. The glass slides were then immersed in a mixture of 200 mL ethanol, 10.5 mL water, 200 µL acetic acid, and 2100 µL (3-glycidyloxypropyl)trimethoxysilane, shaken for 120 min, flushed with ethanol, followed by annealing at 80 °C overnight. For ConA functionalization, the glass slides were immersed in PBS (pH 7.4) containing 0.05 mg ml^{-1} ConA for 1 h, followed by rinsing with PBS, rinsing with 10 mM HEPES buffer (pH 7.4), then rinsing with lectin binding buffer (pH 7.4).

Determination of the polymer functionalization degree: The colorimetric quantification of carbohydrates via the sulfuric acid phenol test was based on a well-established procedure.[49] Briefly, a calibration curve was measured using a dilution series of MeMan (320 µM, 160 µM, 80 µM, 40 µM and 20 µM) in microplates. To 125 µL of each solution 125 µL of a 5wt% solution of phenol in water was added and vigorously shaken. 625µL of concentrated sulfuric acid were added afterward, vigorously shaken and reacted at 30°C for 30 min. Next, the absorbance for each solution was analyzed at a wavelength of 490 nm (FLUOstar Omega, BMG Labtech, Germany). For analysis of the polymer samples 125 µL of polymer solution at varying concentration depending on the expected functionalization degree was used for analysis using the same procedure.

Determination of the SCPs functionalization degree via TBO titration: First the crotonic acid functionalization degree of the SCP before polymer conjugation was determined: 1.0 mL of a dispersion containing crotonic acid functionalized SCPs were dried by first exchanging the water by ethanol and then treating in a vacuum oven at 50°C until constant weight was reached. After the dry mass was determined, 1.0 mL of 312.5 µM toluidine blue O solution at pH 10 was added and shaken in the dark for 12 h. Next, 0.3 mL of the toluidine blue O solution supernatant of the was diluted with 1.7 mL water at pH 10 and the absorbance at 633 nm was detected to calculate the degree of functionalization with the following equation $D_{CGF} = N_R(1\text{-}A_S/A_E)/W_{Dry}$ where D_{CGF} is the carboxylic acid functionalization degree, A_S and A_R is the UV-VIS absorbance of the sample and reference, W_{Dry} is the dry weight of 1.0 mL SCPs, N_R is the amount of TBO in the reference in units of µmol. For each group of SCPs, the TBO titration was repeated three times and the average carboxylic group functionalization degree to obtain the average degree of functionalization with crotonic acid. To determine the SCPs' polymer functionalization degree, the decrease in the adsorption of toluidine blue O of polymer functionalized SCPs compared to crotonic acid functionalized SCPs was determined: 125 µL of polymer functionalized SCPs dispersion were dyed by removing the storage water and adding 125 µL of 312.5 µM TBO solution at pH 10 and shaking in the dark overnight (as for the crotonic acid functionalized SCPs). Afterward the SCPs were washed with water at pH 10 and the grey value was measured by optical microscopy and compared to the grey values of non-functionalized SCPs and carboxylic acid functionalized SCPs to determine the functionalization via the equation $D_{PGF} = (1\text{-}(G_N/G_{SCP})/\Delta G_B$ where D_{PGF} is the polymer functionalization degree, ΔG_B is the difference of grey values between non-functionalized and carboxylic acid functionalized SCPs ($\Delta G_B > 0$), G_N is the grey value of non-functionalized SCPs and G_{SCP} is the average grey value of polymer functionalized SCPs.

SCP adhesion measurements: To obtain the contact area between SCPs and glass coverslips RICM on an IX 73 inverted microscope (Olympus, Japan) was applied. For illumination, an Hg-vapor arc lamp was used with a green monochromator (546 nm). An UPlanFL N 60x/0.90 dry objective (Olympus Corporation, Japan), and uEye CMOS camera (IDS Imaging Development Systems GmbH, Germany) were used to image the RICM patterns. The contact radius and the particle radius were determined using the RICM patterns (supporting information S8). Images with RICM patterns were read out using self-written image analysis software, contact areas and particle profiles were evaluated using

home written software.[51] After adding the SCPs to the ConA coated glass slides the temperature dependent adhesion measurement were conducted in three cycles: 1) at 20°C after 30 min equilibration, 2) at 45°C after 60 min equilibration, 3) 20°C after 60 min equilibration.

Fluorescence microscopy: For fluorescence microscopy measurements 100 µL of polymer functionalized particles were centrifuged, the supernatant was exchanged by 100 µL of PBS and afterward 400 µL of type 1 fimbrated *E. coli* in PBS with an optical density of 0.4 at 600 nm (OD600) were added to the SCPs and shaken for 1 h at either 20°C or 40°C. After that 20 µL of this solution was added into microwells (µ-slide 18 well ibidi GmbH, Germany). The fluorescence images were taken from the same particles for location of particles in fluorescence images. For illumination of fluorescence images an Hg-vapor arc lamp in combination with a GFP filter set.

Conclusion

In summary, a series of different thermoresponsive glycopolymers was synthesized varying the mannose density and linker hydrophobicity and grafted onto soft colloidal probes to quantify their temperature-controlled adhesion on ConA surfaces. It was found that the ligand receptor interactions were influenced by the number of sugar ligands incorporated into the polymer and that they could be switched upon temperature increase. When increasing the temperature above the LCST the glycopolymers with the hydrophilic linker showed larger adhesion, whereas the polymers with the hydrophobic showed no clear temperature dependent adhesion. Thus, linker-type may have played an important role in the accessibility of the ligands in the extended coil and collapsed globule conformations of the polymers. Importantly, a strong hysteresis was observed, i.e. cooling back to 20°C did not reduce the adhesion back to the initial value before heating. Also the adhesion of *E. coli* with the mannose presenting SCPs could be facilitated by a temperature increase, whereas the detachment upon cooling was not possible. This suggests, that the design of polymer surfaces with externally controllable ligand-receptor interactions should avoid entanglements and nonspecific interaction between the polymer scaffold on order to achieve reversible adhesion upon temperature stimulus. These results give a first quantitative insight into the changes of in carbohydrate mediated adhesion of thermoresponsive glycopolymers and provide avenues for the design of capture-release materials addressing drugs or pathogens.

Supporting Information

Supporting Information is available from the Wiley Online Library or from the author.

Acknowledgements

The authors acknowledge funding from the German Research Foundation (DFG) within project SCHM 2748/5-1.

Received:

Revised:

Published online:

References

[1] T. Manouras, M. Vamvakaki, *Polym. Chem.* **2017**, *8*, 74.
[2] M. A. Stuart, W. T. Huck, J. Genzer, M. Muller, C. Ober, M. Stamm, G. B. Sukhorukov, I. Szleifer, V. V. Tsukruk, M. Urban, F. Winnik, S. Zauscher, I. Luzinov, S. Minko, *Nat. Mater.* **2010**, *9*, 101.
[3] P. M. Mendes, *Chem. Soc. Rev.* **2008**, *37*, 2512.
[4] F. Dalier, F. Eghiaian, S. Scheuring, E. Marie, C. Tribet, *Biomacromolecules* **2016**, *17*, 1727.
[5] C. von der Ehe, T. Buś, C. Weber, S. Stumpf, P. Bellstedt, M. Hartlieb, U. S. Schubert, M. Gottschaldt, *ACS Macro Lett.* **2016**, *5*, 326.
[6] M. R. Kim, J. H. Jeong, T. G. Park, *Biotechnol. Prog.* **2002**, *18*, 495.
[7] J. Zhan, L. Wang, Y. Zhu, H. Gao, Y. Chen, J. Chen, Y. Jia, J. He, Z. Fang, Y. Zhu, C. Mao, L. Ren, Y. Wang, *ACS Appl. Mater. Interfaces* **2018**, *10*, 35830.
[8] B. Trzebicka, R. Szweda, D. Kosowski, D. Szweda, Ł. Otulakowski, E. Haladjova, A. Dworak, *Prog. Polym. Sci.* **2017**, *68*, 35.
[9] A. Pich, W. Richtering, "Microgels by Precipitation Polymerization: Synthesis, Characterization, and Functionalization", in *Chemical Design of Responsive Microgels*, A. Pich and W. Richtering, Eds., Springer-Verlag Berlin, Berlin, 2010, p. 1.
[10] J. E. Hudak, C. R. Bertozzi, *Chem. Biol.* **2014**, *21*, 16.
[11] S. Reitsma, D. W. Slaaf, H. Vink, M. A. van Zandvoort, M. G. oude Egbrink, *Pflugers Arch.* **2007**, *454*, 345. [12] G. Conzatti, S. Cavalie, C. Combes, J. Torrisani, N. Carrere, A. Tourrette, *Colloid Surf. B-Biointerfaces* **2017**, *151*, 143.
[13] J. Siirilä, S. Hietala, F. S. Ekholm, H. Tenhu, *Biomacromolecules* **2020**.
[14] J. S. J. Tang, S. Rosencrantz, L. Tepper, S. Chea, S. Klopzig, A. Kruger-Genge, J. Storsberg, R. R. Rosencrantz, *Molecules* **2019**, *24*, 22.
[15] T. J. Paul, S. Rubel, M. Hildebrandt, A. K. Strzelczyk, C. Spormann, T. K. Lindhorst, S. Schmidt, *ACS Appl. Mater. Interfaces* **2019**, *11*, 26674.
[16] R. B. Vasani, N. Janardanan, B. Prieto-Simon, A. Cifuentes-Rius, S. J. Bradley, E. Moore, T. Kraus, N. H. Voelcker, *ACS Appl. Mater. Interfaces* **2015**, *7*, 27755.
[17] S. Won, S. Hindmarsh, M. I. Gibson, *ACS Macro Lett.* **2018**, *7*, 178.
[18] S. Won, S. J. Richards, M. Walker, M. I. Gibson, *Nanoscale Horiz.* **2017**, *2*, 106.
[19] C. S. Mahon, G. C. Wildsmith, D. Haksar, E. de Poel, J. M. Beekman, R. J. Pieters, M. E. Webb, W. B. Turnbull, *Faraday Discuss.* **2019**, *219*, 112.
[20] G. Pasparakis, A. Cockayne, C. Alexander, *J. Am. Chem. Soc.* **2007**, *129*, 11014.
[21] S. R. S. Ting, G. J. Chen, M. H. Stenzel, *Polym. Chem.* **2010**, *1*, 1392.
[22] S. Vandewalle, S. Wallyn, S. Chattopadhyay, C. R. Becer, F. Du Prez, *Eur. Polym. J.* **2015**, *69*, 490.
[23] Y. N. Wang, Y. Kotsuchibashi, Y. Liu, R. Narain, *ACS Appl. Mater. Interfaces* **2015**, *7*, 1652.
[24] K. Nagase, J. Kobayashi, T. Okano, *J. R. Soc. Interface* **2009**, *6 Suppl 3*, S293.
[25] S. Schmidt, M. Zeiser, T. Hellweg, C. Duschl, A. Fery, H. Mohwald, *Adv. Funct. Mater.* **2010**, *20*, 3235.
[26] K. Uhlig, T. Wegener, J. He, M. Zeiser, J. Bookhold, I. Dewald, N. Godino, M. Jaeger, T. Hellweg, A. Fery, C. Duschl, *Biomacromolecules* **2016**, *17*, 1110.
[27] F. Jacobi, A. Camaleno de la Calle, S. Boden, A. Grafmuller, L. Hartmann, S. Schmidt, *Biomacromolecules* **2018**, *19*, 3479.
[28] D. Pussak, D. Ponader, S. Mosca, S. V. Ruiz, L. Hartmann, S. Schmidt, *Angew. Chem.-Int. Edit.* **2013**, *52*, 6084.
[29] S. Schmidt, H. Q. Wang, D. Pussak, S. Mosca, L. Hartmann, *Beilstein J. Org. Chem.* **2015**, *11*, 720.
[30] D. Pussak, M. Behra, S. Schmidt, L. Hartmann, *Soft Matter* **2012**, *8*, 1664.
[31] N. Helfricht, E. Doblhofer, V. Bieber, P. Lommes, V. Sieber, T. Scheibel, G. Papastavrou, *Soft Matter* **2017**, *13*, 578.
[32] K. L. Johnson, K. Kendall, A. D. Roberts, *Proc. R. Soc. A* **1971**, *324*, 301.
[33] V. T. Moy, Y. K. Jiao, T. Hillmann, H. Lehmann, T. Sano, *Biophys. J.* **1999**, *76*, 1632.
[34] J. Erath, S. Schmidt, A. Fery, *Soft Matter* **2010**, *6*, 1432.

[35] S. Schmidt, T. J. Paul, A. K. Strzelczyk, *Macromol. Chem. Phys.* **2019**, *220*, 1900323.
[36] M. Dubois, K. A. Gilles, J. K. Hamilton, P. A. Rebers, F. Smith, *Anal. Chem.* **1956**, *28*, 350.
[37] Y. Wang, Y. Kotsuchibashi, Y. Liu, R. Narain, *ACS Appl. Mater. Interfaces* **2015**, *7*, 1652.
[38] H. Wang, F. Jacobi, J. Waschke, L. Hartmann, H. Löwen, S. Schmidt, *Adv. Funct. Mater.* **2017**, *27*, 1702040. [39] M. Glaubitz, N. Medvedev, D. Pussak, L. Hartmann, S. Schmidt, C. A. Helm, M. Delcea, *Soft Matter* **2014**, *10*, 6732.
[40] H. Lis, N. Sharon, *Chem. Rev.* **1998**, *98*, 637.
[41] E. A. Smith, W. D. Thomas, L. L. Kiessling, R. M. Corn, *J. Am. Chem. Soc.* **2003**, *125*, 6140.
[42] A. Camaleno de la Calle, C. Gerke, X. J. Chang, A. Grafmuller, L. Hartmann, S. Schmidt, *Macromol. Biosci.* **2019**, *19*, e1900033.
[43] T. K. Dam, S. Oscarson, J. C. Sacchettini, C. F. Brewer, *J. Biol. Chem.* **1998**, *273*, 32826.
[44] T. K. Dam, C. F. Brewer, *Biochemistry* **2008**, *47*, 8470.
[45] D. A. Sanders, D. N. Moothoo, J. Raftery, A. J. Howard, J. R. Helliwell, J. H. Naismith, *J. Biol. Chem.* **2001**, *310*, 875.
[46] S. Igde, S. Roblitz, A. Muller, K. Kolbe, S. Boden, C. Fessele, T. K. Lindhorst, M. Weber, L. Hartmann, *Macromol. Biosci.* **2017**, *17*, 1700198.
[47] J. Israelachvili, *Proc. Natl. Acad. Sci. U. S. A.* **1997**, *94*, 8378.
[48] R. Schroeder, W. Richtering, I. I. Potemkin, A. Pich, *Macromolecules* **2018**, *51*, 6707.
[49] S. Boden, K. G. Wagner, M. Karg, L. Hartmann, *Polymers (Basel)* **2017**, *9*, 716.
[50] A. K. Strzelczyk, H. Q. Wang, A. Lindhorst, J. Waschke, T. Pompe, C. Kropf, B. Luneau, S. Schmidt, *Gels* **2017**, *3*, 13.
[51] J. Waschke, T. Pompe, D. Rettke, S. Schmidt, M. Hlawitschka, *PLOS ONE* **2019**, *14*, e0214815.

TOC

The temperature-controlled specific adhesion of carbohydrate functionalized LCST polymers is analyzed as a function polymer composition. Adhesion energies upon heating and cooling show that the coil-globule transition of the LCST polymers controls the specific binding of carbohydrates. However strong hysteresis effects hamper switchability, e.g. capturing carbohydrate binding bacteria upon heating is feasible whereas release upon cooling is not possible.

Thermoresponsive glycopolymers

*Alexander Klaus Strzelczyk, Tanja Janine Paul and Stephan Schmidt**

Quantifying thermo-switchable carbohydrate mediated interactions via soft colloidal probe adhesion studies

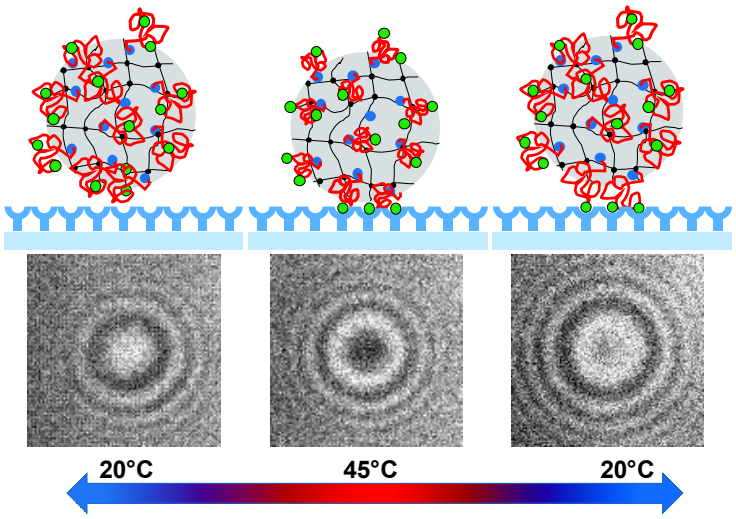

Supporting Information

Quantifying thermo-switchable carbohydrate mediated interactions via soft colloidal probe adhesion studies

*Alexander Klaus Strzelczyk, Tanja Janine Paul and Stephan Schmidt**

A. K. Strzelczyk, Tanja Janine Paul, Jun. Prof. Dr. S. Schmidt

Institute of Organic and Macromolecular Chemistry, Heinrich-Heine-University Düsseldorf, Universitatsstraße 1, 40225 Dusseldorf, Germany,

* E-mail: stephan.schmidt@hhu.de

Contents

S1 Synthesis of *N*-acryloxysuccinimide

The synthesis of *N*-acryloxysuccinimide was adapted from Dalier et al.[1] *N*-Hydroxysuccinimide (14.4 g, 125 mmol) was dissolved in 200 mL chloroform at 0°C. Triethylamine (22 mL, 155 mmol) was added and afterwards acryloyl chloride (10 mL, 125 mmol) was added dropwise. After addition the solution was stirred at 0°C for 30 min and washed with sodium hydrogencarbonate solution, dried over sodium sulfate. Chloroform was removed under vacuum until 1/3 of volume was left. By adding 70 mL of n-hexane the NAS was precipitated. The turbid supernatant was removed and hexane was removed under reduced pressure (yield 18.09 g, 88%). The remaining yellow oil was dissolved in Chloroform. This cycle was repeated until the remaining oil was not soluble in chloroform.

^{1}H-NMR (600 MHz, Chloroform-*d*) δ 6.74 - 6.67 (dd, ^{3}J = 17.4, 0.8 Hz, 1H, *H1*), δ 6.38 - 6.27 (dd, ^{3}J = 16.6, 10.3 Hz, 1H, *H2*), δ 6.20 - 6.14 (dd, ^{3}J = 10.7, 0.8 Hz, 1H, *H3*), δ 2.89 - 2.81 (s, 4H, *H4-7*).

^{13}C-NMR (600 MHz, Chloroform-*d*) δ 169,17 ($C_{quart.}$, 2C, *C3*), δ 161,18 ppm ($C_{quart.}$, 2C, *C4+5*), δ 136,33 (CH_2, 1C, *C1*), δ 123,08 (CH, 1C, *C2*), δ 25,75 (CH_2, 2C, *C6+7*).

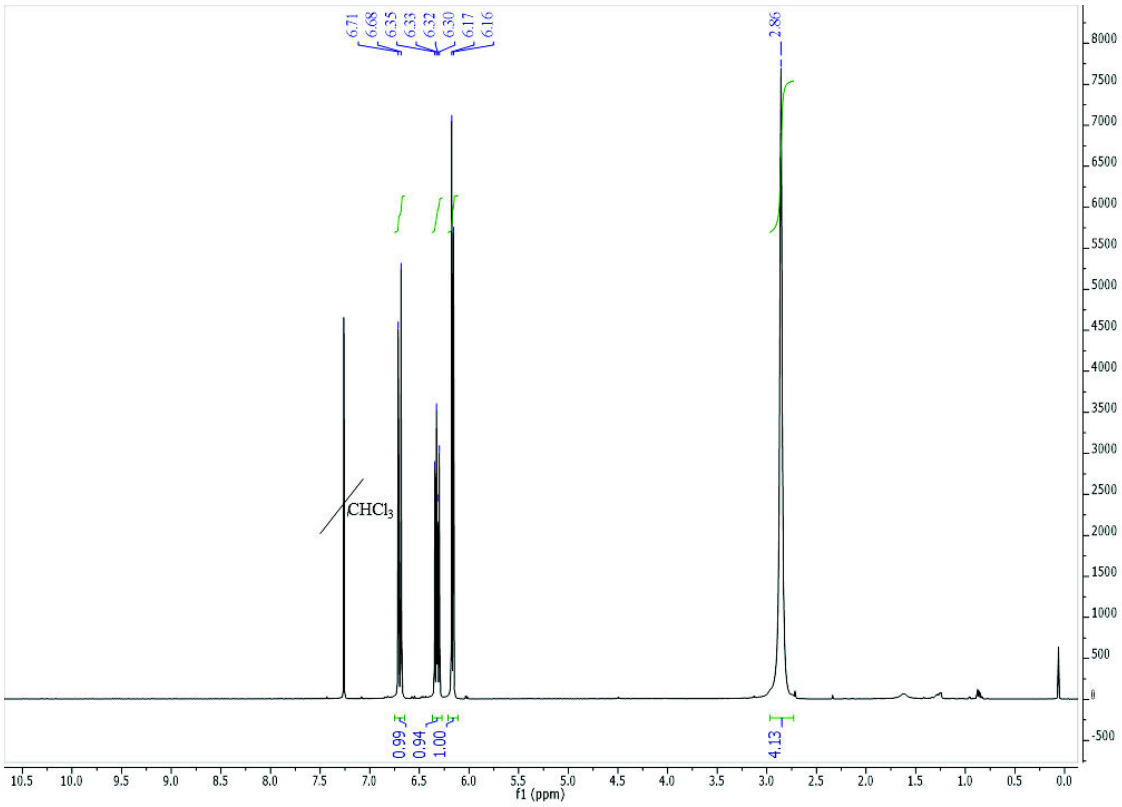

Figure S1a ^{1}H-NMR (600 MHz, $CDCl_3$) *N*-acryloxysuccinimide.

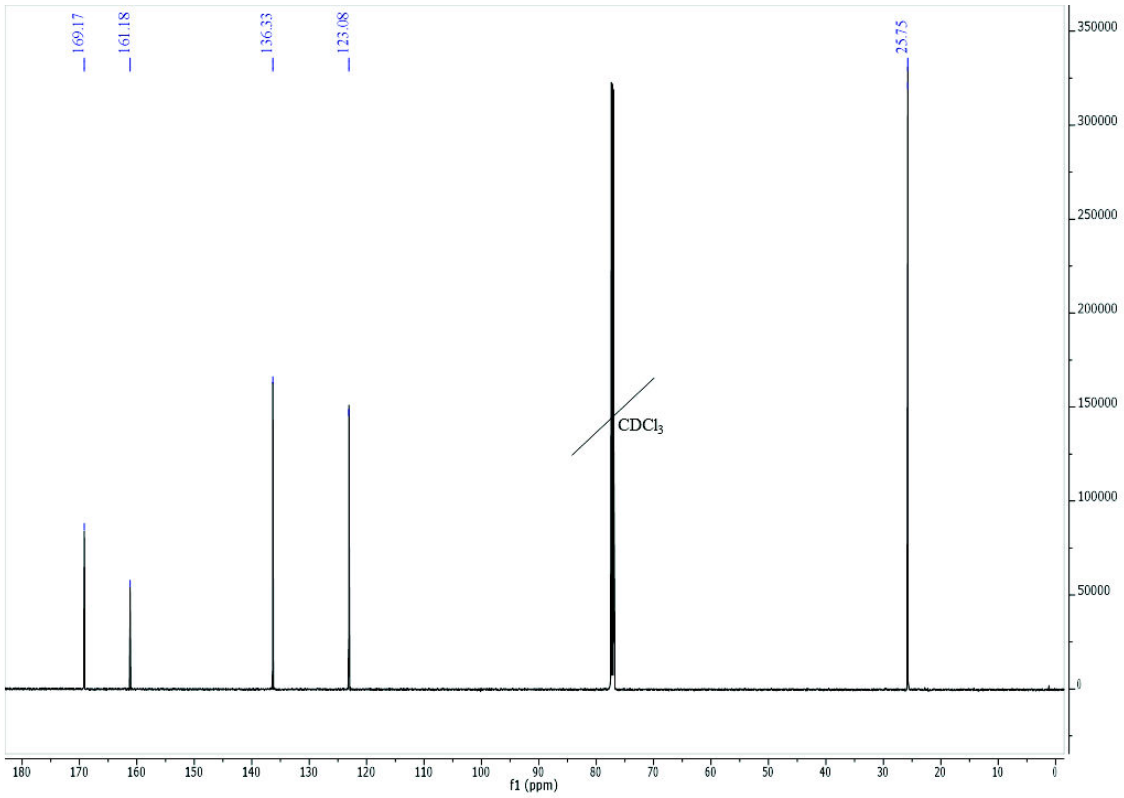

Figure S1b ^{13}C-NMR (600 MHz, $CDCl_3$) *N*-acryloxysuccinimide.

S2 Synthesis of carbohydrate ligands with different linkers

Synthesis of 3-amino-2-hydroxypropyl-linker functionalized ligands

Synthesis of 1,2,3,4,6-penta-*O*-acetyl-α-$_D$-mannopyranoside

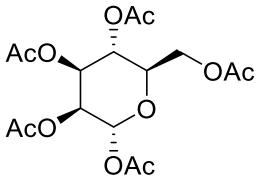

Scheme S2a: Structure of 1,2,3,4,6-penta-*O*-acetyl-α-$_D$-mannopyranoside.

α-$_D$-mannose (30.0 g, 166.6 mmol) was dissolved in 500 mL acetonitrile at 0 °C. Then *p*-toluenesulfonic acid (3.18 g, 18.5 mmol) was added and the solution was flushed with nitrogen for 20 min and over the next 20 min acetic anhydride (100 mL, 1.1 mole) was added and the solution was stirred at room temperature for 48 h. Afterwards the solvent was removed and the residue was dissolved in 600 mL ethyl acetate and washed with saturated sodium bicarbonate solution, water and dried over magnesium sulfate. Solvent was removed under reduced pressure and the product was dried under vacuum (yield: 64.2 g, 99%).

^{1}H-NMR (600 MHz, $CDCl_3$) δ 6.11 - 5.83 (dd, $^{3}J_{HH}$ = 67.2, 1.8 Hz 1H, *H1*), δ 5.50 - 5.09 (m, 3H, *H2-4*), δ 4.34 - 4.24 (m, 1H, *H5*), δ 4.18 - 3.75 (m, 2H, *H21+22*), δ 2.23 - 2.20 (s, 3H, *H6-20*), δ 2.18 - 2.15 (d, $^{3}J_{HH}$ = 2.4 Hz, 3H, *H6-20*), δ 2.09 - 2.07 (s, 3H, *H6-20*), δ 2.06 - 2.02 (s, 3H, *H6-20*), δ 2.02 - 1.96 (s, 3H, *H6-20*).

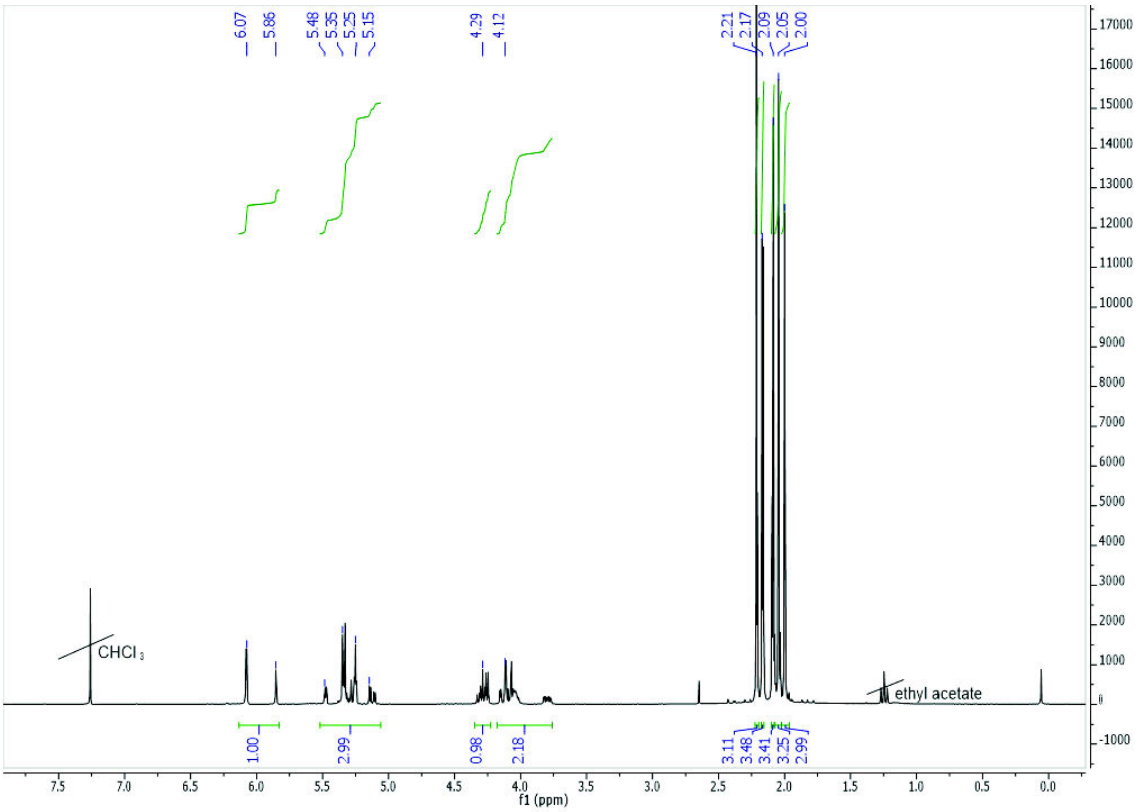

Figure S2a: ^{1}H-NMR (600 MHz, $CDCl_3$) 1,2,3,4,6-penta-*O*-acetyl-α-$_D$-mannopyranoside.

Synthesis of allyl-2,3,4,6-tetra-*O*-acetyl-α-$_D$-mannopyranoside and allyl-2,3,4,6-tetra-*O*-acetyl-β-$_D$-galactopyranoside

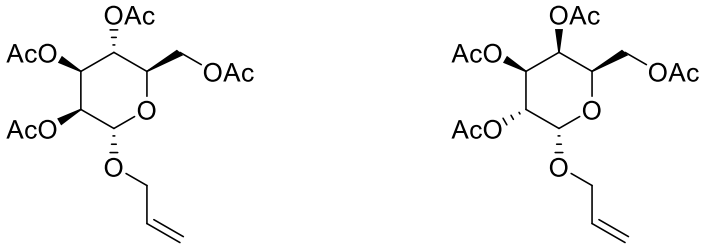

Scheme S2b: Structures of allyl-2,3,4,6-tetra-*O*-acetyl-α-$_D$-mannopyranoside (left) and allyl-2,3,4,6-tetra-*O*-acetyl-β-$_D$-galactopyranoside (right).

The synthesis was done according to literature.[2] The protected sugar (25.5 g, 65.4 mmol) was dissolved in 410 mL dichloromethane before allyl alcohol (25 mL, 360.9 mmol) was added. After 30 min of flushing with nitrogen at 0 °C boron trifluoride diethyl etherate

(250 mL, 1.97 mol) was added dropwise over 15 min and the solution was then stirred for 72 h at room temperature. Afterwards the solution was poured into 1000 mL of ice water. The organic phase was washed with saturated sodium bicarbonate, water and dried over magnesium sulfate. Solvent was removed and product was purified via column chromatography using n-hexane:ethyl acetate (1:1) (yield mannose: 15.99 g, 63%; galactose 17.75 g, 69%).

^{1}H-NMR allyl-2,3,4,6-tetra-*O*-acetyl-α-$_{D}$-mannopyranoside: (600 MHz, $CDCl_3$) δ 5.93 - 5.86 (tdd, $^{3}J_{HH}$ = 11.3, 5.3, 0.9 Hz, 1H, *H8*), δ 5.38 - 5.35 (dd, $^{3}J_{HH}$ = 10.0, 3.5 Hz, 1H, *H4*), δ 5.33 - 5.26 (m, 2H, *H9+10*), δ 5.26 - 5.22 (m, 2H, *H2+3*), δ 4.88 - 4.85 (d, $^{3}J_{HH}$ = 1.7 Hz, 1H, *H1*), δ 4.30 - 4.26 (dd, $^{3}J_{HH}$ = 12.1, 5.3 Hz, 1H, *H23+24*), δ 4.21 - 4.16 (ddt, $^{3}J_{HH}$ = 12.8, 5.3, 1.4 Hz, 1H, *H5*), δ 4.12 - 4.08 (dd, $^{3}J_{HH}$ = 12.3, 2.4 Hz, 1H, *H23+24*), δ 4.05 - 3.99 (m, 2H, *H6+7*), δ 2.17 - 2.14 (s, 3H, *H11-22*), δ 2.12 - 2.09 (s, 3H, *H11-22*), δ 2.05 - 2.03 (s, 3H, *H11-22*), δ 2.00 - 1.97 (s, 3H, *H11-22*).

^{1}H-NMR allyl-2,3,4,6-tetra-*O*-acetyl-β-$_{D}$-galactopyranoside (600 MHz, $CDCl_3$) δ 5.90 - 5.80 (td, $^{3}J_{HH}$ = 11.3, 4.9 Hz, 1H, *H8*), δ 5.48 - 5.40 (dd, $^{3}J_{HH}$ = 3.7, 1.0 Hz, 1H, *H1*), δ 5.39 - 5.32 (m, 1H, *H3*), δ 5.31 - 5.25 (dd, $^{3}J_{HH}$ = 17.2, 1.4 Hz, 1H, *H2*), δ 5.22 - 5.18 (dd, $^{3}J_{HH}$ = 10.4, 1.1 Hz, 1H, *H5*), δ 5.15 - 4.97 (m, 2H, *H9+10*), δ 4.25 - 4.19 (t, $^{3}J_{HH}$ = 6.4 Hz, 1H, *H4*), δ 4.19 - 4.13 (dd, $^{3}J_{HH}$ = 13.0, 5.1 Hz, 1H, *H23+24*), δ 4.13 - 4.03 (m, 2H, *H6+7*), δ 4.03 - 3.96 (dd, $^{3}J_{HH}$ = 13.1, 6.1 Hz, 1H, *H23+24*), δ 2.14 - 2.11 (s, 3H, *H11-22*), δ 2.08 - 2.04 (s, 3H, *H11-22*), δ 2.04 - 2.01 (s, 3H, *H11-22*), δ 1.97 - 1.94 (s, 3H, *H11-22*).

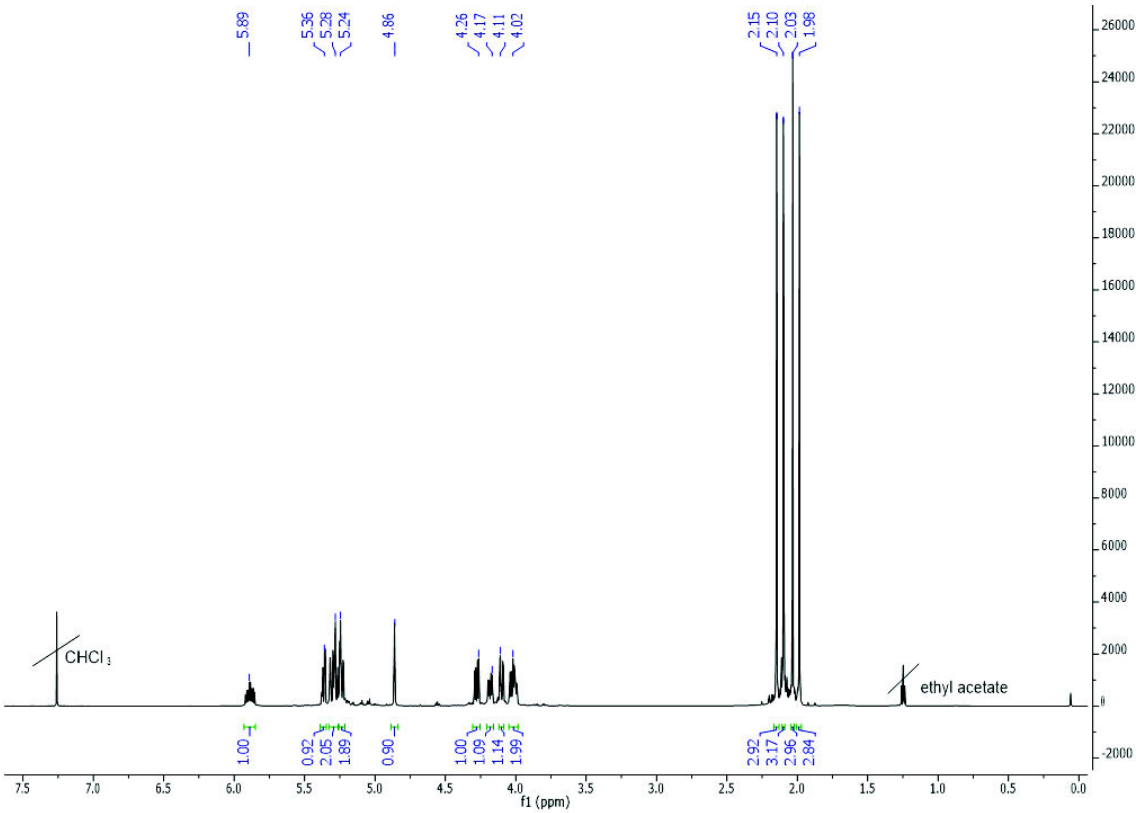

Figure S2b: ^{1}H-NMR (600 MHz, $CDCl_3$) allyl-2,3,4,6-tetra-*O*-acetyl-α-$_D$-mannopyranoside.

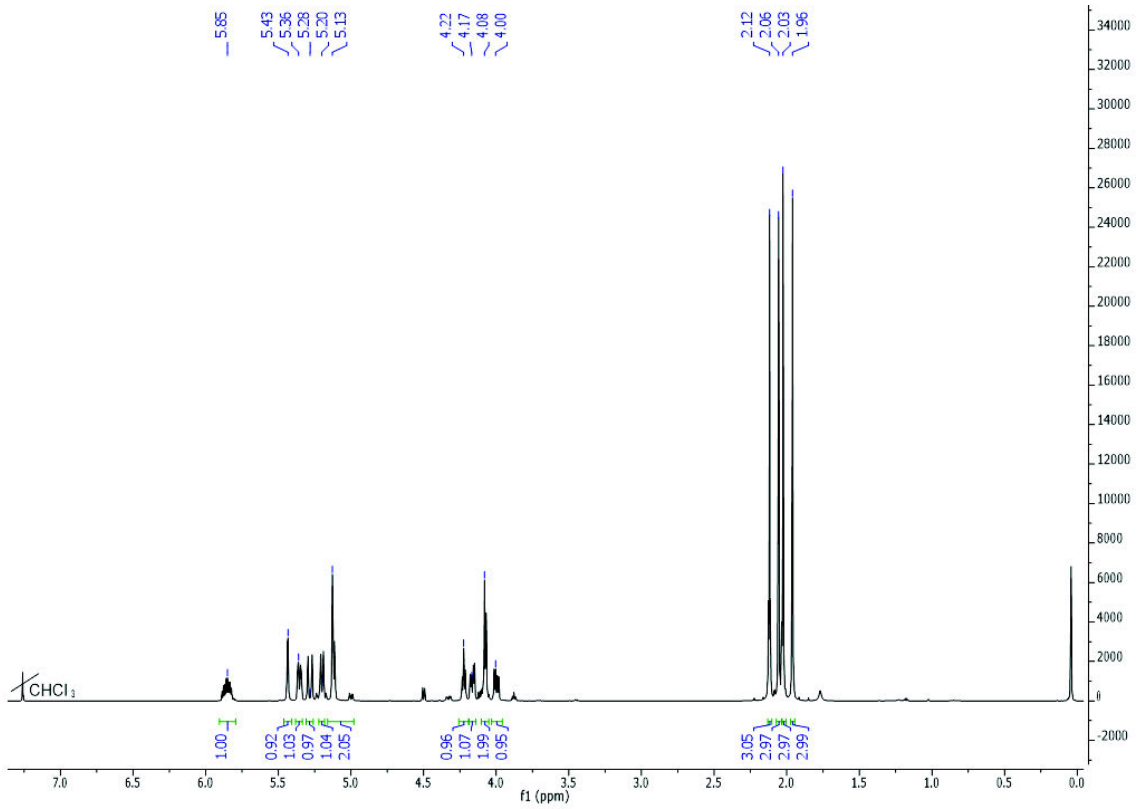

Figure S2c: ^{1}H-NMR (600 MHz, $CDCl_3$) allyl-2,3,4,6-tetra-*O*-acetyl-α-$_D$-galactopyranoside.

Synthesis of 2',3'-epoxypropyl-2,3,4,6-tetra-*O*-acetyl-α-$_D$-mannopyranoside and 2',3'-epoxypropyl-2,3,4,6-tetra-*O*-acetyl-β-$_D$-galactopyranoside

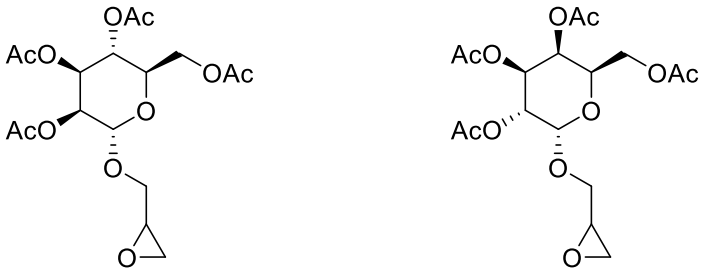

Scheme S2c: Structures of 2',3'-epoxypropyl-2,3,4,6-tetra-*O*-acetyl-α-$_D$-mannopyranoside (left) and 2',3'-epoxypropyl-2,3,4,6-tetra-*O*-acetyl-β-$_D$-galactopyranoside (right).

The allyl-functionalized sugar (15.5 g, 40 mmol) was dissolved in 300 mL dichloromethane and flushed with nitrogen. Then *m*-chloroperoxybenzoic acid (14 g, 81.2 mmol) was added and the solution was stirred for 48 h. After that additional *m*-chloroperoxybenzoic acid (4.24 g, 24.2 mmol) was added and stirred for another 24 h. After that 20 ml of dichloromethane was added and washed with saturated sodium bicarbonate before dried with sodium sulfate. Solvent was removed under reduced pressure and product was purified via column chromatography using n-hexane:ethyl acetate (3:2) (yield mannose: 10.1 g, 63%; galactose: 9.86 g, 61%).

^{1}H-NMR 2',3'-epoxypropyl-2,3,4,6-tetra-*O*-acetyl-α-$_D$-mannopyranoside (600 MHz, $CDCl_3$) δ 5.39 - 5.33 (m, 1H, *H4*), δ 5.32 - 5.26 (m, 2H, *H2+3*), δ 4.93 - 4.84 (dd, $^3J_{HH}$ = 34.3, 1.6 Hz, 1H, *H1*), δ 4.30 - 4.26 (m, 1H, *H5*), δ 4.14 - 4.10 (m, 1H, *H23+24*), δ 4.07 - 4.02 (m, 1H, *H23+24*), δ 3.92 - 3.79 (ddd, $^3J_{HH}$ = 57.3, 11.9, 3.0 Hz, 1H, *H6+7*), δ 3.59 - 3.52 (ddd, $^3J_{HH}$ = 25.0, 11.7, 5.6 Hz, 1H, *H6+7*), δ 3.22 - 3.18 (m, 1H, *H8*), δ 2.85 - 2.82 (m, 1H, *H9+10*), δ 2.65 - 2.62 (m, 1H, *H9+10*), δ 2.18 - 2.14 (s, 3H, *H11-22*), δ 2.11 - 2.08 (s, 3H, *H11-22*), δ 2.06 - 2.03 (s, 3H, *H11-22*), δ 2.02 - 1.98 (s, 3H, *H11-22*).

^{1}H-NMR 2',3'-epoxypropyl-2,3,4,6-tetra-*O*-acetyl-β-$_D$-galactopyranoside (600 MHz, $CDCl_3$) δ 5.48 - 5.42 (m, 1H, *H1*), δ 5.39 - 5.33 (m, 1H, *H3*), δ 5.20 - 5.14 (dd, $^3J_{HH}$ = 17.2, 3.7 Hz, 1H, *H2*), δ 5.14 - 5.11 (m, 1H, *H4*), δ 4.30 - 4.25 (ddt, $^3J_{HH}$ = 6.7, 3.3, 1.2 Hz, 1H, *H5*), δ 4.13 - 4.05 (m, 2H, *H23+24*), δ 3.92 - 3.79 (ddd, $^3J_{HH}$ = 55.5, 11.8, 3.0 Hz, 1H, *H6+7*), δ 3.64 - 3.46 (ddd, $^3J_{HH}$ = 82.8, 12.2, 5.4 Hz, 1H, *H6+7*), δ 3.20 - 3.12 (m, 1H, *H8*), δ 2.84 - 2.77 (dd, $^3J_{HH}$ = 10.2, 4.8 Hz, 1H, *H9+10*), δ 2.69 - 2.58 (ddd, $^3J_{HH}$ = 46.4, 5.3, 2.7 Hz, 1H, *H9+10*), δ 2.16 - 2.12 (d, $^3J_{HH}$ = 1.8 Hz, 3H, *H11-22*), δ 2.10 - 2.06 (d, $^3J_{HH}$ = 2.9 Hz, 3H, *H11-22*), δ 2.04 - 2.02 (s, 3H, *H11-22*), δ 2.00 - 1.97 (s, 3H, *H11-22*).

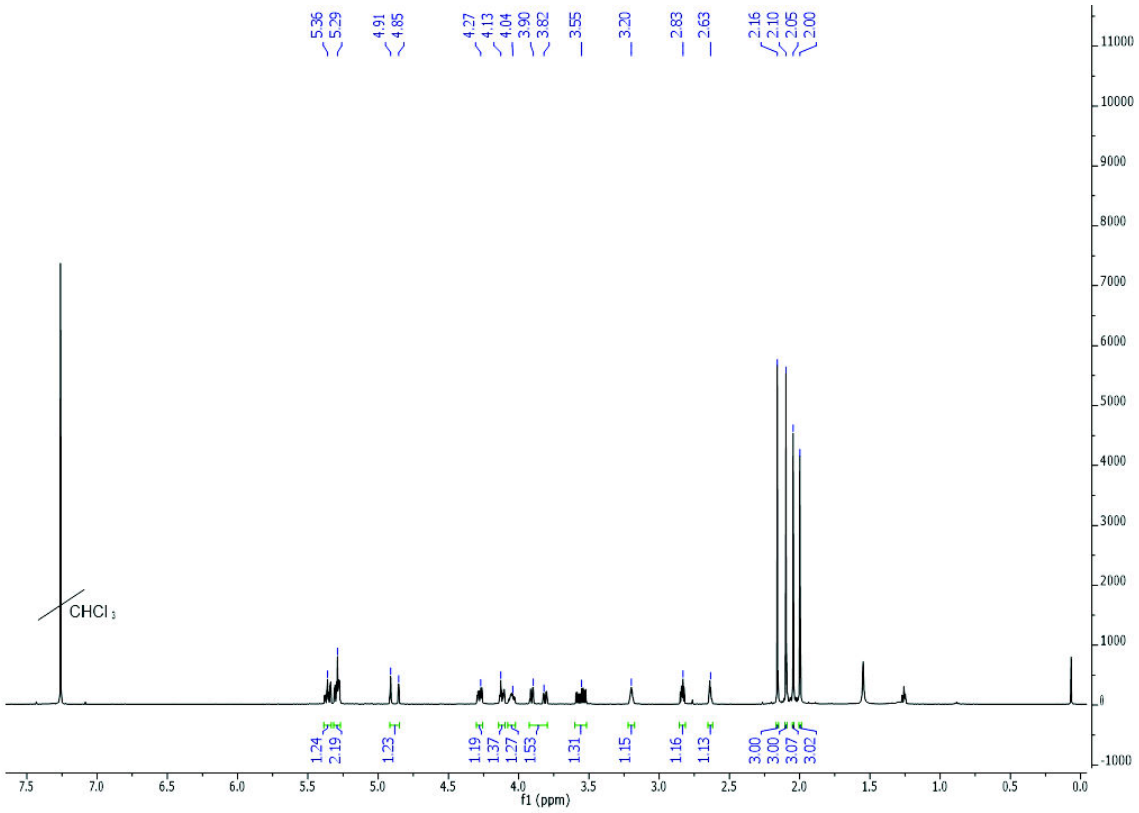

Figure S2d: ^{1}H-NMR (600 MHz, $CDCl_3$) 2',3'-epoxypropyl-2,3,4,6-tetra-*O*-acetyl-α-$_D$-mannopyranoside.

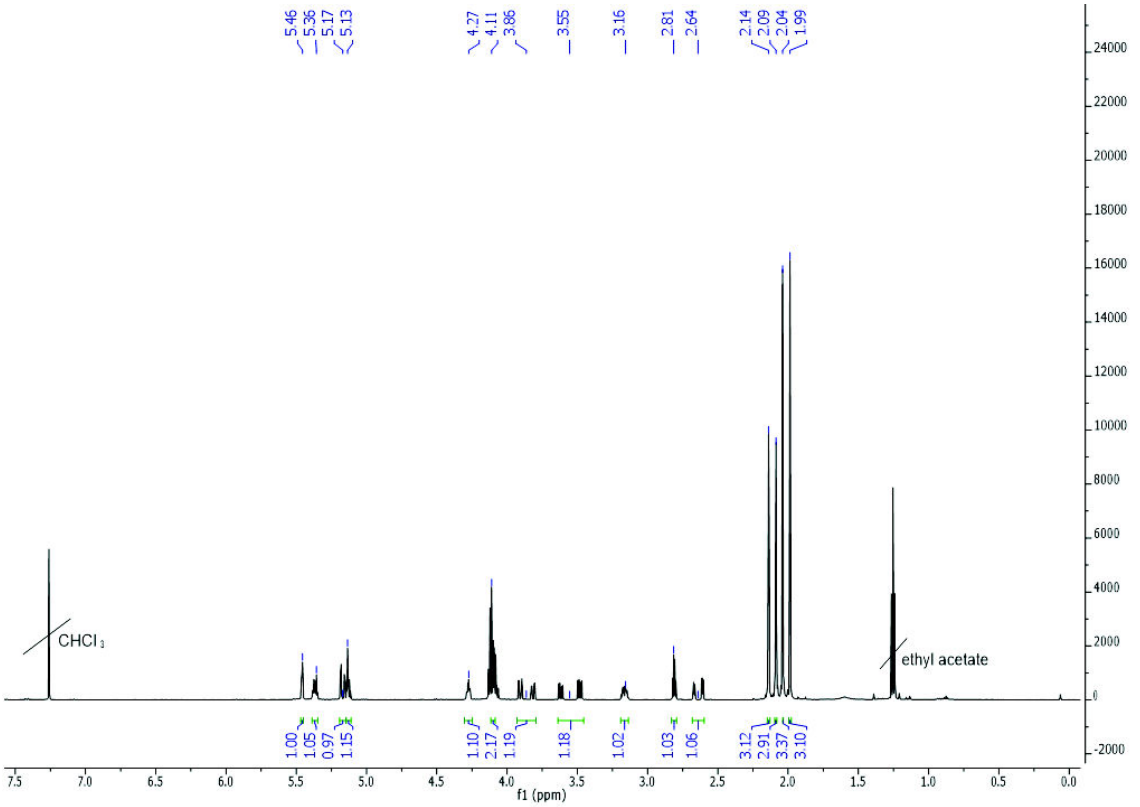

Figure S2d: ^{1}H-NMR (600 MHz, $CDCl_3$) 2',3'-epoxypropyl-2,3,4,6-tetra-*O*-acetyl-α-$_D$-galactopyranoside.

Synthesis of 3-amino-2-hydroxypropyl-α-$_D$-mannopyranoside and 3-amino-2-hydroxypropyl-β-$_D$-galactopyranoside

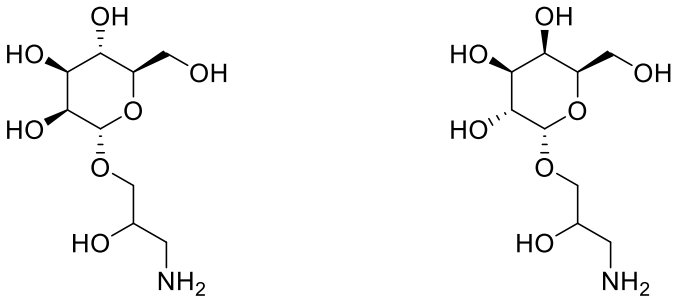

Scheme S2d: 3-amino-2-hydroxypropyl-α-$_D$-mannopyranoside (left) and 3-amino-2-hydroxypropyl-β-$_D$-galactopyranoside (right).

The epoxy-functionalized sugar (9.7 g, 24.2 mmol) was dissolved in 3 mL acetonitrile. After dissolving the sugar ammonia solution (25%, 21 mL) was added and stirred for 72 h. After that the solvent was removed under vacuum and the residue was dissolved in acetone, precipitated in diethyl ether, filtered and dried under vacuum (yield mannose: 5.16 g, 85%; galactose: 3.71 g, 61%).

^{1}H-NMR 3-amino-2-hydroxypropyl-α-$_D$-mannopyranoside (600 MHz, CD_3OD) δ 4.80 - 4.76 (s, 1H, *H1*), δ 3.87 - 3.81 (m, 3H, *H8-10*), δ 3.76 - 3.68 (dd, $^3J_{HH}$ = 12.4, 1.5 Hz, 3H, *H2+6+7*), δ 3.63 - 3.58 (m, 1H, *H4*), δ 3.56 - 3.51 (m, 1H, *H3*), δ 3.47 - 3.42 (m, 1H, *H5*), δ 2.95 - 2.68 (m, 2H, *H11+12*), δ 1.91 - 1.89 (s, 1H, *H13+14*),

^{1}H-NMR 3-amino-2-hydroxypropyl-β-$_D$-galactopyranoside (600 MHz, CD_3OD) δ 4.85 - 4.83 (s, 1H, *H1*), δ 3.84 - 3.65 (m, 8H, *H2-4+6-10*), δ 3.91 - 3.77 (td, $^3J_{HH}$ = 10.3, 3.4 Hz 1H, *H5*), δ 2.99 - 2.77 (m, 2H, *H11+12*), δ 1.91 - 1.88 (s, 2H, *H13+14*).

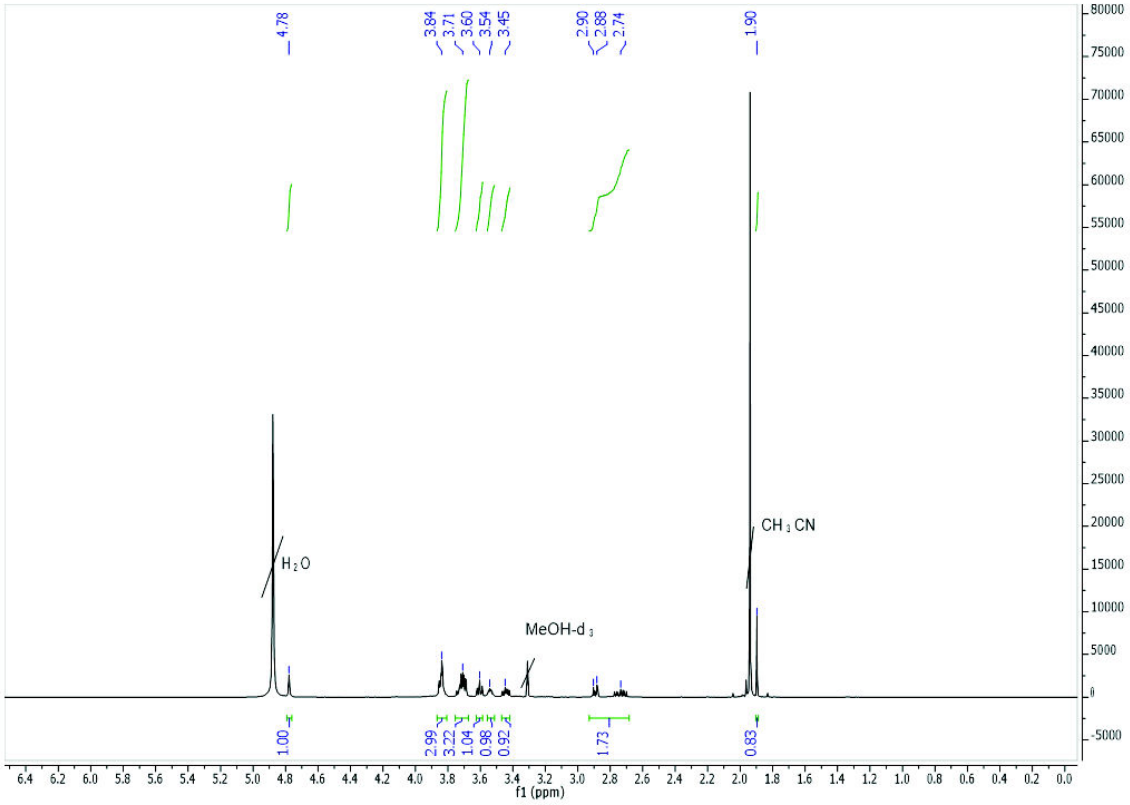

Figure S2e: ^{1}H-NMR (600 MHz, CD_3OD) 3-amino-2-hydroxypropyl-α-$_D$-mannopyranoside.

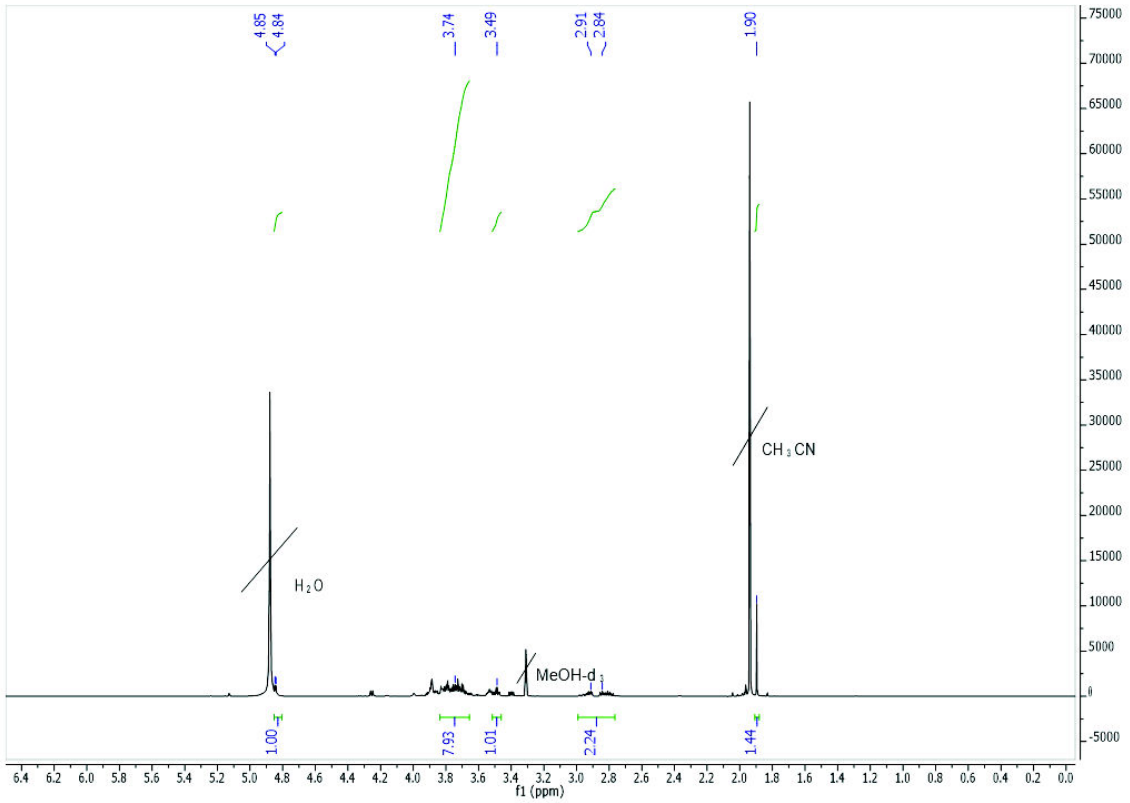

Figure S2f: ^{1}H-NMR (600 MHz, CD_3OD) 3-amino-2-hydroxypropyl-α-$_D$-galactopyranoside.

Synthesis of ethyl-linker functionalized ligand

Synthesis of 2-aminoethyl-α-$_D$-mannopyranoside

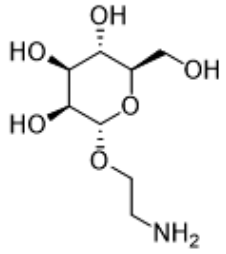

Scheme S2e: 2-aminoethyl-α-$_D$-mannopyranoside.

2-azidoethyl-2,3,4,6-tetra-*O*-acetyl-α-$_D$-mannopyranose was synthesized according to literature.[3] 0.2 M sodium methoxide in methanol solution (8 mL) was added to 2-azidoethyl-2,3,4,6-tetra-*O*-acetyl α-$_D$-mannopyranose (1.5 g, 3.6 mmol) and shaken for 48 h. Afterwards Amberlite-IR120® was added until pH6 was reached. Afterwards, Amberlite-IR120 was filtered off and methanol was added to the filtrate up to a volume of 25 mL. Then palladium on charcoal (10wt%, 106.5 mg, 1 mmol) was added and the solution was flushed three times with hydrogen. The solution was stirred for 24 h under hydrogen atmosphere, filtered and dried under vacuum giving 0.68 g product (yield: 84%).

^{1}H-NMR (600 MHz, DMSO-d_6) δ 4.63 - 4.57 (dd, $^3J_{HH}$ = 8.9, 1.4 Hz, 1H, *H1*), δ 3.66 - 3.62 (dd, $^3J_{HH}$ = 11.6, 2.1 Hz, 1H, *H14-16*), δ 3.62 - 3.59 (dd $^3J_{HH}$ = 3.5, 1.7 Hz, 1H, *H14+16*), δ 3.59 - 3.54 (m, 1H, *H14-16*), δ 3.49 - 3.45 (dd, $^3J_{HH}$ = 8.9, 3.4 Hz, 1H, *H17*), δ 3.45 - 2.41 (dd, $^3J_{HH}$ = 11.6, 6.1 Hz, 1H, *H2*), δ 3.39 - 3.28 (m, 3H, *H3-7+12+13*), δ 3.17 - 3.16 (s, 4H, *H3-7+12+13*), δ 2.77 - 2.63 (o, $^3J_{HH}$ = 6.1 Hz, 2H, *H8+9*), δ 1.85 - 1.78 (s, 2H, *H10+11*).

S3 Synthesis of Poly(N-isopropylacrylamide-co-N-(2-hydroxypropyl) α-$_D$-mannopyranoside acrylamide) and Poly(N-isopropylacrylamide-co-N-ethyl α-$_D$-mannopyranoside acrylamide)

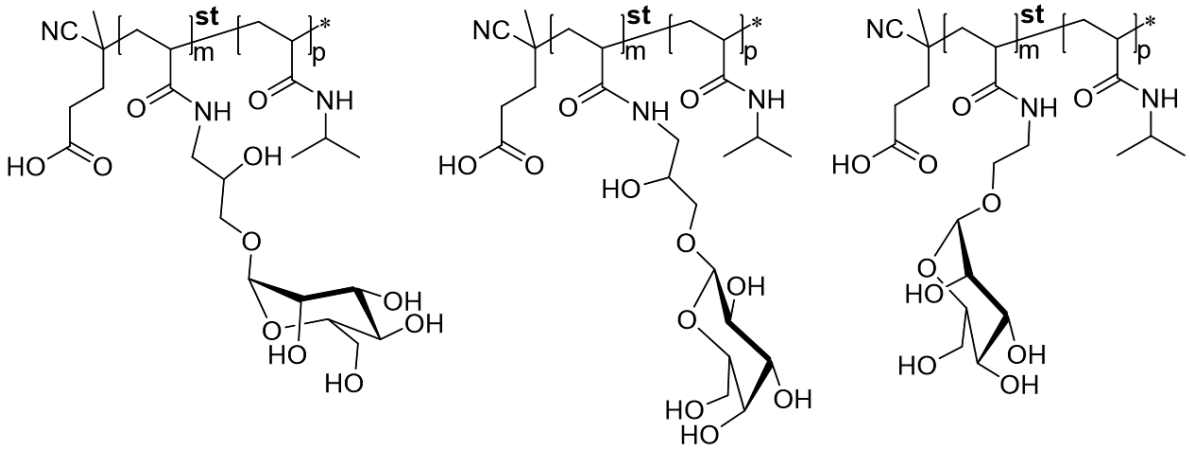

Scheme S3a: General structures of Poly(*N*-isopropylacrylamide-co-*N*-(2-hydroxypropyl) α-$_D$-mannopyranoside acrylamide) (left), Poly(*N*-isopropylacrylamide-co-*N*-ethyl α-$_D$-mannopyranoside acrylamide) (right) and Poly(*N*-isopropylacrylamide-co-*N*-(2-hydroxypropyl) α-$_D$-galactopyranoside acrylamide) (middle) polymers.

Table S3a: Amount of sugar added during polymer functionalization and reaction yield after dialysis.

Polymer	Amount of sugar added [mg]		Yield	
	3-amino-2-hydroxypropyl-α-D-mannopyranose*	2-aminoethyl-α-D-mannopyrannose	[mg]	[%]
Man0	---	---	452	67
Man(HP)1.4	60	---	438	64
Man(HP)1.9	120	---	435	63
Man(HP)7.5	150	---	540	74
Man(HP)97	3200	---	1358	80
Man(E)1.1	---	26	415	61
Man(E)2.2	---	53	421	61
Man(E)4.6	---	132	441	61
Gal(HP)2.7	150	---	456	63

*for **Gal(HP)2.7** 3-amino-2-hydroxypropyl-β-D-galactopyranose was used.

Molecular weight of PNAS was calculated from ^{1}H-NMR spectroscopy giving a $\bar{M}_n$ = 15340 g mol^{-1}, divided by the molecular weight of the monomer giving a number of repeating units of 90. The ratio of the anomeric hydrogen integral at the carbohydrate in comparison to the backbone CH-group integral gave similar results to the colorimetric carbohydrate assay (PSA method). The PSA functionalization degrees were used due to higher accuracy of the method. By multiplication of functionalization degrees with number of repeating units and molecular weight of the monomers the molecular weights were calculated.

Table S3b: Funtionalization degrees determined by ^{1}H-NMR-spectroscopy and phenol sulphuric acid (PSA) method and the molecular weight calculated from PSA methods functionalization degree.

Polymer	Functionalization degree (^{1}H-NMR) [%]	Functionalization degree (PSA) [%]	Molecular weight (PSA) [g mol^{-1}]
Man0	0	0	10300
Man(HP)1.4	1.3	1.4	10480
Man(HP)1.9	1.8	1.9	10650
Man(HP)7.5	7.4	7.5	11525
Man(HP)97	89.3	96.9	27770
Man(E)1.1	1.3	1.1	10450
Man(E)2.2	2.8	2.2	10600
Man(E)4.6	4.2	4.6	11040
Gal(HP)2.7	2.6	2.7	10825

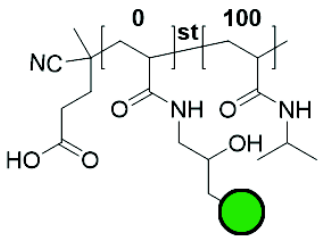

Scheme S3b: Structure of **Man0**. Green circle indicating α-$_D$-mannopyranoside.

^{1}H-NMR **Man0** (600 MHz, $CDCl_3$) δ 7.15 - 5.90 (s, 1H, *H4*), δ 4.15 - 3.90 (s, 1H, *H5*), δ 2.32 - 1.96 (s, 1H, *H3*) δ 1.95 - 1.30 (s, 2H, *H1+2*), δ 1.28 - 0.94 (s, 6H, *H6-11*).

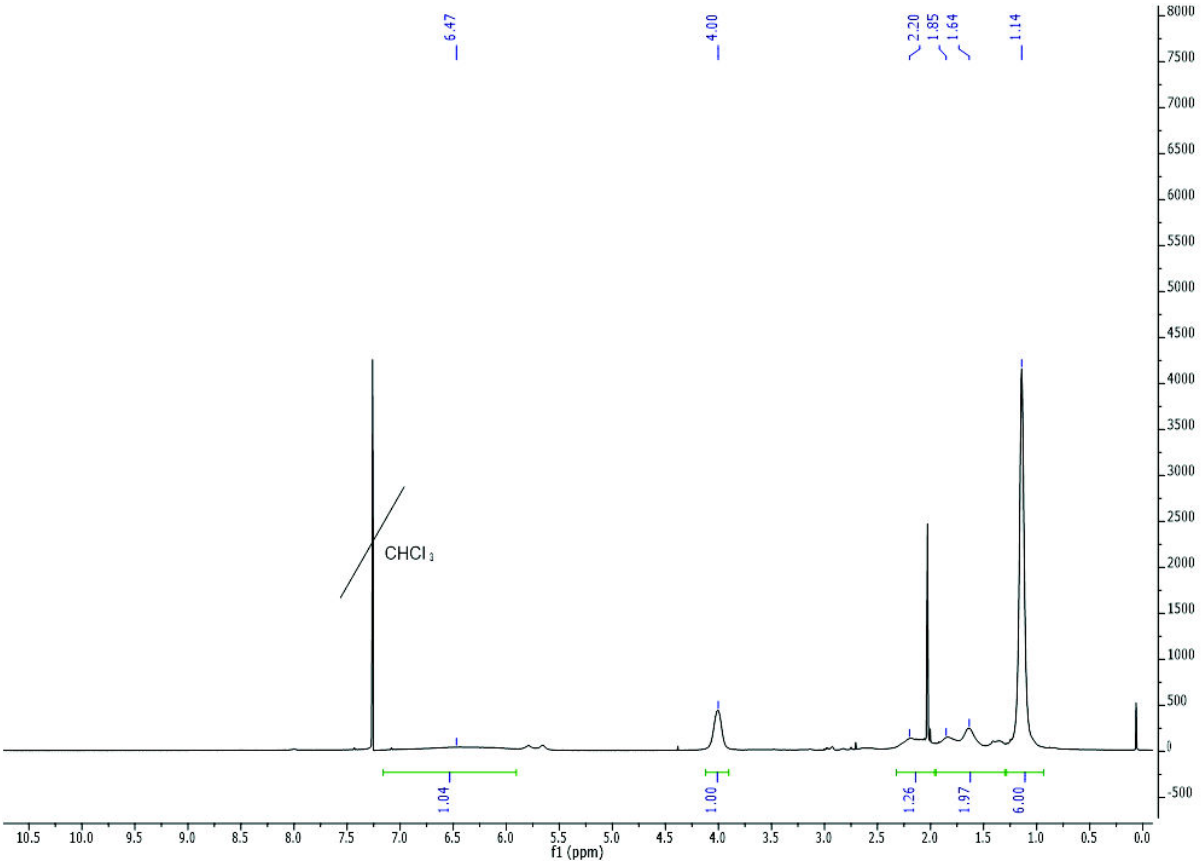

Figure S3a: ^{1}H-NMR (600 MHz, $CDCl_3$) of Man0.

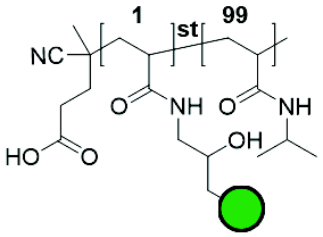

Scheme S3c: Structure of **Man(HP)1.4**. Green circle indicating α-$_D$-mannopyranoside.

^{1}H-NMR **Man(HP)1.4** (600 MHz, $CDCl_3$) δ 4.97 - 4.85 (s, 1H, *H12*), δ 4.07 - 3.95 (s, 75H, *H5*) δ 2.32 - 1.99 (s, 76H, *H3*), δ 1.93 - 1.55 (s, 152H, *H1+2*), δ 1.31 - 0.94 (s, 305H, *H6-11*).

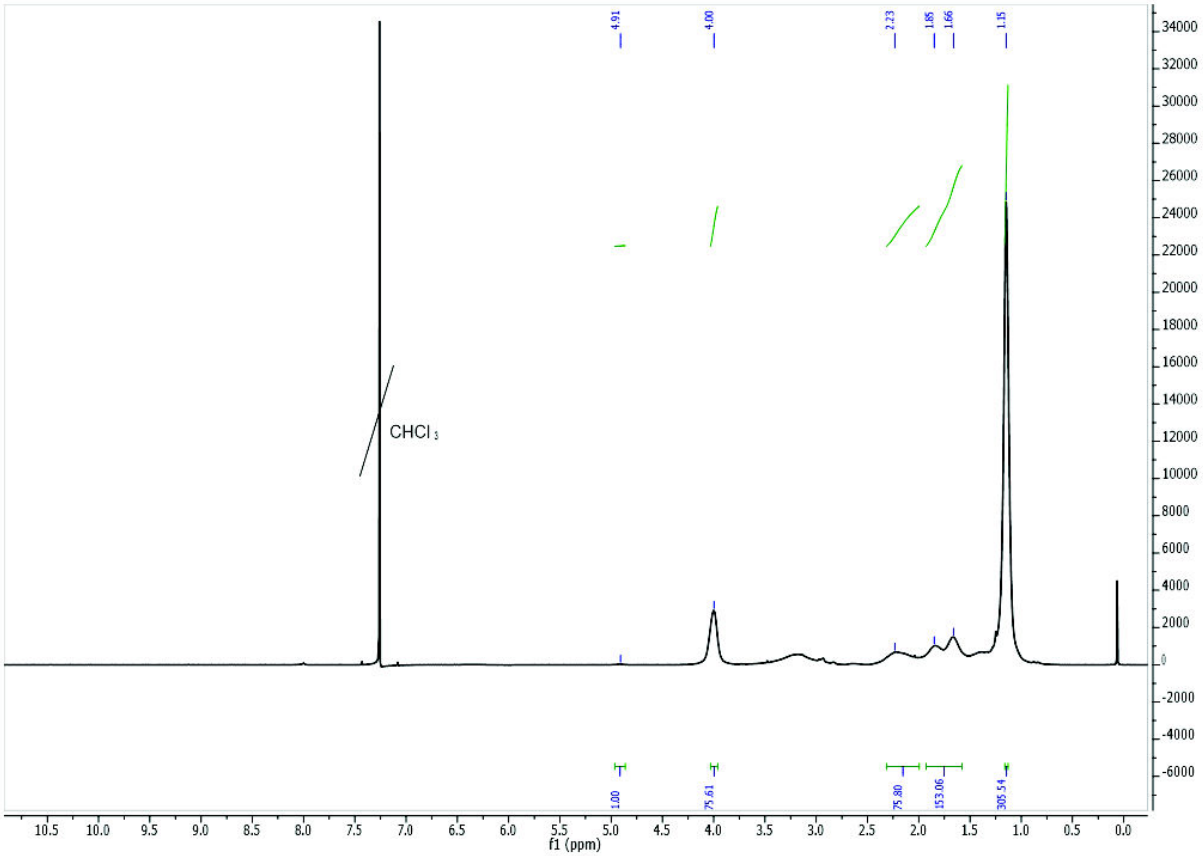

Figure S3b: ^{1}H-NMR (600 MHz, $CDCl_3$) of Man(HP)1.4.

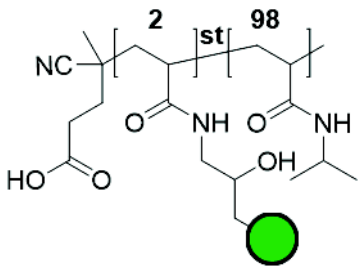

Scheme S3d: Structure of **Man(HP)1.9**. Green circle indicating α-$_D$-mannopyranoside.

^{1}H-NMR **Man(HP)1.9** (600 MHz, $CDCl_3$) δ 7.03 - 5.57 (s, 55H, *H4*), δ 4.92 - 4.86 (s, 1H, *H12*), δ 4.07 - 3.92 (s, 56H, *H5*) δ 2.65 - 1.98 (s, 55H, *H3*), δ 1.95 - 1.25 (s, 111H, *H1+2*), δ 1.19 - 1.03 (s, 334H, *H6-11*).

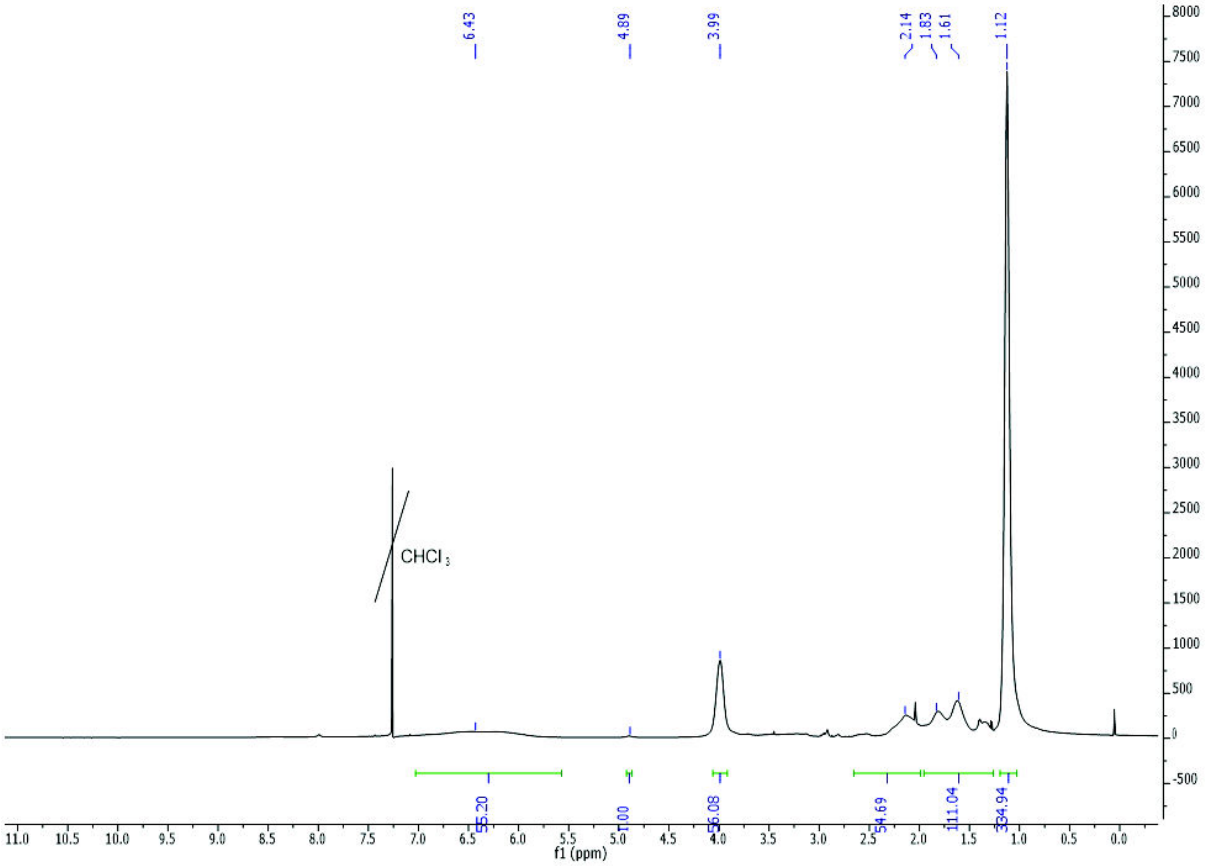

Figure S3c: ^{1}H-NMR (600 MHz, $CDCl_3$) of Man(HP)1.9.

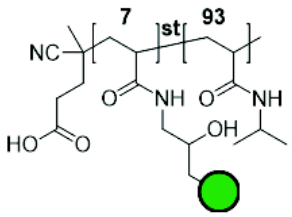

Scheme S3e: Structure of **Man(HP)7.5**. Green circle indicating α-$_D$-mannopyranoside.

^{1}H-NMR **Man(HP)7.5** (600 MHz, $CDCl_3$) δ 6.95 - 5.68 (s, 14H, *H4*), δ 4.95 - 4.83 (s, 1H, *H12*), δ 4.07 - 3.92 (s, 14H, *H5*) δ 2.40 - 1.92 (s, 14H, *H3*), δ 1.91 - 1.25 (s, 28H, *H1+2*), δ 1.17 - 0.98 (s, 84H, *H6-11*).

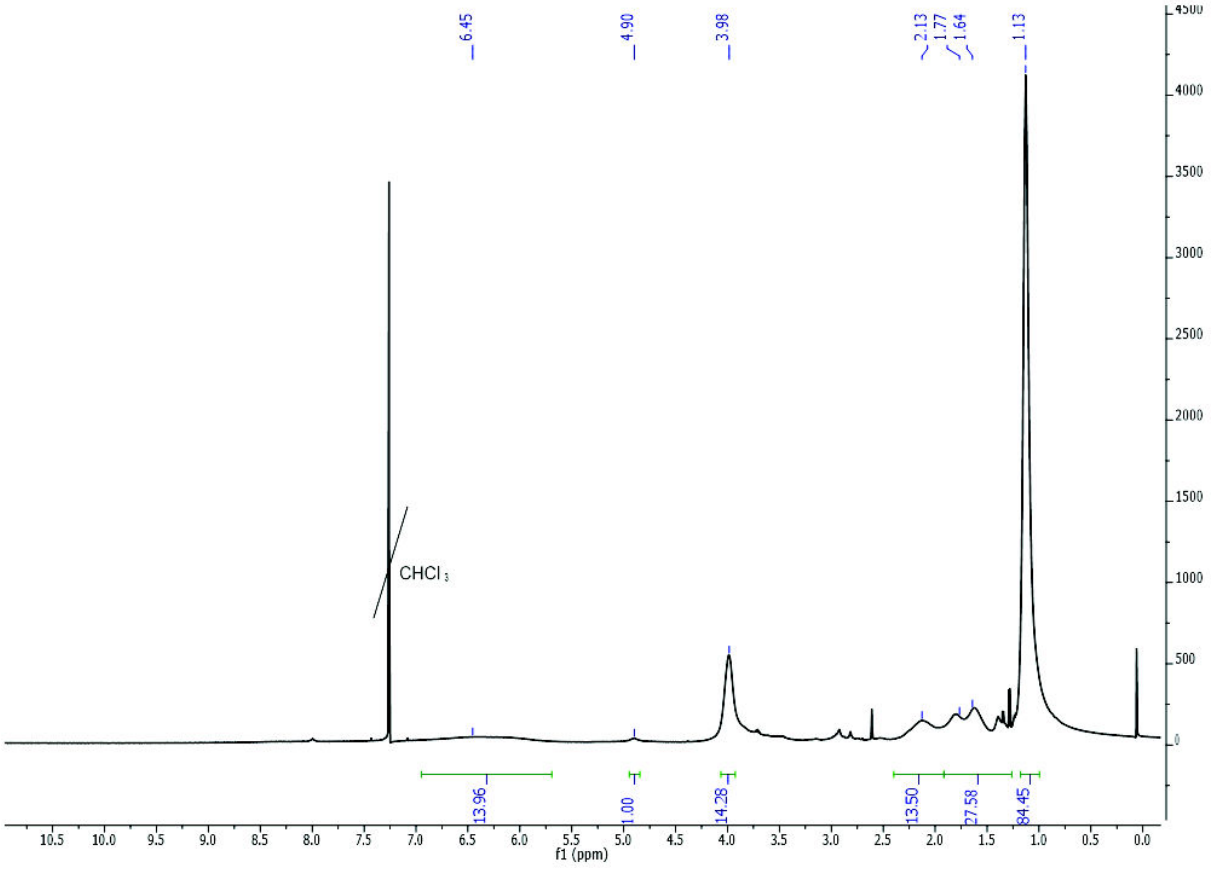

Figure S3d: ^{1}H-NMR (600 MHz, $CDCl_3$) of Man(HP)7.5.

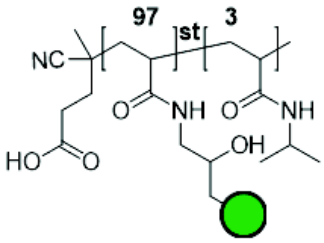

Scheme S3g: Structure of **Man(HP)97**. Green circle indicating α-$_D$-mannopyranoside.

^{1}H-NMR **Man(HP)97** (600 MHz, D_2O) δ 4.95 - 4.85 (s, 1H, *H12*), δ 2.60 - 1.96 (s, 1.18H, *H3*), δ 1.95 - 1.25 (s, 2.14H, *H1+2*) δ 1.18 - 1.12 (s, 0.12H, *H6-11*).

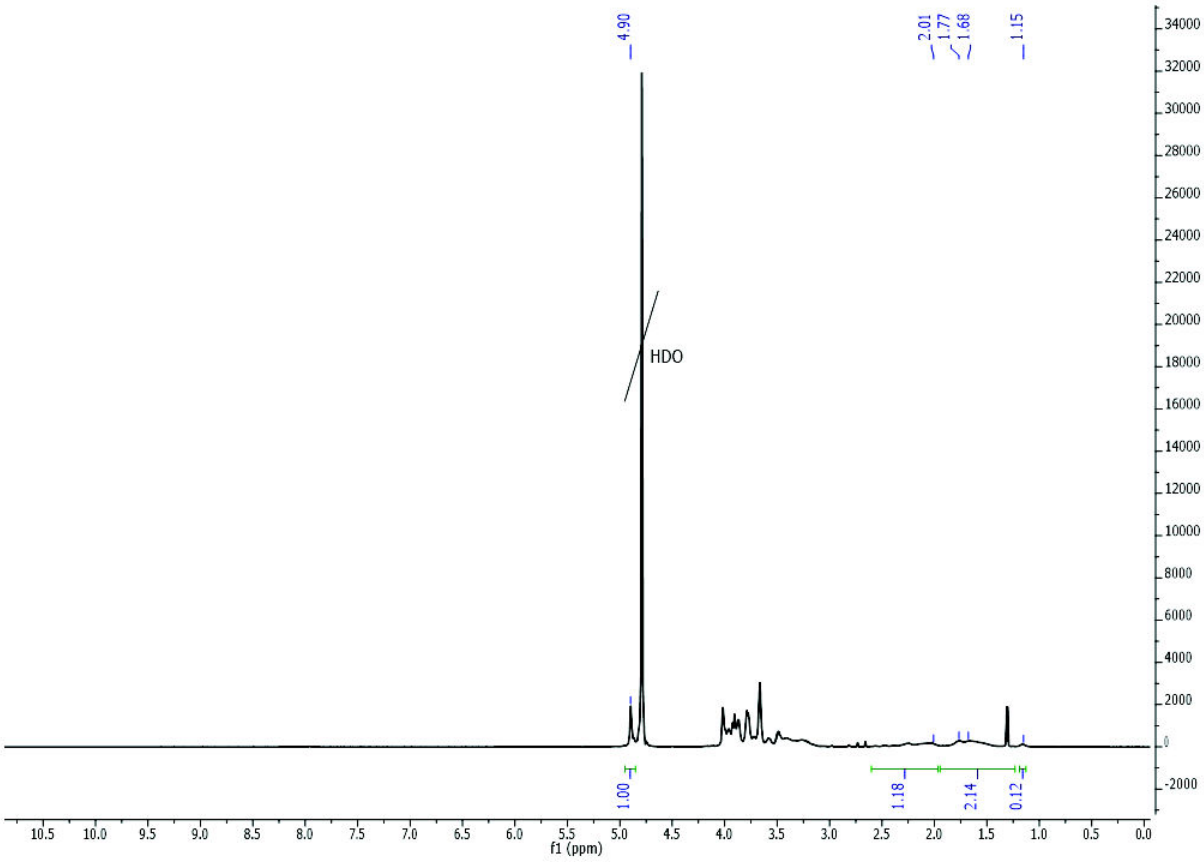

Figure S3f: ^{1}H-NMR (600 MHz, D_2O) of Man(HP)97.

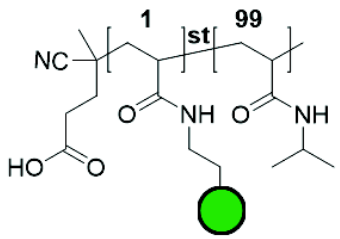

Scheme S3h: Structure of **Man(E)1.1**. Green circle indicating α-D-mannopyranoside.

^{1}H-NMR **Man(E)1.1** (600 MHz, $CDCl_3$) δ 7.10 - 5.85 (s, 75H, *H4*), δ 4.90 - 4.85 (s, 1H, *H12*), δ 4.07 - 3.91 (s, 77H, *H5*) δ 2.40 - 1.95 (s, 79H, *H3*), δ 1.90 - 1.30 (s, 158H, *H1+2*), δ 1.24 - 0.95 (s, 463H, *H6-11*).

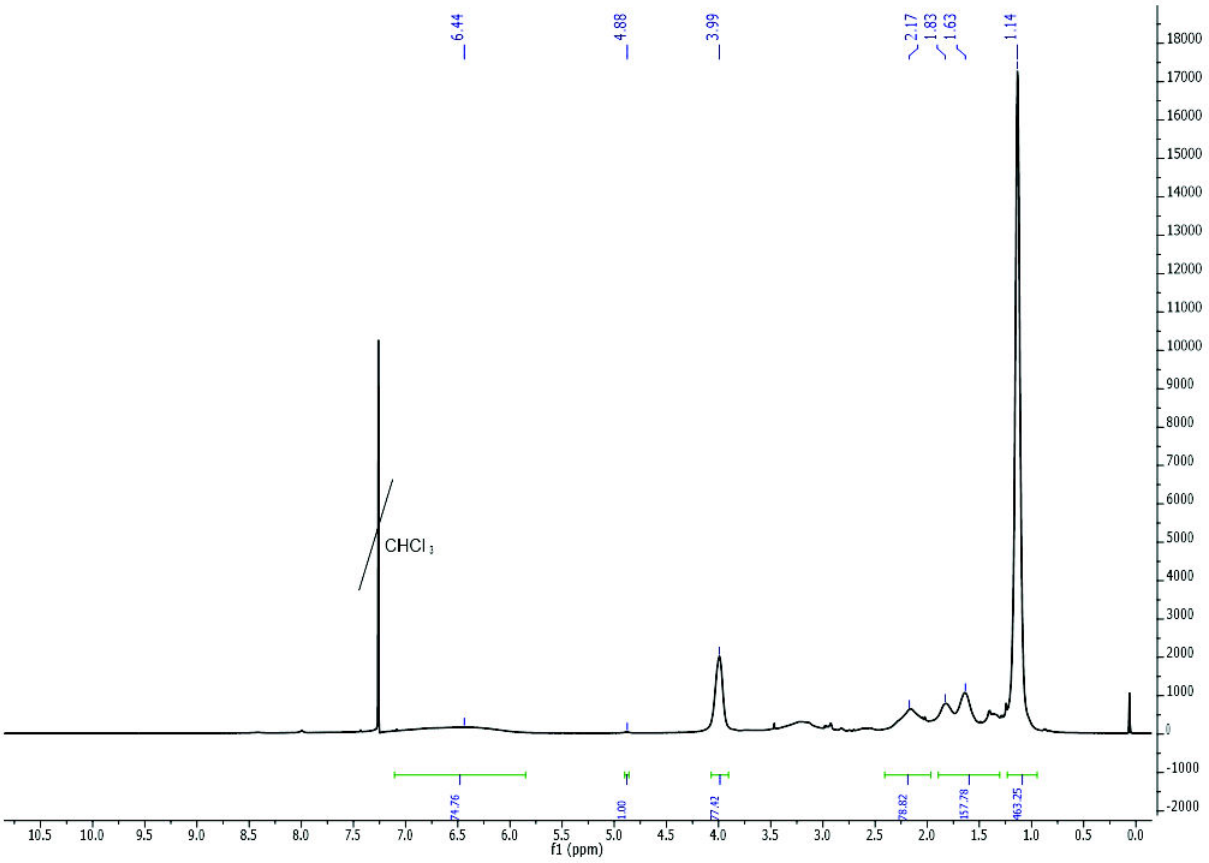

Figure S3g: ^{1}H-NMR (600 MHz, $CDCl_3$) of Man(E)1.1.

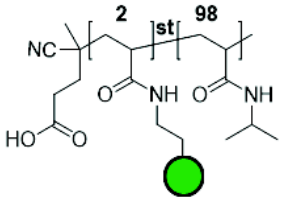

Scheme S3i: Structure of **Man(E)2.2**. Green circle indicating α-$_D$-mannopyranoside.

^{1}H-NMR **Man(E)2.2** (600 MHz, $CDCl_3$) δ 7.00 - 6.05 (s, 32H, *H4*), δ 4.91 - 4.87 (s, 1H, *H12*), δ 4.20 - 3.82 (s, 40H, *H5*) δ 2.40 - 1.98 (s, 35H, *H3*), δ 2.00 - 1.31 (s, 72H, *H1+2*), δ 1.30 - 0.75 (s, 203H, *H6-11*).

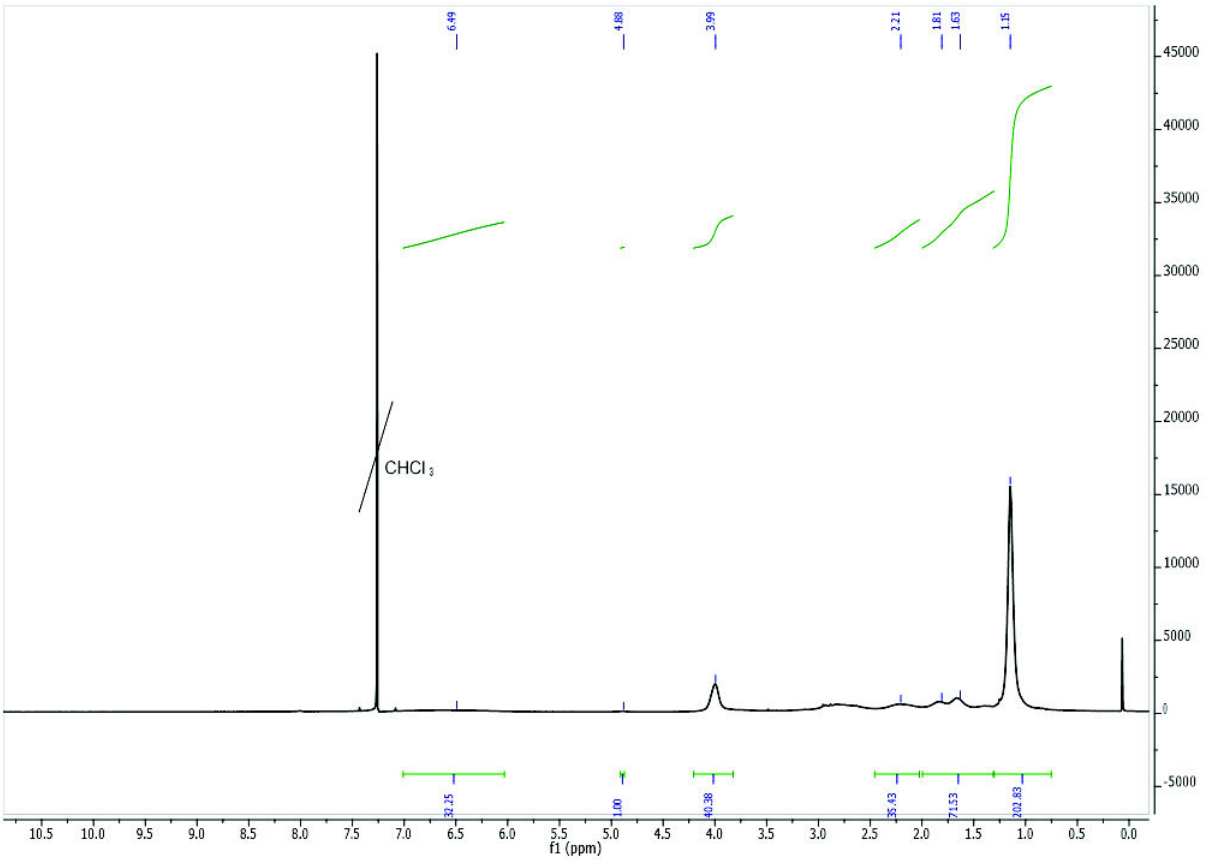

Figure S3h: ^{1}H-NMR (600 MHz, $CDCl_3$) of Man(E)2.2.

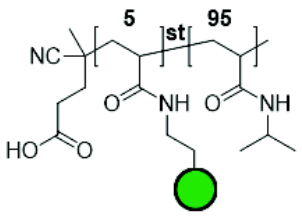

Scheme S3j: Structure of **Man(E)4.6**. Green circle indicating α-$_D$-mannopyranoside.

^{1}H-NMR **Man(E)4.6** (600 MHz, $CDCl_3$) δ 6.97 - 5.68 (s, 24H, *H4*), δ 4.90 - 4.84 (s, 1H, *H12*), δ 4.09 - 3.87 (s, 29H, *H5*) δ 2.66 - 1.98 (s, 24H, *H3*), δ 1.95 - 1.25 (s, 48H, *H1+2*), δ 1.20 - 0.96 (s, 149H, *H6-11*).

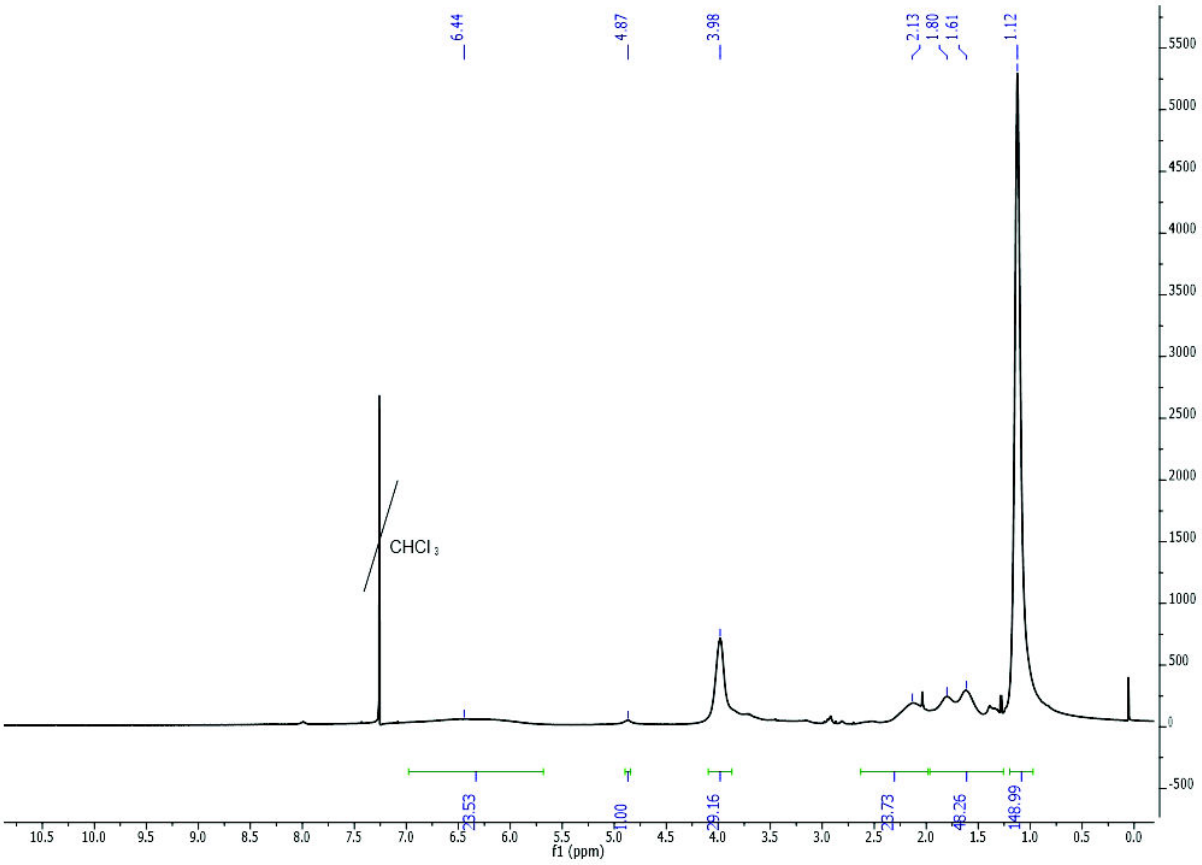

Figure S3i: ^{1}H-NMR (600 MHz, $CDCl_3$) of Man(E)4.6

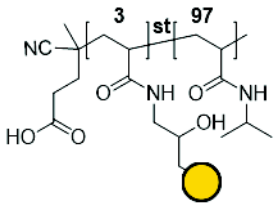

Scheme S3k: Structure of **Gal(HP)2.7**. Green circle indicating β-$_D$-galactopyranoside.

^{1}H-NMR **Gal(HP)2.7**(600 MHz, $CDCl_3$) δ 6.79 - 5.82 (s, 22H, *H4*), δ 4.97 - 4.90 (s, 1H, *H12*), δ 4.06 - 3.90 (s, 31H, *H5*) δ 2.72 - 1.95 (s, 30H, *H3*), δ 1.91 - 1.25 (s, 51H, *H1+2*), δ 1.17 - 1.05 (s, 151H, *H6-11*).

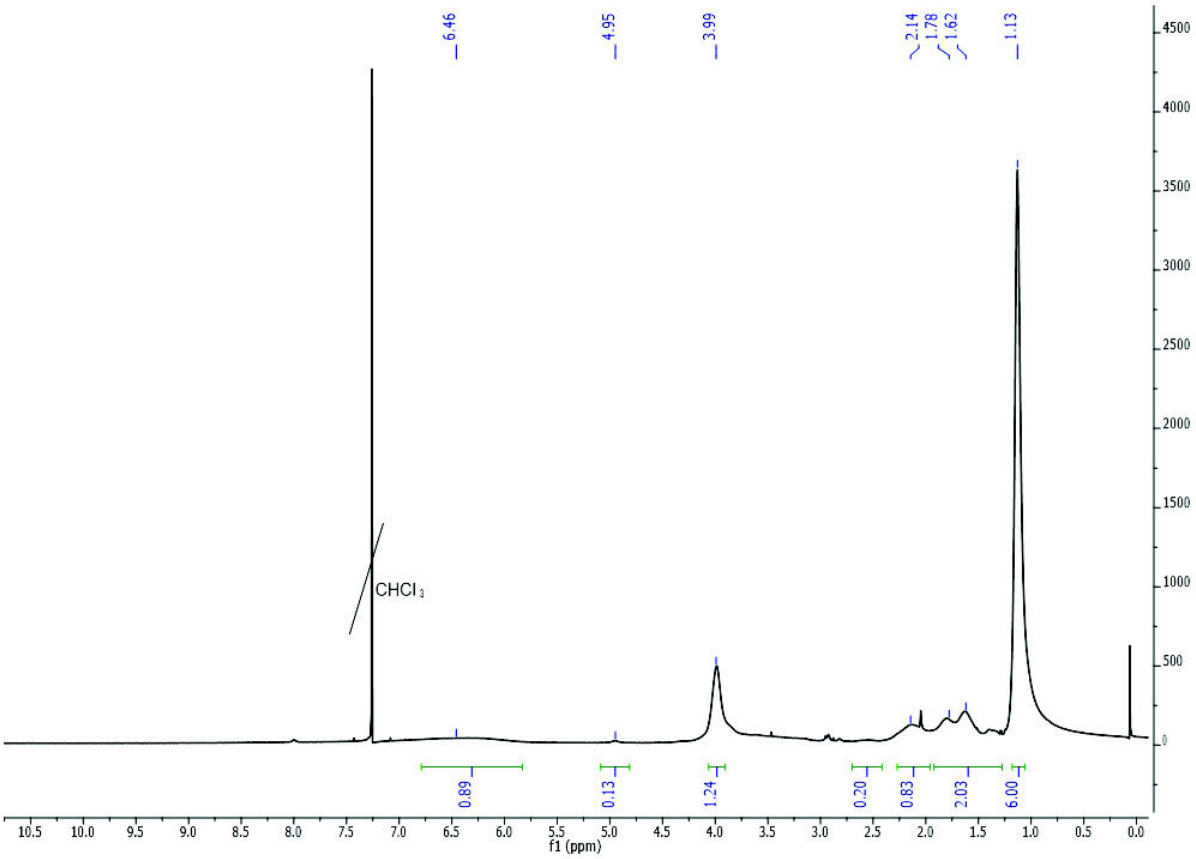

Figure S3j: ^{1}H-NMR (600 MHz, $CDCl_3$) of Gal(HP)2.7.

S4 Size exclusion chromatography

Man(HP)97 was insoluble in DMF, therefore, no SEC measurement were executed for this samples. Having only polystyrene standard at hand and without suitable Marc-Houwink parameters, the SEC measurements were done for determination of Đ-values and not for molecular weight. These measurements show that carbohydrate ligand act as intermolecular bridges between two polymer backbones. The molecular weight was determined via ^{1}H-NMR spectroscopy.

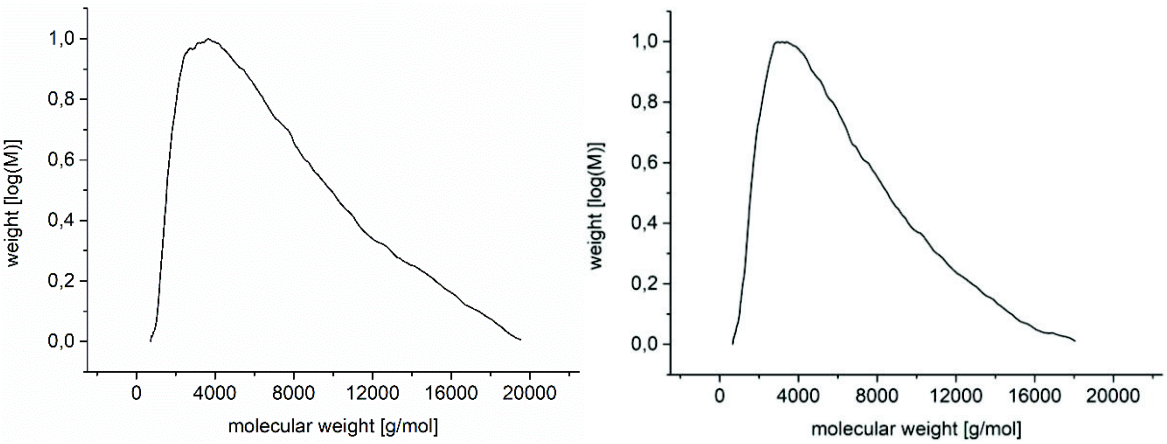

Figure S4a: Size exclusion chromatographies of polymer precursor poly(N-acryloxysuccinimide) (left) and negative control Man0 (right).

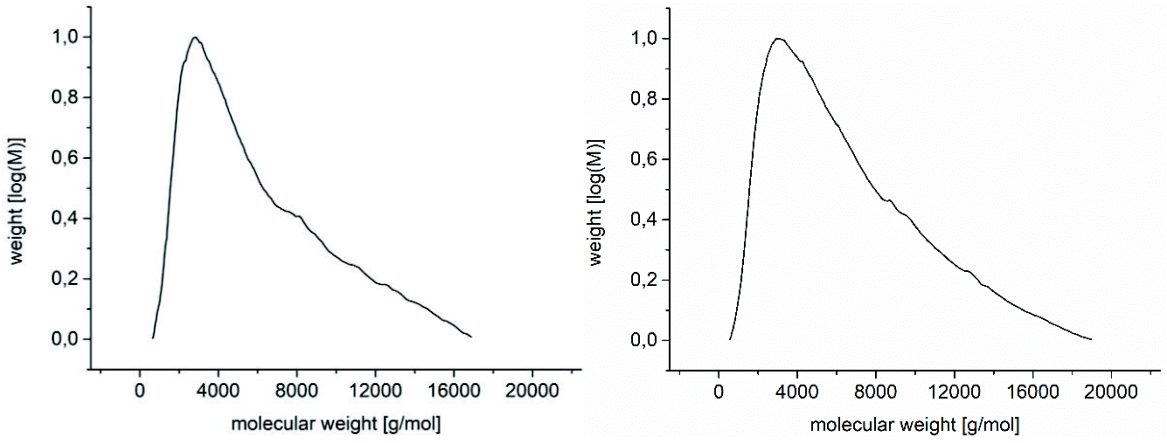

Figure S4b: Size exclusion chromatographies of glycopolymers Man(HP)1.4 (left) and Man(HP)1.9 (right).

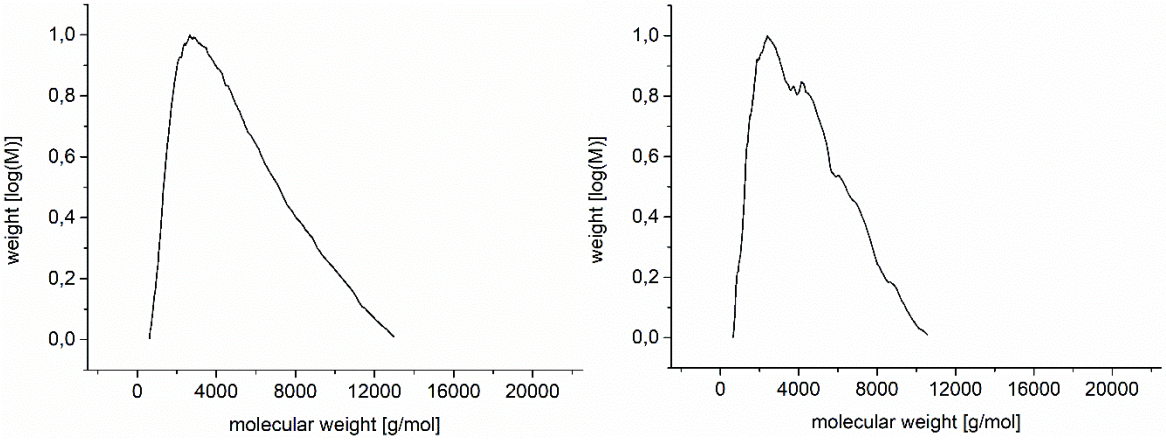

Figure S4c: Size exclusion chromatographies of glycopolymer Man(HP)7.5 (left) and negative binding control Gal(HP)2.7 (right).

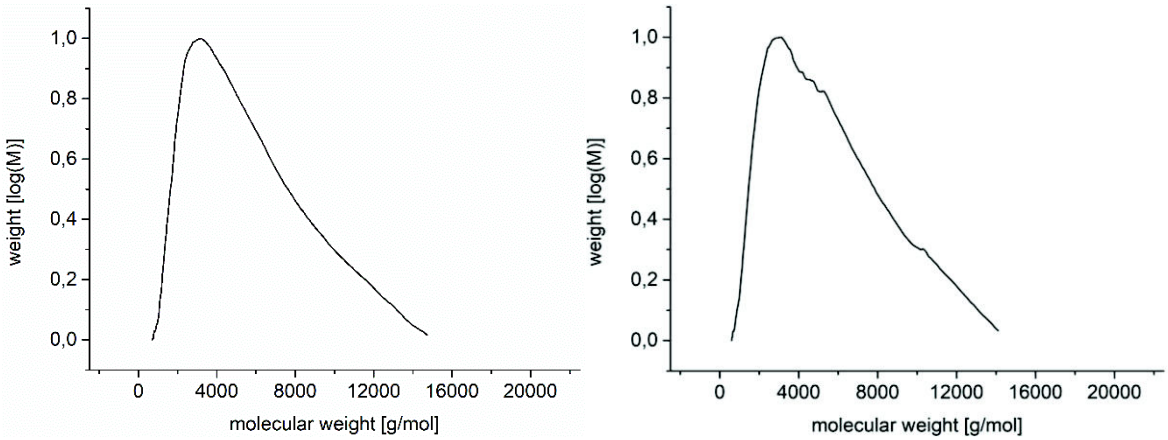

Figure S4d: Size exclusion chromatographies of glycopolymers Man(E)1.1 (left) and Man(E)2.2 (right).

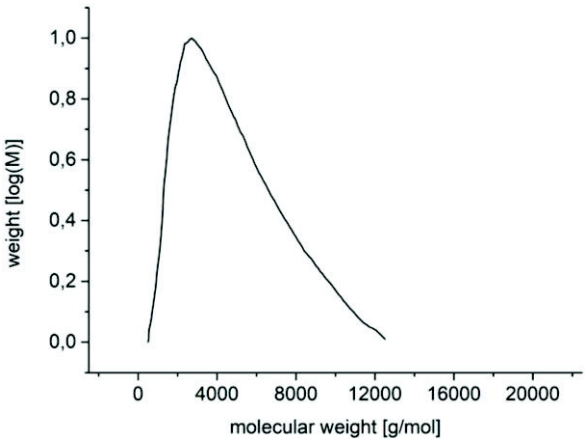

Figure S4e: Size exclusion chromatography of glycopolymer Man(E)4.6.

S5 Phenol sulfuric acid method (PSA)

For analysis of the polymer samples to 125 µL of polymer solution with a specific concentration depending on the expected functionalization degree of the polymer (see Table S5) was used. Procedure for polymer sample was the same as for the calibration curve.

Table S5: For sulfuric acid phenol method used concentration of polymer concentration based on the expected functionalization degree.

Polymer	Amount of polymer used [mg mL^{-1}]
Man0	5.84
Man(HP)1.4	5.83
Man(HP)1.9	2.75
Man(HP)7.5	0.62
Man(HP)97	0.12
Man(E)1.1	5.74
Man(E)2.2	2.66
Man(E)4.6	1.26
Gal(HP)2.7	2.92

S6 Determination of the SCPs elastic modulus

Force-indentation measurement with a NanoWizard 2 AFM provided the elastic modulus of the SCPs. A silica bead with a radius of 2.3 µm was glued with an epoxy glue onto a tipless, non-coated cantilever (spring constant 0.32 N/m; NanoAndMore GmbH). Several force curves were recorded from different particles and analyzed with the novel contact model developed by Glaubitz et al.[4] The model considers deformation of the object at two sites: the indentation site of the AFM probe and at the contact with the solid support. The respective deformation (δ) –force (F) dependence reads:

$$\delta(F) = \left(\frac{3F}{4E}\cdot\frac{1-\upsilon^2}{R_{AFM}^{\frac{1}{2}}}\right)^{\frac{2}{3}} + \left[\frac{3(1-\upsilon^2)\left(F+6W\pi R_{SCP}+\sqrt{12W\pi R_{SCP}F_c(6W\pi R_{SCP})^2}\right)}{4E\cdot R_{SCP}^{\frac{1}{2}}}\right]^{\frac{2}{3}} - \left[\frac{9W\pi(1-\upsilon^2)}{E}\right]^{\frac{2}{3}}\cdot R_{SCP}^{\frac{1}{3}}$$

where E is the elastic modulus of the indented SCP, R_{SCP} its radius, υ the Poisson ratio of the SCP, W the SCP adhesion energy with the support surface and R_{AFM} the radius of the indenter. The Poisson ration was assumed to be 0.5 (volume conservation upon indentation). E and W were free fit parameters. The elastic moduli of FN SCPs were on the order of 72 kPa and their surface energy varied only marginally between 20 and 30 µJ/m^2 for the different fits.

S7 Reflection Interference Contrast Microscopy (RICM) measurements

Setup

RICM on an inverted microscope (Olympus IX73) was used to obtain the contact area between the microparticles and a hard glass surface. For illumination a monochromatic (530 nm) collimated LED (Thorlabs, Germany, M530L2-C1) was used. An UPlanFL N 60x/0.90 dry objective (Olympus Corporation, Japan), additional polarizers and a quarter waveplate (Thorlabs, germany) to avoid internal reflections and a monochrome CMOS camera (DMK 33UX174, The Imaging Source Europe GmbH, Germany) were used to image the RICM patterns.

Determination of the Contact Radius

RICM was used to measure the contact radius formed by the SCPs resting on the polymer surface (Figure S2). Polarized light waves reflected from the upper glass surface (I_1) and the surface of the bead (I_2) interact to create an interference image. The intensity at a given position in the image depends on the separation $h(x)$ between the two surfaces: $I(x) = I_1 + I_2 + 2 \cdot \mathrm{sqrt}(I_1 \cdot I_2) \cos[2k \cdot h(x) + \pi]$, where $k = 2\pi n/\lambda$, and n and λ are the index of refraction of water and the wavelength of the monochromatic light, respectively. In order to detect the interference pattern, stray light was reduced by an 'antiflex' technique. This is accomplished by crossed polarizer and analyzer filter with a $\lambda/4$-plate placed between the objective lens and the analyzer.[5]

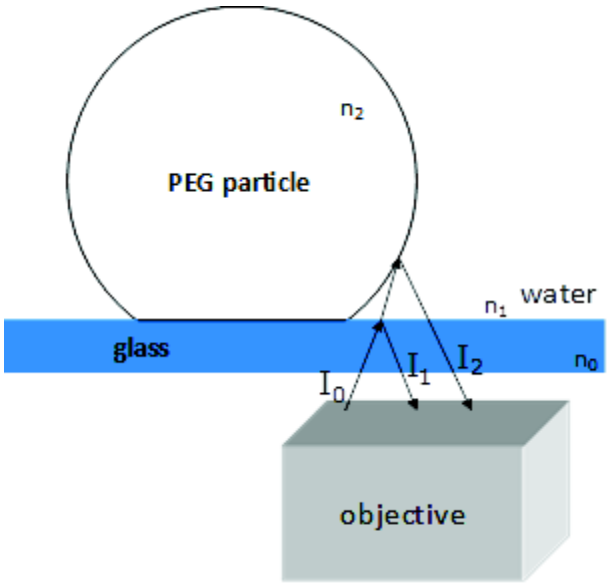

Figure S7a: Schematic drawing of the RICM principle.

Correction Factors

For analysis of the RICM patterns correction factors must be determined for finite aperture and geometry effects. To obtain the correction factors, we imaged hard, non-deformable glass beads on a glass surface in RICM mode with a known size and curvature. We recorded 5 glass beads with a diameter in the range of 20-40 µm (polysciences) and extracted the intensity profile. Using the profiles, we reconstructed the shape of the beads and compared it to the known spherical shapes of the glass beads (glass bead radius R measured by light microscope), and determined the correction factors, see Pussak et al.[6]

Contact radius determination

To determine the contact radius a of the SCP on the polymer surface we reconstructed the height profile of the particles from the RICM images (see Figure S3). This was done by determining the lateral $x(i)$ positions of the i-th minima and maxima by a self-written IgorPro procedure (Wavemetrics, USA). Next, the vertical position $y(i)$ of the maxima and minima were determined by

$$y(i) = \frac{i\lambda}{4n} + c_i ,$$

where n is the refractive index and λ the wavelength. The height profile was then reconstructed by plotting $y(i)$ vs $x(i)$ and fitting the data by a circle equation representing the assumed shape of the SCP:

$$y(x) = y_0 + \sqrt{R^2 - x^2} .$$

where R is the independently measured SCP radius and y_0 the vertical shift of the SCP center due to flattening of the SCP upon adhesion. The fit with y_0 as the only free fit parameter intersects with the x-axis and gives the contact radius a.

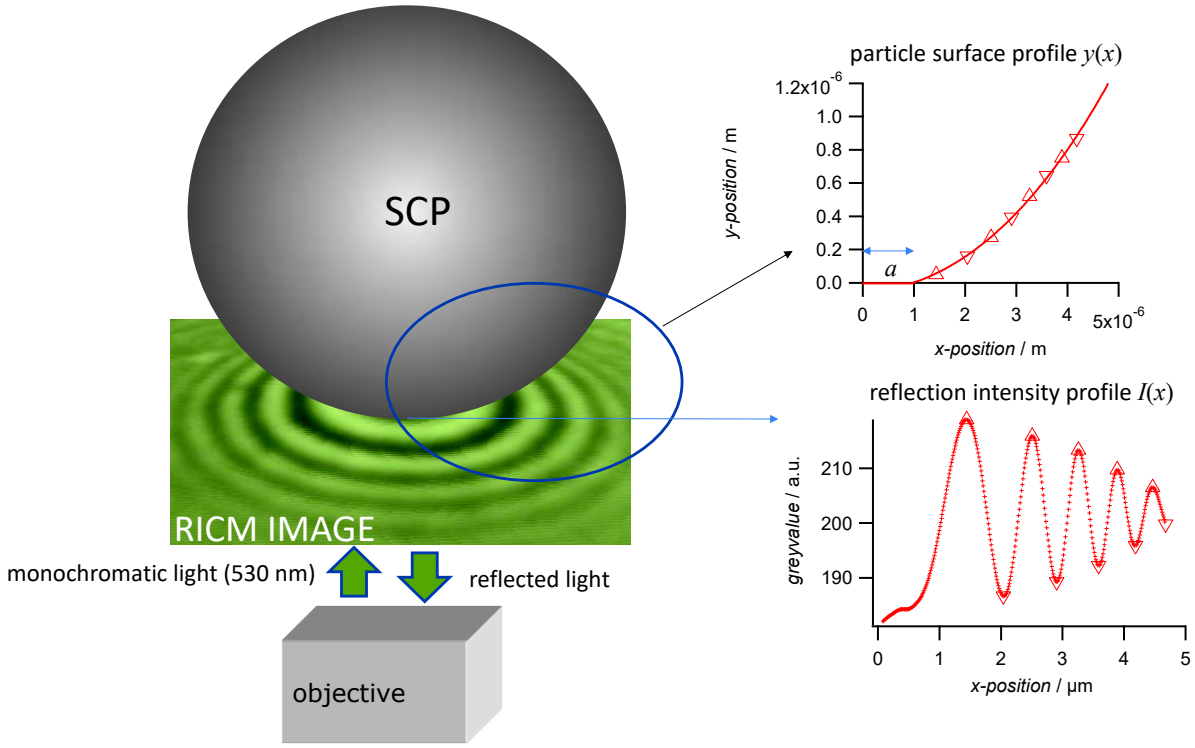

Figure S7b Left: schematic representation of the measurement setup. Bottom right: actual intensity profile of an adherent SCP showing 5 minima and 5 maxima. Top right: reconstructed surface profile of the SCP and the contact radius a at the intersection of the profile at y = 0.

S8 Instrumentation

Nuclear Magnetic Resonance Spectroscopy (NMR)

^{1}H-NMR and ^{13}C-NMR (600 MHz) were measured on a Bruker AVANCE III 600 (Bremen, Germany). As internal standard chemical shifts were referenced to the residual non-deuterated solvents ($CDCl_3$: ^{1}H 7.26, ^{13}C 77.16, D_2O: ^{1}H 4.79). All chemical shifts are reported in delta (δ) expressed in parts per million (ppm). The following abbreviations were used to indicate multiplicities: s = singlet, d = doublet, t = triplet, m = multiplet.

Size exclusion chromatography (SEC)

SEC measurements were performed using a ViscotekGPCmax VE2001 system. The System has a column set compromising one TSK HHR-H, 100 Å pore size and 10 µm particle size, 800 × 5.0 mm [Length × ID]pre-column and two Viskotek TSK GMHHR-M linear, 10 µm particle size, 300 × 8.0 mm [Length × ID]columns. The columns were constantly heated to a temperature of 60 °C. N,N-Dimethylformamide (0.05 M LiBr) was used as eluent at a flow rate of 1 mL min^{-1}. For detection a Viscotek VE 3500 RIdetector was used. The system was calibrated with poly(methyl methacrylate) standards of a molecular range from 1430 g mol^{-1} to 1250000 g mol^{-1}.

Freeze Dryer

An Alpha 1-4 LD plus instrument from Martin Christ Freeze Dryers GmbH (Osterrode, Germany) was used for lyophilization of all microgel samples. The main drying method was set to -54 °C and 0.1 mbar.

UV-Vis Spectroscopy

On a dual-trace spectrometer Specord® 210 Plus from *Analytik Jena AG* (Jena, Germany) all UV-Vis measurements were performed at 25 °C. Using Win ASPECT PLUS software the instrument was operated. Protein concentration measurements were pereformed in a cuvette QX quartz cuvette (d = 1 cm, V = 3.5 mL) from Hellma Anayltics (Mühlheim, Germany). For determination of sugar concentration the absorption from 350-550 nm was measured. Using the absorption and a calibration curve the concentration of carbohydrates was calculated.

Turbidity measurements

Turbidity measurements were executed on a Tepper turbidity photometer with a class 2 laser with a wavelength from 630-690 nm and a light intensity of < 1 mW.

Buffer and media

LB-Medium (PKL1162): 12.5 g of LB Broth (Miller) (powder microbial growth medium) were dissolved in 500 mL ultrapure water. The powder contains tryptone (5.0 g), sodium chloride (5.0 g) and yeast extract (2.5 g). Afterwards the solution was sterilized for 30 min at 121 °C and cooled to room temperature. 50.0 mg of ampicillin and 25.0 mg of chloramphenicol were added.

PBS buffer

Five tablets of phosphate buffered saline was dissolved in 1 L of ultrapure water. The final concentrations of the buffer were 0.01 M phosphate buffer, 0.0027 M potassium chloride and 0.137 M sodium chloride. The pH was checked with a potentiometer and set to 7.4.

LBB buffer

Lectin binding buffer (LBB) was used for all measurements with Concanavalin A. Lectin binding buffer contains 10 mM HEPES ((4-(2-hydroxyethyl)-1-piperazineethanesulfonic acid) as buffering agent, which was adjusted to a pH of 7.4 with 1 M NaOH. Thereafter, calcium chloride (1 mM) and manganese chloride (1 mM) and sodium chloride (50 mM)

were dissolved in the solution. To prevent bacterial growth in the buffer sodium azide was added to a final concentration of 0.05 wt%

Bacterial culture

E. coli PKL 1162 were grown in LB medium (PKL 1162) overnight in a sterilized test tube, which was covered with aluminum foil at 37 °C. The tubes were shaken with a speed of 140 rpm to guarantee a constant mixing of the solution.

Supporting references

1. Dalier, F.; Eghiaian, F.; Scheuring, S.; Marie, E.; Tribet, C., Temperature-Switchable Control of Ligand Display on Adlayers of Mixed Poly(lysine)-g-(PEO) and Poly(lysine)-g-(ligand-modified poly-N-isopropylacrylamide). Biomacromolecules 2016, 17 (5), 1727-1736.
2. Himanen, J. A.; Pihko, P. M., Synthesis of Trisaccharides by Hetero-Diels-Alder Welding of Two Monosaccharide Units. Eur. J. Org. Chem. 2012, (20), 3765-3780.
3. Hayes, W.; Osborn, H. M. I.; Osborne, S. D.; Rastall, R. A.; Romagnoli, B., One-pot synthesis of multivalent arrays of mannose mono- and disaccharides. Tetrahedron 2003, 59 (40), 7983-7996.
4. Glaubitz, M.; Medvedev, N.; Pussak, D.; Hartmann, L.; schmidt, s.; Helm, C. A.; Delcea, M., A novel contact model for AFM indentation experiments on soft spherical cell-like particles. Soft Matter 2014.
5. Limozin, L.; Sengupta, K., Quantitative Reflection Interference Contrast Microscopy (RICM) in Soft Matter and Cell Adhesion. ChemPhysChem 2009, 10 (16), 2752-2768.
6. Pussak, D.; Ponader, D.; Mosca, S.; Ruiz, S. V.; Hartmann, L.; Schmidt, S., Mechanical Carbohydrate Sensors Based on Soft Hydrogel Particles. Angewandte Chemie International Edition 2013, 52 (23), 6084-6087.

6. Unpublished results

The stiffness of cellular microenvironments is an important factor controlling many biological processes.[173] Changes in material stiffness of cell environments are translated into biochemical signals and this translation is called mechanotransduction. Mechanotransduction is responsible for a lot of different processes, e.g. stem cell differentiation or sensing.[174,175] Moreover, it could be shown in previous work, how the elasticity influences ligand-receptor interaction.[165] Due to its high influence on ligand-receptor binding the changes in elastic modulus of thermoresponsive polymer functionalized SCPs were investigated in dependence of temperature.

At first, thermoresponsive polymers were synthesized via a polymer analog reaction using the poly (active ester) poly (*N*-Acryloxysuccinimide) as a polymer precursor. In the next step, an amine functionalized carbohydrate was reacted towards the polymer backbone before the remaining active esters were quenched with isopropylamine to create thermoresponsive polymers with different amounts of carbohydrates and lower critical solution temperatures (LCST). These polymers were then grafted onto poly (ethylene glycol) based SCPs. After functionalization, six different SCPs were obtained. One unfunctionalized SCP only presenting carboxylic acid groups and five SCPs functionalized with thermoresponsive polymers with different amounts of carbohydrates incorporated in a range from 0 to 97%.

The elastic modulus was measured via AFM colloidal probe force indentation measurements. AFM Cantilevers were prepared by UV/Ozone cleaning and application of two-component epoxy adhesive. The adhesive was used to attach a SiO_2 colloidal probe with a diameter of 4.6 µm onto the cantilever. After the curing of the glue, the measurements were performed in lectin binding buffer (LBB). This buffer was used because it is mandatory for measuring ligand-receptor interactions between the carbohydrate and lectin due to the activation of lectin binding sites by Ca^{2+} and Mn^{2+} cations added in the buffer. The measurement was performed by pressing the glass probe onto the SCPs at below and above the LCST of the thermoresponsive polymers grafted onto the SCPs (see Figure 18). The polymers LCSTs were between 32.6 °C for PNIPAM and 40.2 °C for polymer containing 7% carbohydrates. The polymer bearing 97% carbohydrate did not show LCST behavior and was, therefore, used as a non-LCST control

polymer. To guarantee a full collapse of polymer chains above the LCST a temperature of 45°C was chosen.

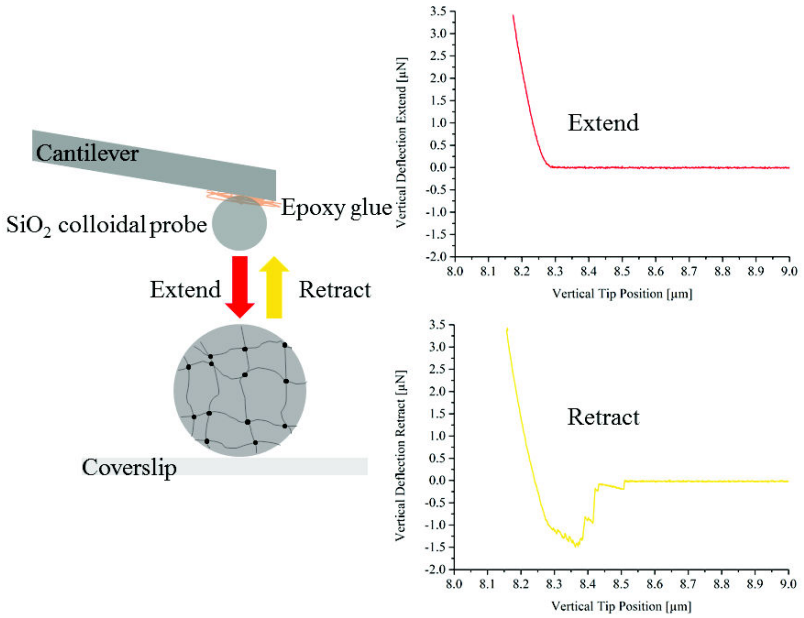

Figure 18 Scheme of AFM colloidal probe force indentation measurements. The SiO_2 colloidal probe glued to the cantilever is pressed onto the SCP (Extend) and retracted again. The elastic modulus is calculated from the extend curve (red).

As a control experiment crotonic acid (CA) functionalized SCPs were measured at the same temperatures. Here, the elastic modulus increases with increasing temperature, which is in accordance with De Gennes:

$$E \sim \frac{k_B T}{\xi^3} \qquad (7)$$

with E as elastic modulus, T as temperature and ξ as mesh size of the particle. Not only the increase in temperature explains the increase in elastic modulus, but also the decrease in mesh size. The decrease in mesh size comes from the so-called “entropic spring” effect. The polymer chains crosslinked in the SCPs are in a coiled conformation and, due to temperature increase, pulling the chain ends together resulting in a contraction and decreasing mesh size (see Figure 19).

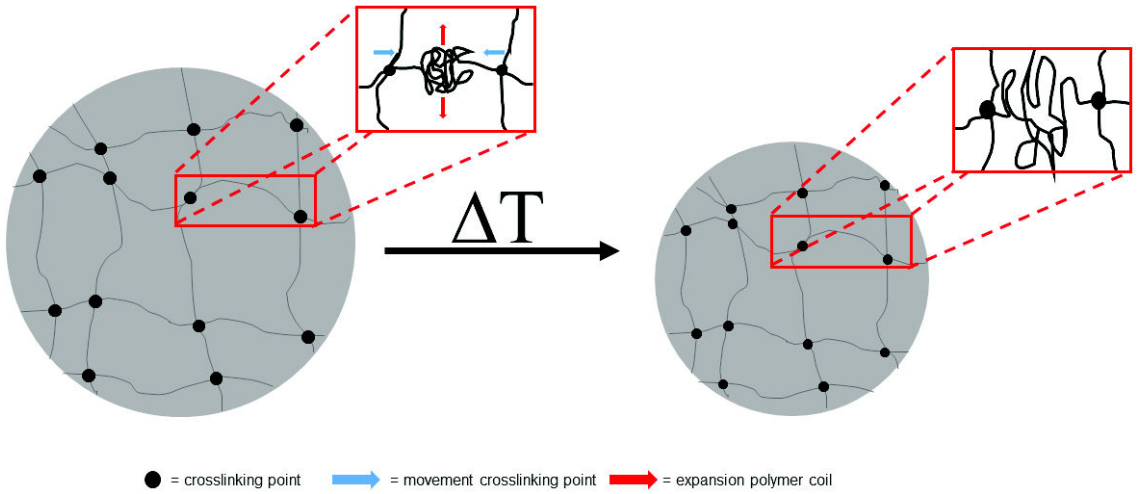

Figure 19 Scheme explaining the entropic spring effect. Upon temperature increase the crosslinking ends of polymer chains (black dots) contract due to an expansion of the coiled polymer chains.

SCPs functionalized with thermoresponsive polymers show a completely different behavior. The first effect of polymer functionalization is that the mesh size is decreased because the polymers "fill out" the space between PEG chains (see Figure 20). When increasing the temperature, according to the temperature dependence of De Gennes, the elastic modulus should increase but instead, it decreases. The thermoresponsive behavior leads to a collapse of the grafted polymer chains instead of an expansion. Therefore, the effective mesh size that was decreased by grafting before is now increased again due to the polymer collapse. Thus, the decrease in mesh size shows a higher influence than the temperature increase which is again in accordance with De Gennes. Moreover, the polymer with 97% of incorporated carbohydrates shows the same behavior as the CA functionalized SCPs before due to its lack of thermoresponsiveness.

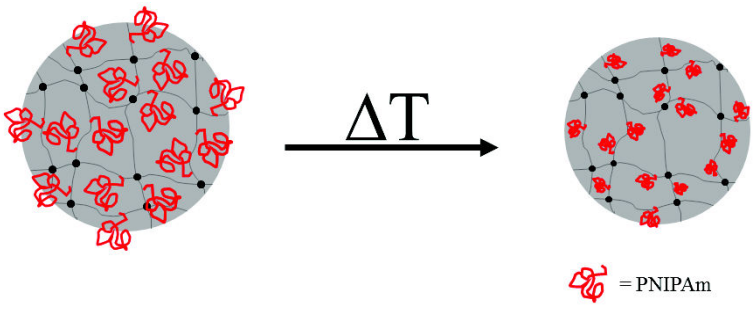

Figure 20 Schematic explanation of increase of the effective mesh size of the SCPs when crossing the LCST of the thermoresponsive polymer. The swollen polymer coils (left)

decrease the mesh size of the SCP but when exceeding the LCST they collapse and the mesh size increases.

The elastic moduli for all thermoresponsive polymers decrease for around 20% (see Figure 21). Due to the use of the same polymer precursor for the synthesis of all those polymers, it can be analyzed in further studies how the number of repeating units of the polymer can influence the changes of the elastic modulus.

Additionally, it should be noted that the maximum value for elastic modulus seems to be given by the polymeric network of the SCP. This is because the values for SCPs functionalized with CA, PNIPAM and polymer with 97% carbohydrate show the same maximum value for elastic modulus. This threshold may be reached when the mesh size of the SCP cannot decrease any further.

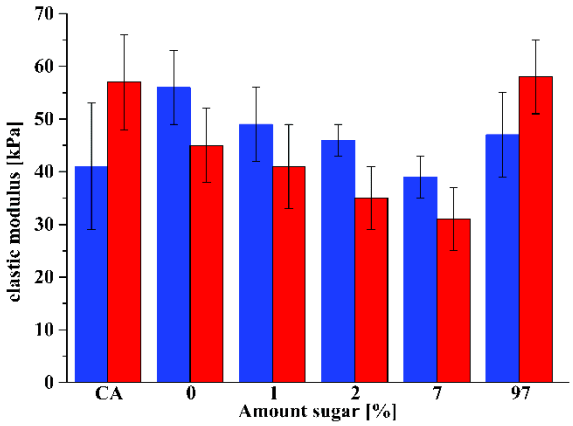

Figure 21 Elastic modulus measured for CA and polymer functionalized SCPs in dependence of sugar amount. Blue bars show values at 20 °C and red bars show values at 40 °C.

7. Appendix

7.1. List of Abbreviations

General abbreviations

e.g.	exempli gratia (for example)
IUPAC	International Union of Pure and Applied Chemistry
US	United States
MFP	mussel foot protein
P. aeruginosa	*Pseudomonas aeruginosa*
UCST	upper critical solution temperature
LCST	lower critical solution temperature
SPR	surface plasmon resonance
QCM	quartz crystal microbalance
AFM	atomic force microscopy
SM-AFM	single-molecule-atomic force microscopy
SCP-RICM	Soft Colloidal Probe adhesion assay
RICM	reflection interference contrast microscopy
SCP	soft colloidal probe
JKR	Johnson-Kendall-Roberts
E. coli	*Escherichia coli*
E-modulus	Elastic modulus / Youngs modulus

Carbohydrate abbreviations

Man	mannose
Glu	glucose
Gal	galactose
GlcNAc	*N*-Acetyl-glucoseamine
Neu5Ac	*N*-Acetylneuraminic Acid
Fuc	fucose
C2	carbonatom number 2 of carbohydrate
C3	carbonatom number 3 of carbohydrate
C4	carbonatom number 4 of carbohydrate

C6	carbonatom number 6 of carbohydrate

Amino acid abbreviations

A/Ala	alanine
S/Ser	serine
Y	dihydroxyphenylalanine
Tyr	tyrosine
G/Gly	glycine
P/Pro	proline
N/Asn	asparagine
R/Arg	arginine
W/Trp	tryptophan
K/Lys	lysine
D/Asp	aspartate
H/His	histidine
T/The	threonine
L/Leu	leucine

Chemical Abbreviations

O	oxygen
N	nitrogen
C	carbon
Cl	chlorine
DOPA	3,4-dihydroxyphenylalanine
NAS	*N*-acryloxysuccinimide
PNAS	poly(*N*-acryloxysuccinimide)
PNIPAM	poly(*N*-isopropyl acrylamide)
E/EL	ethyl linker
HP/HPL	2-hydroxypropyl linker
PEG	poly(ethylene glycol)
CA	crotonic acid
ConA	concanavalin A
NaCl	sodium chloride
LBB	lectin binding buffer

Units, parameters and symbols

%	percent
°C	degree Celsius
T	temperature
nm	nanometer
n_1	refractive index water
n_0	refractive index glass
I_0	starting light intensity
$I_{1/2}$	refracted light intensity
a	contact radius
R	sphere radius
P	external load
k	elastic constant of sphere
E	Youngs modulus/elastic modulus
υ	Poisson ratio
γ	Energy per unit of contact area
W_{adh}	adhesion energy
E_{eff}	effective elastic modulus
R_{eff}	effective radius
F	Force
wt%	weight percent
M	mol/liter
<	below
>	above
mol%	percent of molecules
UV	ultra violoett
k_B	Boltzmann constant
ξ	mesh size

7.2. List of Figures

Figure 7 Structures of terminal monosaccharide moieties found on cell surfaces and their frequency of occurrence as determined by the group of Seeberger.[63] Colored symbols are the symbol nomenclature of those carbohydrates for a schematic presentation of oligo- and polysaccharides.

Figure 8 Binding site of Concanavalin A with manganese and calcium ions and mannose moiety in the binding site with hydrogen bonds between amino acids and binding partners (left) (adapted from 71). Additionally, α-D-Glucose and α-D-Galactose for comparison (right). The hydroxyl group on C2 (red circle) does not have an influence on the binding between mannose and ConA, therefore glucose can also bind to ConA, whereas the difference in the binding hydroxyl group at C4 (green circle) leads to non-binding of galactose.

Figure 9 Schematic presentation of mimicking the membrane bound glycocalyx. The membrane of the cell (left) is exchanged by a polymer backbone and the terminal sugar of membrane bound oligo- and polysaccharides are presented on the polymer backbone (right) in a homovalent (right top) or heterovalent (right bottom) fashion. (Glycans adapted from 54).

Figure 10 Typical routes providing glycopolymers via radical polymerization. Homopolymerization of glycomonomer giving a homopolymer with high ligand density (a), copolymerization of glycomonomer with acrylate or acrylamide based co-monomer giving a copolymer with adjustable ligand density depending on the ratio of m and n and potentially adjustable architecture (b) and polymeric analog reaction based on polymerization of an active ester and functionalization afterwards to adjust ligand density exemplary on active ester *N-acryloxysuccinimide* (NAS) (c)**.**

Figure 11 Illustration of different classification possibilities of stimuli-responsive polymers. One possibility is the classification by the stimulus (top) and the other one by physical appearance (bottom).

Figure 12 Schematic presentation of a stimulus-responsive polymer undergoing a temperature induced change in water. Below the lower critical solution temperature (LCST) the polymer backbone of the polymer coil builds hydrogen bonds to water molecules. After exceeding the LCST hydrogen bonds are broken and intramolecular polymer-polymer interactions take place increasing the order in the polymer globule in comparison to the swollen coil. The release of water increases the systems entropy**.**

Figure 13 Schematic image of reflection interference contrast microscopy based soft colloidal probe (SCP) adhesion assay. When the SCP is not in contact with the glass surface the interference pattern formed by reflected light leads to a bright spot in the middle (left). When the SCP gets in contact with the surface the interference pattern has a dark spot in the middle (right). From this interference pattern radius of contact area (a) and radius of the particle (R) can be calculated. Two different exemplary images show the differences visible during the measurement (bottom).

Figure 14 Schematic light beam path during the RICM measurement leading to the interference pattern by reflection at the interfaces with different refractive indices.

Figure 15 Schematic display of the difference between Hertz and JKR theory. Two spheres are pressed together with R1 and R2 as sphere radii, load P0, and contact radii a0 depending on Hertz theory and a1 considering additional attractive forces depending on JKR theory (adapted from 162).

Figure 16 Schematic presentation of an AFM force indentation measurement to determine the SCP´s elastic modulus. Shown are the three steps that a measurement can be divided into (top). The first step (left) is the positioning of the cantilever in the center above the SCP. In the second step (middle) the glass bead glued to the cantilever is pressed onto the SCP (extend) before it is drawn into the starting position (retract, right). On the bottom exemplary extend and retract curves are shown. The numbers show the influence of each step onto the curve. 1) is the starting position, 2) is the contact between glass bead and SCP and 3) is the energy needed to overcome adhesive interactions between the glass bead the SCP.

Figure 17 Schematic structures of oligomers used for adhesion studies. Three groups of oligomers can be differed: homovalent structures bearing the same functional groups (left), heterovalent structures bearing two different functional groups (middle) and heterovalent structures with changed positioning and spacing (right).

Figure 18 Scheme of AFM colloidal probe force indentation measurements. The SiO2 colloidal probe glued to the cantilever is pressed onto the SCP (Extend) and retracted again. The elastic modulus is calculated from the extend curve (red).

Figure 19 Scheme explaining the entropic spring effect. Upon temperature increase the crosslinking ends of polymer chains (black dots) contract due to an expansion of the coiled polymer chains.

Figure 20 Schematic explanation of increase of the effective mesh size of the SCPs when crossing the LCST of the thermoresponsive polymer. The swollen polymer coils (left) decrease the mesh size of the SCP but when exceeding the LCST they collapse and the mesh size increases.

Figure 21 Elastic modulus measured for CA and polymer functionalized SCPs in dependence of sugar amount. Blue bars show values at 20 °C and red bars show values at 40 °C.

8. Acknowledgments

Zum Schluss möchte ich all denen, die mich während der Promotion unterstützt und begleitet haben danken.

Zu allererst gilt mein Dank Jun. Prof. Dr Stephan Schmidt für die Möglichkeit diese Arbeit in seiner Arbeitsgruppe anzufertigen. Des Weiteren möchte ich meinen Dank ausdrücken für die Unterstützung und Anregungen bei der Ausarbeitung der verschiedenen Projekte und der Anfertigung der Veröffentlichungen.

Außerdem möchte ich Prof. Dr. Matthias Karg meinen Dank aussprechen für die Übernahme des zweiten Korrektors dieser Arbeit.

Prof. Dr. Laura Hartmann gilt mein Dank für die Unterstützung und die Zusammenarbeit im Projekt mit der Firma Henkel.

Meinen Kooperationspartnern der Firma Henkel Dr. Christian Kropf und Dr. Nils Wedler möchte ich für die gute und spannende Zeit danken, ebenso wie den Kooperationspartnern des AK Hartmann Lukas Fischer und Lorand Bonda.

Danke sagen möchte ich auch zu allen Angestellten des Lehrstuhls Makromolekulare Chemie. Danke an Stephanie Scheelen, Sonja Coors, Birgit Ohler, Maria Breuer, Michaela Kitza und Viola Schürmanns.

Bedanken möchte ich mich außerdem bei Dr. Monir Tabatabai für die durchgehende Unterstützung während der Promotion und die Möglichkeit das „Makropraktikum“ zu betreuen. Außerdem möchte ich mich bei allen die bedanken, die das Praktikum mit mir zusammen betreut haben. Tanja Paul, Markus Giesler, Sebastian Bauer und Dr. Stephen Hill. Tut mir leid Markus aber du kannst nicht mehr Kuchenstriche verteilen als ich.

Vielen Dank an alle Kollegen und Freunde die ich während der Zeit im Institut gewonnen habe und diese unvergesslich gemacht haben durch Events auch außerhalb der Universität und auch fachliche Diskussionen und Unterstützung. Danke an Hanqing Wang, Christoph Gerke, Markus, Giesler, Mischa Baier, Sophia Boden, Dana Itskalov, Fawad Jacobi, Sebastian Bauer, Theresa Seiler, Tanja Freichel, Peter Pasch, Patrick Konietzny, Philipp Reuther, Miriam Hoffmann, Michelle Illmann, Serap Üclü, Robert Steinfort, Lennart Hofert, Katharina Bücher und Nina Jahnke.

Außerdem möchte ich mich bei allen Bürokollegen aus der Arbeitsgruppe AK BM Schmidt für die interessanten, hilfreichen und lustigen Gespräche bedanken: Robin Küng, Esther Nieland und Tom Kunde.

Dann möchte ich noch allen Studenten danken, die bei mir Ihre Masterarbeit, Bachelorarbeit oder ein Forschungspraktikum gemacht haben. Florian Malotke, Melina Feldhof, Bastian Springer und Luca-Cesare Blawitzki.

Mein Dank geht auch an Dennis Dietrich und Sebastian Glomb, die während der Bachelorarbeit und auch danach sowohl innerhalb als auch außerhalb der Universität immer für einen Spaß zu haben waren und geholfen haben, wenn Bedarf bestand.

Nicht zu vergessen sind meine Kollegen des AK Schmidt. Danke für die spannende und gute Zeit in Büro und Labor. Ihr habt mir die Zeit sehr angenehm gemacht. Danke an Alberto Camaleño de la Calle, Xi „Jeffrey“ Chang, Fabian Schröer und Dimitri Wilms.

Meiner Familie möchte ich danken für die Unterstützung während der Zeit der Promotion aber auch während des Studiums. Danke, dass ihr immer ein offenes Ohr für meine Probleme hattet und mich in jeder Hinsicht unterstütz habt.

Als letztes möchte ich der wichtigsten Person danken, die mich die ganze Zeit von Anfang des Studiums bis zum Ende der Promotion durch alle Höhen und Tiefen begleitet hat: Tanja Paul. Danke dass du mich immer unterstützt hast egal mit welcher Art von Problemen oder Hindernissen ich konfrontiert war. Danke, dass du immer für mich da warst und alles mit mir durchgestanden hast. Danke, dass du dir meine Präsentationen immer und immer wieder angehört hast und mich besser gemacht hast. Du bist der Grund, dass ich so weit gekommen bin. Ohne dich hätte ich es nicht geschafft. Ich kann dir nicht genug dafür danken.